

Radius	R	105	mm
Insert radius	r_i	7	mm
Hole radius	r_p	10	mm
Face thickness	t_f	0.2	mm
Core thickness	t_c	20	mm
Insert height	h_i	17	mm
Face stiffness	E_f	70.5	GPa
Core stiffness	E_c	310	MPa
Core shear modulus	G_c	138	MPa
Pull out load	P	1000	N

Table 1: Dimensions and material properties used in the benchmarking

$$D = \frac{Et_f d^2}{2} \quad (2)$$

$$S = \frac{G_c d^2}{t_c} \quad (3)$$

In eqns. (2) and (3) E is the Young's modulus of the face sheet, G_c is the shear stiffness of the core material, t_f is the face sheet thickness, t_c is the core thickness, and $d = t_f + t_c$. The analytical expression for the vertical deflection considers a simply supported circular sandwich plate with a centered point load. It consists of two parts; one part describing the deflection due to bending, eqn. (4), and one part describing the deflection due to shear, eqn. (5). A more thorough definition of eqns. (4 - 5) can be found in [13].

$$w_b = \frac{P(1 - \nu)}{16\pi D} \left[\frac{3 + \nu}{1 + \nu} (R^2 - r^2) - 2r^2 \ln \frac{R}{r} \right] \quad (4)$$

P is the point load, R is the radius of the plate, and r is the coordinate along the radial axis, see fig 4.

$$w_s = \frac{P}{2\pi S} \ln \frac{R}{r} \quad (5)$$

The total deflection is $w = w_b + w_s$. As can be seen from eqn. (5), the solution is singular at $r = 0$. Therefore the analytical solution is only valid at a certain distance from $r = 0$. 4.5 mm was used in this study.

4.2 Two dimensional axisymmetric plane FE model

The two dimensional finite element model was constructed using eight node plane elements with capability for axisymmetric analysis, Plane82 [12]. The model was parametrized in order to make it easier to conduct a parametric study. Boundary conditions were applied in a similar way to what is described in the section covering boundary conditions of the module. The center

of the plate was only allowed to move along the z -axis. In order to be able to apply boundary conditions, the FE model was extended by 10 mm compared to the analytical model. In the simply supported model, the extended portion of the top face sheet was restrained in the z -direction. In order to ensure that the stress gradients and peeks were captured a model with a very fine mesh was used. The model had 450611 degrees of freedom, and 74565 elements. Figure 7 shows the area where the top face sheet, potting and insert meet. As can be seen from the figure, the face sheets were modeled with 3 elements through the thickness, the potting was modeled with 36 elements in the r -direction, and the material between the two face sheets, i.e. insert, potting and core, were modeled with 129 elements in the z -direction. The potting measured 3 mm in the r -direction, and the face sheet was 0.2 mm thick. The finely meshed model did, however, not produce any significantly different results from a coarser model with 51214 degrees of freedom and 8386 elements.

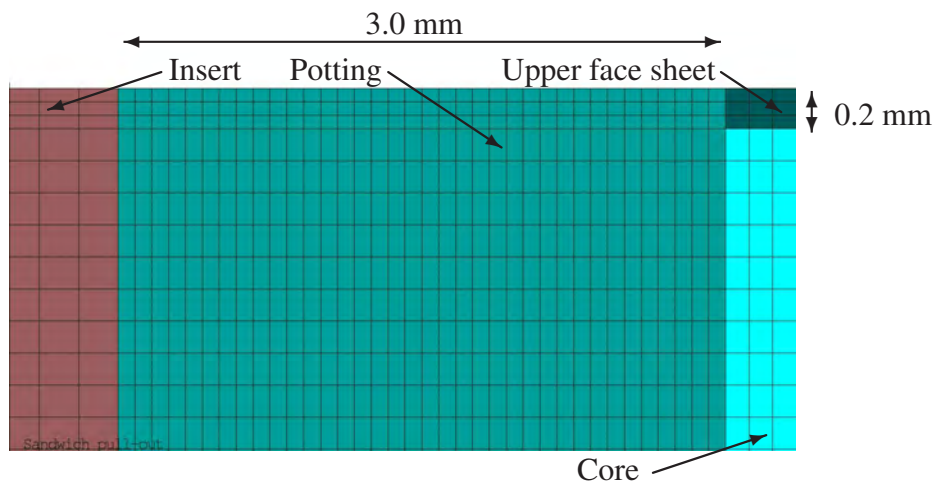


Figure 7: Mesh density in the area where the insert, potting, core and upper face sheet meet.

4.3 3 dimensional plate FE model

The 3 dimensional finite element model was constructed using eight node layered shell elements, Shell91 [12], with the capability to deform in shear. Only a quarter of a circular plate was used, and in order to keep the model as simple as possible, there was no insert modeled at its center. The two radial edges were given symmetry boundary conditions. Thus in-plane translation, and rotation around the edge was restrained. The circumferential edge was restrained in the z -direction for the simply supported model.

4.4 Deflections

Figure 8 shows the predicted deflections of a simply supported sandwich plate according to the different models used. Since the analytical model is singular at $r = 0$ those predictions are only used for $r \geq 4.5mm$. The analytical model, the three dimensional FE model and the developed analysis model show quite good agreement, whereas the two dimensional axisymmetric

model predicts a somewhat lower deflection. The reason for this is believed to be that the model is a plane 2D model not allowing for displacement in the θ -direction or rotation around the θ or z -axis, thus generating a somewhat stiff model.

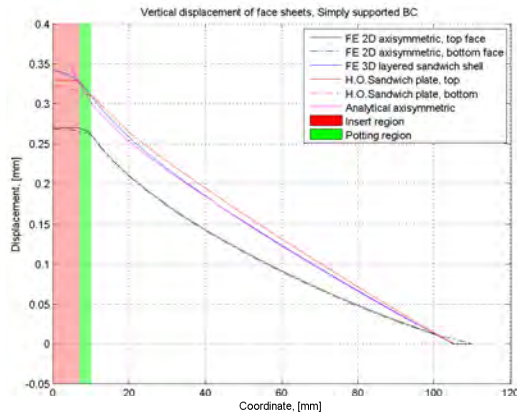


Figure 8: Predicted deflection of simply supported sandwich plate at $P = 1000N$

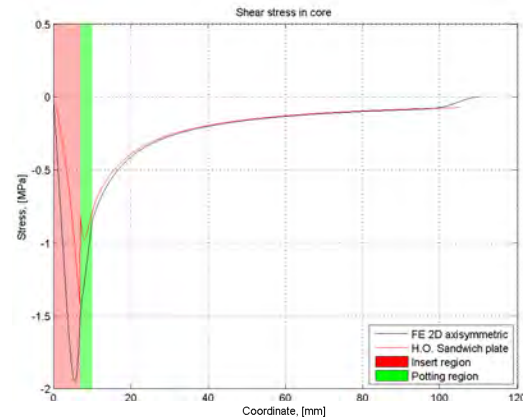


Figure 9: Predicted shear stress distribution in core at $P = 1000N$

4.5 Stress levels

Since the insert was not modeled in the three dimensional plate FE model and the shell elements used did not resolve local stress gradients through the thickness of the plate, the stress results from the high-order model were only compared with the results from the two dimensional plane axisymmetric FE model. Figure 9 shows the predicted shear stress in the center plane of the sandwich panel, with insert and potting region marked in red and green respectively. Outside the potting the two models show good agreement. Within the potting there is a certain disagreement which may be attributed to a finite element mesh that was not fine enough. Tests with mesh refinement did however not show any significant changes in the predicted shear stresses within the potting. The agreement between the two models is not good within the insert. However, the most common modes of failure in pull out of inserts in sandwich panels are shear failure in the core material or disbonding between the core material and face sheets or disbonding between the potting and the face sheets [2]. Therefore the results within the insert are assumed not to affect the prediction of the failure loads in the governing failure mechanisms.

Transverse normal, peel, stress, or tensile stress, along the upper interface is shown in figure 10. The upper interface is defined as a line at the height of the lower side of the upper face sheet where it connects to the core material. The line also goes through the top of the potting and the insert. The predictions from the two dimensional axisymmetric FE model and the proposed model show good agreement along most of the interface. The area where the agreement is not so good is within the insert. This is assumed to be because the loads are applied in different ways in the two models. In the FE model the load is applied as a point load, whereas in the proposed model it is applied as a distributed load spread out over the surface of the insert.

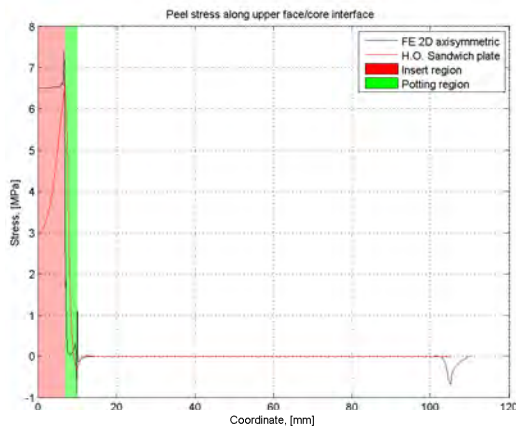


Figure 10: predicted stress distribution in interface between top face sheet and core constituents at $P = 1000N$

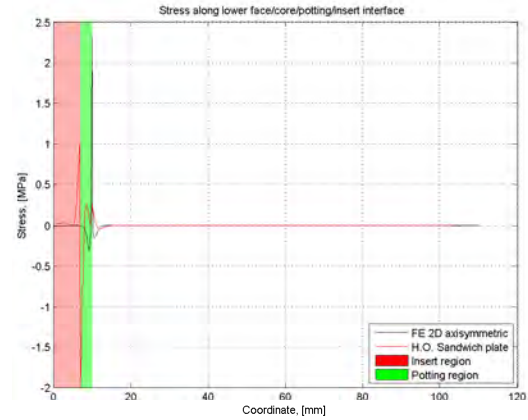


Figure 11: Predicted stress distribution in interface between bottom face sheet and core constituents at $P = 1000N$

Figure 11 shows the predicted peel stress, or tensile stress, along the lower interface. The lower interface is defined as a line at the height of the top side of the bottom face sheet where it connects to the potting and the core material. Along most of the interface the stresses are predicted to be zero, or very close to zero. At the transition between the core and the potting the predictions show some stress singularities. Since the stress levels are relatively low they are assumed not to be of significance to the pull-out strength of the insert, but to be sure it should be assessed with material tests.

5 Failure analysis

Two examples of possible output from the proposed analysis model are given below. This is not an exhaustive list, only a presentation of two possibilities which are believed to be most interesting when analyzing pull-out strength of inserts in sandwich plates. The loading, boundary conditions, and geometry are the same as used in the benchmarking section. Material properties for the potting are taken from the material data sheet for 3M DP760, and the material data for the core material are taken from the material data sheet for Hexcel HexWeb CRF-1/4-ACG-.002-3.4. Because of limited availability of material properties, the compressive strength is assumed to be equal to the tensile strength for both materials. The material data used are presented in table 2. A test series to verify the predictions shown here is initiated, but not finalized therefore experimental data cannot be presented.

Shear failure in core or potting

One of the common modes of failure in pull-out of inserts in sandwich panels is core shear failure [2], [8], [14], and [15]. A quadratic shear failure criterion according to eqn. 6 was implemented in the proposed analysis model. The predicted failure index is shown in figure 12. The upper graph shows the distribution within the potting, and the lower graph shows the

Core Young's modulus	E_c	540	MPa
Core shear modulus	G_c	195	MPa
Core shear strength	$\hat{\tau}_l$	1.4	MPa
Core shear strength	$\hat{\tau}_w$	0.85	MPa
Core compressive strength	$\hat{\sigma}_c$	0.85	MPa
Potting Young's modulus	E_p	5.9	GPa
Potting shear modulus	G_c	2.2	GPa
Potting shear strength	$\hat{\tau}_p$	29	MPa
Potting compressive strength	$\hat{\sigma}_c$	79	MPa

Table 2: Material properties for core material and potting used in the examples below

distribution within the core material.

$$S_{sc} = \left(\frac{\tau_{rz}}{\hat{\tau}_{rz}} \right)^2 + \left(\frac{\tau_{\theta z}}{\hat{\tau}_{\theta z}} \right)^2 \leq 1 \quad (6)$$

In eqn. 6 τ_{ij} is the stress level in the ij direction according to the analysis, and $\hat{\tau}_{ij}$ is allowable stress in the same direction. The criterion predicts failure when the value is equal to or greater than one. With the material properties in table 2 inserted into the analysis model, shear failure is predicted to occur in the potting at a pull out load of 844 kN, and shear failure in the core is predicted to occur at a pull out load of 3.10 kN. As can be seen in the lower graph in figure 12 failure is predicted to occur in the core at the intersection between core and potting.

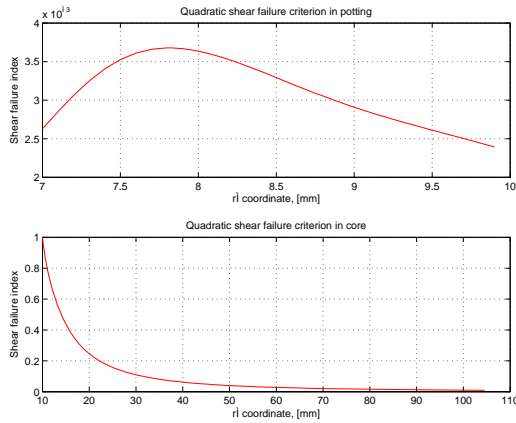


Figure 12: Predicted shear failure criterion, failure due to stress is predicted when $S_{sc} \geq 1$. Predicted mode of failure, shear failure in core at a predicted failure load $P_{crit} = 3.10kN$

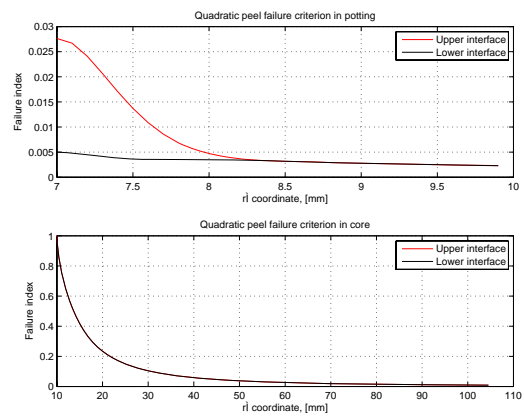


Figure 13: Predicted peel failure criterion, failure due to peel is predicted when $S_{pc} \geq 1$. Predicted mode of failure, peel of face sheet from core at a predicted failure load $P_{crit} = 2.96kN$

Peel of face sheet from core or potting

Another important mode of failure in pull-out of fully potted inserts in sandwich panels is peel, or separation, of the rear side face sheet from the core material or potting [2]. A quadratic criterion taking both tensile stresses and shear stresses according to eqn. (7) into account was implemented into the analysis model. The upper graph in figure 13 shows the failure index at the interface between the face sheet and potting, and the lower graph in figure 13 shows the failure index at the interface between the face sheet and the core material.

$$S_{pc} = \left(\frac{\sigma_z}{\hat{\sigma}_z} \right)^2 + \left(\frac{\tau_{rz}}{\hat{\tau}_{rz}} \right)^2 + \left(\frac{\tau_{\theta z}}{\hat{\tau}_{\theta z}} \right)^2 \leq 1 \quad (7)$$

In eqn. (7) σ_z is the predicted stress, and $\hat{\sigma}_z$ the allowable tensile stress in the interface. Failure is predicted to occur when the value equals or exceeds one. Using the material data in table 2; peel failure in the upper interface between the face sheet and the core is predicted to occur at a pull out load of 2.96 kN, and peel failure between the lower face sheet and the core is predicted to occur at a pull out load of 2.98 kN. As figure 13 shows, failure is predicted to occur in the core at the intersection between the core and the potting.

6 Conclusion

A model for the analysis of the pull-out strength of inserts in sandwich panels has been assessed. The predicted deflections showed good agreement compared with predictions made with an analytical expression, a 2 dimensional axisymmetric plane FE model, and a 3 dimensional sandwich plate model. Stress levels were compared between the proposed model and a 2 dimensional FE model; shear stress levels in the middle of the sandwich plate, and peel stress levels along the interface between the top face sheet and core and potting as well as the interface between the bottom face sheet and core and potting. Good agreement was found between predictions along the interfaces between the face and core, and also in the interface between the face and potting. For initial calculations of the strength of an insert in a sandwich panel, the proposed model could prove to be a very powerful and relatively simple tool to use.

7 Acknowledgments

The work presented herein was conducted under ESA/ESTEC/Contract No. 19860/06/NL/PA - "Failure Analysis for Inserts in Sandwich Plates". ESA is the European Space Agency, and ESTEC is the ESA Technology Center. The ESTEC Project Officer was Dr. Andreas Obst. The support received is gratefully acknowledged.

REFERENCES

- [1] D. Zenkert, editor. *The handbook of sandwich construction*. Engineering Materials Advisory Services Ltd., London, UK, 1997.

- [2] *Insert design handbook*. ESA-PSS-03-1202. ESA Publication Division, ESTEC, Noordwijk, The Netherlands, 1987.
- [3] O.T. Thomsen. Analysis of sandwich panels with 'through-the-thickness' inserts using a high-order sandwich plate theory. Technical report, ESTEC, 1994. EWP-1807.
- [4] O.T. Thomsen. Analysis of sandwich panels with 'fully potted' inserts using a high-order sandwich plate theory. Technical report, ESTEC, 1995. EWP-1827.
- [5] O.T. Thomsen and W. Rits. Analysis and design of sandwich plates with inserts – a high-order sandwich plate theory approach. *Composites Part B*, 29:795 – 807, 1998.
- [6] O.T. Thomsen. Sandwich plates with 'through-the-thickness' and 'fully potted' inserts: evaluation of differences in structural performance. *Composite structures*, 40(2):159 – 174, 1998.
- [7] K.B. Kristensen. Stress singularities caused by inserts in sandwich structures. Technical report, Aalborg University, Department of Mechanical Engineering, 1994. Report no 64.
- [8] P. Bunyawanchakul. *Contribution l'étude du comportement des inserts dans les structures sandwichs composites*. PhD thesis, L'cole nationale supérieure de l'aéronautique et de l'espace, 2005. N° d'ordre: 422.
- [9] E. Bozhevolnaya and A. Lyckegaard. Local effects in the vicinity of inserts in sandwich panels. *Composites Part B*, 35:619 – 627, 2005.
- [10] E. Bozhevolnaya and A. Lyckegaard. Structurally graded core inserts in sandwich panels. *Composite Structures*, 68:23 – 29, 2005.
- [11] N.G. Tsouvalis and M.J. Kollarini. Parametric study of stress concentrations caused by inserts in sandwich panels. In *Proceedings to the 12th European Conference on Composite Materials*, 2006.
- [12] SAS IP, Inc., Canonsburg, USA. *Release 11.0 Documentation for ANSYS*, 2007.
- [13] D. Zenkert. *An Introduction to Sandwich Construction*. Engineering Materials Advisory Services, London, UK, 1995.
- [14] P. Bunyawanchakul and B. Castanie. Experimental and numerical analysis of inserts in sandwich structures. *Applied Composite Materials*, 12:177 – 191, 2005.
- [15] F. Noirot, J.-F. Ferrero, J.-J. Barrau, B. Castanie, and M. Sudre. Analyse d'inserts pour les structures sandwich composites. *Mcanique & Industries*, 1:241 – 249, 2000.

EFFECT OF PHYSICAL NON-LINEARITY ON LOCAL BUCKLING IN SANDWICH BEAMS

Vitaly Koissin ¹, Andrey Shipsha ² and Vitaly Skvortsov ³

¹ Dept. of Metallurgy and Materials Engineering, Katholieke Universiteit Leuven,
Kasteelpark Arenberg 44, B-3001 Heverlee, Belgium
e-mail: vitaly@kth.se, web-page: www.mtm.kuleuven.be

² Inspecta Technology AB, Box 30100, S-104 25 Stockholm, Sweden
e-mail: andrey.shipsha@inspecta.com, web-page: www.inspecta.se

³ Dept. of Strength of Materials, State Marine Technical University,
Leninski prospect 101, 198 262 St.-Petersburg, Russia
e-mail: skv@vs4113.spb.edu, web-page: www.smtu.ru

Key words: Sandwich structure, Wrinkling, Local buckling, Modelling.

Summary. *This article deals with experimental, theoretical, and FE characterization of the local buckling in foam-core sandwich beams. In the theoretical approach, this phenomena is considered in a periodic formulation (unbounded wrinkle wave); a non-linear stress-strain response of the face material is accounted for. In the FE approach, non-linearity of the core material is modelled also. Full-field strain measurement is employed in the tests showing that the commonly used edgewise compression set-up can cause premature waviness of the faces and, therefore, nonlinear local deformations in the core layer.*

1 INTRODUCTION

The wrinkling (local buckling) problem is an important part of the sandwich design, since the core layer provides a limited support for the in-plane compressed face sheets. This has been investigated in many studies, and a number of experimental findings and theoretical approaches appeared. The known solutions usually assume an explosive (bifurcation-type) and unbounded propagation of the wrinkle waviness and a purely elastic behaviour of the core material. The face sheet material is also often considered as ideally elastic. However, many materials (polymer composites, metals, etc.) exhibit a non-linear deformation prominent under high stresses. The foam materials can also show a nonlinear response even at small strains. Finally, the local buckling usually does not occur simultaneously on the entire sandwich panel. All these features can cause the failure onset at a significantly lower load than that predicted by a linear-elastic model.

In this article, the local buckling of a typical foam-core sandwich is studied under uniaxial edgewise compression. The test set-up is shown to produce a complex stress-strain field in the core layer. Due to the nonlinear core material response, this effect results in a premature failure that can be adequately predicted only using an FE model.

Table 1: Basic mechanical properties of the sandwich constituents (tension/compression).

material	thickness, mm	E, MPa	ν	ε_{ult} , %	σ_{ult} , MPa	γ_{ult} , grad	τ_{ult} , MPa
GFRP	2.4	24540 ^a	0.25	2.2 ^a /1.4 ^b	295 ^a /291 ^b	–	–
WF51	50	85 ^c	0.32	3.3 ^d /2.3 ^c	1.42 ^d /0.90 ^c	1.2 ^e	0.5 ^e

^a ASTM D 638M ^b ASTM D 3410 ^c ASTM D 1623-78 (out-of-plane of the foam block)
^d ASTM D 3039 (in-plane of the foam block) ^e ASTM C 273 (in-plane of the foam block)

2 EXPERIMENTAL

The object of study are straight beams (47×270 mm in-plane dimension) comprised of thick Rohacell WF51 foam core and relatively thin transversely quasi-isotropic faces. The latter is made of 4 layers (symmetric lay-up) of E-glass non-crimp fabric impregnated with vinylester resin. Basic material data (the Young’s modulus E , ultimate stress, σ_{ult} , τ_{ult} , and strain, ε_{ult} , γ_{ult}) are listed in Table 1. The Poisson’s ratio, ν , is either estimated by the laminate theory or taken from the core manufacturer’s data sheet, Ref. [1]. Figures 1 and 2 show typical load curves and tangent moduli (derived by differentiation of the curves) of these materials under a quasi-static uniaxial loading. Large drop in the tangent moduli prior to the failure can be seen in Fig. 2, especially for the compressed foam material.

The edgewise compression tests are performed according to ASTM C364–94. The specimen edges are reinforced with 15 mm long tabs made of the same laminate as the face sheets and glued at their outer surfaces. Then, the edges are milled to ensure that they are flat and parallel. The specimens are compressed between two rigid plates at the cross-head displacement rate of 2 mm/min. Series of 10 specimens is tested.

A full-field displacement registration equipment (one digital camera with 1 fps picture frequency and Limes software) was used for several tests. Figure 3 shows a typical

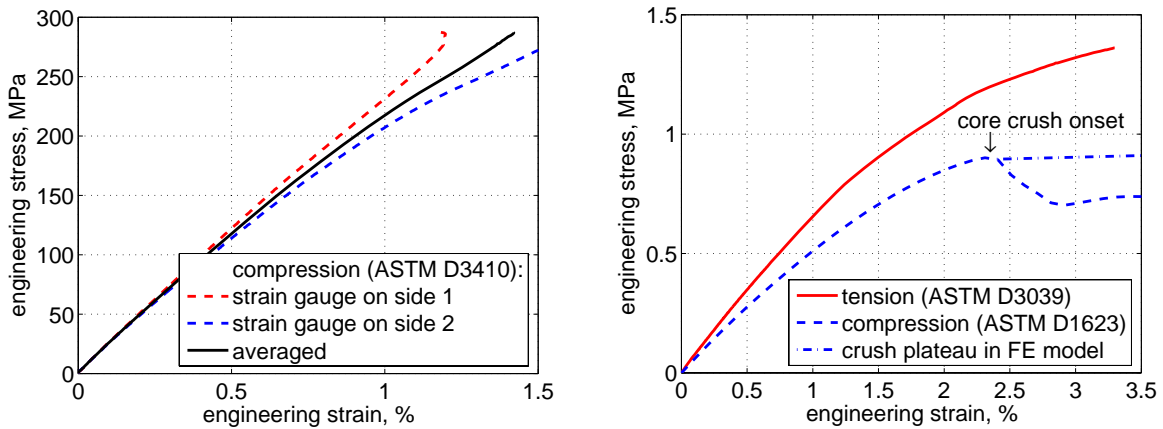


Figure 1: Stress-strain curves for GFRP (left) and WF51 (right) under uniaxial loading.

transversal strain field observed prior to the failure. It is seen that a significant local deformation occurs in the core due to the face sheet waviness. This waviness appears already at the early loading stage, obviously due to 1) a load eccentricity (because of tabs) and 2) self-fixation of the edges at the loading plates that results in a slight swell of the specimen (because of the Poisson's effect). In principle, the first difficulty can be overcome by gluing extra tabs into the core underneath the face sheets. The second difficulty seems to be an inherent property of this standard test, since the friction inevitably prevents free transversal displacements of the specimen edges.

Figure 4 shows typical strain distributions along the face-core interface (at about 1 mm distance below the interface) for two loading stages. Particularly, Fig. 4(right) shows the strain components measured under the bottom face in Fig. 3 (i.e. less than 1 sec before the failure). Data shown in Fig. 4(left) are measured at the same line but much earlier (under approximately 1/2 of the ultimate load). Both plots exhibit waviness having prominent maximums near the tabs. At the moment of failure, the maximal compressive strain underneath the face-core interface is about 4% that is two times more than the yield strain typical for this foam grade, Table 1. Corresponding inward transversal displacements are

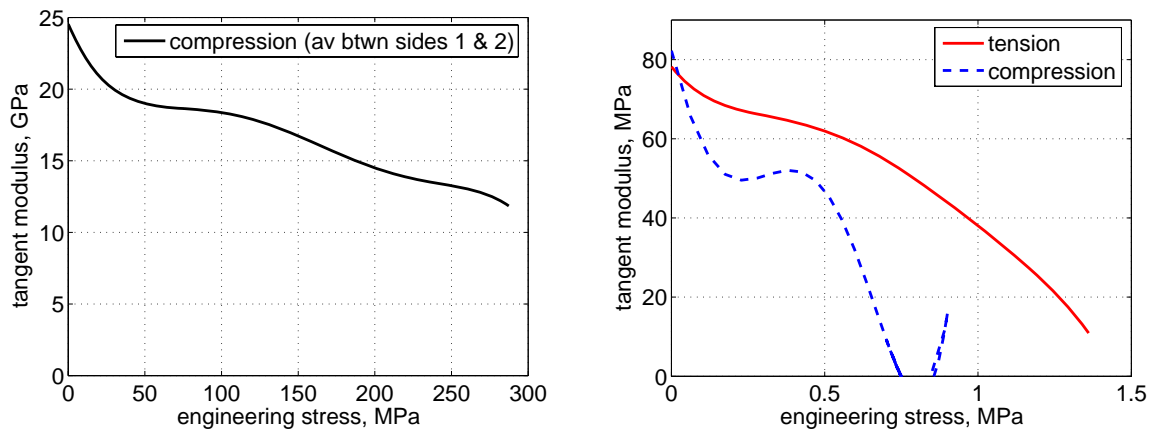


Figure 2: Tangent moduli for GFRP (left) and WF51 (right) under uniaxial loading. Fitted with the 5-th order polynomials, since the original data show a large scatter.

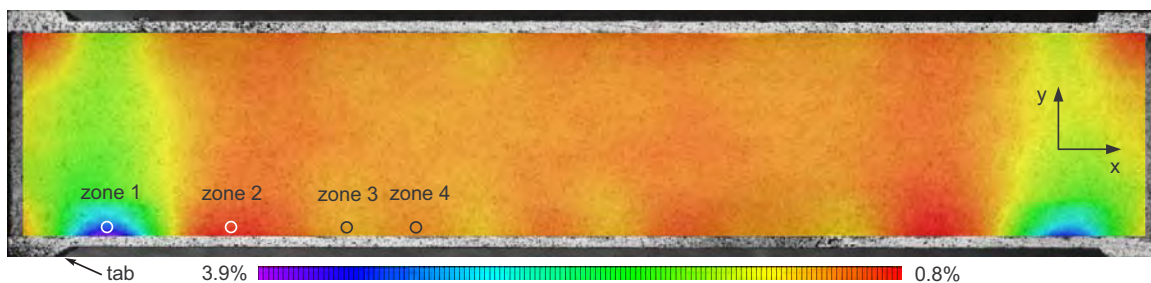


Figure 3: Typical strain field (ϵ_y) observed in the core prior to the failure.

about 0.6–0.8 mm. The tensile strain in the adjacent bulges approaches 1%; the maximal outward displacement is about 0.4–0.5 mm . Taking into account the non-linear material response, Fig. 1(right), it is obvious that the supporting effect of the core layer decreases or even vanishes (due to the core crushing in compression) in these local areas.

Figure 5(left) shows progression of several strain maximums (compressive and tensile) during the loading. The strains are measured and averaged within small circles near the bottom face as shown in Fig. 3. The 1st and 2nd maximums show almost constant strain rate until a certain moment, when it increases suddenly. This can be attributed to the local buckling onset. The 3rd and 4th maximums do not show such a behaviour. Thus, the buckling is localized near the tabs and, in spite of a continuous waviness of face sheets, does not occur in the central part of the specimen, obviously due to almost intact (stiffer) support of the core layer. The face sheet debonding apparently starts in the 2nd zone, most likely by a shear or tensile fracture of the foam material at the face-core interface.

The load curve (load cell signal vs. edge displacement), especially after its differentiation as shown in Fig. 5(right), can also be an indicator of the local buckling onset. It is seen that, after a short period of the clearance adjustment, the overall stiffness culminates in step #20 and then decreases gradually by about 25%. This effect should be attributed to a gradually increasing face sheet waviness as well as to a non-linear behaviour of the face and core materials. At step #98, the stiffness starts to degrade rapidly. This moment coincides with the local buckling onset seen in Fig. 5(left).

The test data are given in Table 2 in comparison with the theoretical and FE results discussed below. The ultimate stress is used, because they differ very little from the buckling onset values. Since the in-plane stiffness of the laminate is much larger than that of the core layer, the compressive stress in the face sheet is calculated as

$$\sigma = P/2h_f b, \tag{1}$$

where P is the total load, h_f is the face thickness, and b is the beam width.

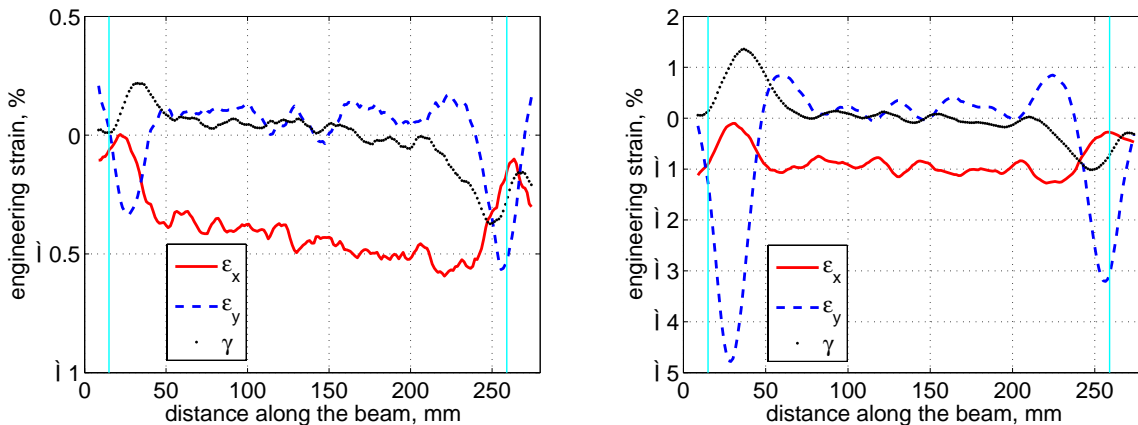


Figure 4: Typical distribution of strains at the face-core interface (bottom face in Fig. 3): step #51 (left) and #102 (right). Vertical lines indicate ends of the tabs.

Table 2: Ultimate strength obtained experimentally vs. theoretical and FE predictions.

	test data, Eq.(1)	all linear-elastic Eq.(2) FE		nonlinear-elastic face Eq.(3) FE		all nonlinear-elastic FE
σ_{ult} , MPa	168.3–192.4	317.1	344.1	279.9	293.0	216.8

3 THEORETICAL

Consider static bending of an infinite beam (which represents the face sheet) having thickness h_f and bonded to an isotropic half-plane (which represents an infinitely thick core layer). The beam is axially compressed by a “dead” force σh_f (per unit width). The face sheet is assumed to be thin and non-stretchable and to keep the straight form of equilibrium up to the critical state. Thus, there is no difference between displacements at its midplane and at the face-core interface, and no influence of the interfacial shear stress. As a first approximation, both the face and core materials are considered as ideally linear-elastic. Using the thin plate Kirchoff-Love theory for the face and Lamé equations for the core, the critical (in the Euler’s sense) stress for this model is, Ref. [2],

$$\sigma_{ult} = \frac{3}{\sqrt[3]{4}} \frac{x_n}{h_f} E_1, \quad x_n^3 = \frac{D_f}{E_1}, \quad D_f = \frac{E_f h_f^3}{12}, \quad E_1 = \frac{2E_c}{(1 + \nu_c)(3 - \nu_c)}, \quad l = \pi \sqrt[3]{2} x_n \quad (2)$$

where D_f is the flexural rigidity of the face sheet, E_1 is the reduced elastic modulus of the core layer (plane stress state is assumed), and l is the natural wavelength.

Using Eq. (2) and elastic properties from Table 1, the critical stress is easily calculated. However, its value exceeds the average test data (175.7 MPa) in 80%, Table 2. The natural wavelength is estimated to be about 33 mm that also disagrees with Fig. 4.

Of course, a better approach is to account for the nonlinear behaviour of the face sheet material. For example, the reduced modulus of elasticity (called also the von Kármán’s

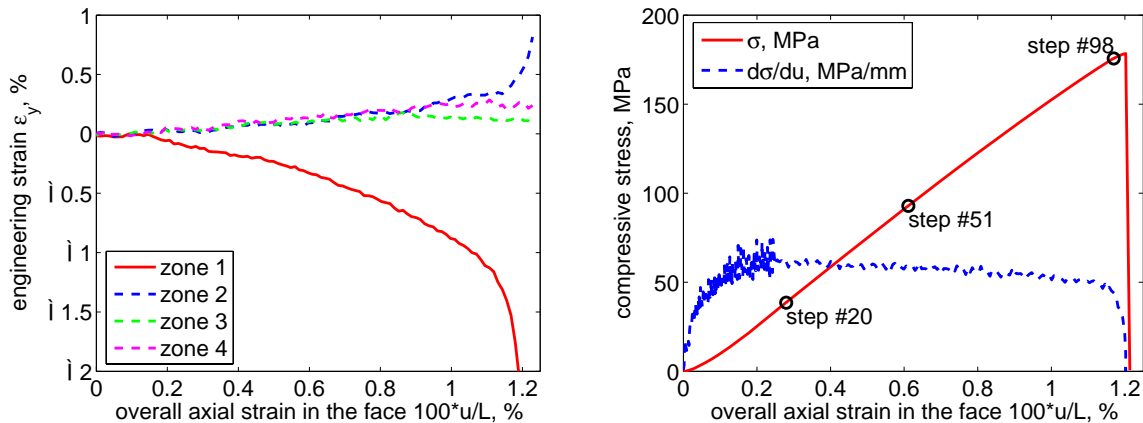


Figure 5: Typical growth of the max. strain in the core (left) and typical load-displacement response (right, σ is given by Eq. (1)) under edgewise compression. L is the beam length; u is the edge displacement.

modulus) can be used. In the present case of a rectangular cross-section its reads as

$$E_r(\sigma) = \frac{4E_f E_t(\sigma)}{(\sqrt{E_f} + \sqrt{E_t(\sigma)})^2}, \quad (3)$$

where E_t is the tangent modulus, Fig. 2(left). The reduced modulus theory assumes that a stress release occurs on the convex side of the beam simultaneously with the buckling onset. For a short-length wrinkle wave the use of Eq. (3) is even conservative, since certain portions of the face sheet undergo mainly rotation with a minor bending and thus have a stress release on both sides. This is because the wrinkled face sheet is less shortened than in the case of an ideally uniaxial deformation. Therefore, the “correct” critical stress will lie somewhere above the value calculated using the reduced modulus, Refs. [3, 4].

After substitution of Eq. (3), Eq. (2) becomes non-linear and requires a numerical procedure. Solution is given in Table 2. As can be seen, the reduced modulus theory gives more realistic estimation of the critical stress if compare with the purely elastic solution; however, the predicted value is still 60% higher than the experimental one. The natural wavelength is estimated to be about 29 mm that is also still not realistic.

Thus, the face sheet material nonlinearity has important but not primary destabilizing influence on the structure. To approach a more accurate solution, it is necessary to account for localization of the face sheet bending and for local nonlinear deformation of the core material, which are observed in the experimental study. Obviously this can not be achieved analytically, and an FE analysis should thus be applied.

4 FE ANALYSIS

The FE package COSMOSM is used. Since the core layer is thick and the strains decay rapidly through its thickness, Fig. 3, only one face sheet and half of the core thickness are modelled. Schematic of the model with applied boundary conditions is shown in Fig. 6.

The core is meshed as a rectangular domain with 4-node isotropic shell elements (SHELL4). The face and tabs are meshed with 2-node beam elements (BEAM2D). The model is composed of 10 elements through the core and 108 elements lengthwise, i.e. a 2.5×2.5 mm mesh is created. The tabs have the same mesh density and are coupled node-to-node to the face, enforcing the two nodes to rotate and move by the same amount.

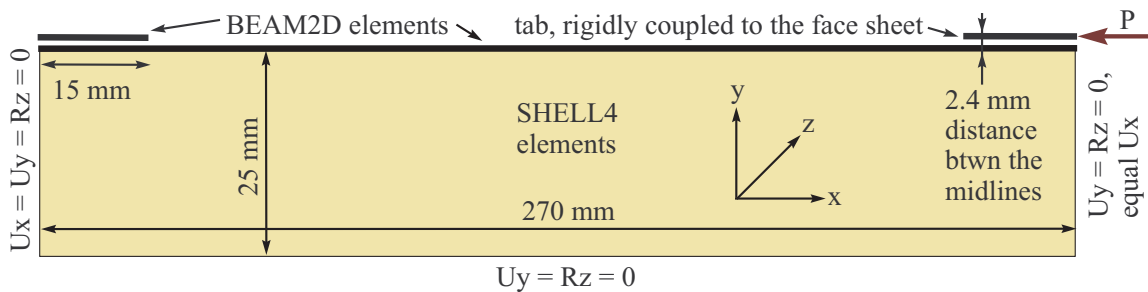


Figure 6: Schematic of the FE model, not scaled.

A conservative compressive load (concentrated force) is applied at the edge of one of the tabs. Actually, it should be applied somewhere in between the tab midplane and the face midplane, or applied in two portions at both midlines. The used way is a conservative simplification resulting in a larger load eccentricity.

The linear-elastic analysis is performed first. The buckling mode (only the 1st mode is considered here) is shown in Fig. 7(top); a slight non-symmetry is seen which can be attributed to a limited length of the model. The critical stress agrees well with the theoretical estimation by Eq. (2), Table 2; the difference does not exceed 10%. The wavelength is about 30 mm that is also close to the theoretical results.

A more refined model accounts for the nonlinear elastic response of the face sheet material, Fig. 1(left). In the software, the nonlinear elastic model relies on the assumption of proportional loading, when components of the stress tensor vary monotonically in a constant ratio to each other. Then, the total strain vector is used to compute the effective strain to obtain the current position at the defined stress-strain curve, Ref. [5].

Result of a geometrically linear FE analysis is given in Table 2 and shows a minor (about 5%) discrepancy with the theoretical value calculated using the reduced modulus theory. The buckling mode (again non-symmetric with respect to the centre) is shown in Fig. 7(bottom). However, the wavelength is about two times smaller than the theoretical one (12 mm vs. 29 mm). The reason for this effect is not yet clear for the authors.

Finally, nonlinear response of the core material is also introduced into the FE model, according to Fig. 1(right). The same nonlinear elastic material model is used as for the face sheet; the foam crush plateau is modelled as almost horizontal line producing very low tangent modulus, see the dash-and-dot line in Fig. 1(right). Geometrically nonlinear analyses are performed to calculate the equilibrium displacement solutions for a number of given loads, by using the modified Newton-Raphson method under the load control.

The deformed shape and strain fields are shown in Fig. 8 for the load step #18 at which, as proved below, the local buckling occurs. Comparison with the full-field measurements, Fig. 3, reveals a good agreement of the strain pattern. However, the FE analysis overestimates the maximal strains by a factor of 2. This can be due to 1) significantly increased, if compare to a real specimen, load eccentricity and 2) localization of the core “crushing” in the elements adjoining the face sheet (in a real specimen, the foam cells are filled with the resin at the interface and thus have a smoother strain field).

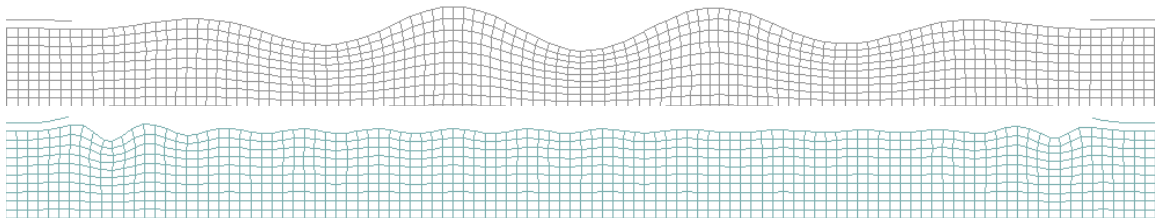


Figure 7: Buckling modes: linear-elastic face and core (top) or nonlinear elastic face and linear-elastic core (bottom). Geometrically linear solutions.

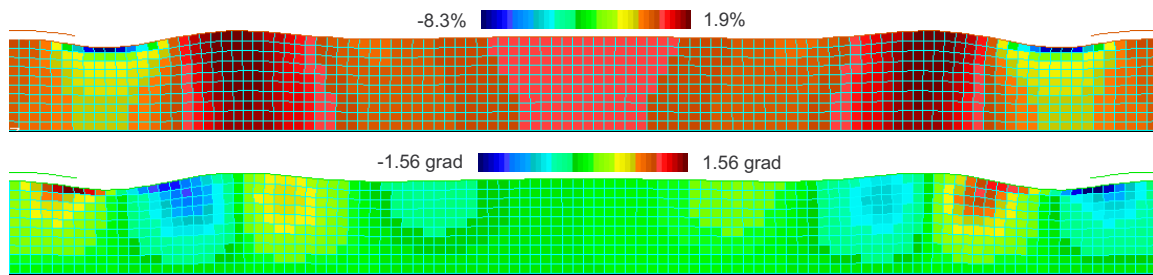


Figure 8: Strain fields at the load step #18: transversal, ε_y , (top) and shear, γ , (bottom). Nonlinear elastic face and core, geometrically nonlinear solution. The deformed shape is scaled by a factor of 5.

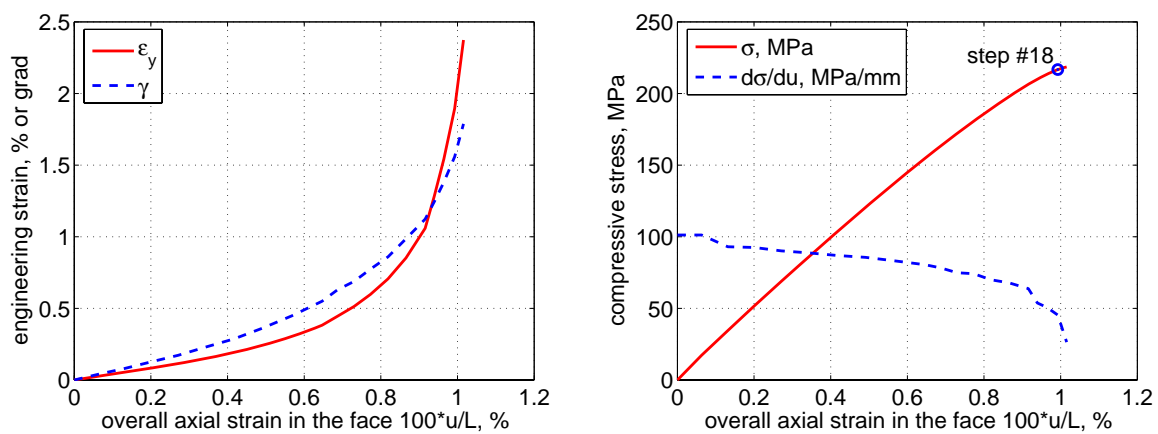


Figure 9: Growth of the max. strains in the core (left) and load-displacement response (right) in the nonlinear FE analysis. L is the beam length; u is the edge displacement. Positive strains are displayed.

Figure 9(left) shows growth of the maximal strains in the core during the loading. It is seen that the tensile strain under the bulge (that corresponds to zone #2 in Fig. 3) can not initiate the failure, since the ultimate value (3.3%, Table 1) is not reached. The model can most likely fail by the shear fracture, since the maximal shear stress exceeds the ultimate value of 1.2 grad. But these are very rough speculations hardly applicable to the real sandwich beams, because the shear strength data are obtained on large foam specimens, which failed due to a stress concentration, Ref. [6]. Last but not least, the used rheological model (nonlinear elasticity with proportional strain growth) and uniaxial test data can not provide a quantitatively correct results for the strain fields.

The load curve is shown in Fig. 9(right), along with the stiffness function. They generally resemble Fig. 5(right), although the FE model produces a stiffer response. As in the real specimens, the stiffness degradation accelerates at a certain moment (step #18), which may be considered as the local buckling onset. The corresponding stress, Table 2, is close to the upper limit of the test data, the difference is only 13%. Taking into account imperfections existing in the real specimens and simplifications introduced in the FE analysis, such a result is wholly satisfactory.

5 CONCLUSIONS

The main results of this preliminary study can be outlined as

- the specimen configuration commonly used in the edgewise compression testing of sandwich beams has a load eccentricity due to the presence of tabs. This causes a local bending of the face sheet accompanying by a nonlinear deformation of the foam core. As a result, the buckling is localized, and the ultimate load can significantly be lower than that predicted by a linear stability analysis;
- therefore, for some combinations of the sandwich constituents, nonlinearity of the face sheet and core materials can be very important for a correct prediction of the ultimate load. These effects can adequately be accounted for only in an FE analysis. It is demonstrated that the simplest uniaxial test data combined with a low-CPU FE model can provide a solution sufficient for the engineering purposes;
- the results can be improved by introducing more realistic rheological behaviour and by using more complex test data (e.g. for multi-axial strain state) in the FE model, especially for the core material. Also, a better load application can be modelled by using the shell or solid elements for the face sheet (and, consequently, for the core layer in the latter case) as well as by accounting for non-uniformity of the density distribution through-the-thickness of the foam core, Ref. [6].

6 ACKNOWLEDGEMENTS

This study was done within the I-TOOL (“Integrated Tool for Simulation of Textile Composites”) project founded by the European Commission. The authors are thankful to Prof. Stepan Lomov (Dept. MTM, Katholieke Universiteit Leuven, Belgium) for his interest to this study. Mr. Dmitry Ivanov (ibid) is gratefully acknowledged for his help with full-field strain measurements. Authors would also like to thank Mr. Kris Van de Staey (ibid) for assistance with the mechanical testing.

REFERENCES

- [1] ROHACELL. *Technical manual*. Darmstadt: Röhm GmbH. (1987).
- [2] V. Koissin V., Skvortsov, A. Shipsha. Stability of the face layer of sandwich beams with sub-interface damage in the foam core. *J. Compos. Struct.*, 78(4):507–518 (2007)
- [3] A.S. Vol'mir. *Stability of Structures*. Nauka, Moscow (1967). [in Russian]
- [4] Z.P. Bažant and L. Cedolin. *Stability of Structures: elastic, inelastic, fracture, and damage theories*. Dover Publications Inc., New York (2003).
- [5] Cosmos/M 2.0 User's guide (1998).
- [6] V. Koissin and A. Shipsha. Residual in-plane mechanical properties of transversely crushed structural foams. To appear in *J. Sandwich Struct. Mater.*

PROBABILISTIC HOMOGENIZATION ANALYSIS OF SOLID FOAMS ACCOUNTING FOR DISORDER EFFECTS

Jörg Hohe* and Volker Hardenacke*

* Fraunhofer Institut für Werkstoffmechanik (IWM)
Wöhlerstr. 11, 79108 Freiburg, Germany
e-mail: joerg.hohe@iwm.fraunhofer.de

Key words: Core materials, Modeling, Micro structural disorder, Probabilistic analysis.

Summary. *The present study is concerned with a probabilistic homogenization analysis of solid foams. In order to account for the effect of micro structural disorder, a local probabilistic approach is proposed. The analysis is applied to different two-dimensional model foams, where the effects of the disordered microstructure on the effective properties are outlined.*

1 INTRODUCTION

Solid foams are important core materials in modern sandwich construction. The main advantages of this class of materials are their low specific weight in conjunction with their ability to perform additional, non-mechanical functions such as e.g. heat insulation. Disadvantage is the disordered random microstructure leading in many cases to a distinct scatter in the macroscopic material response.

Since the pioneering work of Gent and Thomas [6] appeared, numerous studies on the mechanics of foamed materials and the numerical homogenization analysis of these materials have been published (e.g. Gibson and Ashby [7], [8], Warren and Kraynik [16]). Most of these analyses are based on a regular periodic model of the micro structure. On the other hand, structural foams may exhibit a distinct micro structural disorder resulting in a distinct uncertainty in the effective properties whether determined experimentally or numerically. Experimentally, the distinct variability has been proven especially in the recent systematic studies by Blazy et al. [1] as well as by Ramamurthy and Paul [11] where strong variabilities of all effective mechanical properties have been observed. Especially in the latter study, local variations in the relative density of the material have been identified as an important source of macroscopic uncertainties in the material response.

Most of the numerical approaches dealing with the effects of micro structural disorder are based on a homogenization analysis using a single large scale representative volume element where the micro structural geometry is determined in a randomized manner (e.g. Huyse and Maes [10], Roberts and Garboczi [12], Shulmeister et al. [13], Zhu et al. [17]). The computational foam model is in most cases generated using a Voronoi [15] tessellation of the representative volume element, either in its direct (Γ -) version or in a constrained form (δ -Voronoi

tessellation) requiring a minimum distance of neighboring cell nuclei (e.g. Chen et al. [2]). Although these approaches are able to account for the effects of the randomness of the micro structure on the average material properties, they are unable to assess the scatter of the properties. Furthermore, extremely large representative volume elements are required in order to get convergent results. Evidence are the remaining numerical anisotropies observed in several studies.

In order to circumvent the mentioned problems, Fortes and Ashby [5] have proposed a direct probabilistic approach based on the probability of the cell wall orientations in space. Other probabilistic approaches have been proposed by Cuitiño and Zheng [3] based on a Taylor averaging technique. In order to assess especially the scatter in the effective properties, Hohe and Becker [9] have used a numerical technique based on the multiple analysis of a small scale volume element with randomized micro structure in conjunction with a stochastic evaluation of the results.

In the present study, a different approach is employed, where a large scale statistically representative volume element for the micro structure is subdivided into small, statistically non representative testing volume elements. For the testing volume elements, the homogenization analysis is performed and the results are evaluated by stochastic methods, providing the probability distributions for the effective properties. The computational foam models are generated using a Voronoi technique in Laguerre geometry (see e.g. Fan et al. [4]) which was found to provide the most appropriate models for foamed materials. For simplicity, all analyses are performed in two dimensions. Nevertheless, an extension to three dimensions can be performed in a straight forward manner.

2 LOCAL PROBABILISTIC HOMOGENIZATION

2.1 Strain energy based concept

The homogenization analyses in the present study are based on a strain energy based concept presented earlier (Hohe and Becker [9]). This approach is based on the concept of the representative volume element (Fig. 1). Hence, the effective stresses and the effective material properties are determined such that the behavior of a representative volume element consisting of the given microstructure and a similar volume element consisting of the quasi homogeneous effective medium is equivalent on the mesoscopic level of structural hierarchy. Mesoscopically equivalent mechanical behavior of both volume elements is assumed if the volume average

$$\bar{w} = \frac{1}{V^{RVE}} \int_{\Omega^{RVE}} w dV = \frac{1}{V^{RVE}} \int_{\Omega^{RVE*}} w^* dV^* = \bar{w}^* \quad (1)$$

of the recoverable strain energy density in both volume elements is equal, provided that both volume elements are subject to a mesoscopically equivalent state of deformation, defined by the condition that the volume average

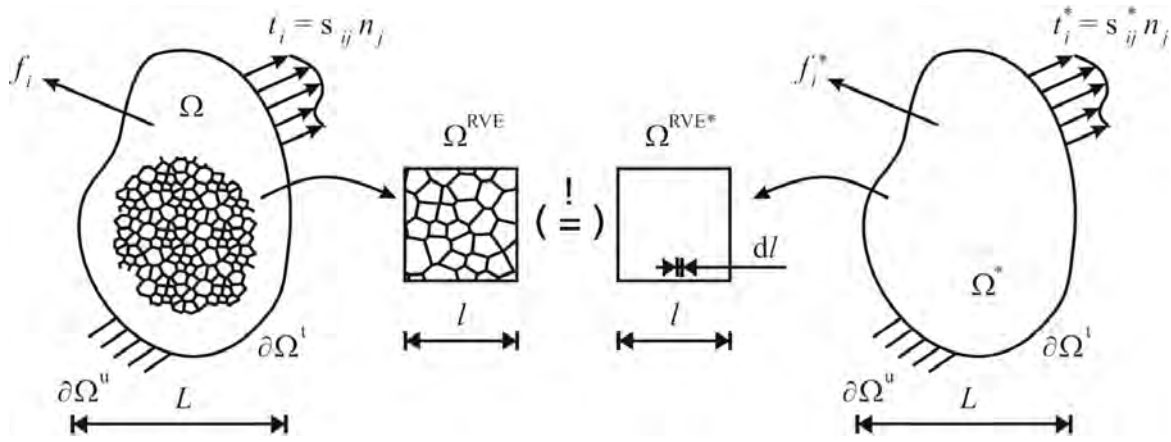


Figure 0: Concept of the representative volume element.

$$\bar{F}_{ij} = \frac{1}{V^{RVE}} \int_{\Omega^{RVE}} F_{ij} dV = \frac{1}{V^{RVE}} \int_{\Omega^{RVE*}} F_{ij}^* dV^* = \bar{F}_{ij}^* \quad (2)$$

of the components F_{ij} of the deformation gradient for both elements is equal. The effective strains are described in terms of the components

$$\bar{\gamma}_{ij} = \frac{1}{2} (\bar{F}_{ki} \bar{F}_{kj} - \delta_{ij}) \quad (3)$$

of the Green-Lagrange strain tensor or its infinitesimal counterpart ϵ_{ij} . The effective stress state is then described in terms of the components

$$\bar{\tau}_{ij} = \left. \frac{\partial \bar{w}}{\partial \bar{\gamma}_{ij}} \right|_{d\bar{\gamma}_{ij}^{pl} = 0} \quad (4)$$

of the second Piola-Kirchhoff stress tensor as the energy conjugate to the chosen effective strain measure. If the strain energy density w is computed numerically, the partial differentiation in Eq. (4) has to be performed by means of an appropriate numerical differentiation scheme.

2.2 Local stochastic enhancement

The standard probabilistic enhancement of the methodology for determination of the effective material properties as proposed in section 2.1 consists either in the single analysis of a large scale representative volume element with a random micro structure or in the repeated analysis of a small scale volume element in conjunction with a stochastic evaluation of the results. Whereas the scatter of the effective material properties is not accessible in the first

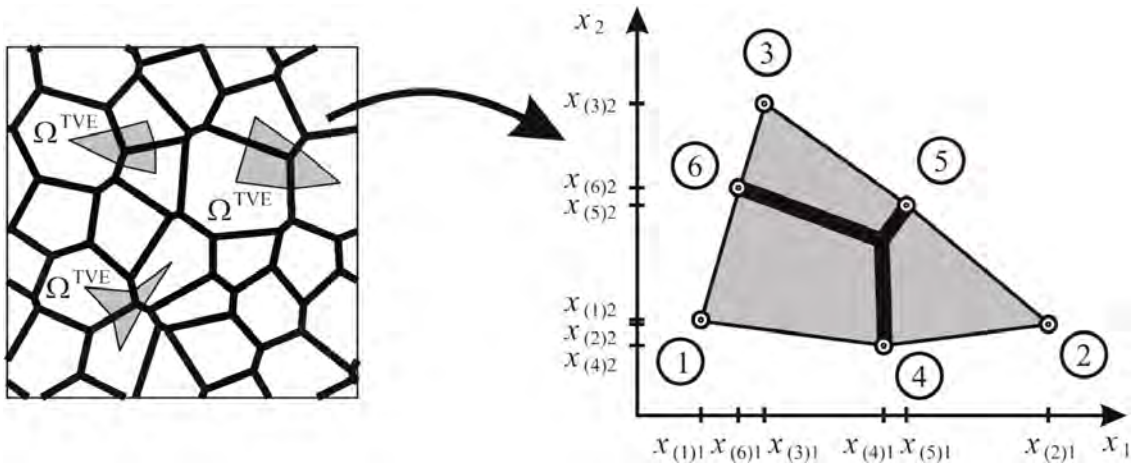


Figure 2: Subdivision of the computational foam model into testing volume elements.

case, problems may arise in the second case due to the exclusive consideration of small scale volume elements consisting of a limited number of pores which may exclude several specific effects such as the occurrence of a single large pore surrounded by much smaller ones.

In order to avoid these problems, an alternative route is proposed in the present study. In a first step, a large scale, statistically representative computational foam model is generated using a random number generator. The computational foam model is subjected to a prescribed effective strain state in conjunction with periodic boundary conditions along the external surfaces of the model. In a second step, the large scale computational foam model is subdivided into small scale testing volume elements consisting of a single cell wall intersection and half of the adjacent cell walls (see Fig. 2). For each of the testing volume elements, the effective strains are determined by means of Eqns. (2) and (3) which are evaluated with respect to the area Ω^{TVE} of the individual testing volume elements. In a similar manner, the effective stresses are obtained by means of a local evaluation of Eq. (4).

The results are assessed in a stochastic manner. In this context, the probability distribution for the effective property y is obtained by rearranging the individual results y_i for the effective property y into ascending order and assigning a cumulative probability

$$F(y_i) = \frac{i - \frac{1}{2}}{q}, \quad i = 1, \dots, q \quad (5)$$

to each of the data. In Eq. (5), q denotes the total number of testing volume elements in the model. The corresponding probability density distribution $f(y)$ for the effective material property y can then be obtained as the (numerical) partial derivative of the cumulative probability distribution $F(y)$ with respect to its argument y . Alternatively, a simplified stochastic assessment can be performed in terms of the expectation value

$$E(y) = \sum_{i=1}^q y_i p(y_i) \quad (6)$$

and the variance

$$V(y) = \sum_{i=1}^q (E(y) - y_i)^2 p(y_i) \quad (7)$$

of the macroscopic material property y where $p(y_i)$ is the individual probability for the occurrence of the result y_i . Although the present study is restricted to two-dimensional examples, the method can be extended to the three-dimensional case in a straightforward manner without any restrictions.

3 COMPUTATIONAL FOAM MODELS

3.1 Strategies for the division of space

For the randomized generation of computational foam models, different strategies have been proposed in the literature. The most basic procedure is a Voronoi [15] tessellation of the representative volume element. In this approach, first a number of nucleation points is randomly generated within the area Ω^{RVE} of the representative volume element. In a second step, the area of the cell belonging to nucleation point p_i is defined through

$$\Omega(p_i) = \{p \mid p \in R^2, r_E(p, p_i) < r_E(p, p_j) \text{ } j \neq i\} \text{ , } \quad i, j = 1, \dots, n \quad (8)$$

by all spatial points p featuring an Euclidean distance

$$r_E(p, p_i) = \left((x_1 - x_1^{(i)})^2 + (x_2 - x_2^{(i)})^2 \right)^{1/2} \quad (9)$$

to nucleation point p_i which is smaller than the distance to all other nucleation points. Since this procedure results in a Γ -distribution of the cell size, the Voronoi tessellation in its direct form is often termed Γ -Voronoi tessellation. A variant of this procedure avoiding the occurrence of small cells is the δ -Voronoi process where the distance between the individual nuclei is constrained by introduction of a minimum distance

$$r_E^{\min} < r_E(p_i, p_j) \text{ , } \quad i = 1, \dots, n \text{ , } \quad j = i + 1, \dots, n \quad (10)$$

between all nucleation points.

As mentioned by Fan et al. [4], further improvements may be obtained by using the Laguerre distance

$$r_L(p, p_i) = \left(r_E(p, p_i)^2 - (r_i^*)^2 \right)^{1/2} \quad (11)$$

with an individual radius r_i^* assigned to all nucleation points p_i in conjunction with Eq. (8) instead of its Euclidean counterpart (9).

Within the present study, all of the mentioned procedures are used in a periodic manner by copying all nucleation points into the direct neighborhood of the representative volume element so that random, but periodic micro structures are obtained.

3.2 Assessment in terms of quantitative criteria

The three different methods for generation of computational foam models described in section 3.1 are applied in a comparative study for an assessment of the quality of the obtained models regarding their ability to recapture the most important features of the micro structure of solid foams. The assessment is performed in a quantitative manner based on two criteria using objective parameters rather than by a simple visual qualitative check.

The first parameter to be used is based on Kelvin's [14] criterion, requiring minimum surface energy for the developing cellular micro structure. For the two-dimensional cellular structures considered in the present study, this criterion results in the requirement that the ratio of the total length of the cell walls surrounding an individual cell to the area covered by the cell has to be minimum for all cells in the respective computational foam model. A weighted averaging of this ratio for all cells in the representative volume element results in a quality criterion based on the requirement that the average Kelvin parameter

$$K_{avg} = \frac{1}{A^{RVE}} \sum_{i=1}^n S_i \quad (12)$$

with the area A^{RVE} of the representative volume element and the lengths S_i of the cell walls surrounding cell no. i has to be minimum for a high quality computational foam model.

A second important criterion for the quality of computational foam models is the statistical size distribution of the individual cells in the model. As it has been pointed out, among others, by Fan et al. [4], the cell size distribution for real solid foams is of the logarithmic normal type featuring the probability density distribution

$$f(A) = \frac{1}{\sigma(2\pi)^{\frac{1}{2}}} \frac{1}{A} e^{-\frac{(\ln A - \mu)^2}{2\sigma^2}} \quad (13)$$

for the area A of the individual cells with the shape and position parameters σ and μ respectively. An assessment of the proximity of the cell size distribution of a given computational foam model to the logarithmic normal distribution is made by adapting the shape and position parameters σ and μ of the logarithmic normal distribution such that the least square error sum

$$e = \sum_{i=1}^n (F_{discr}(A_i) - F_{cont}(A_i))^2 \quad (14)$$

between the given discrete distribution and the adapted continuous distribution becomes minimum. The final error sum e is then employed as a quality criterion for assessment of the ability of the respective strategy for the division of space to recapture the experimentally observed cell size distribution.

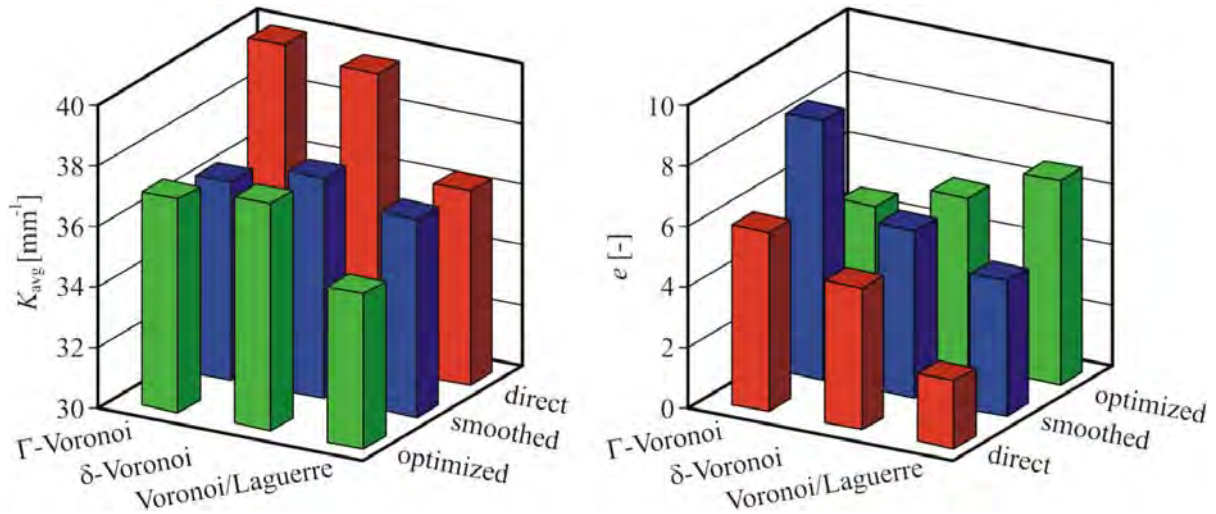


Figure 3: Quality assessment of different strategies for generation of computational foam models.

The quality assessment is performed for the strategies for the division of space sketched in Section 3.1. All three strategies are employed in their direct form as well as with a subsequent smoothing and optimization of the computational foam models. The smoothing procedure consists in a simple re-positioning of the cell wall intersections to the centroid of the corresponding Delaunay triangle. In the optimization procedure, the cell wall intersections are re-positioned such that the Kelvin parameter K_{avg} according to Eq. (12) is minimized.

For each procedure, 100 models are generated. The results for the averaged parameters K_{avg} and e are presented in Fig. 3. In terms of the energetic Kelvin criterion, the best results are obtained by means of the Voronoi process in Laguerre geometry, whereas both the Γ - and the δ -Voronoi processes result in computational foam models with inferior quality. Although the quality of the foam models based on the Γ - and δ -Voronoi tessellations might be improved by subsequent smoothing or optimization, these models are still outperformed by the models generated by a Voronoi tessellation in Laguerre geometry.

With respect to the cell size distribution, again the qualitatively best results are obtained by the Voronoi tessellation in Laguerre geometry, whereas poor models are obtained by means of the Voronoi process using the Euclidean distance, especially in the unconstrained (Γ -) version. In general, the quality of the foam models regarding the cell size distribution decreases, if a subsequent smoothing or optimization is applied to the computational foam models, since both of these procedures have the sole objective of an improvement in terms of the Kelvin criterion. Since the Voronoi process in Laguerre geometry provides reasonable results in terms of both criteria, this procedure is exclusively used for generation of the foam models employed in the subsequent parameter studies of this study.

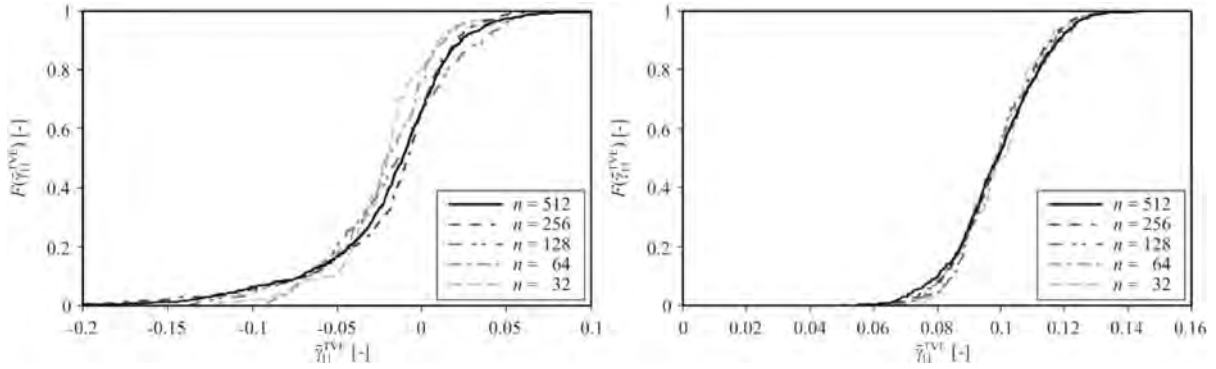


Figure 4: Study of convergence.

4 EXAMPLES

4.1 Convergence

In a preliminary analysis, the convergence of the proposed method regarding the necessary size of the representative volume element and thus the necessary number of testing volume elements is assessed. For this purpose, different computational foam models with 32 to 512 Voronoi cells are generated and subjected to uniaxial tensile and compressive states of deformation $\gamma_{11} = 0.1$ and $\gamma_{11} = -0.025$ respectively and $\gamma_{22} = \gamma_{12} = 0$.

The resulting probability distributions for the corresponding local effective strains γ_{11}^{TVE} on testing volume element level are plotted in Fig. 4. For both, the tensile and the compressive state of deformation, convergent results with smooth probability distributions $F(\gamma_{11}^{\text{TVE}})$ are obtained for 512 Voronoi cells and thus 1024 testing volume elements. Although lower numbers of cells might be sufficient for the tensile case, all subsequent analyses are based on this model size.

4.2 Effective material response

As an illustrative micro structural example, the probabilistic homogenization scheme proposed in the present study is applied to the prediction of the effective material response of a hyperelastic two-dimensional model foam. The material behavior on the cell wall level is assumed to be governed by a compressible Ogden type constitutive relation

$$w = \sum_{k=1}^2 \frac{\mu_k}{\alpha_k} \left(\left(J^{-\frac{1}{3}} \lambda_1 \right)^{\alpha_k} + \left(J^{-\frac{1}{3}} \lambda_2 \right)^{\alpha_k} + \left(J^{-\frac{1}{3}} \lambda_3 \right)^{\alpha_k} - 3 \right) + \sum_{k=1}^2 \kappa_k (J-1)^{2k} \quad (15)$$

where λ_i are the principal values of the deformation gradient and J is the corresponding Jacobian. The material parameters are given by $\alpha_1 = 2$, $\mu_1 = 0.5$ GPa, $\kappa_1 = 0.6$ GPa, $\alpha_2 = -2$, $\mu_2 = -0.1$ GPa and $\kappa_2 = \infty$. Externally, the computational foam model is subjected to uniaxial

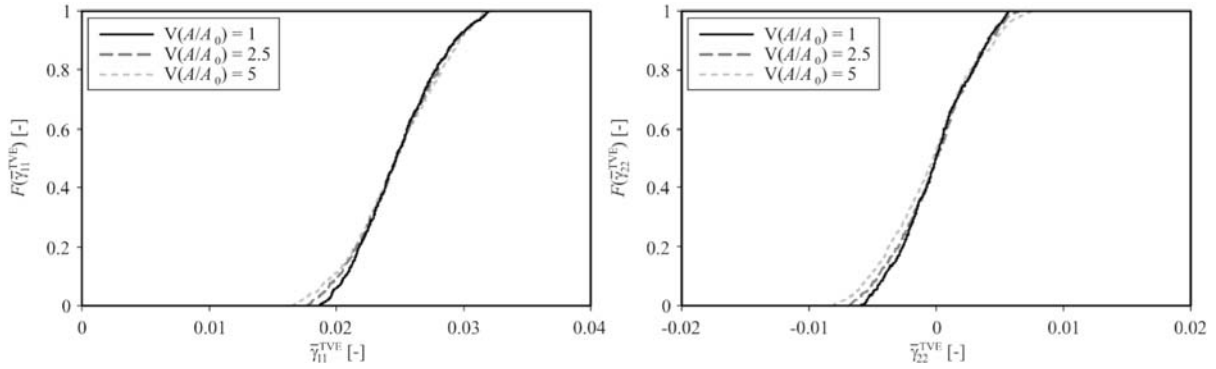


Figure 5: Probability distributions for the testing volume element strains, uniaxial tension.

tensile and compressive states of deformation with an applied external Green-Lagrange strain of $\gamma_{11} = \pm 0.025$, whereas all other macroscopic strain components are assumed to vanish. The relative density of the foam is assumed to be $\rho = 0.05$.

In Fig. 5, the probability distributions $F(\gamma_{ij})$ for the local (testing volume element) strains γ_{11}^{TVE} and γ_{22}^{TVE} longitudinal and perpendicular to the external straining direction are presented for the tensile load case. The probability distributions for the corresponding local stress components τ_{11}^{TVE} and τ_{22}^{TVE} are presented in Fig. 6. Three different degrees of micro structural disorder are considered, characterized by the variance $V(A/A_0)$ of the cell size distribution ranging from regular to highly disordered micro structures. The local effective strain components are distributed around the values of the corresponding applied strains with $\gamma_{11} = 0.025$ and $\gamma_{22} = 0$ which are recovered as the corresponding expectation values. For both components, similar variances are obtained, indicated by similar slopes of the probability distributions. Increasing degrees $V(A/A_0)$ of micro structural disorder lead to increasing uncertainties for the local effective strain components, nevertheless, only minor quantitative effects

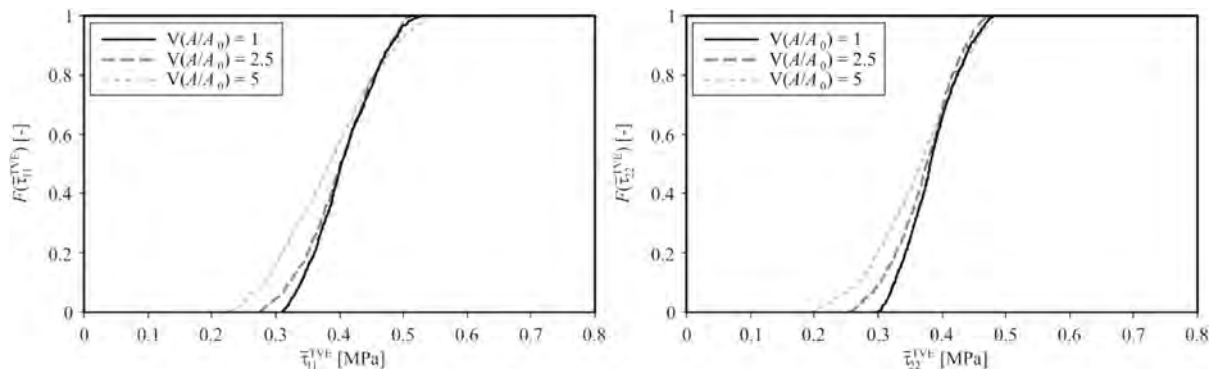


Figure 6: Probability distributions for the testing volume element stresses, uniaxial tension.

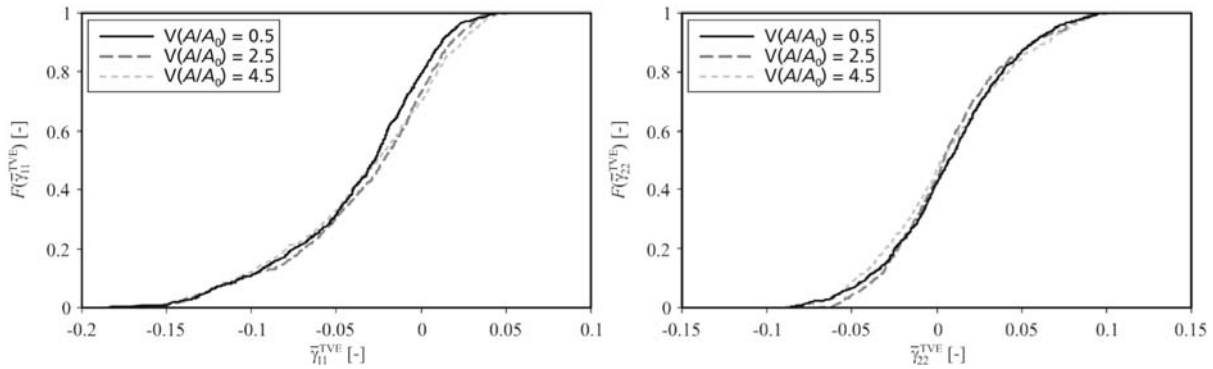


Figure 7: Probability distributions for the testing volume element strains, uniaxial compression.

are observed. Stronger quantitative effects of the degree of micro structural disorder on the uncertainties of the effective properties are obtained in the case of the local effective stresses (see Fig. 6). This discrepancy is caused by the fact that the effective stress components are governed by both, the effective stiffness and the effective strain state of the respective testing volume element which are both affected by the degree of micro structural disorder.

The counterparts of Figs. 5 and 6 for the compressive load case are presented in Figs. 7 and 8 respectively. Again, the x_1 -direction is the macroscopic straining direction and again, three different degrees of micro structural disorder are considered. Compared to the tensile load case, higher degrees of uncertainty are obtained for the effective strain components (see Figs. 5 and 7). This effect is caused by the occurrence of micro structural instabilities leading to strain localization in areas consisting of weaker foam cells. The occurrence of micro structural instabilities in general results in a limitation of the corresponding local effective stresses in the following postbuckling range. Hence, the probability distributions for the local effective stresses under externally applied compression feature smaller scatter band widths compared to the tensile load case (see Figs. 6 and 8). Nevertheless, the average level of the effective stress

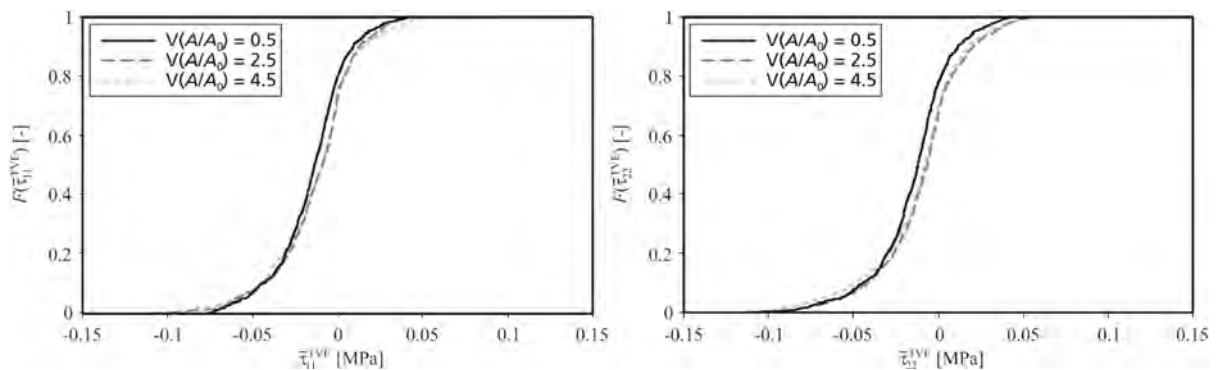


Figure 8: Probability distributions for the testing volume element stresses, uniaxial compression.

components is also found to be much lower in overall compression compared to the tensile load case. Since the compressive range is strongly governed by micro structural instabilities and the corresponding effects, the degree $V(A/A_0)$ of micro structural disorder has only minor effects on both the effective strain and stress components, provided that the degree of disorder is sufficient to prevent the occurrence of instability effects in the rigorous Eulerian sense as they would occur in the case of perfectly regular periodic micro structures.

5 CONCLUSION

The present study is concerned with a probabilistic homogenization analysis for structural foams as they are common as core materials in sandwich construction. The proposed procedure provides an efficient numerical tool for assessment of the scatter in the effective material response of solid foams both, on the lowest possible level of structural hierarchy and on higher levels. The scatter of the effective material behavior is found to be mostly controlled by uncertainties in the geometry and especially by fluctuations in the local relative density.

ACKNOWLEDGEMENT

This work has been financially supported by the Deutsche Forschungsgemeinschaft (DFG) under grant no. Ho 1852/6-1.

REFERENCES

- [1] J.S. Blazy, A. Marie-Louise, S. Forest, Y. Chastel, A. Pineau, A. Awade, A., C. Groleron and F. Moussy, F., "Deformation and fracture of aluminium foams under proportional and multi-axial loading: statistical analysis and size effect", *Int. J. Mech. Sci.* 46, 217-244 (2004).
- [2] C. Chen, T.J. Lu and N.A. Fleck, N.A., "Effect of imperfection on the yielding of two-dimensional foams", *J. Mech. Phys. Solids* 47, 2235-2272 (1999).
- [3] A.M. Cuitiño and S. Zheng, S., "Taylor averaging on heterogeneous foams", *J. Compos. Mat.* 37, 701-713 (2003).
- [4] Z. Fan, Y. Wu, X. Zhao and Y. Lu, "Simulation of polycrystalline structure with Voronoi diagram in Laguerre geometry based on random closed packing of spheres", *Comput. Mat. Sci.* 29, 301-308 (2004).
- [5] M.A. Fortes and M.F. Ashby, "The effect of non-uniformity on the in-plane modulus of honeycombs", *Acta Mat.* 47, 3469-3473 (1999).
- [6] A.N. Gent and A.G. Thomas, A.G. "Mechanics of foamed elastic materials", *Rubber Chem. Techn.* 36, 597-610 (1963).
- [7] L.J. Gibson and M.F. Ashby, M.F., "The mechanics of three-dimensional cellular materials", *Proc. Royal Soc.A* 382, 43-59 (1982).
- [8] L.J. Gibson and M.F. Ashby, *Cellular Solids --- Structure and Properties*. Cambridge University Press (1997).
- [9] J. Hohe and W. Becker, "A probabilistic approach to the numerical homogenization of irregular solid foams in the finite strain regime", *Int. J. Solids Struct.* 42, 3549-3569 (2005).

- [10] L. Huyse and M.A. Maes, M.A., “Random field modeling of elastic properties using homogenization”, *J. Eng. Mech.* 127, 27-36 (2001).
- [11] U. Ramamurty and A. Paul, A., “Variability in mechanical properties of a metal foam”, *Acta Mat.* 52, 869-876 (2004).
- [12] A.P. Roberts and E.J. Garboczi, “Elastic properties of model random three-dimensional open-cell solids” *J. Mech. Phys. Solids* 50, 33-55 (2002).
- [13] V. Shulmeister, M.W.D. van der Burg, E. van der Giessen, E. and R. Marissen, R., “A numerical study of large deformation of low-density elastomeric open-cell foams”, *Mech. Mat.* 30, 125-140 (1998).
- [14] W. Thomson (Lord Kelvin), “On the division of space with minimum partitional area”, *Phil. Mag.* 24, 503-514 (1887).
- [15] G. Voronoï, “Nouvelles applications des paramètres continus à la théorie des formes quadratiques” *J. Reine Ang. Math.* 134, 198-312 (1908).
- [16] W.E. Warren and A.M. Kraynik, A.M., “The linear elastic properties of open-cell foams”, *J. Appl. Mech.* 55, 341-346 (1988).
- [17] H.X. Zhu, J.R. Hobdell and A.H. Windle, “Effects of cell irregularity on the elastic properties of open-cell foams”, *Acta Mat.* 48, 4893-4900 (2000).

A NEW 2D LOCAL VIBRATIONAL MODEL FOR UNIDIRECTIONAL CLAMPED-CLAMPED SANDWICH STRUCTURE WITH EDGE STIFFENERS

S. Karczmarzyk *

* Institute of Machine Design Fundamentals of the Warsaw University of Technology
Narbutta 84, 02-524 Warszawa, Poland
e-mail: karczmarzyk_st@poczta.onet.pl

Key words: Flexural vibration, Eigenfrequencies, Sandwich beam, Edge stiffeners, 2D local model, Linear elastodynamics.

Summary. *Flexural vibration of a clamped-clamped, three-layer, one-span sandwich, unidirectional structure composed of isotropic layers is considered in the paper. A new model obtained within the local linear theory of elastodynamics is presented. Very realistic boundary conditions at edges of the structure, which correspond to the engineering solution with the edge stiffeners, are introduced and satisfied. Eight eigenfrequencies of the structure, calculated according to the model, are given. A comparative analysis of the results is done and some conclusions are presented.*

1 INTRODUCTION

The eigenvalue problem of sandwich structures is still not solved analytically with a sufficient exactitude and accuracy. The existing theories predict eigenfrequencies which are not close to the experimental data - see e.g., [1-2, 5-8]. In particular, eigenfrequencies of the lower modes of vibration are usually much lower than the measured values. Obviously, there are high differences between predictions of different analytical models. For instance, the percentage difference in the fundamental frequencies of simply supported sandwich panel predicted by two models presented in [9] is about 15%. The same phenomenon, i.e., lower computational eigenfrequencies (predicted by analytical models) than the corresponding experimental data, is observed when the C-C structures are considered. It is not easy to explain the differences when the analytical model (e.g., [6]) is capable to satisfy very refined (accurate) edge boundary conditions. The probable explanation in the case is that the model [6] is a particular case of more general model (model I) given in [9].

It is an aim of the presentation to discuss the new model that is to show both its mathematical details and some comparisons of numerical results. The present author obtained within the local linear elastodynamics several vibrational models for the unidirectional, both

cantilever [1] and clamped-clamped (C-C) [2], sandwich structures. However, the models have been obtained for some specific, realistic but simplified, edge boundary conditions, referring only to the faces of the structures. The models were obtained without expanding the displacement and stress fields (within the structures) into series. All through-the-thickness boundary conditions and the compatibility equations of the local linear elastodynamics have been satisfied in the models [1,2] and their final (numerical) form in the case of the free vibration has been expressed as follows,

$$\begin{aligned} \alpha_m \operatorname{th}(\alpha_m L/2) + \gamma_m \operatorname{tg}(\gamma_m L/2) &= 0, & m=1,3,5,\dots, \\ \alpha_m \operatorname{ctgh}(\alpha_m L/2) - \gamma_m \operatorname{ctg}(\gamma_m L/2) &= 0, & m=2,4,6,\dots \end{aligned} \quad (1)$$

$$\begin{aligned} \underline{A}_m^I \underline{C}_m^I = \underline{0} &\Rightarrow \det(\underline{A}_m^I) \equiv F_m^I(\alpha_m, \omega_m) = 0, \\ \underline{A}_m^{II} \underline{C}_m^{II} = \underline{0} &\Rightarrow \det(\underline{A}_m^{II}) \equiv F_m^{II}(\gamma_m, \omega_m) = 0. \end{aligned} \quad (2)$$

The symbols α_m , γ_m and ω_m , in the Eqs (1,2), are unknown while ω_m is the eigenfrequency.

The new model presented here has been elaborated for the assumption that $\alpha_m = \gamma_m$. Due to this, the set of Eqs. (2) had to be reduced to one equation. Thus, the final form of the new model consists of two coupled, transcendental equations. It is also noted that apart from the edge conditions for the faces (also) some reasonable edge boundary conditions for the core have been satisfied within the new model. The edge conditions for the core, satisfied in the new model, correspond to the conditions employed in the papers [3,4], however, instead of the stresses the stress resultants have been equated to zero at the edges of the core (in the new model). The number of the final equations and inclusion of the edge boundary conditions for the core make the new model quite different than the previous models [1,2]. In order to verify the new model some numerical results were obtained and are compared with results predicted by other models, published in [5,6].

It is noted that the assumption $\alpha_m = \gamma_m$ was introduced in a simplified manner and checked numerically, by the present author, in paper [7]. However, it was done without a theoretical justification. It is an aim of the paper to supply the theoretical justification for the assumption $\alpha_m = \gamma_m$. Details are given in sections 3 and 4. The local linear elastodynamics approach is worthwhile (to develop it) since it can be easily applicable for the analysis of more advanced sandwich structures consisting of more than three layers. Such a possibility and application to a five-layer sandwich strip was presented in [7].

The new model is presented here as follows. All the equations and conditions are listed in section 2. Four new solutions to the local equations of motion of the linear elastodynamics, derived and applied here by the present author, are described in section 3. In section 4 the total displacements and stresses within the C-C structure are presented. Some numerical results and comparisons as well as a comment are given in section 5. Section 6 contains some conclusions.

2 EQUATIONS SATISFIED BY THE NEW MODEL

The structure considered in the paper is shown in Fig. 1. It is assumed that the U-inserts (sometimes called as C-profiles) are much stiffer than the faces. The gap occurring between the profiles and the core means that the normal and shear stresses at the ends of the middle layer are equivalent to zero.

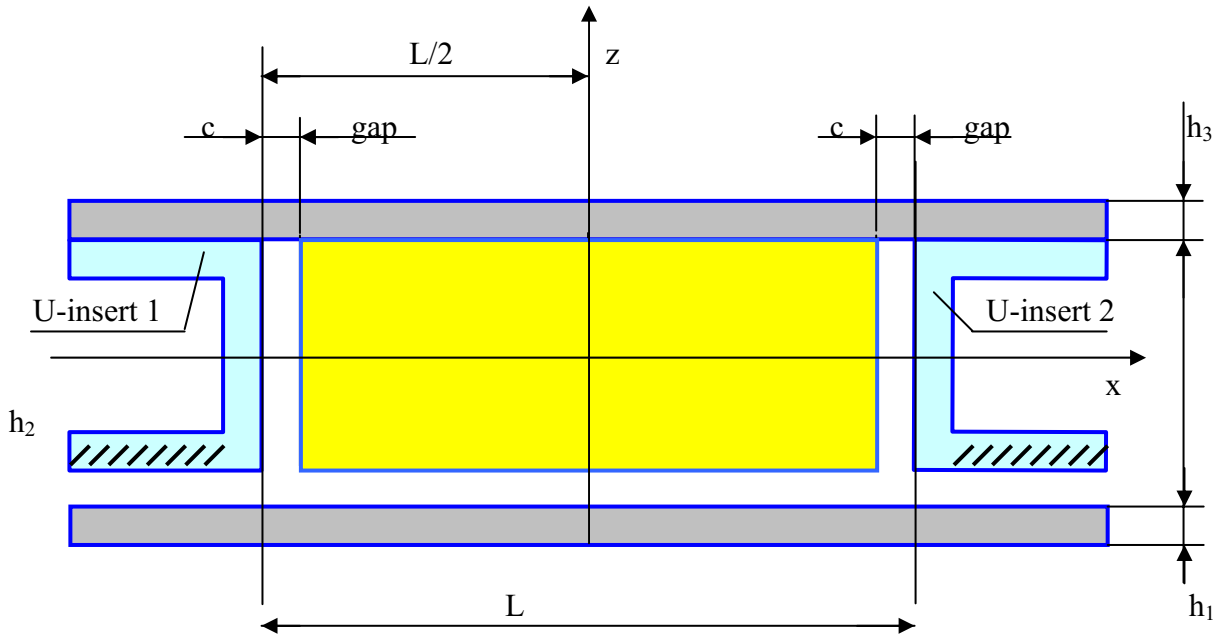


Figure 1: Geometry of the sandwich structure considered in the paper.

The following boundary conditions are satisfied, in the present paper, for the structure. Both in-plane and the out-of-plane displacements as well as slopes of the faces are equated to zero at the outer corners of the inserts, i.e.,

$$u_{xj}(x = \pm L/2, z = \pm h_2/2) = 0, \quad u_{zj}(x = \pm L/2, z = \pm h_2/2) = 0, \quad (3)$$

$$\frac{\partial u_{zj}}{\partial x} \left(x = \pm \frac{L}{2}, z = \pm h_2/2 \right) = 0, \quad j = 1 \text{ for } z = -h_2/2, \quad j = 3 \text{ for } z = h_2/2$$

It is noted that the edge boundary conditions (4) are the same as in [3,4]. Boundary conditions at ends of the core are as follows,

$$\int_{-h_2/2}^{+h_2/2} z \sigma_{xxj}(x = \pm(L/2 - c), z) dz = 0, \quad \int_{-h_2/2}^{+h_2/2} \sigma_{zxy}(x = \pm(L/2 - c), z) dz = 0, \quad j = 2. \quad (4)$$

As far as the present author knows, and it is stressed here, both the conditions (3) and (4) at

the ends of the sandwich strip are quite new within the local linear elastodynamics approach. The conditions introduced here are very close to the boundary conditions for the realistic structure.

Through-the-thickness boundary conditions and compatibility equations are as follows,

$$\begin{aligned} \sigma_{zz1}(x, -(h_1 + h_2/2)) &= 0, & \sigma_{zz3}(x, (h_3 + h_2/2)) &= 0, \\ \sigma_{zx1}(x, -(h_1 + h_2/2)) &= 0, & \sigma_{zx3}(x, (h_3 + h_2/2)) &= 0, \\ \underline{u}_j(x, \hat{z}_j) &= \underline{u}_{j+1}(x, \pm h_2/2), & \underline{\sigma}_j(x, \hat{z}_j) &= \underline{\sigma}_{j+1}(x, \pm h_2/2), \\ \underline{u}_k &= [u_{xk} \ u_{zk}], & \underline{\sigma}_k &= [\sigma_{zzk} \ \sigma_{zvk}], \quad j = 1, 2.. \end{aligned} \quad (5)$$

The equations of motion, satisfied by the stresses and displacements within each layer separately, are as follows,

$$\partial(\sigma_{kl})_j / \partial x_l = \rho_j \partial^2 u_{ij} / \partial t^2, \quad k, l = 1, 3, \quad j = 1, 2, 3. \quad (6)$$

Apart from (3-6) the Hooke law is satisfied in the model considered. To satisfy the above edge boundary conditions some new solutions of the equations of motion have been derived by the present author and composed with the former solutions outlined in the appendix.

3 NEW SOLUTIONS TO THE EQUATIONS OF MOTION

The solutions (i.e., displacement and stress fields) found lately by the present author are denoted with IIIT, IIIH, IVT and IVH where T means solutions with trigonometric functions of the space variable x while H denotes solutions with hyperbolic functions of the variable x. β_{12m} , r_{12m} are given in the Appendix, constants ${}^2C_{1m}^{III}$, ${}^2D_{1m}^{III}$, ... with the subscripts are unknown. The solutions refer to the core but one may introduce the same (kind) solutions for the faces by replacing β_{12m} with β_{11m} (or β_{13m}) and r_{12m} with r_{11m} (or r_{13m}) - see later.

3.1 Vibrational solution IIIT

The following displacements and stresses satisfy the 3D linear elastodynamics equations of motion and the Saint-Venant compatibility equations for the core,

$$\begin{aligned} u_z &= +(\alpha_m^2 / \beta_{12m}^2) ({}^2C_{1m}^{III}) X_{T_m}(x) \cosh(\beta_{12m} y) T_m(t), & T_m(t) &= \exp(i\omega_m t), \\ u_x &= -[z ({}^2C_{1m}^{III}) + {}^2C_{2m}^{III}] X_{T_m, x} \cosh(\beta_{12m} y) T_m(t), \\ u_y &= -(\alpha_m^2 / \beta_{12m}^2) [z ({}^2C_{1m}^{III}) + {}^2C_{2m}^{III}] X_{T_m}(x) \beta_{12m} \sinh(\beta_{12m} y) T_m(t), \quad m = 1, 2, 3, \dots, \end{aligned} \quad (7)$$

$$\begin{aligned}
 \sigma_{xx} &= +2\mu_2\alpha_m^2[z(^2C_{1m}^{III}) + ^2C_{2m}^{III}]X_{T_m}(x)\cosh(\beta_{12m}y)T_m(t), & \sigma_{yy} &= -\sigma_{xx}, & \sigma_{zz} &= 0, \\
 \sigma_{zx} &= +\mu_2(\alpha_m^2 / \beta_{12m}^2 - 1)(^2C_{1m}^{III})X_{T_m,x}\cosh(\beta_{12m}y)T_m(t), & \sigma_{yz} &= 0, \\
 \sigma_{xy} &= -\mu_2(\alpha_m^2 / \beta_{12m}^2 + 1)[z(^2C_{1m}^{III}) + ^2C_{2m}^{III}]X_{T_m,x}\beta_{12m}\sinh(\beta_{12m}y)T_m(t), & m &= 1, 2, 3, \dots
 \end{aligned} \tag{8}$$

The symbol α_m is defined in section 4, β_{12m} , referring to the core, is defined in the appendix, the function X_{T_m} is defined in section 4. It is noted that the constant with the subscripts $_{2m}$ is not necessary when flexural vibration of the symmetric (about the mid-plane) structure are considered. For an enough narrow structure the following approximations of the fields (7), (8), referring to the underlined factors, are valid and taken into the further consideration,

$$u_z \cong +(\alpha_m^2 / \beta_{12m}^2)(^2C_{1m}^{III})X_{T_m}(x)T_m(t), \tag{9}$$

$$u_x \cong -[z(^2C_{1m}^{III}) + ^2C_{2m}^{III}]X_{T_m,x}T_m(t), \quad u_y \cong 0, \quad m=1, 2, 3, \dots,$$

$$\begin{aligned}
 \sigma_{xx} &\cong +2\mu_2\alpha_m^2[z(^2C_{1m}^{III}) + ^2C_{2m}^{III}]X_{T_m}(x)T_m(t), & \sigma_{yy} &= -\sigma_{xx}, & \sigma_{zz} &= 0, \\
 \sigma_{zx} &\cong +\mu_2(\alpha_m^2 / \beta_{12m}^2 - 1)(^2C_{1m}^{III})X_{T_m,x}T_m(t), & \sigma_{xy} &\cong 0, & \sigma_{yz} &= 0.
 \end{aligned} \tag{10}$$

3.2 Vibrational solution IIIH

The following displacements and stresses satisfy the 3D linear elastodynamics equations of motion and the Saint-Venant compatibility equations for the core,

$$\begin{aligned}
 u_z &= +(\alpha_m^2 / r_{12m}^2)(^2D_{1m}^{III})X_{H_m}(x)\cos(r_{12m}y)T_m(t), \\
 u_x &= -[z(^2D_{1m}^{III}) + ^2D_{2m}^{III}]X_{H_m,x}\cos(r_{12m}y)T_m(t),
 \end{aligned} \tag{11}$$

$$u_y = +(\alpha_m^2 / r_{12m}^2)[z(^2D_{1m}^{III}) + ^2D_{2m}^{III}]X_{H_m}(x)r_{12m}\sin(r_{12m}y)T_m(t), \quad m=1, 2, 3, \dots,$$

$$\sigma_{xy} = +\mu_2(\alpha_m^2 / r_{12m}^2 + 1)[z(^2D_{1m}^{III}) + ^2D_{2m}^{III}]X_{H_m,x}r_{12m}\sin(r_{12m}y)T_m(t), \quad m=1, 2, 3, \dots, \tag{12a}$$

$$\begin{aligned}\sigma_{xx} &= -2\mu_2\alpha_m^2[z(^2D_{1m}^{III}) + ^2D_{2m}^{III}]X_{Hm}(x)\underline{\cos(r_{12m}y)}T_m(t), & \sigma_{yy} &= -\sigma_{xx}, & \sigma_{zz} &= 0, \\ \sigma_{zx} &= +\mu_2(\alpha_m^2/r_{12m}^2 - 1)(^2D_{1m}^{III})X_{Hm,x}\underline{\cos(r_{12m}y)}T_m(t), & \sigma_{yz} &= 0.\end{aligned}\quad (12b)$$

The symbol r_{12m} , referring to the core, is defined in the appendix. It is noted that the constant with the subscripts $_{2m}$ is not necessary when flexural vibration of the symmetric (about the mid-plane) structure are considered. For an enough narrow structure the following approximations of the fields (11), (12), referring to the underlined factors, are valid and applied in the further consideration,

$$u_z \cong +(\alpha_m^2/r_{12m}^2)(^2D_{1m}^{III})X_{Hm}(x)T_m(t), \quad (13)$$

$$u_x \cong -[z(^2D_{1m}^{III}) + ^2D_{2m}^{III}]X_{Hm,x}T_m(t), \quad u_y \cong 0, \quad m=1, 2, 3, \dots,$$

$$\sigma_{xx} \cong -2\mu_2\alpha_m^2[z(^2D_{1m}^{III}) + ^2D_{2m}^{III}]X_{Hm}(x)T_m(t), \quad \sigma_{yy} = -\sigma_{xx}, \quad \sigma_{zz} = 0, \quad (14)$$

$$\sigma_{zx} \cong +\mu_2(\alpha_m^2/r_{12m}^2 - 1)(^2D_{1m}^{III})X_{Hm,x}T_m(t), \quad \sigma_{xy} \cong 0, \quad \sigma_{yz} = 0.$$

3.3 Vibrational solution IVT

The following displacements and stresses, again with the trigonometric functions of variable x appearing in (7-10), satisfy the 3D linear elastodynamics equations of motion and the Saint-Venant compatibility equations for the core,

$$\begin{aligned}u_z &= +\cos(\alpha_m z)(^2C_{1m}^{IV})X_{Tm}(x)\underline{\cosh(p_{T2m}y)}T_m(t), & u_y &\equiv 0, \\ u_x &= -[\sin(\alpha_m z)/\alpha_m](^2C_{1m}^{IV})X_{Tm,x}\underline{\cosh(p_{T2m}y)}T_m(t),\end{aligned}\quad (15)$$

$$p_{T2m}^2 = 2\alpha_m^2 - \rho_2\omega_m^2/\mu_2, \quad m=1, 2, 3, \dots,$$

$$\sigma_{xx} = +2\mu_2\alpha_m \sin(\alpha_m z)({}^2C_{1m}^{IV})X_{T_m}(x)\cosh(\underline{p_{T2m}y})\underline{T_m}(t), \quad \sigma_{zz} = -\sigma_{xx}, \quad \sigma_{yy} = \sigma_{zx} \equiv 0, \quad (16a)$$

$$\sigma_{xy} = -\mu_2[\sin(\alpha_m z) / \alpha_m]({}^2C_{1m}^{IV})X_{T_m,x} \underline{p_{T2m} \sinh(p_{T2m}y)T_m}(t),$$

$$\sigma_{yz} = +\mu_2 \cos(\alpha_m z)({}^2C_{1m}^{IV})X_{T_m}(x)\underline{p_{T2m} \sinh(p_{T2m}y)T_m}(t), \quad m=1, 2, 3, \dots \quad (16b)$$

For an enough narrow structure the following approximations of the fields (15), (16), referring to the underlined factors, are valid and taken into the further consideration,

$$u_z \cong +\cos(\alpha_m z)({}^2C_{1m}^{IV})X_{T_m}(x)T_m(t), \quad u_y \equiv 0, \quad (17)$$

$$u_x \cong -[\sin(\alpha_m z) / \alpha_m]({}^2C_{1m}^{IV})X_{T_m,x} T_m(t), \quad p_{T2m}^2 = 2\alpha_m^2 - \rho_2\omega_m^2 / \mu_2, \quad m=1, 2, 3, \dots,$$

$$\begin{aligned} \sigma_{xx} \cong +2\mu_2\alpha_m \sin(\alpha_m z)({}^2C_{1m}^{IV})X_{T_m}(x)T_m(t), \quad \sigma_{zz} = -\sigma_{xx}, \quad \sigma_{yy} = \sigma_{zx} \equiv 0, \\ \sigma_{xy} \cong 0, \quad \sigma_{yz} \cong 0. \end{aligned} \quad (18)$$

3.4 Vibrational solution IVH

The following displacements and stresses, again with the hyperbolic functions of variable x appearing in (11-14), satisfy the linear elastodynamics equations of motion and the Saint-Venant compatibility equations for the core,

$$u_z = +\cosh(\alpha_m z)({}^2D_{1m}^{IV})X_{H_m}(x)\cos(\underline{p_{H2m}y})\underline{T_m}(t), \quad u_y \equiv 0,$$

$$u_x = -[\sinh(\alpha_m z) / \alpha_m]({}^2D_{1m}^{IV})X_{T_m,x} \underline{\cos(p_{H2m}y)T_m}(t), \quad (19)$$

$$p_{H2m}^2 = 2\alpha_m^2 + \rho_2\omega_m^2 / \mu_2, \quad m=1, 2, 3, \dots,$$

$$\begin{aligned} \sigma_{xx} &= -2\mu_2\alpha_m \sinh(\alpha_m z) (\underbrace{D_{1m}^{IV}})^2 X_{Hm}(x) \cos(\underline{p_{H2m}y}) T_m(t), & \sigma_{zz} &= -\sigma_{xx}, & \sigma_{yy} &= \sigma_{zx} \equiv 0, \\ \sigma_{xy} &= -\mu_2 [\sinh(\alpha_m z) / \alpha_m] (\underbrace{D_{1m}^{IV}})^2 X_{Hm,x} [-\underline{p_{H2m} \sin(p_{H2m}y)}] T_m(t), \\ \sigma_{yz} &= +\mu_2 \cosh(\alpha_m z) (\underbrace{D_{1m}^{IV}})^2 X_{Hm}(x) [\underline{-p_{H2m} \sin(p_{H2m}y)}] T_m(t), & m &= 1, 2, 3, \dots \end{aligned} \quad (20)$$

For an enough narrow structure the following approximations of the fields (19), (20), referring to the underlined factors, are valid and applied in the further consideration,

$$\begin{aligned} u_z &\cong +\cosh(\alpha_m z) (\underbrace{D_{1m}^{IV}})^2 X_{Hm}(x) T_m(t), & u_y &\equiv 0, \\ u_x &\cong -[\sinh(\alpha_m z) / \alpha_m] (\underbrace{D_{1m}^{IV}})^2 X_{Tm,x} T_m(t), & p_{H2m}^2 &= 2\alpha_m^2 + \rho_2 \omega_m^2 / \mu_2, & m &= 1, 2, 3, \dots, \end{aligned} \quad (21)$$

$$\begin{aligned} \sigma_{xx} &\cong -2\mu_2\alpha_m \sinh(\alpha_m z) (\underbrace{D_{1m}^{IV}})^2 X_{Hm}(x) T_m(t), & \sigma_{zz} &= -\sigma_{xx}, & \sigma_{yy} &= \sigma_{zx} \equiv 0, \\ \sigma_{xy} &\cong 0, & \sigma_{yz} &\cong 0. \end{aligned} \quad (22)$$

It is noted that in the solutions denoted with superscript III the normal stress σ_{zz} is equivalent to zero while in the solutions with superscript IV the shear stress σ_{zx} is equivalent to zero. The functions X_{Tm} , X_{Hm} are defined in the next section.

4 TOTAL FIELDS WITHIN THE FACES AND CORE

The displacements in the faces are composed of two ingredients as follows [1,2],

$$\begin{aligned} u_{xj} &= -\left[\sum_m g_{jm}^I(z) \frac{dW_m^I(x)}{dx} - \sum_m g_{jm}^{II}(z) \frac{dW_m^{II}(x)}{dx} \right] T_m(t), \\ u_{zj} &= +\left[\sum_m f_{jm}^I(z) W_m^I(x) - \sum_m f_{jm}^{II}(z) W_m^{II}(x) \right] T_m(t), \end{aligned} \quad (23)$$

$$W_m^I(x) \equiv X_{Tm}(x) = \frac{\cos(\alpha_m x)}{\cos(\alpha_m L/2)}, \quad W_m^{II}(x) \equiv X_{Hm}(x) = \frac{\cosh(\alpha_m x)}{\cosh(\alpha_m L/2)}.$$

It is noted that assuming $T_m(t) \equiv 1$ in expressions (23) one obtains the kinematic assumptions applied in [3,4]. The functions of variable x refer to the case of symmetric modes of vibration. When the unsymmetric (about the mid-span) modes of vibration are analysed the

'cos' and 'cosh' functions must be replaced by the 'sin' and 'sinh' functions, respectively. The functions dependent on the variable z , derived eg. in [1,2], are defined in the appendix. One can see that each of the solutions denoted by superscripts I and II contains four unknown constants, which can be calculated after solving the eigenvalue problem. Thus, the total fields within the faces contain eight unknown constants.

The displacements in the core are composed here of all the functions denoted with superscripts I, II and III, IV defined above. Obviously, all the functions can be arranged into two groups, one with the $X_{Tm}(x)$ (and its derivative) and the other group with the $X_{Hm}(x)$ (and its derivative). The total fields within the core contain, in a general case, sixteen unknown constants. In the case of symmetry of the structure about the middle plane the number of unknown constants for the core can be reduced to eight. Let us conclude finally that the total displacement and stress fields within the whole structure symmetric about the middle plane contain sixteen unknown constants.

It is explained here that all through-the-thickness boundary conditions and the compatibility equations are satisfied separately by the ingredients containing the trigonometric functions of the space variable x and (separately) by the ingredients containing the hyperbolic functions of variable x . For the classical three-layer sandwich structure it means, in a general case, twenty four equations while for the structure symmetric about the middle plane it means only twelve equations for the total fields.

Thus, to satisfy the edge boundary conditions (3), (4) additional four equations are needed and therefore the following relationships are introduced,

$$g_{jm}^I(\pm h_2/2) = g_{jm}^{II}(\pm h_2/2), \quad f_{jm}^I(\pm h_2/2) = f_{jm}^{II}(\pm h_2/2), \quad (24)$$

$$\int_{-h_2/2}^{+h_2/2} z [S_{xx2}^I + S_{xx2}^{IIIT} + S_{xx2}^{IVT}] dz = \int_{-h_2/2}^{+h_2/2} z [S_{xx2}^{II} + S_{xx2}^{IIIH} + S_{xx2}^{IVH}] dz, \quad (25)$$

$$\int_{-h_2/2}^{+h_2/2} [S_{xz2}^I + S_{xz2}^{IIIT} + S_{xz2}^{IVT}] dz = \int_{-h_2/2}^{+h_2/2} [S_{xz2}^{II} + S_{xz2}^{IIIH} + S_{xz2}^{IVH}] dz,$$

where symbols appearing in the parentheses of Eqs (25) denote the functions included in formulas for the stresses occurring in (4) dependent (only) on the space variable z .

As far as the present author knows, the Eqs (25) are introduced here for the first time within the local linear elastodynamics. It is noted that assumption (24), together with (23) and (3), implies the following relationships,

$$u_{xj} = + \sum_m g_{jm}^I(z) \alpha_m \left[\frac{\sin(\alpha_m x)}{\cos(\alpha_m L/2)} + \frac{\sinh(\alpha_m x)}{\cosh(\alpha_m L/2)} \right] T_m(t), \tag{26}$$

$$u_{zj} = + \sum_m f_{jm}^I(z) \left[\frac{\cos(\alpha_m x)}{\cos(\alpha_m L/2)} - \frac{\cosh(\alpha_m x)}{\cosh(\alpha_m L/2)} \right] T_m(t),$$

$$\frac{\sin(\alpha_m L/2)}{\cos(\alpha_m L/2)} + \frac{\sinh(\alpha_m L/2)}{\cosh(\alpha_m L/2)} = 0. \tag{27}$$

The equation (27) enables us to calculate the parameter α_m recognized as that one resulting from the Bernoulli-Euler beam theory.

5 NUMERICAL RESULTS

In Table 1 eight eigenfrequencies for the C-C structure with the data given in [5-7], predicted by the new model, are presented. The eigenfrequencies are denoted by ω_{SK} . Apart from the new results the reader will find in Table 1 eigenfrequencies existing (for the structure) in the literature i.e., ω_{SKs} - predicted by the simplified (efficient) model presented in [7], ω_{Exp} - obtained experimentally [5], ω_{RAV} - predicted by the model [5], ω_{VSS} - obtained according to the model given in [6].

Vibr. mode (m)		1(s)	2(a)	3(s)	4(a)	5(s)	6(a)	7(s)	8(a)
ω_{SK}	[rad/s]	245.94	677.97	1329.1	2197.2	3282.4	4585.0	6105.4	7844.1
ω_{SKs}	[rad/s]	220.50	597.91	1144.0	1834.7	2645.1	3551.4	4537.4	5568.3
ω_{Exp}	[rad/s]	-	-	1165.5	1761.2	2509.5	3362.8	4277.0	5448.8
ω_{RAV}	[rad/s]	229.88	617.81	1173.8	1872.0	2685.6	3596.0	4575.3	5618.7
ω_{VSS}	[rad/s]	217.40	584.96	1113.4	1776.9	2552.9	3419.9	4358.6	5353.3

Table 1: Eigenfrequencies of the sandwich C-C structure according different models.

The percentage differences between the results predicted by different models are presented in Fig. 2.

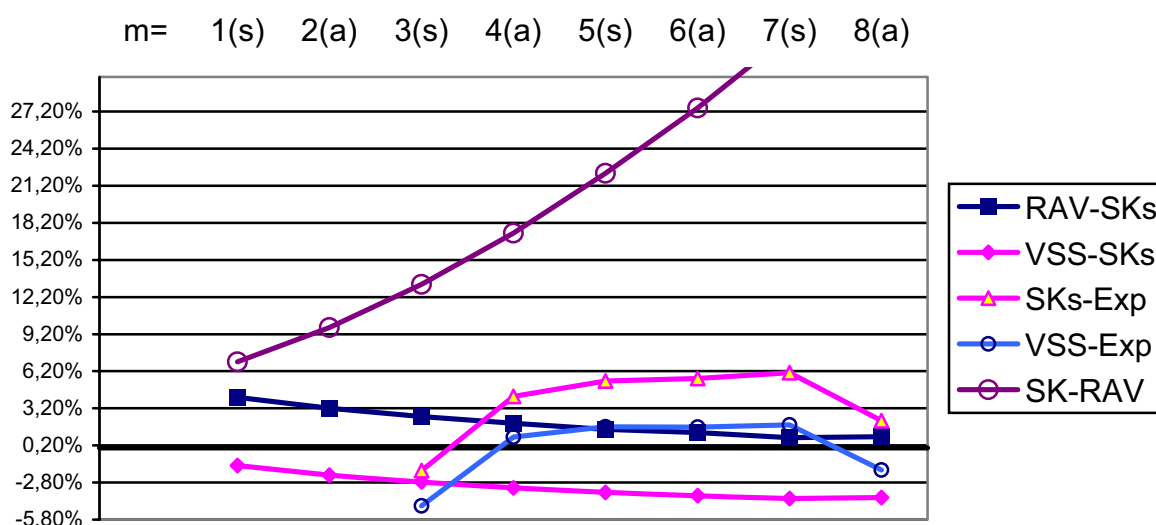


Figure 2: Percentage differences between eigenfrequencies from Table 1.

It is seen from Table 1 and in Fig. 2 that the new 2D model gives higher eigenfrequencies than the models [5,6]. The eigenfrequencies ω_{SK} are also higher than the experimental data ω_{Exp} from [5]. (Unfortunately, the eigenfrequencies of the first symmetric mode and first unsymmetric mode of vibration are not explicitly given in [5,6]). However, the analysis in Fig. 2 shows clearly that the models [5,6], as well as the simplified (efficient) model [7], predict inaccurately the lower, both symmetric and unsymmetric, eigenfrequencies of the structure. Therefore, we can say that the new 2D model predicts accurately the eigenfrequencies of the lower modes of vibration.

6 CONCLUSIONS

A new 2D model for the sandwich structure with edge stiffeners was presented and assessed. Most probably, the model predicts accurately eigenfrequencies of lower modes of vibration of the C-C sandwich structure with the edge stiffeners. It is evident that models [5-7] predict much lower eigenfrequencies of the lower modes of vibration of the structure than the real (experimental) values. Since the percentage differences between predictions of the new model and the other models for the higher modes of vibration are high it is concluded that the new model must be more extensively investigated.

ACKNOWLEDGMENT

The author wishes to thank to Professor Dr. A.J.M. Ferreira, the Chairman of the 8th International Conference on Sandwich Structures, and to the University of Porto as well as to the Organising Committee for exempting him from paying the registration fee.

APPENDIX

Functions of the space variable z denoted by superscript I occurring in Eqs (23) [1,2],

$$\begin{aligned} g_{jm}(z) &= g_{jml}(z) + g_{jm2}(z), & f_{jm}(z) &= f_{jml}(z) + f_{jm2}(z), \\ d^2 g_{jml} / dz^2 - \beta_{1jm}^2 g_{jml} &= 0, & d^2 f_{jml} / dz^2 - \beta_{1jm}^2 f_{jml} &= 0, \\ d^2 g_{jm2} / dz^2 - \beta_{2jm}^2 g_{jm2} &= 0, & d^2 f_{jm2} / dz^2 - \beta_{2jm}^2 f_{jm2} &= 0, \end{aligned} \quad (A1)$$

$$\beta_{1jm}^2 = \alpha_m^2 - \rho_{jm} \omega_m^2 / \mu_j, \quad \beta_{2jm}^2 = \alpha_m^2 - \rho_{jm} \omega_m^2 / (\lambda_j + 2\mu_j), \quad \alpha_m^2 > 0.$$

Functions of the space variable z denoted by superscript II occurring in Eqs (23) [1,2],

$$\begin{aligned} g_{jm}(z) &= g_{jml}(z) + g_{jm2}(z), & f_{jm}(z) &= f_{jml}(z) + f_{jm2}(z), \\ d^2 g_{jml} / dz^2 + r_{1jm}^2 g_{jml} &= 0, & d^2 f_{jml} / dz^2 + r_{1jm}^2 f_{jml} &= 0, \end{aligned} \quad (A2a)$$

$$\begin{aligned} d^2 g_{jm2} / dz^2 + r_{2jm}^2 g_{jm2} &= 0, & d^2 f_{jm2} / dz^2 + r_{2jm}^2 f_{jm2} &= 0, \end{aligned} \quad (A2b)$$

$$r_{1jm}^2 = \alpha_m^2 + \rho_{jm} \omega_m^2 / \mu_j, \quad r_{2jm}^2 = \alpha_m^2 + \rho_{jm} \omega_m^2 / (\lambda_j + 2\mu_j), \quad \alpha_m^2 > 0.$$

The following relationships are valid both for the functions (A1) and (A2),

$$\begin{aligned} g_{jml} &= g_{jml1} {}^j C_{1m} + g_{jml2} {}^j C_{2m}, & f_{jml} &= f_{jml1} {}^j C_{1m} + f_{jml2} {}^j C_{2m}, \\ g_{jm2} &= g_{jm21} {}^j C_{3m} + g_{jm22} {}^j C_{4m}, & f_{jm2} &= f_{jm21} {}^j C_{3m} + f_{jm22} {}^j C_{4m}, \end{aligned} \quad (A3)$$

$$f_{jml1}(z) = f_{jml1}(-z), \quad f_{jml2}(z) = -f_{jml2}(-z), \quad f_{jm21}(z) = f_{jm21}(-z), \quad f_{jm22}(z) = -f_{jm22}(-z),$$

$$g_{jml1}(z) = -g_{jml1}(-z), \quad g_{jml2}(z) = g_{jml2}(-z), \quad g_{jm21}(z) = -g_{jm21}(-z), \quad g_{jm22}(z) = g_{jm22}(-z).$$

REFERENCES

- [1] Karczmarzyk S.: An Exact Elastodynamic Solution to Vibration Problems of a Composite Structure in the Plane Stress State. *Journal of Sound and Vibration*, 196, 85-

- 96, (1996).
- [2] Karczmarzyk S.: *An Analytic Model of Flexural Vibrations and the Static Bending of Plane Viscoelastic Composite Structures*. Scientific Works, Mechanics Series, Vol. 172. Publishing House of the Warsaw University of Technology, Warsaw, (1999).
 - [3] Karczmarzyk S.: New 2D Approach and Solution to the Static Transverse Bending Problem for a Sandwich Strip with Realistic Clampings of the Edges. *Journal of Sandwich Structures and Materials*, 6, 7-45, (2004).
 - [4] Karczmarzyk S., Meyer-Piening H.-R. & Caviezel M.: Numerical and Experimental Analysis of the Influence of Edge Conditions on the Deflection of a Clamped-Clamped Asymmetric Sandwich Strip. *Journal of Sandwich Structures and Materials*, 5, 119-145, (2003).
 - [5] Raville M.E., Ueng E.S., Lei M.M.: Natural Frequencies of Vibrations of Fixed-Fixed Sandwich Beams. *ASME Journal of Applied Mechanics*, 28, 367-371, (1961).
 - [6] Sokolinsky V.S. & Nutt S.R.: Boundary Condition Effects in Free Vibrations of Higher-Order Soft Sandwich Beams. *AIAA Journal*, 40, 1220-1227, (2002).
 - [7] Karczmarzyk S.: An Effective 2D Linear Elasticity Vibrational Model for Layered and Sandwich Clamped-Clamped Unidirectional Strips. *Proc. Seventh Int. Conf. on Sandwich Constr.: 577-586*. O.T. Thomsen, E. Bozhevolnaya & A. Lyckegaard, Editors. Aalborg University-Springer, (2005).
 - [8] Sakiyama T., Matsuda H. and Morita C.: Free vibration analysis of continuous sandwich beams with elastic or viscoelastic cores by applying the discrete Green function. *Journal of Sound and Vibration*, 198, 439-454, (1996).
 - [9] Frostig Y., Thomsen O.T.: High-order vibration of sandwich panels with a flexible core. *Int. Journal of Solids and Structures*, 41, 1697-1724, (2004).

SYSTEMATIC VERIFICATION OF SANDWICH MODEL ASSUMPTIONS BASED ON SPECIFIC FINITE ELEMENT FORMULATIONS

M. Linke and H.-G. Reimerdes

Department of Aerospace and Lightweight Structures
RWTH Aachen University
Wüllnerstraße 7, 52062 Aachen, Germany
e-mail: hg_reim@ilb.rwth-aachen.de, web page: <http://www.ilb.rwth-aachen.de>

Key words: Finite element, Sandwich model theory, Sandwich plate, Verification.

Summary. *A systematic approach to verify the applicability of neglecting the in-plane core stiffnesses for the prediction of the structural sandwich behaviour is presented. This approach is based on the comparison between the computation results of standard as well as specific finite elements enabling the estimation of the computation deviation occurring due to neglecting the mentioned stiffnesses.*

1 INTRODUCTION

Sandwich structures with low strength foam cores are increasingly being used due to the achievable high bending stiffness to weight ratio as well as due to the low cost of these foam materials. In comparison to honeycomb cores, foam cores approximately exhibit the same material characteristics in the out-of-plane as well as in the in-plane directions of a sandwich plate. However, analytical solutions which are based on the assumption that the in-plane core stiffnesses can be neglected are also applied to sandwich structures consisting of these cores materials. For honeycomb cores, the assumption of neglectable in-plane core stiffnesses is usually applicable due to the high ratio between the out-of-plane to the in-plane material characteristics (cp. theoretical ratio according to [1, pp. 169-172]). For sandwich structures based on foam cores, it is argued that the stiffnesses of the face sheets are much higher than those of the cores. Therefore, the strain energies due to the in-plane core deformations might be neglected (cp. for example [2, pp. 39-48] or [3, pp. 1-13]). These premises are fulfilled for many sandwich materials. Nevertheless, the question arises for which material combinations, i. e. to which ratios of the face sheet to the core stiffnesses the described approach is still applicable, in particular for sandwich structures consisting of foam cores.

In order to systematically verify the applicability of neglectable in-plane core stiffnesses for the determination of the structural behaviour of sandwich structures composed of foam cores, the Sandwich Master Diagram according to [4] is used. Based on that, the structural sandwich behaviour is described by a dimensionless coefficient enabling the estimation of the sandwich behaviour between its extreme limits of being very stiff to very flexible under transverse shear loading.

For selected points in the Sandwich Master Diagram, finite element analyses are performed using the finite element programme MSC.Marc® (MSC.Software Corporation, 2 MacArthur Place, Santa Ana, CA 92707, USA) as well as specific finite element formulations implemented in MSC.Nastran® (MSC.Software Corporation, 2 MacArthur Place, Santa Ana, CA 92707, USA). Among other things, the developed finite elements are formulated on the basis of a semi-analytical core displacement field. The core displacement pattern is set up using a three-dimensional (3D) material law neglecting the in-plane core stiffnesses and partly solving the underlying differential equations of the sandwich core (cp. deformation field of finite element formulations according to [5] or [6]). The computation results obtained by these finite elements are comparable to numerical exact or completely analytical solutions (cp. for example [7] or [8]). For the selected points in the Sandwich Master Diagram, the analyses using the specific finite elements are compared to the ones carried out using the programme MSC.Marc®. These computations are partly based on a detailed idealisation of the sandwich structures with continuum elements without any neglect of core stiffnesses. In this case, the computation results consequently converge in the theoretical case of an infinite number of elements against the exact solution of continuum mechanics. As a result, the range of applicability of the described sandwich model assumptions can be estimated for a variety of material combinations with respect to the selected points in the Sandwich Master diagram, in particular for sandwich structures with foam cores exhibiting very stiff to flexible behaviour under shear loading.

2 FINITE ELEMENTS BASED ON THREE-LAYER SANDWICH MODEL

The finite sandwich elements are defined using a three-layer sandwich model subdividing the sandwich into the face sheets and the core as individual components. The idealised geometry of the finite elements is illustrated in Figure 1. The face sheet values are marked by f_1 and f_2 for the bottom resp. top face layer whereas the ones of the core are signed with the suffix c . To simplify matters, the element geometry is selected to be rectangular with length a and width b . Furthermore, the face sheet thicknesses d_{f_1} as well as d_{f_2} and the core height are constant at each element node.

The finite element matrices are derived based on the principle of virtual displacements according to [9, pp. 186]:

$$\delta U - \delta W = \int \vec{\sigma}^T \delta \vec{\varepsilon}_l dV = \delta \vec{u}^T \vec{F} \quad (1)$$

where δU is the virtual strain energy, δW is the virtual work of the external forces and $\vec{\varepsilon}$, $\vec{\sigma}$, \vec{F} as well as \vec{u} is the strain, the stress, the force resp. the displacement vector. $\delta \vec{u}$ indicates virtual nodal displacements.

The integral in regard to Equation (1) is solved separately for its individual components. The principle of virtual work yields in the linear range:

$$\int \vec{\sigma}^T \delta \vec{\varepsilon}_l dV = \int \sum_{i=1}^2 \delta \vec{\varepsilon}_{f_i}^T \mathbf{Q}_{f_i} \vec{\varepsilon}_{f_i} dV + \int \delta \vec{\varepsilon}_c^T \mathbf{Q}_c \vec{\varepsilon}_c dV = \delta \vec{u}^T \left(\sum_{i=1}^2 \mathbf{K}_{f_i} + \mathbf{K}_c \right) \vec{u} \quad (2)$$

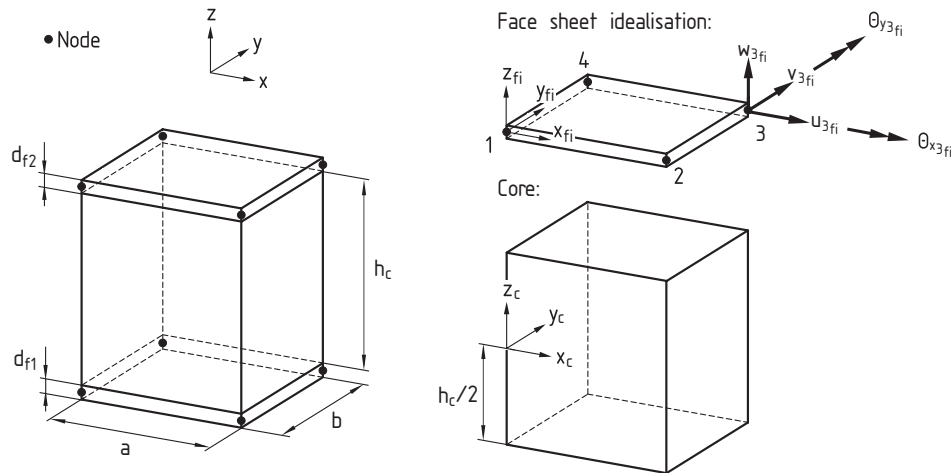


Figure 1: Geometry of developed finite elements and degrees of freedom of face sheets exemplarily illustrated at node 3

where \mathbf{Q}_{fi} is the laminate elasticity matrix of face sheet fi , \mathbf{Q}_c is the core elasticity matrix, \mathbf{K}_{fi} is the linear stiffness matrix of face sheet fi and \mathbf{K}_c is the linear stiffness matrix of the core. The face sheet idealisations of each developed finite sandwich element are identical and are modelled based on the Reissner-Mindlin theory. With respect to the four-node face sheet plate element with five degrees of freedom per node in Figure 1, the linear strain vector is set up with an assumed transverse strain interpolation according to [10]. The laminate elasticity matrix \mathbf{Q}_{fi} is of order eight. The components corresponding to classical laminate theory are determined based on [11] whereas for the transverse shear stiffnesses it is assumed that the shear stresses vary linearly vanishing at the free edges of the sandwich. Based on that approach, the linear stiffness matrix \mathbf{K}_{fi} composed of \mathbf{Q}_{fi} and $\vec{\epsilon}_{fi}$ is clearly defined (cp. [12] for more details).

In the following, three different element formulations are described. They can be distinguished by the formulation of the sandwich core. The first two are based on a core displacement interpolation according to [6] resp. [12] where the displacement pattern is developed based on the analytical solution of the underlying differential equations of the core in the through-thickness direction of the sandwich. The corresponding sandwich elements are formulated in the subsequent paragraph whereas the third core formulation using usual polynomial interpolation functions is described in subsection 2.2.

2.1 ELEMENTS BASED ON ANALYTICAL SOLUTION OF CONSTITUTIVE EQUATIONS

The interpolation functions of the core displacement pattern are determined by solving analytically the underlying differential equations of the core in the through-thickness direction. The differential equations are set up using a 3D material law neglecting the in-plane Young's moduli E_{x_c} and E_{y_c} and the in-plane shear modulus G_{xy_c} of the core. As a result, the in-plane core stresses vanish (σ_{x_c} , σ_{y_c} and $\gamma_{xy_c} \approx 0$), and the core displacement interpolation is defined

in the through-thickness direction according to [6] by:

$$u_c(x, y, z) = a_0(x, y) + a_1(x, y) \cdot z + a_2(x, y) \cdot z^2 + a_3(x, y) \cdot z^3 \quad (3)$$

$$v_c(x, y, z) = b_0(x, y) + b_1(x, y) \cdot z + b_2(x, y) \cdot z^2 + b_3(x, y) \cdot z^3 \quad (4)$$

$$w_c(x, y, z) = c_0(x, y) + c_1(x, y) \cdot z + c_2(x, y) \cdot z^2 \quad (5)$$

where u_c as well as v_c are the in-plane displacements in the x- resp. y-direction of the element coordinate system and w_c is the out-of-plane displacement.

The coefficients $a_i(x, y)$, $b_i(x, y)$ and $c_i(x, y)$ of the displacement pattern depend on the selected state variables of the core. If the continuity conditions between the face sheets and the core are considered, these state variables can be clearly expressed through the introduced face sheet degrees of freedom and an assumption of the core midplane displacement $w_c(x, y, z = 0)$.

Based on a perfect displacement continuity condition between the face sheets and the core, the state variables of the core can be clearly determined by:

$$u_c(x, y, z = -\frac{h_c}{2}) = u_{f1} + \frac{d_{f1}}{2} \cdot \theta_{y_{f1}}, \quad u_c(x, y, z = \frac{h_c}{2}) = u_{f2} - \frac{d_{f2}}{2} \cdot \theta_{y_{f2}} \quad (6)$$

$$v_c(x, y, z = -\frac{h_c}{2}) = v_{f1} - \frac{d_{f1}}{2} \cdot \theta_{x_{f1}}, \quad v_c(x, y, z = \frac{h_c}{2}) = v_{f2} + \frac{d_{f2}}{2} \cdot \theta_{x_{f2}} \quad (7)$$

$$w_c(x, y, z = -\frac{h_c}{2}) = w_{f1}, \quad w_c(x, y, z = \frac{h_c}{2}) = w_{f2} \quad (8)$$

and by an out-of-plane deformation assumption of the core midplane with four additional nodal displacements - each with 1 degree of freedom according to Figure 2.I - resulting in a bilinear pattern.

Based on the afore-mentioned displacement field in the core, two linear stiffness matrices are formulated for the core which can be distinguished by the definition of the core elasticity matrix \mathbf{Q}_c as well as the strain vector $\vec{\varepsilon}_c$. Together with the above-mentioned formulation of the face sheets, the complete finite sandwich element is clearly described. Each consists of 44 degrees of freedom. In the following, both elements formulations are sketched more detailed.

2.1.1 CONSISTENT NEGLECT OF CORE MATERIAL CHARACTERISTICS

For the first finite element formulation, the neglect of the in-plane core material characteristics is also considered during the determination of the stiffness matrix \mathbf{K}_c (not just for the derivation of the core deformation pattern according to the Equations (3) to (5)). If the material as well as the element coordinate system coincide, the neglect of core material characteristics leads to the following core elasticity matrix and strain vector:

$$\mathbf{Q}_c = \begin{bmatrix} E_{z_c} & 0 & 0 \\ 0 & G_{xz_c} & 0 \\ 0 & 0 & G_{yz_c} \end{bmatrix} \quad \text{and} \quad \vec{\varepsilon}_c^T = \left(\frac{\partial w_c}{\partial z}, \frac{\partial u_c}{\partial z} + \frac{\partial w_c}{\partial x}, \frac{\partial v_c}{\partial z} + \frac{\partial w_c}{\partial y} \right)$$

where E_{z_c} is the Young's modulus in the z-direction and G_{xzc} as well as G_{yzc} are the shear moduli in the through-thickness planes of the core (first index of shear modulus marks the direction of the shear stress and the second one the corresponding plane on which the shear acts). This finite element formulation is subsequently called CONSISTENT.

2.1.2 3D CONTINUUM CORE MODEL FOR STIFFNESS MATRIX DERIVATION

In comparison to the definition in paragraph 2.1.1, the second finite element formulation is based on a 3D continuum model of the core used during the calculation of the stiffness matrix \mathbf{K}_c , i.e. the displacement field is selected with respect to the Equations (3) to (5) but the stiffness matrix is set up by considering a complete 3D continuum model for the core. In this case, the elasticity matrix is of order six. It is defined by:

$$\mathbf{Q}_c = \begin{bmatrix} \mathbf{Q}_{c1} & 0 \\ 0 & \mathbf{Q}_{c2} \end{bmatrix} \text{ with } \mathbf{Q}_{c1} = \begin{bmatrix} \frac{1}{E_{xc}} & \frac{-\nu_{xy_c}}{E_{yc}} & \frac{-\nu_{xz_c}}{E_{zc}} \\ \frac{-\nu_{xy_c}}{E_{yc}} & \frac{1}{E_{yc}} & \frac{-\nu_{yz_c}}{E_{zc}} \\ \frac{-\nu_{xz_c}}{E_{zc}} & \frac{-\nu_{yz_c}}{E_{zc}} & \frac{1}{E_{zc}} \end{bmatrix}^{-1}, \mathbf{Q}_{c2} = \begin{bmatrix} G_{xzc} & 0 & 0 \\ 0 & G_{yzc} & 0 \\ 0 & 0 & G_{xy_c} \end{bmatrix} \quad (9)$$

Again, the material and the element coordinate system are equal to simplify matters. The corresponding strain vector is consequently determined through:

$$\vec{\varepsilon}_c^T = \left(\frac{\partial u_c}{\partial x}, \frac{\partial v_c}{\partial y}, \frac{\partial w_c}{\partial z}, \frac{\partial u_c}{\partial z} + \frac{\partial w_c}{\partial x}, \frac{\partial v_c}{\partial z} + \frac{\partial w_c}{\partial y}, \frac{\partial v_c}{\partial x} + \frac{\partial u_c}{\partial y} \right) \quad (10)$$

In the following, this finite element formulation is called SEMI-CONSISTENT.

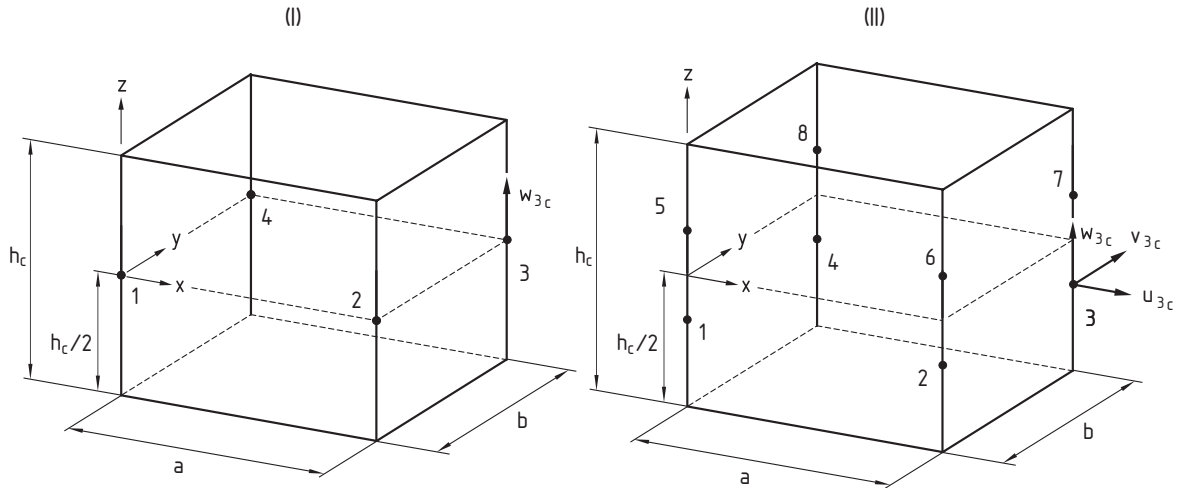


Figure 2: Nodal degrees of freedom of the core of the elements CONSISTENT and SEMI-CONSISTENT (left part) and of the element POLYNOMIAL (right part) exemplary illustrated at core node 3

2.2 CORE INTERPOLATION WITH USUAL POLYNOMIALS

For the third element formulation, a usual displacement pattern with polynomials for the core is used. The core deformations u_c , v_c and w_c are assumed to vary cubically in the through-thickness direction:

$$u_c(x, y, z) = a_0(x, y) + a_1(x, y) \cdot z + a_2(x, y) \cdot z^2 + a_3(x, y) \cdot z^3$$

$$v_c(x, y, z) = b_0(x, y) + b_1(x, y) \cdot z + b_2(x, y) \cdot z^2 + b_3(x, y) \cdot z^3$$

$$w_c(x, y, z) = c_0(x, y) + c_1(x, y) \cdot z + c_2(x, y) \cdot z^2 + c_3(x, y) \cdot z^3$$

The coefficients $a_i(x, y)$, $b_i(x, y)$ and $c_i(x, y)$ are determined in the usual way through the perfect continuity conditions between the face sheets and the core as well as by the introduced degrees of freedom of the core regarding Figure 2.II (8 additional core nodes each with 3 degrees of freedom).

As the selected displacement field in the core agrees with standard displacement-based finite element approaches, the linear stiffness matrix of the core is set up using the 3D continuum modelling approach. As a consequence, the stiffness matrix \mathbf{K}_c is defined by the matrix operation according to Equation (2) with the elasticity matrix \mathbf{Q}_c and the strain vector $\vec{\epsilon}_c$ with regard to Equation (9) resp. (10). Together with the above-mentioned definitions of the face sheets, the finite element approach is clearly defined. It is described by 64 degrees of freedom. In the following, this finite element formulation is called POLYNOMIAL.

3 IMPLEMENTATION OF DEVELOPED ELEMENTS

The derived stiffness matrices of the developed finite elements have been implemented into the finite element program Nastran using a DMAP-program according to [13] and a Fortran77-routine. Based on this approach, the DMAP-program reads the problem formulation through the standard Nastran bulk data set. Furthermore, it subsequently controls the determination of the single element matrices by calling the mentioned Fortran-routine and the solution of the resulting system matrices. The computation results are finally stored in ascii-format for subsequent postprocessing.

4 MARC-IDEALISATIONS FOR VERIFICATION

The developed finite sandwich elements are verified based on computations carried out using the programme MSC.Marc®. Three different Marc-idealizations are utilised. These models are set up either with a combination of shell and solid elements or completely with solid or shell elements only. The Reissner-Mindlin theory is applied for the shell elements.

For the sandwich idealizations consisting of shell and solid elements, the face sheets are modelled by shells which exhibit assumed transverse shear effects. Each interpolation function is bilinear (element 75 according to [14, pp. 444-449]). The core is idealised by eight node solid elements based on trilinear trial functions (element 7 with regard to [14, pp. 127-132]). The latter element type is also used for sandwich models which are only set up based on solid

idealisations. An orthotropic material law is utilised for all core elements. If the sandwich is only modelled by shell elements, the above-mentioned shell type 75 is applied. The three aforementioned idealisations are referred to as Marc7-75 combination of shell and solid elements), Marc7 (complete solid idealisation) and Marc75 (complete shell element model).

5 VERIFICATION

The developed finite elements are systematically verified for linear statics of orthotropic sandwich panels. In order to verify their applicability, the Sandwich Master diagram with respect to [4] is used. On the basis of this diagram, the structural behaviour of sandwich applications is described by a dimensionless coefficient r enabling the estimation of the mechanical behaviour between its extreme limits of being very stiff to very flexible under transverse shear loading. It is applicable to linear statics and linear stability problems.

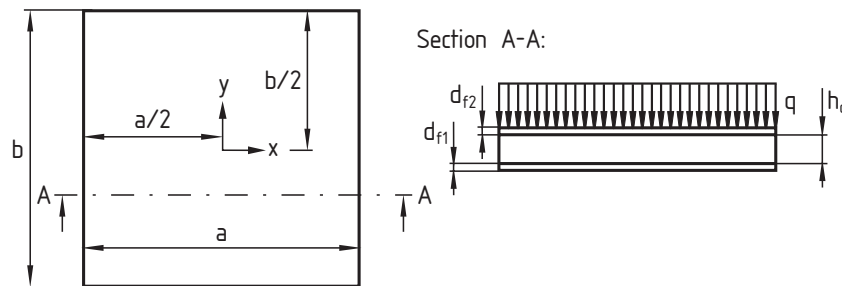


Figure 3: Sandwich panel under uniquely distributed load q

The investigated problem is shown in Figure 3. An uniquely distributed load of $q = 0,1$ MPA acts on the top face layer of the panel. The structure is simply supported along its edges, and the dimensions of the sandwich plate amount to $a, b = 300$ mm. Additional geometry and material data used during the verification can be derived on the basis of the Sandwich Master diagram 4 and Table 1. In general, three different core to face sheet thickness ratios are analysed (cp. Figure 4) The introduced coefficients are determined with respect to [4]:

$$r = \frac{1 + \left(1 - \frac{B_f}{B_{ges}}\right) \frac{\pi^2 B_{ges}}{c^2 B_\tau}}{1 + \left(1 - \frac{B_f}{B_{ges}}\right) \frac{\pi^2 B_f}{c^2 B_\tau}} \quad \text{with} \quad B_f = \frac{E_f b d_f^3}{6},$$

$$B_{ges} = B_f + \frac{E_f b d_f (h_c + d_f)^2}{2}, \quad B_\tau = \frac{G_c b (h_c + d_f)^2}{h_c} \quad \text{and} \quad \frac{1}{c^2} = \frac{1}{a^2} + \frac{1}{b^2}$$

where E_f is the Young's modulus of the face sheets, and G_c is the shear modulus of the core. As the face sheets are assumed to be identical with $d_f = d_{f1} = d_{f2}$, the stiffnesses of the face sheets are summed up, and the resulting characteristics are marked by the suffix f .

In the following, the computation results of two numerical investigations are described. In the first analysis, the premises are approximately fulfilled under which the core displacement field of the finite element formulations according to paragraph 2.1 is derived, i. e. the stiffnesses

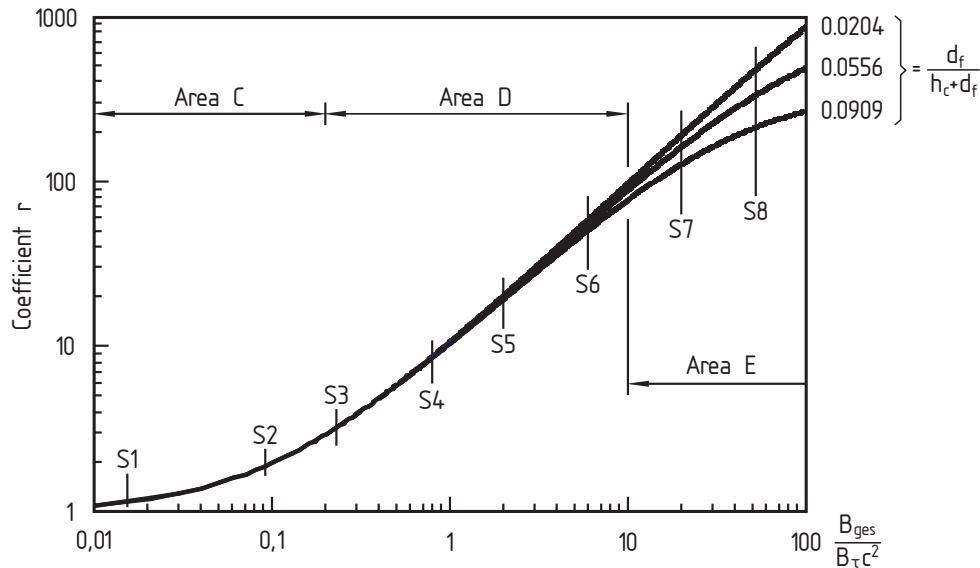


Figure 4: Sandwich Master diagram with regard to [4]

of the face layers are significantly higher than the ones of the core. The corresponding point in the Sandwich Master diagram to this problem is located in section 3 of Figure 4. Based on the findings of the afore-mentioned problem with approximately ideal face sheet to core stiffnesses, a systematic variation within the Sandwich Master diagram is performed in the second investigation. The points considered in the Sandwich Master diagram are located in the sections 1 to 12 intersecting the indicated curves of constant face sheet to core thicknesses. As a consequence of this investigation, the range of applicability of the introduced assumptions can be estimated for sandwich structures consisting of a variety of core materials, in particular, of foam cores.

5.1 APPROXIMATELY IDEAL FACE SHEET TO CORE STIFFNESSES

The investigated sandwich structure is clearly defined by the intersection of the curve for $\frac{d_f}{h_c+d_f} = 0.0204$ resp. $h_c = 24$ mm with section 3 in the Sandwich Master Diagram. In that case, the stiffnesses are significantly higher than the ones of the core.

A quarter of the sandwich panel is idealised due to the doubly symmetric problem. The subsequently described computation results are obtained for regular meshes with convergence rates of the maximum displacement of the upper face sheet which are lower than 0.1 %.

The Marc-analyses are carried out using the idealisations described in paragraph 4. The model Marc7 completely consisting of solid elements is idealised based on two different material laws of the core. The results which are referred to by Marc7_{neg} are obtained for a core material law with neglected in-plane core material characteristics, i. e. the in-plane values are almost set to zero. This approach corresponds to the above described element formulation CONSISTENT. In comparison to that, Marc-results indicated by Marc7_{all} are generated based on the full 3D continuum model for the core. No material characteristics are neglected.

Section	$\frac{d_f}{h_c+d_f}$ [%]	h_c [mm]	$\frac{B_{ges}}{B_r c^2}$ [-]	r [-]	E_f [$\frac{N}{mm^2}$]	ν_f [-]	E_c [$\frac{N}{mm^2}$]
S1	9.09	5	0.015	1.149	1479.9	0.3142	7.7285
	5.56	8.5	0.015	1.149	1479.9	0.3142	13.1160
	2.04	24	0.015	1.150	1479.9	0.3142	37.0000
S2	9.09	5	0.093	1.911	9069.6	0.3142	7.7285
	5.56	8.5	0.093	1.915	9069.6	0.3142	13.1158
	2.04	24	0.093	1.918	9069.6	0.3142	37.0000
S3	9.09	5	0.233	3.269	22674	0.3142	7.7285
	5.56	8.5	0.233	3.285	22674	0.3142	13.1160
	2.04	24	0.233	3.294	22674	0.3142	37.0000
S4	9.09	5	0.800	8.686	22674	0.3142	2.2470
	5.56	8.5	0.800	8.816	22674	0.3142	3.8133
	2.04	24	0.800	8.885	22674	0.3142	10.7573
S5	9.09	5	1.976	19.41	56000	0.3000	2.2470
	5.56	8.5	1.976	20.08	56000	0.3000	3.8134
	2.04	24	1.976	20.44	56000	0.3000	10.7573
S6	9.09	5	6.000	51.67	210000	0.3000	2.7748
	5.56	8.5	6.000	56.71	210000	0.3000	4.7090
	2.04	24	6.000	59.72	210000	0.3000	13.2840
S7	9.09	5	20.00	128.4	210000	0.3000	0.8324
	5.56	8.5	20.00	164.8	210000	0.3000	1.4127
	2.04	24	20.00	193.1	210000	0.3000	3.9853
S8	9.09	5	52.00	213.1	210000	0.3000	0.3202
	5.56	8.5	52.00	336.4	210000	0.3000	0.5433
	2.04	24	52.00	480.0	210000	0.3000	1.5328

Table 1: Isotropic material characteristics selected for the face sheets and the core ($\nu_c = 0, 4231$)

The computation results are illustrated in Table 2 and in the Figures 5 and 6. As the results of the calculations based on the element type SEMI-CONSISTENT agree quite well with the ones of the type POLYNOMIAL (deviations of the shown displacement and stress values are lower than 0.1 %), just the results of the idealisations CONSISTENT and SEMI-CONSISTENT are shown. Furthermore, the results of the computations based on the models Marc7-75 and Marc75 are only illustrated in Table 2 to simplify matters, too.

The good agreement between the computation results based on the element types SEMI-CONSISTENT and POLYNOMIALS can be identified in Table 2. The deviations of the displacement and the stress values to the calculations of MSC.Marc® are almost the same for both idealisations. Moreover, it can be seen that the results of the developed finite elements

	Marc7 _{all}		Marc7 _{neg}	
	Δw_{f2} in %	$\Delta \sigma_{xf2}$ in %	Δw_{f2} in %	$\Delta \sigma_{xf2}$ in %
Marc75	1.15	2.63	-0.20	-1.29
Marc7-75	0.04	0.02	-1.29	-3.80
CONSISTENT	1.35	4.01	0.00	0.04
SEMI-CONSISTENT	-0.01	-0.03	-1.34	-3.85
POLYNOMIALS	-0.01	0.02	-1.33	-3.80

Table 2: Deviation between the computation results of the Marc-analyses Marc7_{all} as well as Marc7_{neg} and calculations based on the developed elements (for model Marc7_{all} all core material characteristics are considered, for idealisation Marc7_{neg} the in-plane core material values are neglected) where Δw_{f2} is the deviation of the z-displacement and $\Delta \sigma_{xf2}$ is the deviation of the normal stress in the global x-direction each at the plate middle of the upper face sheet

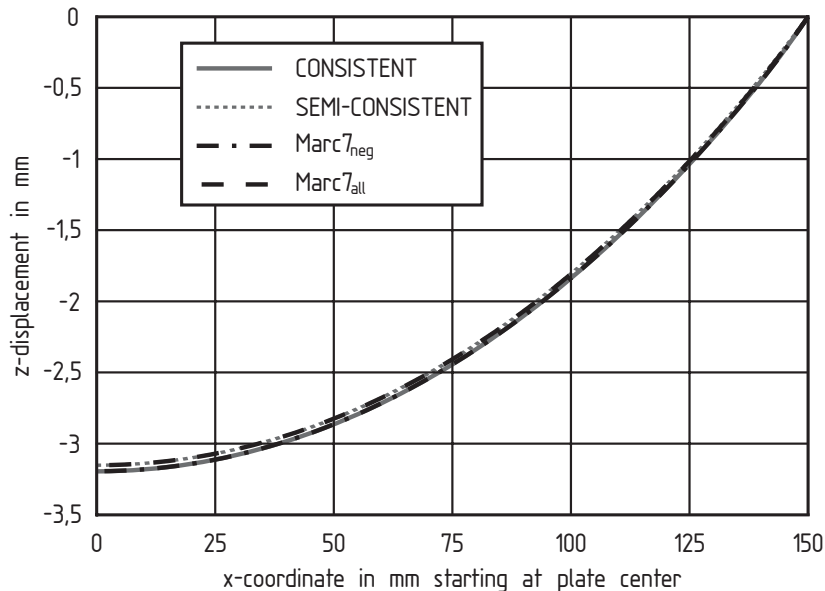


Figure 5: Displacement in the middle of the upper face sheet in z-direction

agree well with the Marc results if the core material laws are selected to be approximately identical during the formulation of the stiffness matrix (CONSISTENT corresponds to Marc7_{neg} and SEMI-CONSISTENT as well as POLYNOMIAL equal Marc7_{all}). In particular, this is the case for the results of the derived elements SEMI-CONSISTENT as well as POLYNOMIAL which agree well with the related idealisation Marc7_{all} enabling a realistic description of the investigated isotropic foam core material. Furthermore, it has to be mentioned that the results based on the element type CONSISTENT with neglected in-plane core stiffnesses still agree well with the ones of the model Marc7_{all} although the introduced core material laws differ between the models. The deviations of the shown displacement and stress values to the model

Marc7_{all} just amount to 1.3 % resp. 4%. This good agreement with regard to Table 2 can also be observed over the whole sandwich plate for the illustrated values (cp. the Figures 5 and 6). As a consequence, the consideration of the in-plane core stiffnesses is of minor importance for the analysed sandwich structure if the face sheet to core stiffnesses are approximately ideal, i. e. for the selected point in the Sandwich Master diagram.

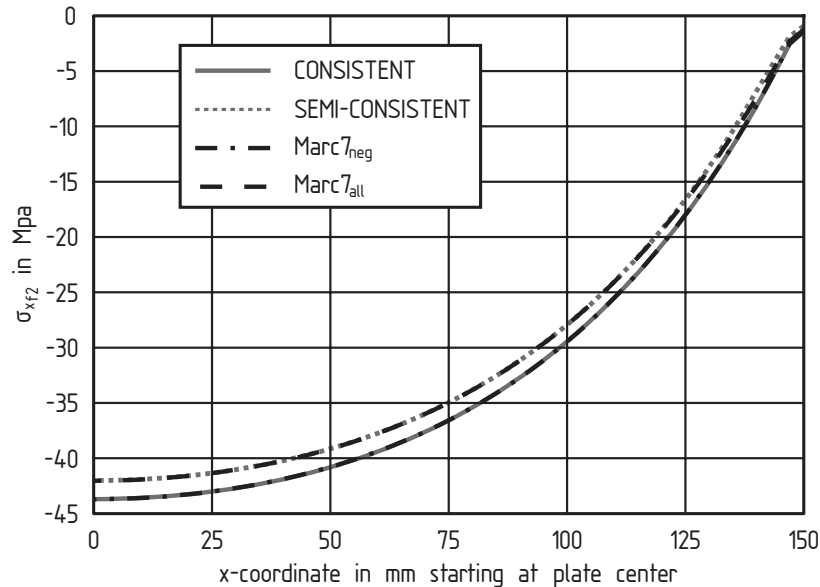


Figure 6: Normal stress $\sigma_{x_{f2}}$ in the middle of the upper face sheet

The Marc-results obtained by the computations based on shell elements with assumed transverse shear strains (Marc75) agree with the ones of the models Marc7_{all} and Marc7_{neg} as it is the case for the idealisation with the element type CONSISTENT (cp. Table 2). With the simple element technology Marc75, good agreement is achieved for the investigated point in the Sandwich Master diagram although a small number of degrees of freedom is used. However, it has to be mentioned that this element technology is not appropriate if local phenomena like peeling stresses in the core or flexible core behaviour in the through-thickness direction has to be adequately predicted.

Almost the same results are determined for the Marc7-75 idealisation (with face sheet elements considering transverse shear strains and solid elements in the core) as it is the case for the models based on the element types SEMI-CONSISTENT and POLYNOMIALS. This is due to the fact that the structural sandwich behaviour is sufficiently predicted by the selected displacement fields in the core and that comparable core material laws are used during the stiffness matrix formulation.

To summarise, good agreement can be achieved between the computation results based on the described finite elements and the ones of realistic finite element idealisations. The latter ones are carried out with the program system MSC.Marc®. Furthermore, the observed deviations are mainly caused by selecting different core material laws for the determination of the stiffness

matrix. Therefore, the core deformation pattern is sufficiently described by the analytically derived core displacement pattern (elements CONSISTENT and SEMI-CONSISTENT) enabling the reduction of the degrees of freedom in comparison to standard finite element idealisations for the analysed the static problem.

5.2 VARIED FACE SHEET TO CORE STIFFNESSES

In order to verify the applicability of the developed elements, the relevant areas in the Sandwich Master diagram are analysed with the derived elements and with idealisations based on the program system MSC.Marc®. The considered points are defined in Figure 4 by the intersection of the curves with constant face sheet to core thickness with the illustrated sections 1 to 8 ($\frac{B_{ges}}{B_r c^2}$ is constant). The investigated sandwich structure is described in Figure 3 and in Table 1. As the applied face sheet elements are based on the assumption that the face layers are thin, the ratio of the face sheet to the core thickness is limited to 10 % ($\frac{d_f}{h_c} \leq 0.1$ leads to $\frac{d_f}{h_c+d_f} \leq 0.0909$).

Again, a quarter of the sandwich panel is idealised due to the doubly symmetric problem. The applied finite elements (CONSISTENT, SEMI-CONSISTENT and POLYNOMIAL) agree with the ones used in the preceding paragraph. The Marc-idealisations Marc75 and Marc7 according to section 4 are utilised.

In the following, the computation results are compared to each other for the maximum deflection at the middle of the upper face sheet. The results are determined for regular meshes with convergence rates of the maximum displacement that are lower than 0.1 %. The results are related to the ones of the idealisation Marc7 as the computation results of this model should converge in the theoretical case of an infinite number of elements against the exact solution of linear continuum mechanics. The deviations are shown in the Figures 7 to 9. As the models based on the developed elements SEMI-CONSISTENT and POLYNOMIAL agree quite well, just the values of type SEMI-CONSISTENT are illustrated to simplify matters.

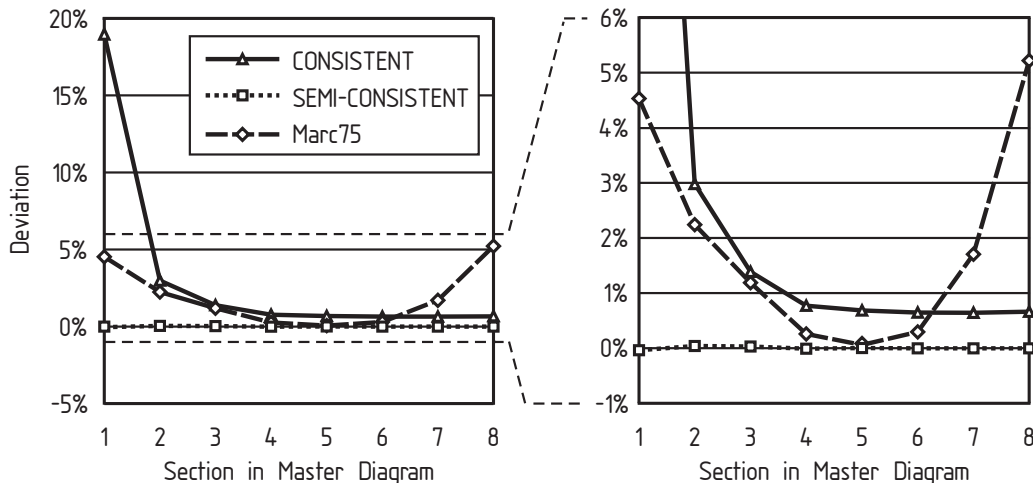


Figure 7: Maximum displacement deviation (related to Marc7 results) for ratio of $\frac{d_f}{h_c+d_f} = 2,04\%$

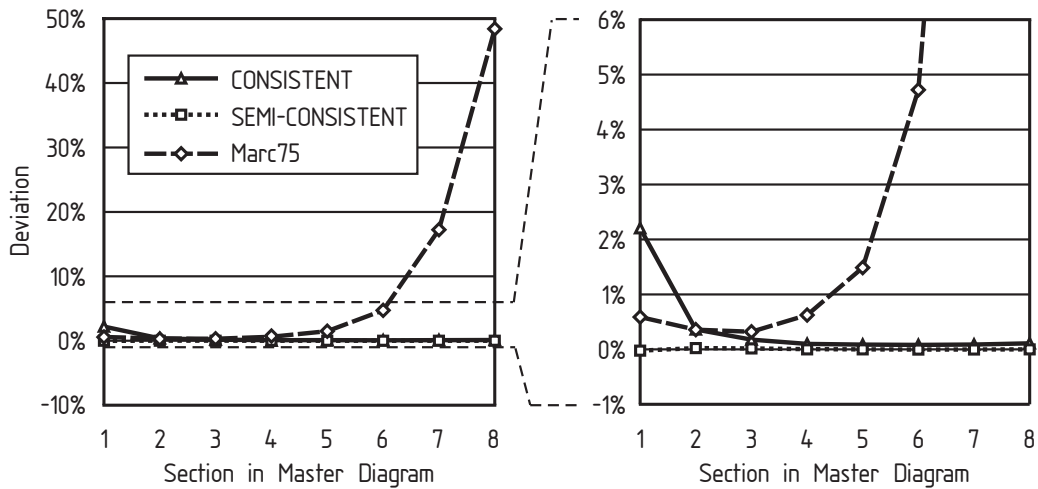


Figure 8: Maximum displacement deviation (related to Marc7 results) for ratio of $\frac{d_f}{h_c+d_f} = 5,56\%$

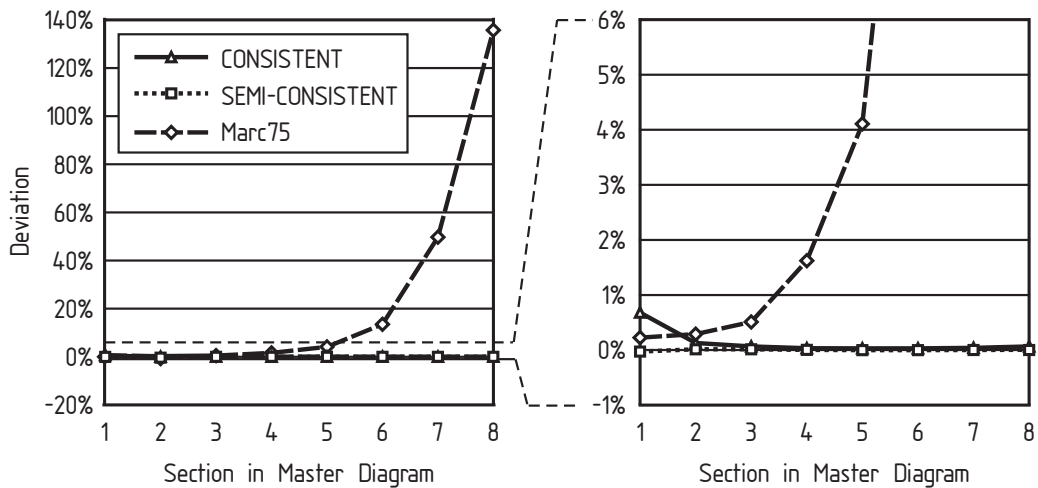


Figure 9: Maximum displacement deviation (related to Marc7 results) for ratio of $\frac{d_f}{h_c+d_f} = 9,09\%$

In the figures, it can be seen that the Marc75 computations (with no solid element idealisation of the core) exhibit increasing deviations with growing $\frac{B_{ges}}{B_{\tau}c^2}$ in the areas D and E in the Sandwich Master diagram (cp. in particular left diagram of the Figures 7 to 9). The deviations grow with the flattening of the curves in the Sandwich Master diagram. This is due to the fact that the face sheets increasingly act as independent, individual plates. Therefore, the mechanical description of the sandwich based on a plate formulation considering transverse shear effects leads to a growing error concerning the prediction of the structural behaviour in the afore-mentioned areas in the Sandwich Master diagram.

The results of the idealisations with the element type CONSISTENT exhibit good agreement with the calculations based on the model Marc7 in the analysed areas of the Sandwich Master diagram. Greater deviations occur for low ratios of $\frac{B_{ges}}{B_{\tau}c^2}$ and increasing core heights. This is due to the fact that the sandwich acts more like a composite plate. Therefore, the bending stiffness

of the core significantly contributes to the overall bending stiffness which is neglected for the element formulation of the element type CONSISTENT.

With regard to the Figures 7 to 9, the deviations of the models based on the element type SEMI-CONSISTENT are significantly reduced in comparison to the ones of the CONSISTENT idealisations (results of SEMI-CONSISTENT and POLYNOMIAL models are approximately the same). Every deviation referred to the Marc7 model is lower than 0.1 % for all investigated points in the Sandwich Master diagram.

6 CONCLUSION

In general, the structural behaviour of sandwich panels can be predicted in the linear range with sufficient precision on the basis of the developed finite elements. Greater deviations can just be observed for the idealisations based on the element type CONSISTENT in the zone of the Sandwich Master diagram where the sandwich plate increasingly acts like composite panel. This is caused by neglecting the in-plane core material characteristics during the derivation of the stiffness matrix. Nevertheless, the analytically determined core displacement pattern used for the elements CONSISTENT as well as SEMI-CONSISTENT sufficiently describes the core behaviour, i. e. the underlying theory of the derived finite elements is applicable to isotropic core materials like foams for a wide range of sandwich structures.

REFERENCES

- [1] L.J. Gibson and M.F. Ashby. *Cellular Solids - Structure and Properties*, Cambridge Univ. Press, 2001.
- [2] D. Zenkert. *An Introduction to Sandwich Construction*, Engineering Materials Advisory Services Ltd., 1995.
- [3] J.R. Vinson. *The Behavior of Sandwich Structures of Isotropic and Composite Materials*, Technomic Publishing Company, Inc., 1999.
- [4] H.G. Allen and Z. Fend. *Classification of Structural Sandwich Panel Behaviour*, A. Vautrin (editor). *Mechanics of Sandwich Structures*, Proceedings of the EUROMECH 360 Colloquium, Saint-Étienne, France, 13-15th May 1997, Kluwer Academic Publishers, 1998.
- [5] S. Oskooei and J.S. Hansen. Higher-Order Finite Element for Sandwich Plates. *AIAA Journal*, **38(3)**, 525–533, 2000.
- [6] M. Linke, W. Wohlers and H.-G. Reimerdes. Finite Element for the Static and Stability Analysis of Sandwich Plates. *Sandwich Structures and Materials*, **9(2)**, 123–142, 2007.
- [7] H. Bansemir. Krafteinleitung in versteifte orthotrope Scheiben. *Ingenieur-Archiv*, **42**, 127–140, 1973.
- [8] Y. Frostig, M. Baruch, O. Vilnay and I. Sheinman. High-Order Theory for Sandwich-Beam Behavior with Transversely Flexible Core. *Journal of Engineering Mechanics*, **118(5)**, 1026–1043, 1992.
- [9] K.-J. Bathe. *Finite-Elemente-Methoden*. 2. Edition, Springer Verlag, Berlin, 2002.

- [10] K.-J. Bathe and E.N. Dvorkin. A Four-Node Plate Bending Element Based on Mindlin/Reissner Plate Theory and a Mixed Interpolation. *International Journal for Numerical Methods in Engineering*, **21**, 367–383, 1985.
- [11] J.-M. Berthelot. *Composite Materials - Mechanical Behavior and Structural Analysis*. Mechanical Engineering Series, Springer Verlag, New York, 1999.
- [12] M. Linke and H.-G. Reimerdes. *Finite Element for Sandwich Panels Based on Analytical Solution of Constitutive Equations*, Experimental Analysis of Nano and Engineering Materials and Structures (ICEM13 - International Conference on Experimental Mechanics, Alexandroupolis, Greece), July 2007
- [13] N.N. MSC.Nastran2001® , DMAP Programmer's Guide. MSC-Software Corporation, 2 MacArthur Place, Santa Ana, CA92707, USA, 2001.
- [14] N.N. MSC.Marc®, Volume B: Element Library. MSC-Software Corporation, 2 MacArthur Place, Santa Ana, CA92707, USA, 2006.

Statistical Regression Analysis of 20 Sandwich Core Materials

Deborah Weissman-Berman

President, dwbus & Assoc. Inc. / Biostatistics and Composites Consulting
Tallahassee, Florida, 32301, USA; email dwbstats@yahoo.com; www.dwbusassoc.com

Keywords: Sandwich structures, Analysis, Statistical regression modeling

Summary. A statistical study of 20 sandwich cored materials with varied fibre orientation and skin thickness is performed to determine the significance of variables in the sandwich including the Modulus of Residual Stiffness α . The results show that α is statistically significant for all tested cores with 1 skin layer, and that the stiffness of the core materials is not significant in the analyses for 3 layers of skin.

1 INTRODUCTION

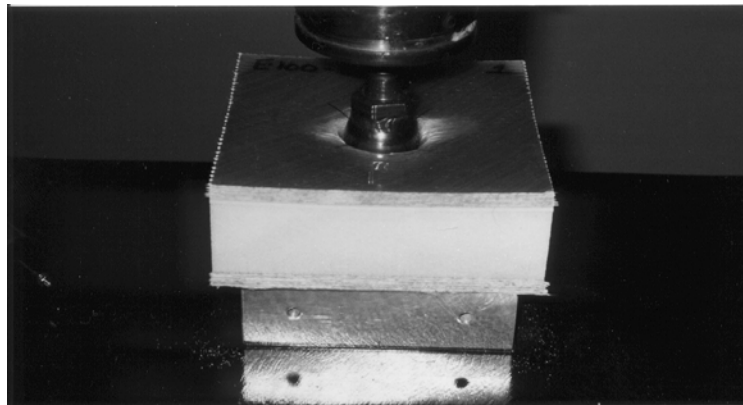


Figure (1) Sandwich core material test for modulus of Residual Stiffness

A sandwich structure is defined by a bi-geometrical structure and sub-structure related by the Modulus of Residual Stiffness, α . These two geometries interact with each other to modify the response of the whole. Typical test materials are shown in Figure (1). Statistical analyses of parameters in modern sandwich construction should be presented in the context of the broader and more identifiable geometry of classical mechanics. Many types of sandwich cores today would be classed as elastic foundations supporting the skins of the sandwich. Modern sandwich construction is mainly fiberglass skin bonded to various types of core materials. These types of materials have been used predominately in the marine industry for the construction of small craft and structural components of ships.

The usual definition of a sandwich assumes an integral bond between skins and core. In this case, each material being of similar overall panel length and width dimensions, the skins and core are loaded in series, thus the same force is transmitted to each layer. Single skin

composites, and by default sandwich construction, have been characterized principally by the stiffness and strength of the short fibers in the mat or in the skins and additionally for sandwich construction by the thickness of the core material. However, when all the properties of the skin matrix and the residual stiffness of the core (α) are taken into account, stress and deflection tests have shown that it is the softer materials – the matrix cushioning the FRP fibers and principally the light weight core material that conforms and bonds to the fibers and the skins that primarily affect the response. A key to the construction of sandwich material is then the statistical significance of sandwich core parameters including α .

2. BACKGROUND

In the last few years, a unified stress theory has been developed by Weissman-Berman [1-9] to model typical sandwich core materials from rigid closed cell foam to end-grain balsa having continuous contact with the faces of a sandwich beam, as shown in Figure (2). These core materials are considered to behave as elastic foundations for those skins. The two geometry's are related by the inclusion of α , a newly defined modulus of residual stiffness within the characteristic length of the beam or plate equation. α defines the elastic curve and is an integral part of the flexural elastic modulus of the sandwich to define the critical compressive stress at secondary yield. The modulus of the residual stiffness is defined as the characteristic of the sub-structure, which is a core bounded by the equivalent skins. Therefore, a sandwich structure may be defined by a bi-geometrical structure and sub-structure related by the Modulus of Residual Stiffness, α .

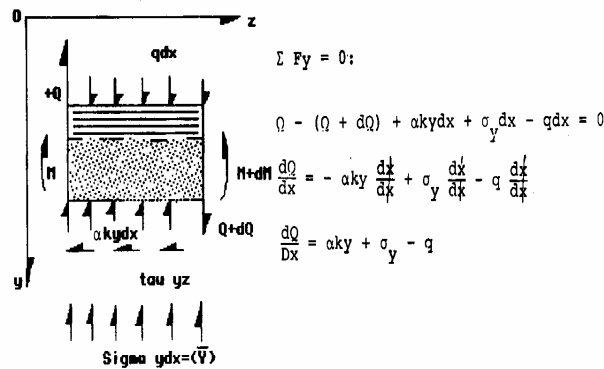


Figure (2) Model of typical sandwich core materials

3. METHODOLOGY

The object of this statistical study of 20 sandwich cored materials is to present the results of regression analyses to determine the significance of five principal components of sandwich structures: (1) alphared (α predicted); (2) Eskin1 (the elastic modulus of the top skin – in

flexure); (3) t_1 (the thickness of the top skin); (4) t_{sand} (the thickness of the total sandwich material); and (5) E_{core} (the elastic modulus of the core material – in flexure). All of these values are taken from an extensive database for a parametric and equally incremented number of skin layers for an extensive range of ten core materials, ranging from highly damped cores such as Airex and EPoly to very stiff cores such as Balsa, on a typical 2.54 cm core thickness [10]. The fibre in the sandwich skins varies from ± 45 degrees to 0/90 degrees, yielding 20 specimens for sandwich with one layer of skins and another 20 with three layers of skins. It has been seen from experimental and correlated predictive data that the value of α goes to unity when the skins have five or more layers.

3.1 Statistical Comparison of α Predicted to α Test Data

The initial analysis will determine the relationship of the variables ‘alphapred’ to ‘alphatest’ to determine the normality of each distribution and the comparison of the predicted and tested value of α . An initial analysis is performed using R for statistical computing for values of α .

The database values for the sandwich cored materials with one skin and three skins are summarized in Table (1,2) below. The initial database variables include five principal components of sandwich structures: (a) α ; (b) E_{skin1} (the elastic modulus of the top skin – in flexure); (c) t_1 (the thickness of the top skin); (d) t_{sand} (the thickness of the total sandwich material); and (e) E_{core} (the elastic modulus of the core material – in flexure). The first two analyses explore the normality of ‘alphapred’ (predicted values of α) for one and three top skins respectively. For both the predicted and tested values of α , the means and median are relatively close values, indicating the normality of the distributions. These values are summarized below.

	Min	1 st Quar	Median	Mean	3 rd Quar	Max
1 skin	.01400	.03550	.05000	.05565	.07425	.12000
3 skins	.0360	.1350	.1755	.2250	.3125	.6100

Table 1: Summary of ‘alphapred’ values with 1 and 3 Top Skins

	Mean	SD	Variance
1 skin	.05565	.02762	.000763
3 skins	.22495	.14426	.020812

Table 2: Summary statistics for ‘alphapred’ with 1 and 3 Top Skins

From Figures (3) and (4), it can be seen that each variable can be considered normal from the histogram, the density plots and the normal quantile plots.

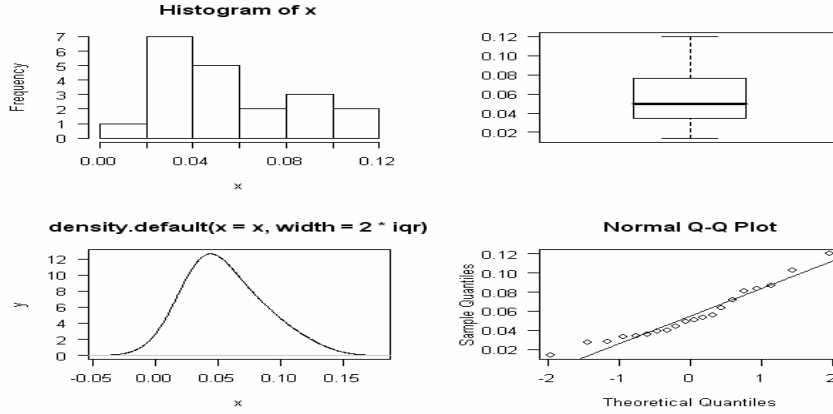


Figure (3) Exploratory Data Analysis Plots-alpha-1 Skin (± 45:0/90 Degrees)

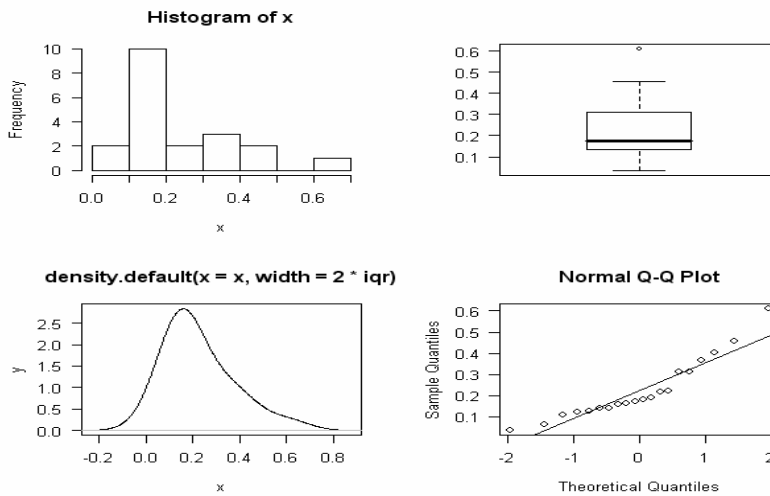


Figure (4) Exploratory Data Analysis Plots-alpha-4 - Skin(± 45:0/90 Degrees)

Then the values of the predicted and tested α are compared using the Welch Two Sample t-test. The null hypothesis is given below:

$$H_0 : \mu_0 = \mu_1 \tag{1}$$

The assumption is that the comparative means are equal to zero or not greatly different from zero. The alternative hypothesis is given as: true difference in means is not equal to 0.

$$H_a : \mu_0 \neq \mu_1 \tag{2}$$

The results show that $t = -0.0282$, $df = 37.96$, $p\text{-value} = 0.9777$, with a 95 percent confidence interval of $(-0.01822594 - 0.01772594)$ and sample estimates of:

$$\begin{array}{ll} \text{mean of x} & \text{mean of y} \\ 0.05565 & 0.05590 \end{array} \quad (3)$$

The result of simply subtracting the means yield a result nearly zero, which is reflected in the value of $p = 0.9777$. The F test to compare two variances yields a $p\text{-value} = 0.8895$, while the ratio of variances = 0.93745. In this test, the alternative hypothesis is accepted only if the true ratio of variances is not equal to 1. Therefore the null hypothesis, accepting ratios nearly equal to 1 is accepted. Therefore, the regression analyses are conducted using the predicted values of α .

It can now be seen that the predictive methodology for α accurately reproduces the test data. This is extremely important for conducting future tests and for implementing tested results in engineering structural analysis. The regression analyses are conducted using the predicted values of α .

3.2 Statistical Linear Models and Multivariate “Loess” Models

Initially, multiple linear regression models are computed using S+ statistical computing methods [5], and finally multivariate ‘loess’ models are computed to determine the model response to the data. The multiple linear regression models are computed using S+ statistical computing methods:

$$y_i = \beta_0 + \beta_1 x_{i1} + \beta_2 x_{i2}, \dots, \beta_p x_{ip}, \quad \text{for } i = 1, 2, \dots, n \quad (4)$$

These linear models are then refit as multivariate ‘loess’ local regression models to determine the adequacy of the residual normality of the predictor variables and the model, where weighted least squares is used to fit linear or quadratic functions of the predictors at centers of neighborhoods. The weighting function is given by α predicted. There are no restrictions on relationships among predictors. The model with one skin layer is given as:

$$\text{loess (formula = Ecore ~ alphapred * t1)} \quad (5)$$

where ‘Ecore’ is the elastic modulus of the core, ‘alphapred’ is the predicted α and ‘t1’ is the top skin thickness. There is a reduced span = 0.75. The multiple $R^2 = 0.90$, indicating that 90% of the variance is accounted for in the data. The model for three skin layers is fit as:

$$\text{loess (formula = t1 ~ alphapred * tsand)} \quad (6)$$

where ‘tsand’ is the sandwich thickness. There is a reduced span = 0.75. The multiple $R^2 = 0.98$, indicating that 98% of the variance is accounted for in the data.

4. RESULTS

The first model is linear and fit for the variable ‘Ecore’ (elastic modulus of the core) on 1 top skin material. The equation in S+ fitting the model on ‘Ecore’ is:

$$lm(formula = Ecore \sim alphapred + t1) \tag{6}$$

Call: `lm(formula = Ecore ~ (alphapred + t1), data = alpha1.df, na.action = na.exclude)`

Residuals:

Min	1Q	Median	3Q	Max
-4542	-1372	-159.8	1633	4128

Coefficients:

	Value	Std. Error	t value	Pr(> t)
(Intercept)	33893.6867	12936.9460	2.6199	0.0179
alphapred	-52073.1730	19125.9032	-2.7227	0.0145
t1	-452324.7249	277762.0362	-1.6285	0.1218

Residual standard error: 2341 on 17 degrees of freedom

Multiple R-Squared: 0.3201

F-statistic: 4.002 on 2 and 17 degrees of freedom, the p-value is 0.03764

Analysis of Variance Table

Response: Ecore

Terms added sequentially (first to last)

	Df	Sum of Sq	Mean Sq	F Value	Pr(F)
alphapred	1	29334139	29334139	5.352874	0.0334633
t1	1	14532529	14532529	2.651886	0.1218165
Residuals	17	93161234	5480073		

Table 3: Linear Model = Sandwich with 1 Top Skin (fitted on Ecore)

The fitted multiple R^2 for parameters fitted on ‘Ecore’ is 0.32. In this model, the $Pr(>|t|) = .0145$ and is highly significant for the variable ‘alphapred’. Furthermore, it can be seen from the histogram that the residuals for this model has no gaps and is fairly normal. The quantiles of the standard normal fitted in Figure (5) are also nearly linear. These quantiles are shown to be normally fitted on ‘Ecore’ in Figure (6). In Figure (7), it can be seen that the fit of the residuals on ‘Ecore’ is well distributed.

In this linear model, the variable ‘alphapred’ is statistically significant, whereas the variable ‘t1’, the top skin thickness, is not. In this model, the correlation coefficient $R = 0.57$, indicates the degree to which the two predictors (independent or X variables) are related to the dependent (Y) variable ‘Ecore’.

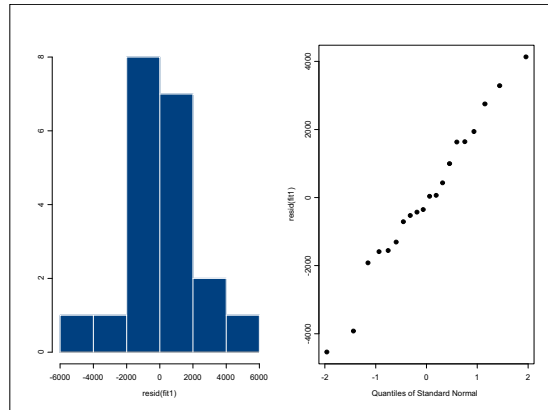


Figure (5) Histogram and Quantile Normal Fit of Residuals on Ecore

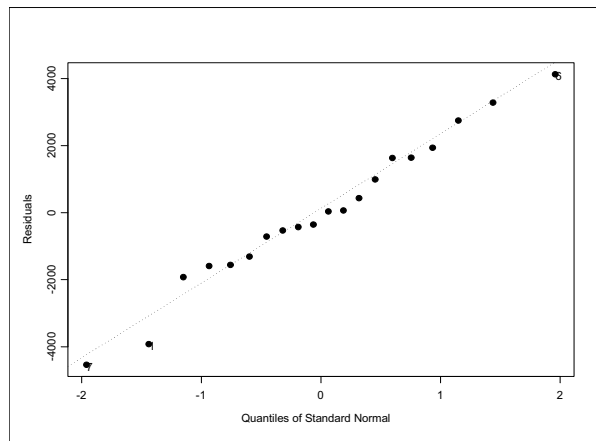
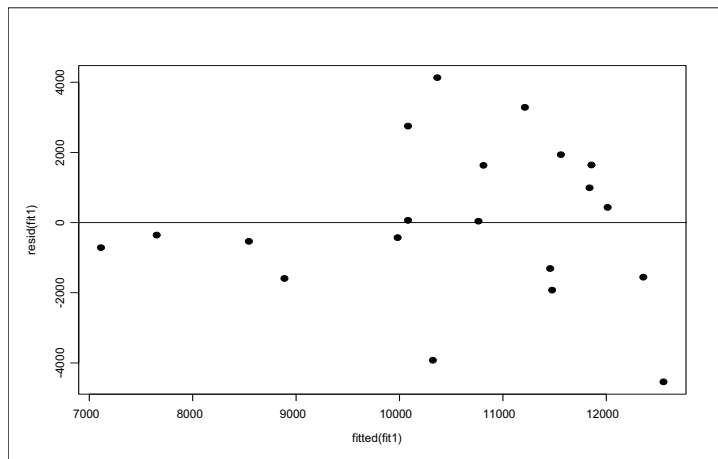


Figure (6) Quantiles of Standard Normal Fitted on Ecore



(7) Fit of Residuals on Ecore

4.1 Fit of Variables in the Linear Model

These results are not surprising for a sandwich with only 1 layer of top skin. In this case, the Modulus of Residual Stiffness, α , has been mathematically predicted to be a controlling variable in sandwich construction with thinner skins. **However, these analyses show that the parameter ‘alphapred’ is statistically significant for all tested cores with 1 skin layer even if the fibres in the skin are +/- 45 degrees or 0/90 degrees. In short, this is true for highly ductile as well as very stiff core materials in the sandwich.**

4.2 Fitting a Multivariate Loess Model for 1 Top Skin

This linear model is then refit as multivariate ‘loess’ model to determine the adequacy of the residual normality of the predictor variables and the model, where weighted least squares is used to fit linear or quadratic functions of the predictors at centers of neighborhoods. The weighting function is given by α predicted. The model with one skin layer is given as:

$$loess(formula = Ecore \sim alphapred * t1) \quad (7)$$

Here ‘Ecore’ is the elastic modulus of the core, ‘alphapred’ is the predicted α and ‘t1’ is the top skin thickness. There is a reduced span = 0.75. **In this multivariate Loess model, the multiple $R^2 = 0.90$, indicating that 90% of the variance is accounted for in the data.**

4.3 Linear Regression Model for 3 Skins

A reduced linear model is run for the parameters that have the highest $Pr > |t|$, for parameters selected from the full model. For sandwich materials with one top skin, these parameters may be given as ‘alphapred’ and ‘Ecore’. The linear model in terms of the observations is again given below:

$$y_i = \beta_0 + \beta_1 x_{i1} + \beta_2 x_{i2}, \dots, \beta_p x_{ip}, \quad for \ i = 1, 2, \dots, n \quad (8)$$

And the equation in S+ is given below for 3 top skins:

$$lm(formula = tsand \sim alphapred + t1) \quad (9)$$

In the fitted linear model, the multiple R^2 for parameters fitted on tsand equals 0.67. The $Pr(>|t|) = .0000$ is significant for the variable ‘t1’. The $Pr(>|t|) = .2769$ is not significant for ‘alphapred’ in skins with 3 layers in a linear additive model. The quantiles of the standard normal are linear as shown in Figure (8). The plot of the residuals shows excellent scatter as shown in Figure (9). In this model, the ‘p’ value of the variable ‘t1’ is significant while the value of ‘alphapred’ is not. In this model, the correlation coefficient $R =$

0.82, indicates the degree to which the two predictors (independent or X variables) are related to the dependent (Y) variable 'tsand'.

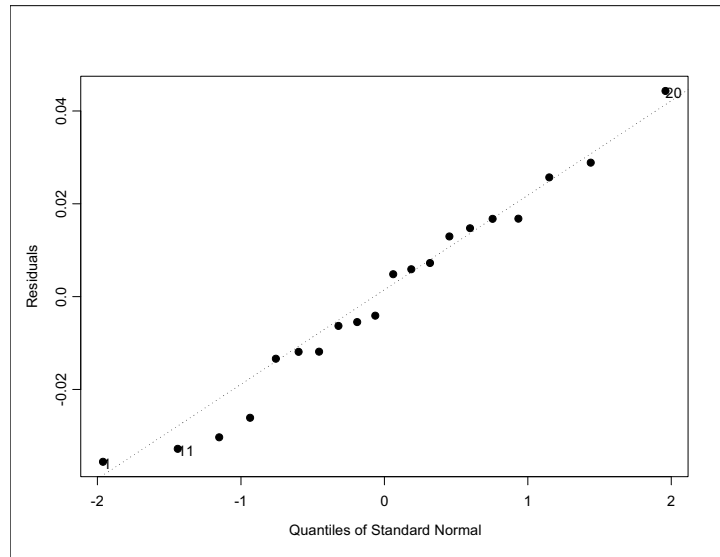


Figure (8) Quantiles of Standard Normal Fitted on tsand

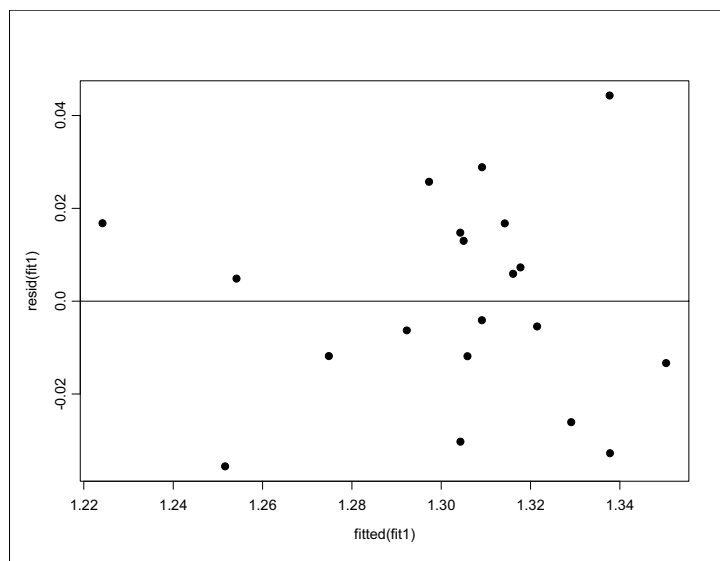


Figure (9) Fit of Residuals on tsand

In this case, the model is refit on the parameter 't1' for completeness of the analysis. The histogram is nearly normal while the quantile fit of the residuals is reasonably well fit as linear, but not in the region -2 to -1, as shown in Figure (10). In this case, the $R^2 = 0.66$, and the $\Pr(>|t|) = .4965$ is again not significant for 'alphapred' in skins with 3 layers in a

linear additive model. In this case, the results are accepted from the model fit on the parameter “tsand” for the linear additive model. In either linear model for 3 layers of skin on the sandwich core, the fitted variables are ‘tsand’, ‘t1’ and ‘alphapred’. The results for the refit model are shown below in Figure (10).

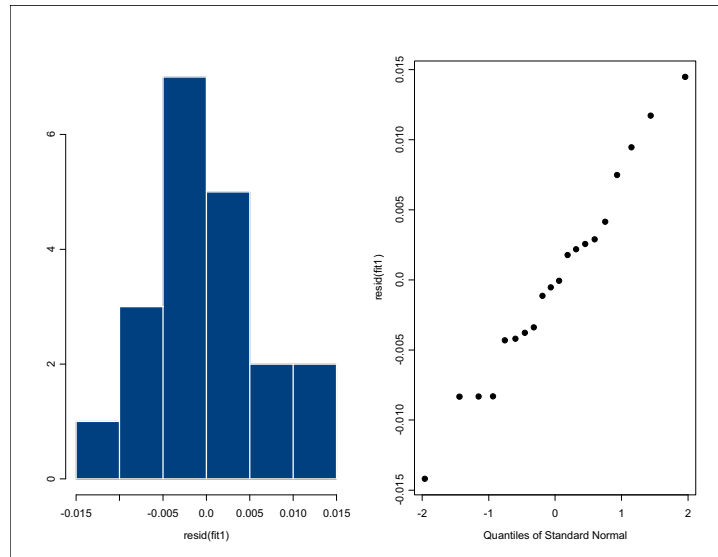


Figure (10) Histogram and Quantile Normal Fit of Residuals on t1

4.4 Fit of Variables in the Linear Models for 3 Top Skins

It has been shown that the correlation of predicted to tested deformation for 3-point load beam tests is dependent on an accurate evaluation of α included in the prediction equation. **What is surprising is that the stiffness of the core materials (Ecore) is not significant in the full or the reduced analyses for a sandwich with 3 layers of skin for all tested cores even if the fibres in the skin are +/- 45 degrees or 0/90 degrees. In short, this is true for highly ductile as well as very stiff core materials in the sandwich.** In these statistical analyses, the results show that for a sandwich with 3 layers of skin materials the relationship of ‘t1’ with ‘tsand’ governs. This result is really a geometric relationship, rather than one primarily of materials properties.

4.3 Fitting a Multivariate Loess Model for 3 Top Skins

The model for three skin layers is fit as:

$$\text{loess (formula = } t1 \sim \text{alphapred} * \text{tsand)} \quad (3)$$

where ‘tsand’ is the sandwich thickness. There is a reduced span = 0.75. **The multiple $R^2 = 0.98$, indicating that 98% of the variance is accounted for in the data.**

Both Loess models fit the data very well, with the fit for 3 skin layers shown in Figure (11).

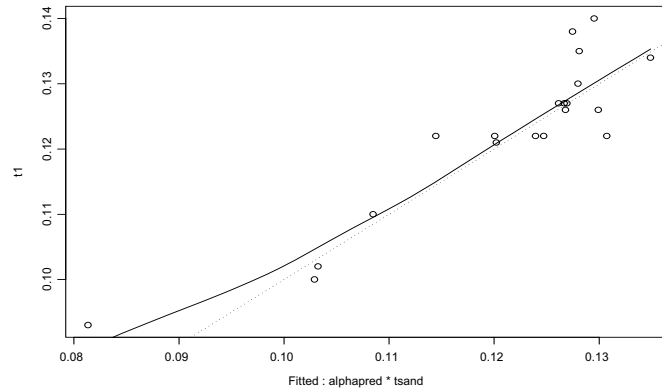


Figure (11) Non-linear and linear 3 skin response

5. CONCLUSIONS

The regression analyses in this report show a distinct difference in statistically significant variables for sandwich materials having 1 top skin and 3 top skins. In defining the initial model, all variables with 1 or 3 skins formed a normal distribution. It does not matter whether the skins have ± 45 degrees or 0/90 degree orientation of the fibres. The initial model used to define ‘alphapred’ compared to ‘alphatest’ and all subsequent regression models show that the thickness of the skin governs, and not the fibre orientation.

In the linear regression model for a sandwich with 1 skin layer, the analyses show that the parameter ‘alphapred’ is statistically significant for all tested cores with 1 skin layer even if the fibres in the skin are ± 45 degrees or 0/90 degrees, when fitted on ‘Ecore’.

In the linear regression model for a sandwich with 3 skins, the parameter ‘alphapred’ is not significant, and ‘t1’ is significant for the linear model fitted on ‘tsand’. The data fit for the multivariate loess model, where ‘alphapred’ and ‘tsand’ are fitted on ‘t1’ show that R^2 is now 0.98 which indicates a very good fit for this model. The stiffness of the core materials (Ecore) is not significant in the full or the reduced analyses for a sandwich with 3 layers of skin for all tested cores even if the fibres in the skin are ± 45 degrees or 0/90 degrees. In short, this is true for highly ductile as well as very stiff core materials in the sandwich.

In these analyses, there are some confirmed results, and some surprising results. Perhaps the most surprising result is the lack of significance of the variable ‘Ecore’ in sandwich materials having 3 skin layers. For the last 30 years, the assumption has been made that the structural integrity of the sandwich with 3 skins is dependent on the stiffness of the core materials. In these statistical analyses, the multivariate Loess results for 3 skin layers show that ‘alphapred’, related to core damping, and 2 geometric parameters define the statistical response of these sandwich materials.

6. REFERENCES

- [1] Weissman-Berman, D., *Sampe Encyclopedia of Composites*; “Structures, Marine Sandwich”, Society for Advancement of Materials and Process Engineering, VCH & Verlagsgesellschaft GmbH, 1991, Vol.6, pp. 445-466.
- [2] Weissman-Berman, D., “Elastic Response of Thermoplastic Sandwich Beams”, *38th International SAMPE Symposium*, Vol. 38, Bk. 2, pp. 2102-2115.
- [3] Weissman-Berman, D., Lahiri, S., and Marrey, R., “Flexural Response of Sandwich Plates with Core as Elastic Foundation”, *Transactions*, Society of Naval architects and Marine Engineers, October 1996, pp. 491-518.
- [4] Weissman-Berman, D., “Viscoelastic Model for an FRP Sandwich beam”, Second International Conference on Sandwich Construction, University of Florida, *Sandwich Constructions 2*, Vol.1, pp.3-33, EMAS-Engineering Materials Advisory Services Ltd.1992.
- [5] Weissman-Berman, D., “Marine Sandwich Structures, (Part I of II)”, *SAMPE Journal*, Vol. 28, No. 4, July/August 1992.
- [6] Weissman-Berman, D., “Marine Sandwich Structures, (Part I Of II)”, *SAMPE Journal*, Vol. 28, No. 5, September/October1992.
- [7] Weissman-Berman, D., “Analytical Investigation of Secondary Yield for Cored Sandwich Beams”, *Sandwich Constructions 3*, Vol.1, EMAS-Engineering Materials Advisory Services Ltd., 1995, pp. 231-242.
- [8] Weissman-Berman, D., *Analytical Investigation of Elastic limit for Cored Sandwich Beams*, Dissertation, Eurotechnical Research University, Hilo, Hawaii 1989.
- [9] Weissman-Berman, D., Petrie, G.L. and Wang, Mo-Wha, “Flexural response of Foam-Cored FRP Sandwich Panels”, *Transactions*, Society of Naval architects and Marine Engineers, November 1988, pp. 73-95.
- [10] Weissman-Berman, D., Jones, D. E., “ Parametric Study of the Modulus of Residual Stiffness for Sandwich Beams”, *MARINE TECHNOLOGY and SNAME News*, The Society of Naval Architects and Marine Engineers, April 2003, pp. 141-148.

ACKNOWLEDGMENT

Many grateful thanks to Dr. Niu, Department of Statistics, Florida State University, for his thoughtful advice, teaching and timely encouragement.

VISCOELASTIC BEHAVIOR OF SOFT CORE SANDWICH PANELS UNDER DYNAMIC LOADING

Ehab Hamed^{*} and Oded Rabinovitch[†]

^{*} Center for Infrastructure Engineering and Safety
School of Civil and Environmental Engineering
The University of New South Wales
UNSW Sydney, NSW 2052, Australia
e-mail: e.hamed@UNSW.edu.au

[†] Faculty of Civil and Environmental Engineering
Technion, Israel Institute of Technology
Haifa, 32000, Israel
e-mail: cvoded@tx.technion.ac.il

Key words: Damping, Structural Dynamics, High Order Sandwich theory, Viscoelasticity.

Summary: *This paper presents a theoretical model for the dynamic analysis of modern sandwich panels with viscoelastic soft cores. The model combines the concepts of the Kelvin-Voigt model of viscoelasticity with the concepts of the high-order sandwich theory and account for the strain rate effect through the shear and normal constitutive laws of the core. A solution procedure that combines time integration through Newmark's method with a numerical solution of the resulting equations in space is adopted. The capabilities of the proposed model are demonstrated through two numerical examples that shed light on the dynamic behavior of sandwich panels with viscoelastic soft cores.*

1 INTRODUCTION

The use of sandwich panels made of thin and stiff face sheets connected by a thick and compliant ("soft") core is widely used in aerospace constructions, as well as in many other structural applications. As such, sandwich panels are often subjected to dynamic loads. One of the main advantages of sandwich constructions, compared with monolithic ones, is the improved damping characteristics, which are mainly attributed to the viscoelastic behavior of the core material [1-8]. However, while the viscoelastic nature of the core damps the overall dynamic and vibratory response of the structure through the time domain, it also modifies the distributions and the magnitudes of the internal stresses and forces in the structure. In particular, it may modify, attenuate, or even magnify the stresses in the core layer and in the core-face sheet interfaces. These stresses play a critical role in the localized and global response of the panel, and in many cases, govern its failure mechanism. Hence, their magnification due to the viscoelastic effect and the influence of the viscoelastic nature of the core on the overall and localized dynamic behavior of the sandwich panel should be clarified.

Many efforts were made to study the vibration response of sandwich panels with viscoelastic cores. Galucio et al. [1] used the finite element formulation assuming Euler-Bernoulli's hypotheses for the elastic faces and Timoshenko's ones for the viscoelastic core. Wang et al. [2], Meunier and Shenoi [3], and Hunston et al. [4] investigated the free and forced vibration response of sandwich beams assuming that the core layer is stiff in the vertical direction and deforms in pure shear only. Pradeep et al. [5] assumed that the dissipation in the core is only due to transverse shear. Nayfeh [6] adopted the lumped mass and stiffness approach to study the flexural vibration response of viscoelastic sandwich beams without the consideration of local effects at the edges or near concentrated loads. These studies, as well as many others, focus on the influence of the viscoelasticity of the core material on the overall dynamic response of the sandwich panel without considering its influence on the local shear and normal stresses in the core. The theoretical models assumed that the height of the core remains unchanged, i.e. incompressible. However, modern sandwich panels are made of compressible foam type core that are usually associated with localized effects and displacements through the depth of the core. To address these effects, an enhanced high-order theory should be used. Bai and Sun [7] used a high-order theory that accounts for the deformability of the core in shear and through its thickness. Yet, the influence of the viscoelastic behavior of the core in the vertical direction was ignored assuming that most of the energy dissipation is attributed to the shear effect. In addition, their model is limited to the response of sandwich panels under forced harmonic loads only. Baber et al. [8] developed a finite element model for harmonically excited viscoelastic sandwich beams based on the theoretical approach of [7]. A high order dynamic theory that accounts for the shear and vertical deformability of the core was presented by Frostig and Baruch [9], Frostig and Thomsen [10] and Schwarts-Givli et al [11-13]. However, these works did not take into account the viscoelastic features of the core or the damping effects in the sandwich structure. The damping and viscoelastic dynamic response of reinforced concrete flexural members strengthened with adhesively bonded composite materials, which uses a high order theory [9], were studied by Hamed and Rabinovitch [14].

In this paper, a theoretical model for the viscoelastic dynamic analysis of sandwich panels made of polymeric foam soft cores and composite laminated face sheets is developed. The theoretical approach combines the concepts of the Kelvin-Voigt model of viscoelasticity [15] with the concepts of the high-order sandwich theory [16]. The model accounts for the high order deformation fields through the height of the core and for the viscoelastic effect in shear and in the vertical normal direction. The model developed here uses variational principles, dynamic equilibrium, and compatibility requirements between the components, and it is applicable to a general combination of boundary conditions and dynamic loads. Hamilton's principle and the small deformations theory are used for the derivation of the equations of motion. The lamination theory is used for the modeling of the composite laminated face sheets. The analytical and numerical procedures for the solution of the damped equations of motion are also addressed. The paper focuses on the influence of the viscoelastic nature of the core material on the deformations of the sandwich panel, on the time dependent distributions of the internal stress resultants, and, especially, on the time evolution of the critical shear and vertical normal stresses in the core and in the core-face sheets interfaces.

2 MATHEMATICAL FORMULATION

The sign conventions for the coordinates, displacements, loads, stresses, and stress resultants appear in Fig. 1. The equations of motion along with the boundary and continuity conditions are derived via the extended Hamilton's variational principle, which requires that:

$$\delta \int_{t_0}^{t_1} (T - (U - W)) dt = 0 \quad (1)$$

where T is the kinetic energy; U is the strain energy, W is the work of the external loads; δ is the variational operator; and t is the time. The first variation of the kinetic energy is:

$$\begin{aligned} \delta T = & \int_{V_t} \rho_t \left(\dot{w}_t(x, z_t, t) \delta \dot{w}_t(x, z_t, t) + \dot{u}_t(x, z_t, t) \delta \dot{u}_t(x, z_t, t) \right) dV_t \\ & + \int_{V_b} \rho_b \left(\dot{w}_b(x, z_b, t) \delta \dot{w}_b(x, z_b, t) + \dot{u}_b(x, z_b, t) \delta \dot{u}_b(x, z_b, t) \right) dV_b \\ & + \int_{V_c} \rho_c \left(\dot{w}_c(x, z_c, t) \delta \dot{w}_c(x, z_c, t) + \dot{u}_c(x, z_c, t) \delta \dot{u}_c(x, z_c, t) \right) dV_c \end{aligned} \quad (2)$$

where t , b , and c refer to the upper face sheet, the lower face sheet, and the core, respectively, ρ_i is the mass density of the upper ($i=t$) and the lower ($i=b$) face sheets and the core ($i=c$), $w_i(x, z_i, t)$ and $u_i(x, z_i, t)$ are the vertical and horizontal displacements of each component, respectively, V_i ($i=t, b, c$) is the volume of each component, and $(\dot{\quad})$ denotes a derivative with respect to time. The first variation of the internal strain energy is

$$\begin{aligned} \delta U = & \int_{V_t} \sigma_{xx}^t(x, z_t, t) \delta \varepsilon_{xx}^t(x, z_t, t) dV_t + \int_{V_b} \sigma_{xx}^b(x, z_b, t) \delta \varepsilon_{xx}^b(x, z_b, t) dV_b \\ & + \int_{V_c} \left(\tau_{xz}^c(x, z_c, t) \delta \gamma_{xz}^c(x, z_c, t) + \sigma_{zz}^c(x, z_c, t) \delta \varepsilon_{zz}^c(x, z_c, t) \right) dV_c \end{aligned} \quad (3)$$

where σ_{xx}^i and ε_{xx}^i ($i=t, b$) are the longitudinal stresses and strains in the upper and lower face sheets, τ_{xz}^c and σ_{zz}^c are the shear and vertical normal stresses in the core, respectively, and γ_{xz}^c and ε_{zz}^c are the shear angle and vertical normal strain in the core, respectively.

The kinematic relations of the face sheets assume small displacements and negligible shear deformations and follow the Bernoulli-Euler theory:

$$\begin{aligned} w_i(x, z_i, t) = w_i(x, t) \quad ; \quad u_i(x, z_i, t) = u_{oi}(x, t) - z_i w_{i,x}(x, t) \\ \varepsilon_{xx}^i(x, z_i, t) = u_{oi,x}(x, t) - z_i w_{i,xx}(x, t) \end{aligned} \quad (4a,b,c)$$

where z_t and z_b are measured from the mid-height of the face sheets downwards, u_{oi} is the longitudinal deformation at the reference line (mid-height) of the face sheets, and $(\quad)_{,x}$ is a derivative with respect to x . The 2D elasticity kinematic relations for the core:

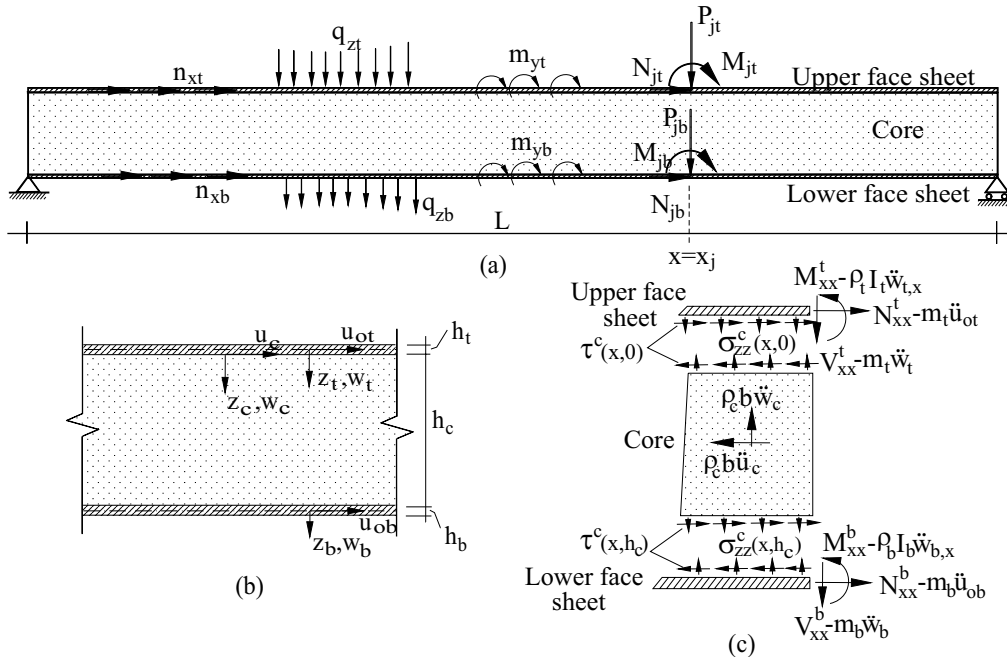


Figure 1: Geometry, loads, sign conventions, and stress resultants: (a) Geometry and loads; (b) Deformations and coordinate system; (c) Stresses and stress resultant.

$$\varepsilon_{zz}^c(x, z_c, t) = w_{c,z}(x, z_c, t) \quad ; \quad \gamma_{xz}^c(x, z_c, t) = u_{c,z}(x, z_c, t) + w_{c,x}(x, z_c, t) \quad (5a,b)$$

The first variation of the work done by the external loads equals:

$$\begin{aligned} \delta W = & \int_{x=0}^{x=L} (q_{zi}(x, t) \delta w_i(x, t) + n_{xi}(x, t) \delta u_{oi}(x, t) + m_{yi}(x, t) \delta w_{i,x}(x, t)) dx \\ & + \sum_{j=1}^{NC} \int_{x=0}^{x=L} (\bar{P}_{ji}(t) \delta w_i(x_j, t) + \bar{N}_{ji}(t) \delta u_{oi}(x_j, t) + \bar{M}_{ji}(t) \delta w_{i,x}(x_j, t)) \delta_D(x - x_j) dx \end{aligned} \quad (i=t,b) \quad (6)$$

where $q_{zi}(x, t)$, $n_{xi}(x, t)$, $m_{yi}(x, t)$ are the time dependent external distributed loads and bending moments exerted at the upper ($i=t$) and the lower ($i=b$) face sheets, respectively, $\bar{P}_{ji}(t)$, $\bar{N}_{ji}(t)$ and $\bar{M}_{ji}(t)$ are dynamic concentrated loads and bending moments at $x=x_j$, δ_D is the Dirac function, NC is the number of concentrated loads, and L is the length of the panel.

The assumption of perfect bonding between the components is introduced through compatibility requirements imposed on the vertical and the longitudinal deformations at the interfaces of the core:

$$w_c(x, z_c = 0, t) = w_t(x, t) \quad ; \quad u_c(x, z_c = 0, t) = u_{ot}(x, t) - Y_t w_{t,x}(x, t) \quad (7a,b)$$

$$w_c(x, z_c = h_c, t) = w_b(x, t) \quad ; \quad u_c(x, z_c = h_c, t) = u_{ob}(x, t) + Y_b w_{b,x}(x, t) \quad (8a,b)$$

where $Y_t=h_t/2$ and $Y_b=h_b/2$ are the heights of the reference level at mid-height of the upper and

lower face sheets, h_c is the thickness of the core, and z_c is measured from the upper core-sheet interface downwards (Fig. 1a).

While the high order terms of the displacement distributions through the thickness of the core are considered, following [14], the distributions of the velocities and accelerations are assumed linear through the thickness of the core. For example, the velocities are:

$$\dot{w}_c(x, z_c, t) = (\dot{w}_b(x, t) - \dot{w}_t(x, t)) \frac{z_c}{h_c} + \dot{w}_t(x, t) \quad (9)$$

$$\dot{u}_c(x, z_c, t) = (\dot{u}_{ob}(x, t) + Y_b \dot{w}_{b,x}(x, t) - \dot{u}_{ot}(x, t) + Y_t \dot{w}_{t,x}(x, t)) \frac{z_c}{h_c} + \dot{u}_{ot}(x, t) - Y_t \dot{w}_{t,x}(x, t) \quad (10)$$

Using the variational principle (Eqs. 1-3,6), along with the kinematic relations (Eqs. 4,5), the compatibility conditions (Eqs. 7,8), and the velocity and acceleration fields of the core (Eqs. 9,10), the equations of motion read:

$$\begin{aligned} N'_{xx,x}(x, t) + b \tau_{xz}^c(x, z_c = 0, t) - m_t \ddot{u}_{ot}(x, t) + \frac{m_c}{3} Y_t \ddot{w}_{t,x}(x, t) - \frac{m_c}{6} Y_b \ddot{w}_{b,x}(x, t) \\ - \frac{m_c}{3} \ddot{u}_{ot}(x, t) - \frac{m_c}{6} \ddot{u}_{ob}(x, t) + n_{xt}(x, t) = 0 \end{aligned} \quad (11)$$

$$\begin{aligned} N^b_{xx,x}(x, t) - b \tau_{xz}^c(x, z_c = h_c, t) - m_b \ddot{u}_{ob}(x, t) + \frac{m_t}{6} Y_t \ddot{w}_{t,x}(x, t) - \frac{m_c}{3} Y_b \ddot{w}_{b,x}(x, t) \\ - \frac{m_c}{6} \ddot{u}_{ot}(x, t) - \frac{m_c}{3} \ddot{u}_{ob}(x, t) + n_{xb}(x, t) = 0 \end{aligned} \quad (12)$$

$$\begin{aligned} M^t_{xx,xx}(x, t) + b Y_t \tau_{xz,z}^c(x, z_c = 0, t) + b \sigma_{zz}^c(x, z_c = 0, t) - m_t \ddot{w}_t(x, t) + \rho_t I_t \ddot{w}_{t,xx}(x, t) \\ - \frac{m_c Y_t}{6} \left(\frac{\ddot{w}_b(x, t) + 2 \ddot{w}_t(x, t)}{Y_t} - 2 Y_t \ddot{w}_{t,xx}(x, t) + Y_b \ddot{w}_{b,xx}(x, t) + 2 \ddot{u}_{ot,x}(x, t) + \ddot{u}_{ob,x}(x, t) \right) \\ + q_{zt}(x, t) - m_{yt,x}(x, t) = 0 \end{aligned} \quad (13)$$

$$\begin{aligned} M^b_{xx,xx}(x, t) + b Y_b \tau_{xz,z}^c(x, z_c = h_c, t) - b \sigma_{zz}^c(x, z_c = h_c, t) - m_b \ddot{w}_b(x, t) + \rho_b I_b \ddot{w}_{b,xx}(x, t) \\ - \frac{m_c Y_b}{6} \left(\frac{\ddot{w}_t(x, t) + 2 \ddot{w}_b(x, t)}{Y_b} + Y_t \ddot{w}_{t,xx}(x, t) - 2 Y_b \ddot{w}_{b,xx}(x, t) - 2 \ddot{u}_{ob,x}(x, t) - \ddot{u}_{ot,x}(x, t) \right) \\ + q_{zb}(x, t) - m_{yb,x}(x, t) = 0 \end{aligned} \quad (14)$$

$$\tau_{xz,x}^c(x, z_c, t) + \sigma_{zz,z}^c(x, z_c, t) = 0 \quad (15)$$

$$\tau_{xz,z}^c(x, z_c, t) = 0 \quad (16)$$

where m_i ($i=t, b, c$) is the mass per unit length of the upper face sheet, the lower face sheet, and the core layer, respectively, N^i_{xx} and M^i_{xx} ($i=t, b$) are the in-plane and the bending moment

stress resultant in the face sheets, b is the width of the panel, and I_i ($i=t,b$) is the geometrical moment of inertia of the face sheets.

2.1 Viscoelastic Constitutive Relations

The constitutive relations for the core material assume a viscoelastic type of behavior and adopt the Kelvin-Voigt model [15]. Yet, it should be noted that alternative and more advanced viscoelastic models can also be implemented in the theoretical platform developed here. The constitutive model reads:

$$\sigma_{zz}^c(x, z_c, t) = E_c \left(\varepsilon_{zz}^c(x, z_c, t) + a_{1\sigma}^c \dot{\varepsilon}_{zz}^c(x, z_c, t) \right) \quad (17)$$

$$\tau_{xz}^c(x, z_c, t) = G_c \left(\gamma_{xz}^c(x, z_c, t) + a_{1\tau}^c \dot{\gamma}_{xz}^c(x, z_c, t) \right) \quad (18)$$

where E_c and G_c are the modulus of elasticity and the shear modulus of the core, respectively, $\dot{\varepsilon}_{zz}^c$ and $\dot{\gamma}_{xz}^c$ are the vertical normal strain rate and the shear angle rate, respectively, and $a_{1\sigma}^c$ and $a_{1\tau}^c$ are viscous constants that represent the material loss (dissipation) factors. Under harmonic vibration conditions, the constitutive relations of Eqs. (17) and (18) reduce to the following form:

$$\sigma_{zz}^c(x, z_c, t) = (E_c + i\omega a_{1\sigma}^c E_c) \varepsilon_{zz}^c(x, z_c, t) = (E'_c + iE''_c) \varepsilon_{zz}^c(x, z_c, t) \quad (19)$$

$$\tau_{xz}^c(x, z_c, t) = (G_c + i\omega a_{1\tau}^c G_c) \gamma_{xz}^c(x, z_c, t) = (G'_c + iG''_c) \gamma_{xz}^c(x, z_c, t) \quad (20)$$

where ω is the vibration frequency, E'_c and G'_c are the elastic and shear storage moduli of the core, respectively, E''_c and G''_c are the elastic and shear loss moduli, respectively; and $i = \sqrt{-1}$ [7,8]. In this paper, the more general case of dynamic time dependent loading is examined and the constitutive relations in the form of Eqs. (17,18) are used.

Limiting the discussion of the viscoelastic effects to the core materials only, the constitutive relations of the face sheets follow the lamination theory and read:

$$N_{xx}^i(x, t) = b \left(A_{xx}^i u_{oi,x}(x, t) - B_{xx}^i w_{i,xx}(x, t) \right) \quad (21)$$

$$M_{xx}^i(x, t) = b \left(B_{xx}^i u_{oi,x}(x, t) - D_{xx}^i w_{i,xx}(x, t) \right) \quad (22)$$

where A_{xx}^i , B_{xx}^i and D_{xx}^i are the extensional, extensional-bending, and flexural rigidities of the face sheets in the x direction

2.2 Viscoelastic Core Layer - Stress and Displacement Fields

Eq. (16) reveals that the shear stresses are uniform through the height of the core and read:

$$\tau_{xz}^c(x, z_c, t) = \tau_{xz}^c(x, t) = \tau^c(x, t) \quad (23)$$

The vertical normal stresses are determined by integration of Eq. (15) yielding:

$$\sigma_{zz}^c(x, z_c, t) = -\tau_{,x}^c(x, t)z_c + C_\sigma(x, t) \quad (24)$$

where $C_\sigma(x, t)$ is a function of x and t only.

The vertical deformation is determined using the kinematic and the constitutive relations (Eqs. 5a,17) and integration through the height of the core:

$$\left(w_c(x, z_c, t) + a_{1\sigma}^c \dot{w}_c(x, z_c, t) \right) = \frac{\left(\frac{-\tau_{,x}^c(x, t)z_c^2}{2} + C_\sigma(x, t)z_c \right)}{E_c} + C_w(x, t) \quad (25)$$

where $C_w(x, t)$ is a second function of x and t only. Using the vertical velocity field of the core layer (Eq. 9), the vertical displacement field takes the following form:

$$w_c(x, z_c, t) = -\frac{a_{1\sigma}^c z_c}{c_c} \left(\dot{w}_b(x, t) - \left(1 - \frac{h_c}{z_c}\right) \dot{w}_t(x, t) \right) - \frac{z_c^2}{2E_c} \tau_{,x}^c(x, t) + \frac{z_c}{E_c} C_\sigma(x, t) + C_w(x, t) \quad (26)$$

The functions $C_\sigma(x, t)$ and $C_w(x, t)$ are determined using the compatibility conditions of the vertical deformations at the core-face sheet interfaces (Eqs. 7a,8a), and the distributions of the vertical deformation and the vertical normal stresses through the thickness of the core read:

$$w_c(x, z_c, t) = -\tau_{,x}^c(x, t) \frac{(z_c^2 - h_c z_c)}{2E_c} + \frac{(w_b(x, t) - w_t(x, t))z_c}{h_c} + w_t(x, t) \quad (27)$$

$$\sigma_{zz}^c(x, z_c, t) = -\tau_{,x}^c(x, t) \frac{(2z_c - h_c)}{2} + \frac{E_c (w_b(x, t) - w_t(x, t) + a_{1\sigma}^c (\dot{w}_b(x, t) - \dot{w}_t(x, t)))}{h_c} \quad (28)$$

The distribution of the axial deformation is determined using the kinematic relation (Eq. 5b) and the constitutive relations (Eq. 18). Integration through the height of the core yields:

$$\left(u_c(x, z_c, t) + a_{1\tau}^c \dot{u}_c(x, z_c, t) \right) = \int_{z_c}^{\tau^c(x, t)} \frac{dz_c}{G_c} - \int_{z_c} \left(w_{c,x}(x, z_c, t) + a_{1\tau}^c \dot{w}_{c,x}(x, z_c, t) \right) dz_c + C_u(x, t) \quad (29)$$

where $C_u(x, t)$ is determined through the compatibility condition of the longitudinal displacement at the upper interface (Eq. 7b). Explicitly, u_c is determined by introducing the velocity fields (Eq. 9,10) and the vertical deformation field (Eq. 27) into Eq. (29):

$$\begin{aligned} u_c(x, z_c, t) = & \frac{\tau^c(x, t)z_c}{G_c} + \frac{\tau_{,xx}^c(x, t)}{2E_c} \left(\frac{z_c^3}{3} - h_c \frac{z_c^2}{2} \right) - \frac{w_{b,x}(x, t)z_c^2}{2h_c} - w_{t,x}(x, t) \left(-\frac{z_c^2}{2h_c} + z_c + Y_t \right) \\ & + u_{ot}(x, t) - a_{1\tau}^c \left(\frac{z_c Y_b}{h_c} + \frac{z_c^2}{2h_c} \right) \dot{w}_{b,x}(x, t) - a_{1\tau}^c \left(z_c - \frac{z_c^2}{2h_c} + \frac{z_c Y_t}{h_c} \right) \dot{w}_{t,x}(x, t) + a_{1\tau}^c \frac{z_c}{h_c} (\dot{u}_{ot}(x, t) - \dot{u}_{ob}(x, t)) \end{aligned} \quad (30)$$

2.3 Dynamic Governing Equations

The dynamic governing equations are derived using the equations of motion (Eqs. 11-16), the constitutive relations (Eqs. 17-22), the compatibility requirements of the longitudinal

deformations at the lower core-sheet interface (Eq. 8b), and the shear and vertical normal stress fields (Eqs. 23 and 28). These equations are stated in terms of the unknown displacements $w_t(x,t)$, $w_b(x,t)$, $u_{ot}(x,t)$, $u_{ob}(x,t)$ and the unknown shear stress $\tau^c(x,t)$ and take the following form (for brevity, the notation of the independent variables is omitted):

$$bA'_{xx}u_{ot,xx} - bB'_{xx}w_{t,xxx} + b\tau^c - m_t\ddot{u}_{ot} + \frac{m_c}{3}\left(Y_t\ddot{w}_{t,x} - \frac{1}{2}Y_b\ddot{w}_{b,x} - \ddot{u}_{ot} - \frac{1}{2}\ddot{u}_{ob}\right) + n_{xt} = 0 \quad (31)$$

$$bA^b_{xx}u_{ob,xx} - bB^b_{xx}w_{b,xxx} - b\tau^c - m_b\ddot{u}_{ob} + \frac{m_c}{3}\left(\frac{1}{2}Y_t\ddot{w}_{t,x} - Y_b\ddot{w}_{b,x} - \frac{1}{2}\ddot{u}_{ot} - \ddot{u}_{ob}\right) + n_{xb} = 0 \quad (32)$$

$$bD'_{xx}w_{t,xxx} - bB'_{xx}u_{ot,xxx} + \frac{bE_c}{h_c}(w_t - w_b) + a_{1\sigma}^c \frac{bE_c}{h_c}(\dot{w}_t - \dot{w}_b) - \frac{b\tau_{,x}^c}{2}(h_c + 2Y_t) + m_t\ddot{w}_t - \rho_t I_t \ddot{w}_{t,xx} + \frac{m_c Y_t}{6}\left(\frac{\ddot{w}_b + 2\ddot{w}_t}{Y_t} - 2Y_t\ddot{w}_{t,xx} + Y_b\ddot{w}_{b,xx} + 2\ddot{u}_{ot,x} + \ddot{u}_{ob,x}\right) - q_{zt} + m_{xt,x} = 0 \quad (33)$$

$$bD^b_{xx}w_{b,xxx} - bB^b_{xx}u_{ob,xxx} - \frac{bE_c}{h_c}(w_t - w_b) - a_{1\sigma}^c \frac{bE_c}{h_c}(\dot{w}_t - \dot{w}_b) - \frac{b\tau_{,x}^c}{2}(h_c + 2Y_b) + m_b\ddot{w}_b - \rho_b I_b \ddot{w}_{b,xx} + \frac{m_c Y_b}{6}\left(\frac{\dot{w}_t + 2\dot{w}_b}{Y_b} + Y_t\ddot{w}_{t,xx} - 2Y_b\ddot{w}_{b,xx} - 2\ddot{u}_{ob,x} - \ddot{u}_{ot,x}\right) + q_{zb} + m_{yb} = 0 \quad (34)$$

$$u_{ot} - u_{ob} + a_{1\tau}^c(\dot{u}_{ot} - \dot{u}_{ob}) - \frac{(h_c + 2Y_t)}{2}w_{t,x} - a_{1\tau}^c \frac{(h_c + 2Y_t)}{2}\dot{w}_{t,x} - \frac{(h_c + 2Y_b)}{2}w_{b,x} - a_{1\tau}^c \frac{(h_c + 2Y_b)}{2}\dot{w}_{b,x} + \frac{\tau^c h_c}{G_c} - \frac{\tau_{,xx}^c h_c^3}{12E_c} = 0 \quad (35)$$

The dynamic governing equations (Eqs. 31-35) form a set of PDEs of order fourteen in space, and eight in time. Correspondingly, seven time-dependent boundary conditions are prescribed at the edges of the beam, fourteen continuity conditions are set at each connection point, and two x dependent initial conditions at $t=t_o$ are defined for each of the four unknown displacements. For brevity, these conditions are not presented here.

The time integration of the governing equations follows the Newmark's approach [17]. The time domain is divided into finite intervals and the acceleration and velocity fields are expressed as explicit functions of the unknown displacement field in the present time step and the known displacement, velocity, and acceleration fields in the preceding time step. Using this procedure, Eqs. (31-35) reduce to a set of ODEs in terms of $w_t(x)_j$, $w_b(x)_j$, $u_{ot}(x)_j$, $u_{ob}(x)_j$, and $\tau^c(x)$. These equations are solved analytically or numerically at each time step. In this paper, a multiple shooting numerical algorithm [18] is adopted.

3 NUMERICAL STUDY

The influence of the viscoelastic characteristics of the core layer on the response of a sandwich panel simply supported at the lower face sheet only and subjected to two types of dynamic loading is numerically investigated. The geometry, mechanical properties, and the dynamic loads appear in Fig. 2. The viscoelastic coefficients of the core material are taken as $a_{1\tau}^a = \eta_\tau / \omega$ and $a_{1\sigma}^a = \eta_\sigma / \omega$, where η_τ and η_σ are the core material loss factors in shear and normal stresses, respectively. Following Dwivedy et al. [19], the magnitudes of the loss factors for Divinycell H60 foam in room temperature are $\eta_\tau = \eta_\sigma = 0.1$. Based on a preliminary free vibrations analysis, the first natural frequency equals about 67Hz.

The interfacial stresses that develop in the panel under a static load of equal magnitude appear in figure 3. These results reveal the shear and vertical normal stress concentrations near the edges. The time variation of the peak stresses, as well as the variation of the peak deflection at midspan under the step load and the harmonic loads is investigated next.

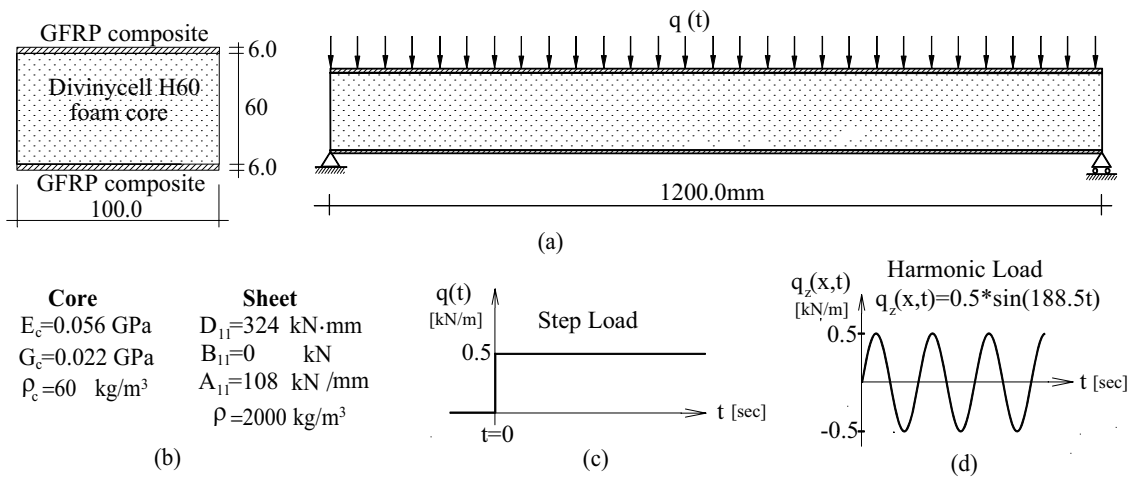


Figure 2: Geometry, material properties and loading: (a) Geometry and cross section; (b) Material properties; (c) Step load; (d) Harmonic loads.

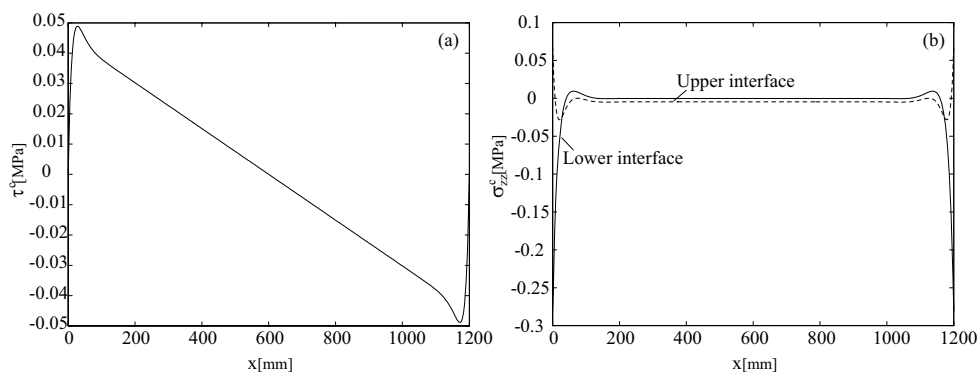


Figure 3: Static response: (a) Shear stresses in the core; (b) Vertical normal stresses at the core interfaces.

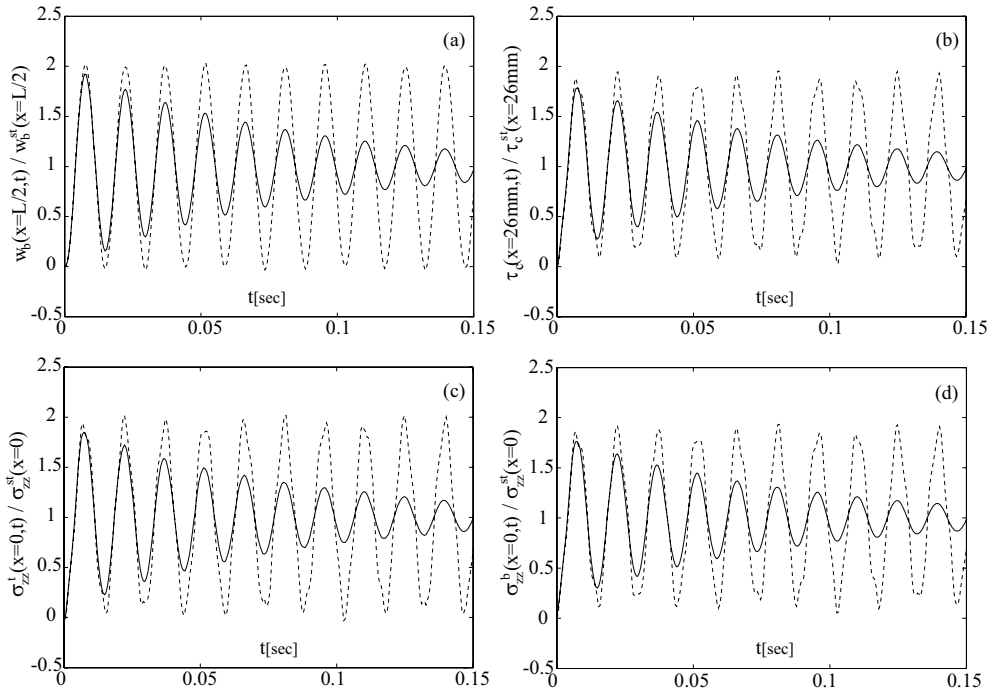


Figure 4: Response to step load: (a) Deflection; (b) Peak shear stresses; (c) Peak vertical normal stresses, upper interface; (d) Peak vertical normal stresses, lower interface. (Legend: — Elastic core, --- Viscoelastic core)

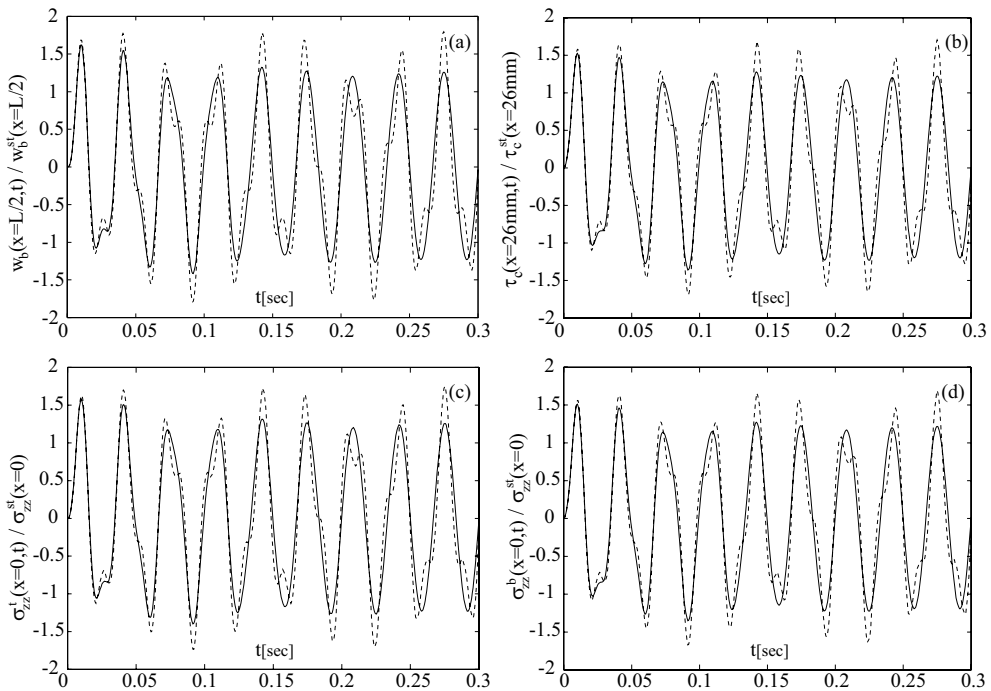


Figure 5: Response to harmonic load: (a) Deflection; (b) Peak shear stresses; (c) Peak vertical normal stresses, upper interface; (d) Peak vertical normal stresses, lower interface. (Legend: — Elastic core, --- Viscoelastic core)

3.1 Response to step load

The dynamic response of the sandwich panel to the step load is studied in Fig. 4. The results are normalized with respect to the static results, thus, the figures describe the dynamic magnification factor (DMF) for the deflections and stresses. For reference, the response of the sandwich panel with an elastic core ($a_{1\tau}^a = a_{1\sigma}^a = 0$) is plotted in dashed lines in Fig. 4. The results show that the sandwich panel with the elastic core vibrates around the static response with a DMF of approximately 2. In the sandwich panel with the viscoelastic core, the DMF is approximately 1.9 at the first vibration cycle and it diminishes to about 1.14 after 11 cycles of vibration. Using the logarithmic decrement technique, it appears that the damping ratio in terms of vertical deflection, as well as in terms of stresses, is about 3% of the critical damping. These observations imply that the viscoelastic nature of the core material effectively damps the magnitudes of the deflections and critical stresses in time.

3.2 Response to harmonic load

The normalized dynamic response of the sandwich panel to the harmonic load is studied in Fig. 5. The results show that the dynamic response of the sandwich panel with elastic core ($a_{1\tau}^a = a_{1\sigma}^a = 0$) is characterized by the forced frequency of the applied load (particular solution) and by the first natural frequency of the panel (homogenous solution) through the entire time domain. However, in the case of the panel with the viscoelastic core, the homogenous solution decays after two cycles and the forced vibrations govern the response. In physical terms, it is seen that the stresses that develop with viscoelastic core after 10 cycles of vibration are about 25% smaller than the ones observed in the elastic sandwich panel without any damping. These observations demonstrate the capabilities of the model to deal with different types of dynamic loading and to address the various aspects of the damped dynamic response of the sandwich structure.

4 CONCLUSIONS

A theoretical model for the dynamic analysis of sandwich panels with soft viscoelastic cores has been developed. The model is applicable to any combinations of boundary conditions and dynamic loading patterns, and it can be augmented to incorporate different viscoelastic constitutive laws. In that sense, it faces the challenge of implementing the damping dissipative effect in the analytical sandwich theory. The numerical study has demonstrated some of the capabilities of the model and revealed some aspects of the damped dynamic behavior of sandwich panels with viscoelastic cores.

REFERENCES

- [1] Galucio, A.C. Deü, J.F. and Ohayon, R. "Finite Element Formulation of Viscoelastic sandwich beams using fractional derivative operators" *Comp. Mech.* **33**(4):282-291 (2004)

- [2] Wang, G., Veeramani, S. and Wereley, N.M. "Analysis of Sandwich Plates with Isotropic Face Plates and a Viscoelastic core" *J. of Vibration and Acoustics* **122**(3):305-312 (2000)
- [3] Meunier, M. and Sheno, R.A., "Forced Response of FRP Sandwich Panels with Viscoelastic Materials". *J. of Sound and Vibration*, **263**(1): 131-151 (2003).
- [4] Hunston, D. Miyagi, Z. Schultheisz, C. and Zaghi, S. "The sandwich bending specimen for characterizing adhesive properties" *Mech. of Time-Dependent Materials* **7**(1):71-88 (2003)
- [5] Pardeep, V., Ganesan, N. and Bhaskar, K. "Vibration and Thermal Buckling of Composite Sandwich Beams with Viscoelastic Core" *Composite Structures*, **81**(1):60-69 (2007)
- [6] Nayfeh, S.A. "Damping of Flexural Vibration in the Plane of Lamination of Elastic-Viscoelastic Sandwich Beams" *Journal of Sound and Vibration*, **276**(3-5): 689-711 (2004)
- [7] Bai, J.M. and Sun, C.T., "The Effect of Viscoelastic Adhesive Layers on Structural Damping of Sandwich Beams" *Mechanics of Structures and Machines*, **23**(1): 1-16 (1995)
- [8] Baber, T.T., Maddox, R.A. and Orozco, C.E., "A Finite Element Model for Harmonically Excited Viscoelastic Sandwich Beams". *Computers and Structures*, **66**(1):105-113 (1998).
- [9] Frostig, Y. and Baruch, M. "Free Vibrations of Sandwich Beams with a Transversely Flexible Core: a High Order Approach" *J. of Sound and Vibration*, **176**(2):195-208 (1994)
- [10] Frostig, Y. and Thomsen, O.T., "High-Order Free Vibration of Sandwich Panels with a Flexible Core" *International Journal of Solids and Structures* **41**(5-6):1697-1724 (2004)
- [11] Schwarts-Givli H. Rabinovitch O. and Frostig Y. "High order nonlinear contact effects in cyclic loading of delaminated sandwich panels" *Composites-B* **38**(1):86-101 (2007)
- [12] Schwarts-Givli, H. Rabinovitch, O., and Frostig, Y., "High Order Nonlinear Contact Effects in the Dynamic Behavior of Delaminated Sandwich Panels with Flexible Core". *International Journal of Solids and Structures*, **44**(1): 77-99 (2007).
- [13] Schwarts-Givli, H. Rabinovitch, O., and Frostig, Y., "Free Vibrations of Delaminated Unidirectional Sandwich Panels with a Transversely Flexible Core – A Modified Galerkin Approach". *Journal of Sound and Vibration*, **301**(1-2): 253-277 (2007).
- [14] Hamed, E. and Rabinovitch O., "Damping and Viscoelastic Dynamic Response of RC Flexural Members Strengthened with Adhesively Bonded Composite Materials". *Journal of Engineering Mechanics*, **133**(12): 1278-1289 (2007).
- [15] Ferry, J.D. *Viscoelastic Properties of Polymers*, Wiley, New York, NY, (1970)
- [16] Frostig, Y., Baruch, M., Vilnai, O., Sheinman, I., "High-Order Theory for Sandwich-Beam Bending with Transversely Flexible Core" *Journal of Engineering Mechanics*, **118**(5): 1026-1043 (1992).
- [17] Newmark, N.M., "A method of computation of structural dynamics". *Journal of the Engineering Mechanics Division*, **85**(EM 3): 67-94 (1959).
- [18] Stoer, J. and Bulirsch, R. *Introduction to numerical analysis*, Springer, New York, NY (1993)
- [19] Dwivedy, S.K., Sahu, K.C. and Babu, SK., "Parametric Instability Regions of Three-Layered Soft-Cored Sandwich Beam using Higher-Order Theory". *Journal of Sound and Vibration*, **304**(1-2): 326-344 (2007).

ON THE EFFECT OF CURVATURE IN DEBONDED SANDWICH PANELS SUBJECTED TO COMPRESSIVE LOADING

Ramin Moslemian^{*}, Christian Berggreen^{*}, Kim Branner[†] and Leif A. Carlsson^{*}

^{*} Department of Mechanical Engineering
Technical University of Denmark
Nils Koppels Allé, Building 403, DK-2800 Kgs. Lyngby, Denmark
e-mail: rmo@mek.dtu.dk and cbe@mek.dtu.dk, web page: <http://www.mek.dtu.dk>

[†] Wind Energy Department, Risø National Laboratory
Technical University of Denmark
Frederiksborgvej 399, Building 118, DK-4000 Roskilde, Denmark
e-mail: kim.branner@risoe.dk, webpage: <http://www.risoe.dk>

^{*} Department of Mechanical Engineering
Florida Atlantic University
777 Glades Road, Boca Raton, FL 33431, USA
e-mail: carlsson@fau.edu, web page: <http://www.me.fau.edu>

Summary. *The aim of this study is to obtain an understanding of the effect of panel curvature on residual compressive strength in debond damaged sandwich panels. Finite element analysis and linear elastic fracture mechanics are employed to analyze the residual compressive strength of curved panels with a circular debond. The Crack Surface Displacement Extrapolation (CSDE) method is used to calculate fracture parameters in the interface. Compression tests were carried out on two types of debonded curved panels with different curvature using Digital Image Correlation (DIC) measurements to determine the full-field distribution of strain. The failure and buckling loads predicted from finite element analyses are in good agreement with experimental results.*

Key words: Sandwich structures, Curved panels, Debond damages, Fracture mechanics, Compressive strength.

1 INTRODUCTION

Composite sandwich structures are well established structural applications. Such structures, however may fail due to a multitude of different failure modes. Debonding of the face and core layer is among the most critical damages a sandwich structure can experience. This type of damage can be highly critical for the structure as the basic sandwich principle is compromised resulting in a lack of structural integrity and reliability as the connection between the face and the core layer is lost.

In the recent years considerable efforts have been directed into investigations of the effect of face/core debonding on the residual strength of sandwich structures. Both analytical and numerical methods have been developed to predict the onset and propagation of debonds in sandwich structures [1,2]. Berggreen [3,4] recently investigated numerically and experimentally debond propagation in flat naval type sandwich panels with circular debonds of different sizes exposed to both uniform and non-uniform in-plane compression. Aviles [5] likewise carried out both numerical and experimental studies on sandwich panels loaded in compression. Nonetheless, all of these studies deal with flat sandwich panels and straight crack flanks and only few works have assessed debond damage in curved sandwich members.

The present study examines the effect of curvature on the residual compressive strength of panels with circular debonds. Finite element analysis and Linear Elastic Fracture Mechanics (LEFM) are employed to predict failure loads. Results are validated against experimental tests and conclusions are drawn with respect to the validity of the developed numerical models.

2 CURVED SANDWICH PANEL SPECIMENS

Seven single curve and two flat sandwich panels were experimentally examined; see Figure 1 and Table 1. The panels were manufactured by LM Glasfiber A/S. The faces consist of three 850 g/m² non-crimp quadro-axial mats (Devold AMT DBLT-850) with polyester resin placed at each side of a Divinycell H100 foam core. The thicknesses of the core and face sheets are 30 and 2 mm, respectively. A face/core debond on the convex side of the panels was defined by inserting two layers of circular Teflon film between the face and core layer at the center of panels. The diameter of the debond is 100 mm. The foam core was bent over a metallic mould after thermal softening. All panels were reinforced with ply-wood inserts at the top and bottom edges of the panel. The panels were then resin injection molded and cured with vacuum consolidation. Furthermore, top and bottom of the panels were machined straight and parallel following the specimen manufacturing. Properties for face and core materials are listed in Table 2 and 3. Face material properties are assumed to be the same as in [6] and core material properties are based on [7].

Panel Type	Radius of curvature (m)	Type	Specimens #
1	0.5 m	Debanded	3
2	1.0 m	Debanded	3
3	1.0 m	Intact	1
4	∞ (Flat)	Intact	2

Table 1: Different panel types for experiments

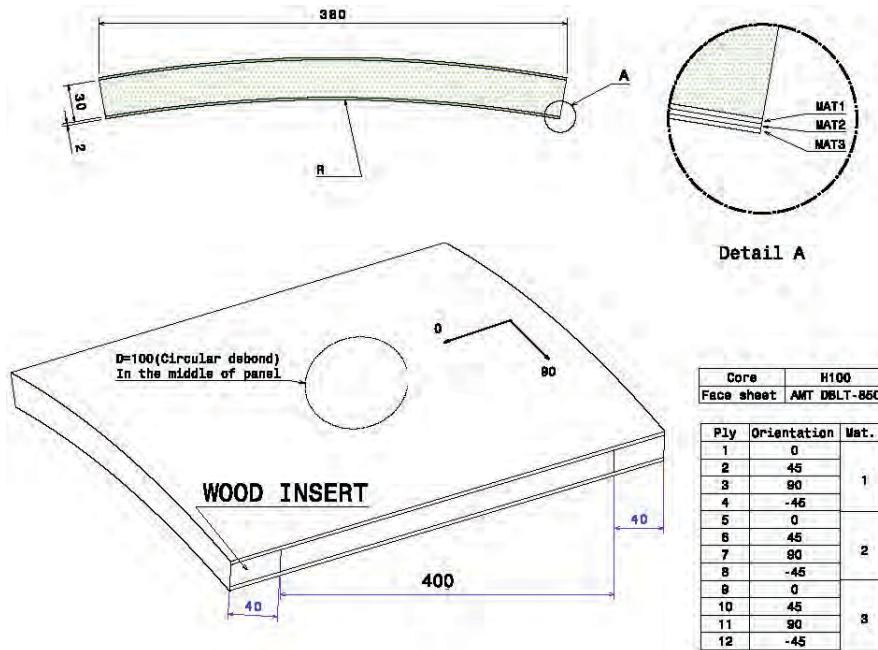


Figure 1: Geometry of a curved panel specimen with a central debond location

Parameter	Designation	Value
Young's Modulus	E_x, E_y	16.6 GPa
Young's Modulus	E_z	8.4 GPa
Shear Modulus	G_{xy}	5.8 GPa
Shear Modulus	$G_{xz}= G_{yz}$	2.7 GPa
Poisson's ratio	ν_{xy}	0.31
Poisson's ratio	$\nu_{xz}= \nu_{yz}$	0.29

Table 2: Material properties of face sheets, x and y are in-plane and z is out-of-plane.

Parameter	Designation	Value
Young's Modulus	E_c	105 MPa
Shear Modulus	G_c	40 MPa
Poisson's ratio	ν_c	0.35

Table 3: Material properties of core (H100)

3 TEST RIG AND SETUP

A new test rig was designed and manufactured at Risø DTU in a project supported by the Danish Energy Research Programme. The test rig consists of two main steel towers that support the vertical edges of the panel specimen. The towers can rotate around their own

vertical axis guided by grooves in the supporting base plates. The distance between the towers is adjustable. Hence, it is possible to test panels with varying size and curvature in the test rig. After adjusting the position of towers, they are fixed by bolts to the two steel base plates. A schematic of the test rig and a photo of the actual test set-up are shown in Figure 2.

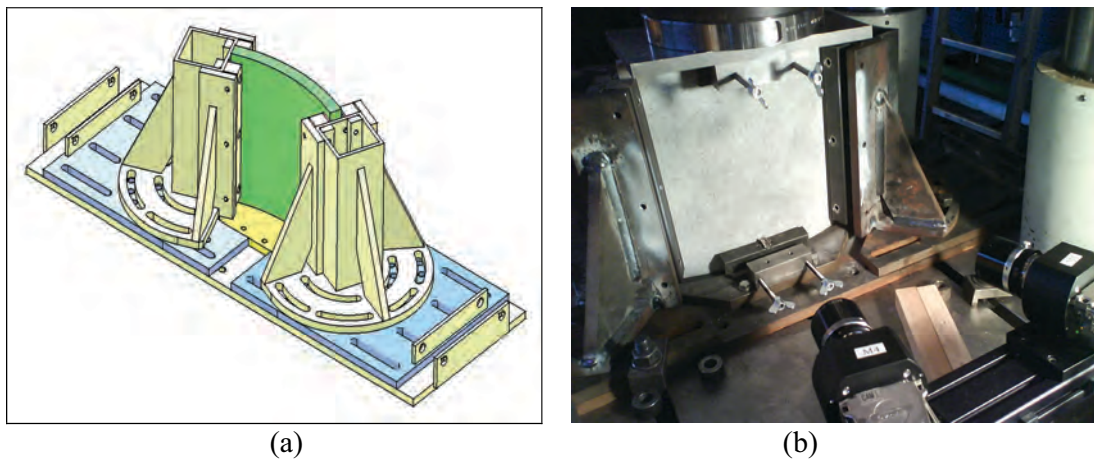


Figure 2: A schematic representation of the test rig (a) and test set-up (b)

To reinforce the loaded edges at the top and bottom of the panel, wooden inserts were inserted as mentioned above. The reinforced edges were subsequently in contact with steel plates bolted to the load cell of test machine (upper) and the base plate (bottom) respectively. The vertical edges the panels were supported by two adjustable steel columns with a width of 40 mm which restrict the edges of the panels from moving horizontally. The two towers restrict movement in the tangential direction. The test rig was inserted into an Instron 8085 5 MN servo-hydraulic universal testing machine, see Figure 2(b). A 4 Mpix Digital Image Correlation (DIC) measurement system (ARAMIS 4M) was used to monitor 3D surface displacements and 2D surface strains during the experiments. The DIC-camera position and test rig can be seen in Figure 2. Ramp displacement control with a cross-head rate of 1 mm/min was applied in all tests. A sample rate of one image per second was used in the DIC-measurements.

4 EXPERIMENTAL TEST RESULTS

The final failure of panels without debonds was accompanied by audible cracking sounds before the load suddenly dropped. The final failure occurred by compression failure of one or both of the face sheets close to the wooden inserts. Failure of panels with implanted debonds occurred suddenly by propagation of the debond. Figure 3 shows a contour plot of the radial displacement of a debonded panel with radius of 1 m at the instance just before and after the debond has propagated. The debond propagated suddenly (less than a second) to the edge of the panel. In all debonded panels the same failure mechanism was observed. However, due to

the rapid propagation,, it was not possible for the DIC system to capture more than one image during propagation with the operating data acquisition frequency. For the debonded panels the dominant mode shape was an opening of the debond overlaid on a global out-plane deformation, see Figure 3(a), of the panel most likely introduced by the boundary conditions of the test rig. However, at the propagation point the mode shape was suddenly changed, and it can be seen that after debond propagation, the final mode shape of the debonded region is similar to the second buckling mode shape for the debond, see Figure 3(b). This behavior has been investigated by eigen-buckling analyses to determine if there is any other buckling load near to the first buckling load, but analyses show that the second buckling load is considerably higher than the first buckling load. Due to the expanding volume of the debond when opening and propagating, it is believed that an internal vacuum pressure is partly responsible for the sharp and localized opening of the debond, see Figure 3. A similar observation can be deduced from the tests carried out by Berggreen [3].

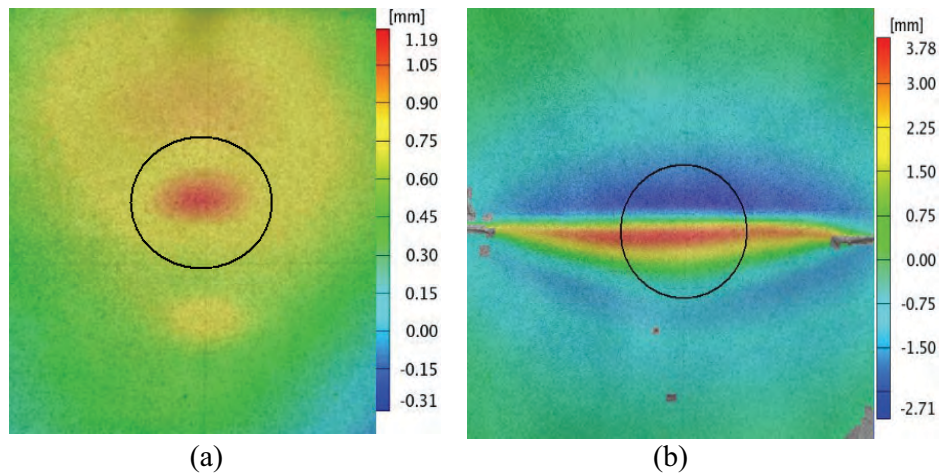


Figure 3: Radial displacement of a debonded panel with 1m radius (a) just before propagation, (b) after propagation.

5 FINITE ELEMENT MODELING

To analyze propagation of the debond, fracture mechanics analysis was conducted using the finite element method. The calculation of fracture parameters in this paper is based on relative nodal pair displacements along the crack flanks which are obtained from finite element analysis. The Crack Surface Displacement Extrapolation (CSDE) method presented by Berggreen [4] is employed for energy release rate and mode-mixity calculations for a bimaterial interface. By application of the definition of mode-mixity suggested by Hutchinson and Suo [8], the mode-mixity can be defined as:

$$\psi_K = \arctan \left[\frac{\Im(Kh^{i\varepsilon})}{\Re(Kh^{i\varepsilon})} \right] \quad (1)$$

where $K=K_1+iK_2$ is the complex stress intensity factor, ε is the oscillatory index (see [4]) and

h is the characteristic length of the crack problem. In sandwich debonding problems the characteristic length is often chosen as the face thickness, which will approximately place the minimum at the fracture toughness distribution vs. mode-mixity at $\psi_K = 0$. However, in order to compare calculated energy release rates with measured fracture toughness, the same characteristic length should be used in both mode-mixity definitions. Explicit formulations for the mode-mixity and the energy release rate as functions of the relative crack flank displacements can be derived as:

$$\psi_K = \arctan\left(\sqrt{\frac{H_{22} \delta_x}{H_{11} \delta_y}}\right) - \varepsilon \ln\left(\frac{|x|}{h}\right) + \arctan(2\varepsilon) \quad (2)$$

$$G = \frac{\pi(1 + 4\varepsilon^2)}{8H_{11}|x|} \left(\frac{H_{11}}{H_{22}} \delta_y^2 + \delta_x^2 \right) \quad (3)$$

where δ_x and δ_y are the relative crack shearing and opening displacements of the crack flanks at the position x . H_{11} and H_{22} are bimaterial constants, see [4].

Thus, using a finite element solution to calculate the relative nodal displacements of the crack flanks these two fracture parameters can be determined. To extract correct energy release rates and mode-mixities, the CSDE-method [4] was employed.

A 3D finite element model was developed in the commercial finite element code, ANSYS version 10, using isoparametric parabolic and linear elements (SOLID95 and SOLID45). Load controlled geometrical nonlinear analyses were performed and initial imperfections introduced by small debond opening displacements in the first load step achieved from scaled eigen-buckling shapes. Because of geometrical and loading symmetry only a 1/4 model was analyzed. Furthermore, overlapping of crack flanks was avoided by use of contact elements (CONTACT173 and TARGET170). The vacuum effect which was mentioned earlier was simulated by the use of a number of spring elements (SPRING14) with variable stiffness between the core and face. Different stiffnesses of the spring elements were chosen in order to investigate the effect of the vacuum on the behavior of the panels. To simulate the boundary conditions similar to the experimental setup, nodes on the top and bottom of the panels were fully clamped except in the vertical direction. At the vertical edges nodes were restricted from moving in radial and tangential directions. However, as it can be seen in Figure 3, a small out-of-plane displacement of the top edge was observed which will violate the ideal boundary conditions. Due to the need of a high mesh density at the crack front when performing the fracture mechanics analysis, a submodeling technique was employed. Interpolated degrees of freedom results at the cut boundaries in the global model were used as boundary conditions in the submodel at the different load steps, allowing a higher mesh density to be employed and thus improving the accuracy of the fracture mechanics analysis. The finite element model and submodel are shown in Figure 4.

In order to predict the debond propagation load, the fracture toughness vs. mode-mixity distribution is assumed on the basis of fracture toughness values similar to what was assumed in Berggreen [9]. In order to extract energy release rates and mode-mixities using the CSDE method, a macro was developed, able to extract these values at crack front positions along the

circular debond. The energy release rate and mode-mixity were calculated at six different positions along the crack front at a 15 degree interval.

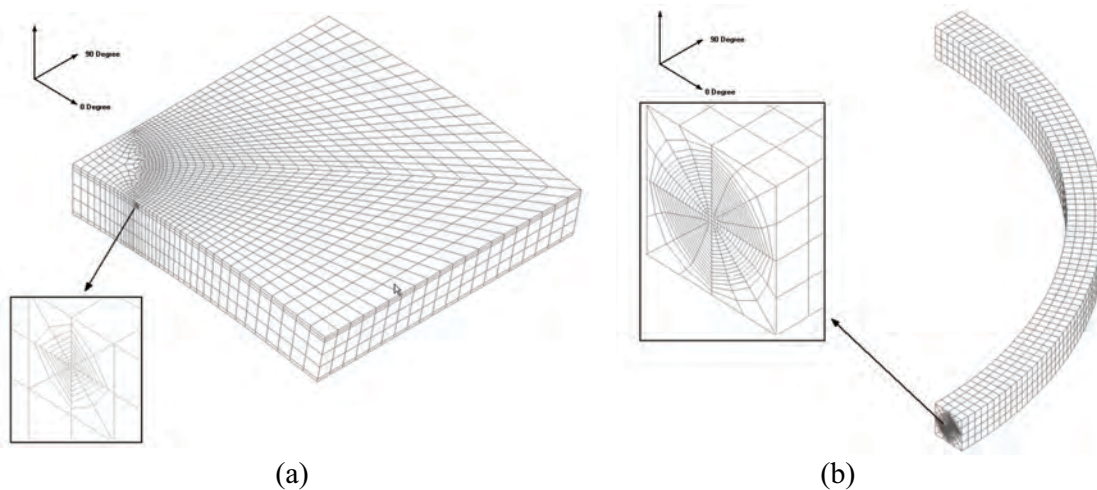


Figure 4: Finite element models (a) 1/4 panel showing the mesh densities applied in the global model. Min. element size is 0.2 mm and (b) sub-model showing the mesh density applied. Min. element size is 0.02 mm

6 COMPARISON OF EXPERIMENTAL AND NUMERICAL RESULTS

The calculated deformed shape of a debonded panel with 0.5 mm radius is shown in Figure 5. From the deformed shape it can be seen that the maximum opening of the crack flanks appears where the crack flanks have maximum curvature which is also the plane at which the load is perpendicular to the same plane. Furthermore, the opening of the crack flanks is decreasing as the curvature of the crack flanks decrease in curvature and the position at the debond front moves to the position at which to the plane is parallel to the loading direction and where the crack flanks are completely straight. Numerically predicted and experimentally determined failure loads for debonded curved panels with 0.5 and 1 m radius of curvature and $K_S = 10 \text{ MPa}$ spring element stiffness are listed in Table 4. From the results in Table 4 it can be concluded that the numerical analysis underestimates the failure load of the panels by about 5-27%, while the stiffness of the panels is accurately predicted as can be seen in Figure 6 (the finite element results in this figure are from 1/4 model of the panel without fracture analysis). The accuracy of the failure load prediction is considerably better for the shallow panels (5%) than the panels with higher curvature (27%). This tendency can be addressed to the straight crack flank assumption in the fracture analysis which for the highly curved panels is questionable.

Normalized energy release rates at the investigated crack front positions at the onset of propagation are shown in Figure 7 in the form of polar diagrams. At propagation the energy release rate along the crack front is binocular-shaped, with a maximum at 0° and 180° and minimum at 90° and 270° , see Figure 4. These diagrams are confirmed by the experimental observations where the crack propagation initiates close to the 0° and 180° positions forming

a propagation band across the panel to the panel edges. The minimum value positions at 90° and 270° confirm the experimental observations of unloaded debond regions at the top and bottom crack front positions.

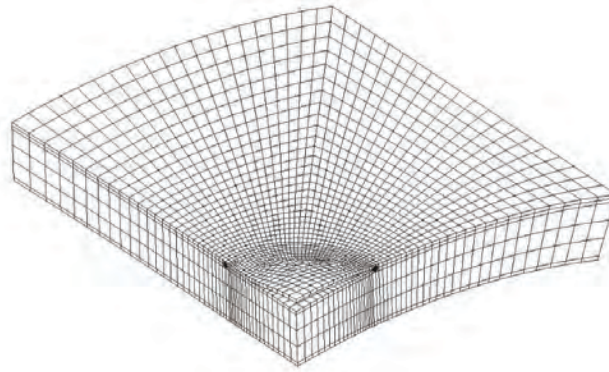


Figure 5: The deformed shape of $\frac{1}{4}$ panel

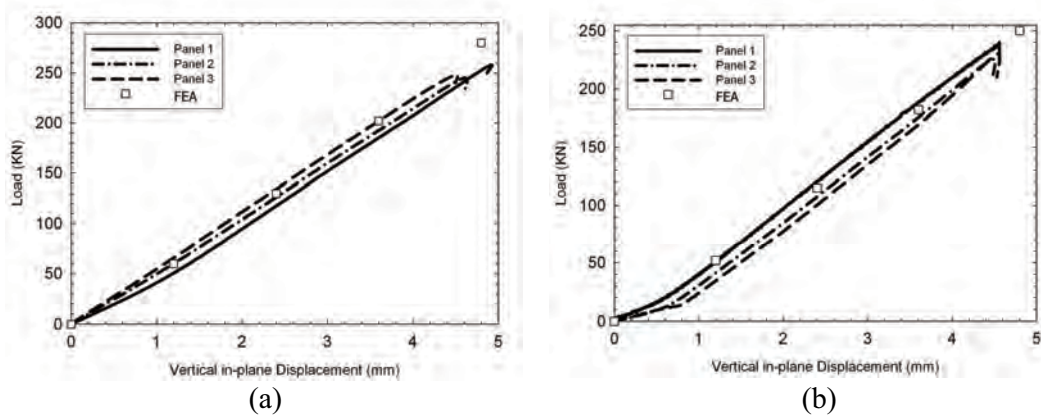


Figure 6: Load-displacement plots from experiments and FEA. (a) curved panel with radius 0.5 m, (b) curved panel with radius 1 m.

Panel type	Experimental value (kN)	Predicted value (kN)
1: $R = 0.5$ m	245 ± 10	178
2: $R = 1.0$ m	230 ± 5	218
4: $R = \infty$	272	----
4	238 ± 7	----

Table 4: Predicted and experimental failure loads. The predicted failure loads are given for the spring stiffness $K_S = 10$ MPa.

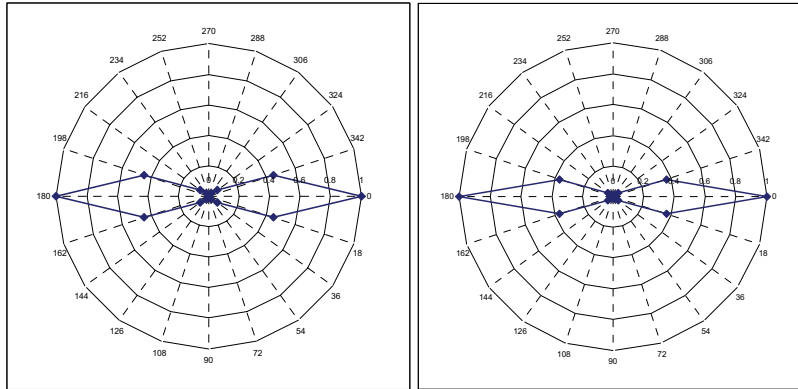


Figure 7: Normalized energy release rate (G/G_c) along the crack front for the panel with 0.5 m (left) and 1 m (right) radius

In order to investigate the buckling¹/instability behavior of the debonded panels, buckling/instability loads were extracted from the tests, eigen-value analysis and nonlinear analysis. Figure 8 shows load vs. radial out-of-plane deflection graphs for panels with debonds from experiments and numerical analysis using different spring element stiffnesses. Initially, the out-of-plane deflection and opening of the debond increases linearly with increasing load indicating a slow opening. However, as the load approaches the critical propagation load for the debond, the debond opening increases nonlinearly. Thus, a clear bifurcation buckling behavior of the debond is not observed either in non-linear analysis or experimental tests. It can be seen that the stiffness of the spring elements used to simulate the vacuum effect between core and debonded face sheet, highly affects the out-of-plane deflection of the debonded face sheet in the post-buckling. In order to extract instability loads from the numerical analysis, a spring stiffness of 10 MPa was applied, as good agreement with the experimental radial opening vs. load results was achieved.

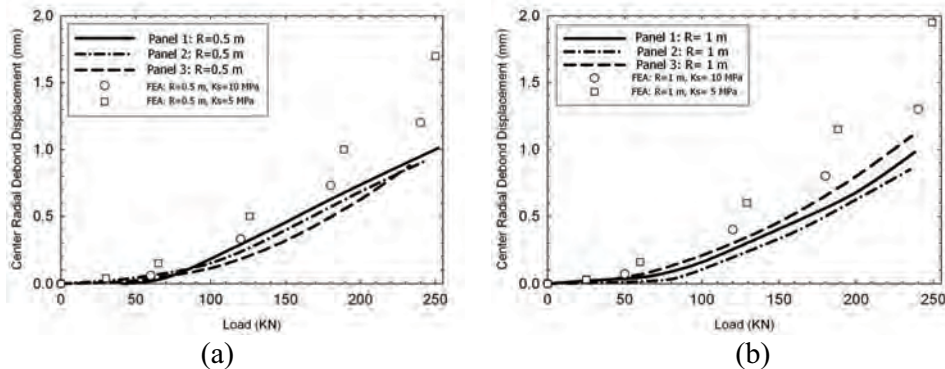


Figure 8: Load vs. Central radial out-of-plane debond deflection for varying spring element stiffness for (a) 0.5 mm radius of curvature and (b) 1 m radius of curvature

¹ The term “buckling” is only used in relation to bifurcation behavior and is only relevant for the eigen-value analysis.

The graphical method developed by Southwell [10] is applied in order to determine the instability loads. Generally, the Southwell method is a method which predicts the global instability load of initially imperfect structural members. The method was originally developed for columns, but experiments indicate that the method may be extended to plates [11]. Southwell plots for the curved debonded panel with 0.5 and 1 m radius of curvature are shown in Figure 9 from the experiments.

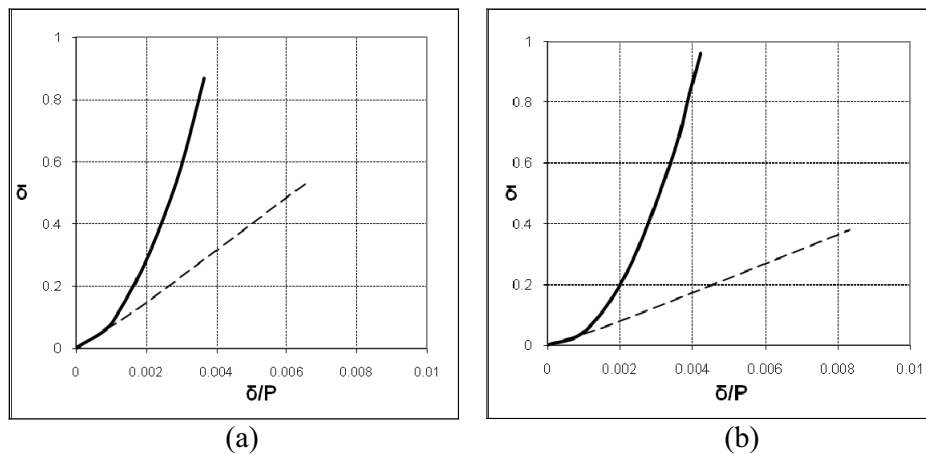


Figure 9: Southwell plots for debonded panels (Panel 1) for R=500 (a) and R=1000 (b) from experiments. The instability load can be found as the inverse of the slope of the linear tendency curve (stippled).

Table 5 summarizes the critical instability loads extracted from finite element analyses (with 10 MPa spring elements stiffness) and Southwell plots (figure 9). The eigen-value analysis results generally predicts buckling loads higher than the values obtained from experiments, while the results from nonlinear analyses are in good agreement with experimental data. This can most likely be addressed to the presence of initial specimen imperfections which effects are not included in the eigen-value analysis which assumes an ideal elastic structure.

Radius (m)	Experiments (kN)	Nonlinear analysis (kN)	Eigen-value (kN)
0.5	81.67±7	76.5	106.8
1	50.81±5	46.7	81.3

Table 5: Theoretical and experimental instability/buckling loads

7 CONCLUSION

The aim of this study was to investigate the applicability of present fracture mechanics models which were originally developed for perfectly flat structures and crack flanks in curved geometries. Using LEFM combined with the Crack Surface Displacement

Extrapolation (CSDE) method and finite element analysis, the residual strength of a limited range of curved sandwich panels with debond damages was predicted. Two types of curved debonded panels with different radius of curvatures were tested to validate finite element results. The debonds had a circular shape at the center location of the panels. In order to simulate the debond vacuum effect observed during the experiments, spring elements with low stiffness were used. The results show that the spring stiffness of these elements highly affects the post-buckling behavior of the panels indicating a similar conclusion for the debond vacuum effect. The presented finite element model was able to predict the failure load with about 5-27% error; however the accuracy is considerably better for the shallow panels (5%) than the panels with higher curvature (27%), indicating that the straight crack flank assumption is increasingly violated for increasing panel curvature. Energy release rates and mode-mixities were calculated at six positions along the debond crack front at a 15 degree interval in order to investigate the effect of the debond crack front position. Results indicate that at propagation the energy release rate distribution along the debond crack front is binocular-shaped, with maximum at 0° and 180° and minimum value at 90° and 270° , similar to earlier reported results for flat panels. The results were also confirmed by experimental observations where the crack propagation initiated around 0° and 180° positions forming a propagation band across the panel to the panel edges supported by the test rig. Using linear eigen-value and geometrically nonlinear analysis, the buckling/instability behavior of the panels was investigated. The Southwell method was employed to extract instability loads. Results from linear eigen-value analysis were higher than the actual values obtained from experiments, while the results of the nonlinear analyses were in good agreement with experimental data, indicating an effect from initial imperfections on the buckling behavior of the tested panels.

The initial findings presented in this paper illustrate that in order to analyze debonded panels with an arbitrary curvature, the present LEFM theory for debonds have to be expanded to account for curvature of the crack flanks. Furthermore, for cases with cyclic loading where gradual fatigue debond propagation can be expected, propagation modeling of the debond front is required..

AWKNOWLEDGEMENTS

This work has mainly been performed within the Network of Excellence on Marine Structures (MARSTRUCT) and has been partially funded by the European Union through the Growth Programme under contract TNE3-CT-2003-506141. The work has also partly been supported by the Danish Energy Authority through the 2005 Energy Research Programme (EFP 2005). The supported EFP-project is titled "Improved design of large wind turbine blades of fibre composites – phase 3" and has journal no. 33031-0078. Furthermore, the sponsoring of test specimens by LM Glasfiber A/S is highly appreciated.

REFERENCES

- [1] Avilés F. and Carlsson L.A. “Analysis of the Sandwich DCB Specimens for Debond Characterization”, *Engineering Fracture Mechanics*, 75, 153-168 (2008).
- [2] L. Falk, “Foam Core Sandwich Panel with Interface Disbands”, *Compos Structures*, 28, 481–90 (1994).
- [3] A. Nøkkentved, C. Lundsgaard-Larsen and C. Berggreen, “Non-Uniform Compressive Strength of Debonded Sandwich Panels - I. Experimental Investigation”, *Journal of Sandwich Structures and Materials*, 7(6), 461-482 (2005).
- [4] C. Berggreen and B.C. Simonsen, “Non-Uniform Compressive Strength of Debonded Sandwich Panels - Ii. Fracture Mechanics Investigation”, *Journal of Sandwich Structures and Materials*, 7(6), 483-517 (2005).
- [5] F. Avilés and L.A. Carlsson, “Post-Buckling and Debond Propagation in Panels Subjected to In-Plane Loading”, *Engineering Fracture Mechanics*, 74, 794-806 (2007).
- [6] C. Berggreen, B. C. Simonsen and K. K. Borum, “Experimental and Numerical Study of Interface Crack Propagation in Foam Cored Sandwich Beams”, *Journal of Composite Materials*, 41(4), 493-520 (2007).
- [7] Diab divinycell, divinycell international, Laholm. Available from: <http://www.Diabgroup.com>.
- [8] Jw. Hutchinson and Z. Suo, “Mixed Mode Cracking in Layered Materials”, *Advances in Applied Mechanics*, 29, 63-191 (1992).
- [9] C. Berggreen, B. C. Simonsen and R. Törnqvist, "Modeling of Debond and Crack Propagation in Sandwich Structures Using Fracture and Damage Mechanics", *Proc. of 6th International Conference on Sandwich Structures*, Ft.Lauderdale, Florida, USA, 682-693 (2003).
- [10] Rv. Southwell, “On the Analysis of Experimental Observations in Problems of Elastic Stability”, *Proceedings of the Royal Society of London*, 601–616 (1932).
- [11] C. Berggreen, C. Jensen And B. Hayman, “Buckling Strength Of Square Composite Plates With Geometrical Imperfections – Preliminary Results”, *Marstruct International Conference On “Advancements In Marine Structures”*, Glasgow, Uk, March 12-14, (2007)

LOCAL EFFECTS IN THE VICINITY OF TRANSITIONS FROM SANDWICH TO MONOLITHIC LAMINATE CONFIGURATIONS

Elena Bozhevolnaya^{*}, Abdul H. Sheikh[†] and Ole T. Thomsen^{*}

^{*} Department of Mechanical Engineering, Aalborg University
Pontoppidanstræde 101, 9220 Aalborg East, Denmark
e-mail: elena_boz@mail.dk, ott@ime.aau.dk

[†] Department of Civil, Environmental and Mining Engineering
University of Adelaide
North Terrace, SA 5005, Australia
e-mail: ahsheikh@civeng.adelaide.edu.au

Key words: Sandwich structures, Local effects, Finite Element modeling, Experimental mechanics.

Summary. *The paper presents the results of a preliminary experimental and numerical study of the local strain and stress concentrations in the vicinity of transition zones from sandwich to monolithic laminate configurations. The numerical modelling was conducted using finite element analysis, and the numerical results have substantiated the presence of the local effects that were measured experimentally. Some simple considerations regarding design optimization of transition zones between sandwich and monolithic composite laminates are also presented.*

1 INTRODUCTION

Sandwich structures are excellent structural elements with respect to their global load-bearing capacity, but their practical functionality necessarily includes the possibility of joining them as well as to introduce rigging/furnishing for various external appliances. This involves the use of different internal sub-structures, which cover a whole range of internal arrangements in sandwich structures/panels, such as core joints, edge and corner stiffeners, through-the-thickness inserts, etc. Despite the many possible types of sandwich sub-structures which differ from each other with respect to their practical use, design, materials and manufacturing techniques, the essence of the local phenomena developing in and around the sub-structure is similar in all cases. This involves stress concentrations due to the presence of material and geometric discontinuities. A core junction can be considered as a generic example or model for all such internal sub-structures, and it was analysed both experimentally and numerically [1-2]. The transition of a sandwich panel/plate to a monolithic laminate is another common design modification, which consists of a gradual reduction of the sandwich core thickness to zero, where the sandwich face sheets meet each other to form a monolithic laminate. The vacuum infusion manufacturing process allows complex tailoring of

composite sandwich panels, and the use of transitions from sandwich to monolithic laminates as a part of the design is widely exploited in aerospace, transportation, boat/ship, wind turbine blade and various other applications [3-6]. In the vicinity of a sandwich to monolithic composite transition zone, local effects will be induced. As such local effects are associated with severe stress concentrations, they may jeopardize the global performance of the whole structure. As there appear to be no studies concerning these effects, the present investigation presents the preliminary results of an experimental investigation and finite element modelling of the stress and strain distributions in sandwich beams (panels) with transitions from sandwich to monolithic laminate configurations.

2 TEST SPECIMENS AND EXPERIMENTAL SET-UP

Sandwich beams with two transition zones from sandwich to monolithic configurations were prepared using the vacuum infusion technique. For simplicity a 3-point loading scheme was chosen, and the load application is illustrated by arrows in Fig.1. The beams marked as Configuration 1 and 2 are the same sandwich beam configurations, and the numbers refer to the loading situation of the beams with respect to the geometry of the monolithic part and the loading direction. For example, sandwich beam configuration 1 is shown in Fig. 3. The geometry of the test specimens is also shown in Fig.1. The face sheets were made from and the glass reinforced epoxy, and two different PVC foams were used as core materials, H60 and H200 from DIAB. The specimens were manufactured using vacuum infusion. The material properties are quoted in Table 1.

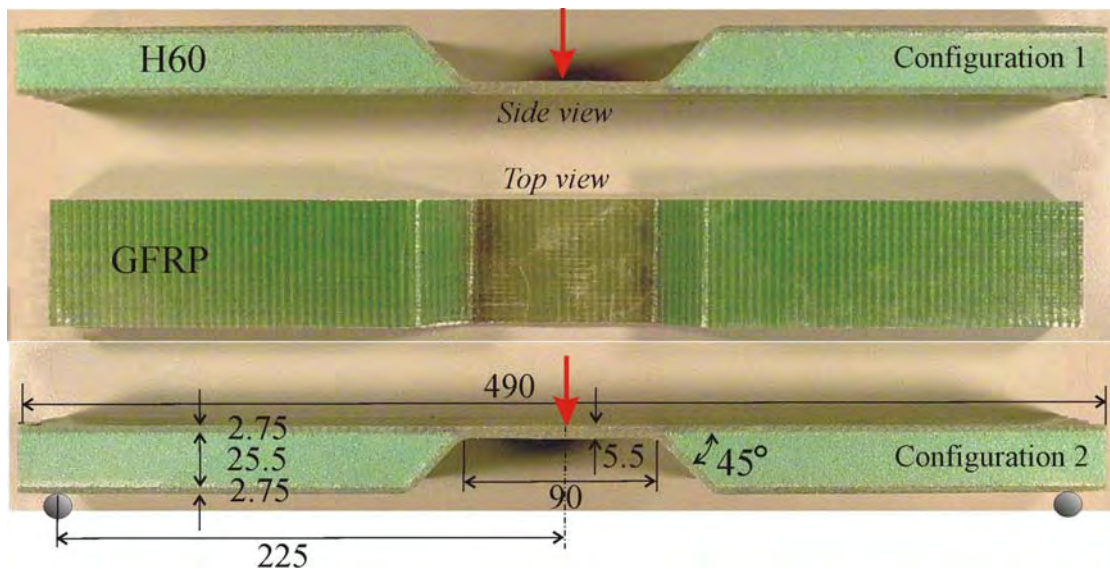


Figure 1: Geometry, boundary conditions and loading scheme of the sandwich test specimens.

The two transition zones are placed close to the beam centre. As sandwich structures are inherently sensitive to failure due to transverse stresses, the specific design was chosen such that it provided two distinct transition zones and prohibited core collapse in the most loaded central part of the specimen. The design of the test specimens has no particular practical relevance and was chosen solely due to experimental reasons, since this design facilitates the controlled loading and measurements of the local effects.

A zoom on the transition zone of the test specimens is shown in Fig. 2(a). Here the outer face surfaces and face-core interfaces are also labeled (“curved, ext.,” “curved, int.” etc), to keep track of the experimental and numerical data in the following analyses. The photo of Fig. 2(b) illustrates the modified transition zone, where an additional core patch of a denser PVC foam H200 was used in order to obtain a more smooth redistribution of the local stresses with the purpose of reduction of the local effects. Fig. 3 presents the set-up used for the experimental investigation.

The sandwich beam specimens were subjected to static loading, and the loading response was kept within the linear range. The main purpose of the experiment was to measure the strain distributions along the outer surfaces of the beam faces with special attention on the transition zones.

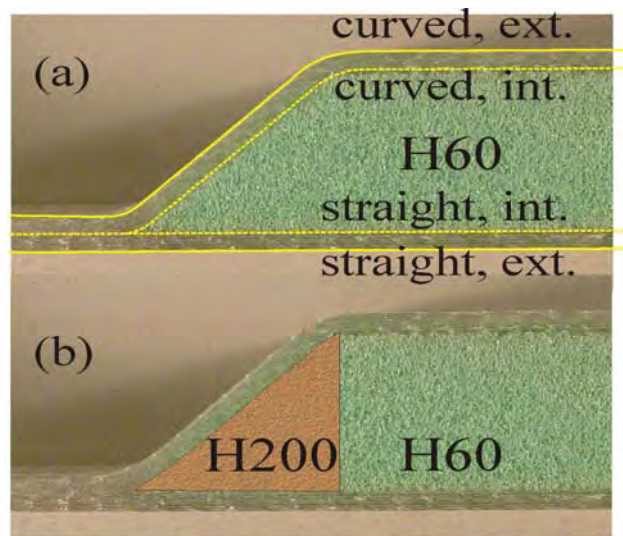


Figure 2: Zoom on the transitions from sandwich to monolithic laminate: (a) – experimentally tested and modelled configuration with interfaces and outer surfaces of the sandwich faces indicated; (b) – “optimized” design configuration with high-density core insert

Therefore the latter were furnished with a chain of five 1 mm strain gauges (situated at a distance 45 mm from the beam centre – cf. Fig. 3). This allowed the monitoring of the strains at the locations where local stress concentrations were expected. One of the strain gauges was placed on the surface of the monolithic laminate close to the centre of the sandwich beams at the distance of 25 mm, and another was placed on the sandwich face laminate at the distance of 150 mm in order to assess the overall strains in the sandwich beam (cf. Fig. 2). These separate strain gauges together with 2 dial gauges for measuring the central beam deflection and the beam deflection 150 mm from the centre made it possible to control the specimens were loaded within the linear load-response domain.

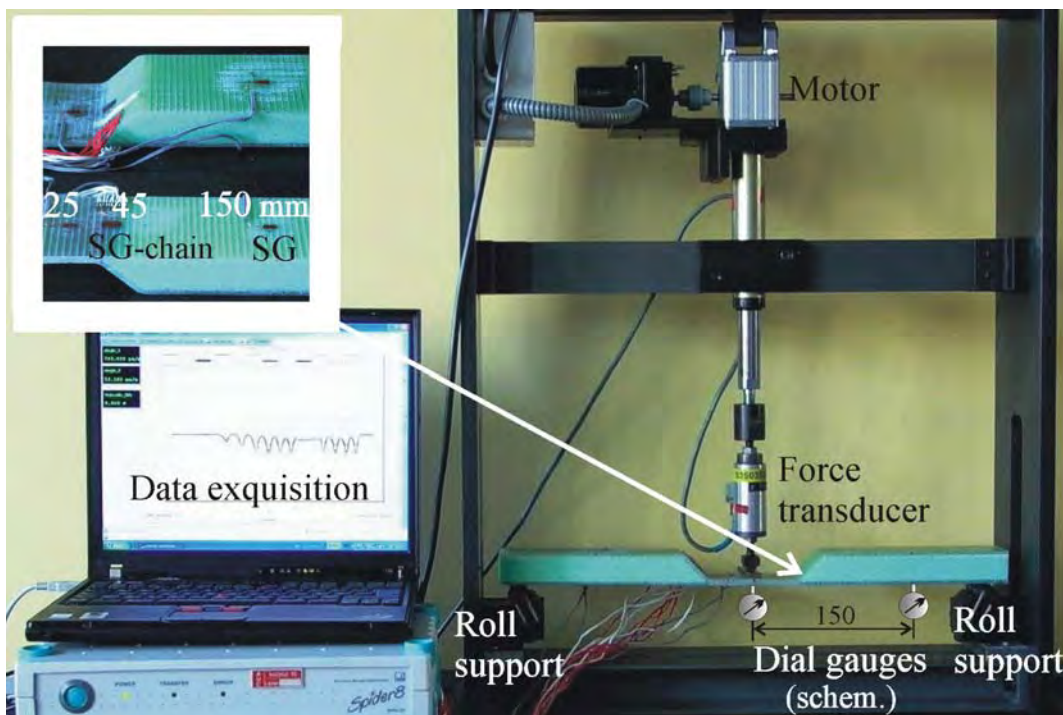


Figure 3: Experimental set-up for 3-point bending of sandwich-monolith sandwich beams with a zoom on the strain-gauge positions in the transition zone.

3 FINITE ELEMENT MODELLING

Finite Element Analysis was used for the numerical modelling of the specimens with sandwich to monolith laminate transitions subjected to 3-point bending. Due to the symmetry of the chosen specimen, only half of the sandwich beam was modelled. For this purpose the

commercially available finite element code ABAQUS Standard 6.6 was used. The face sheets and the main core (H grade PVC foam H60) were modelled with four node quadrilateral plane stress element (CPS4R), while the high density triangular core patch (H grade PVC foam H200) was modelled with three node triangular plane stress element (CPS3). A reasonably fine mesh was used to ensure convergence of the finite element solution. For this purpose the face sheets were modelled using five layers of elements in the thickness direction, while fifty one elements were used along the thickness of the core. The number of elements along the longitudinal direction was appropriately taken to have element aspect ratio of the order of one. Clamped boundary conditions were imposed by restraining all the degrees of freedom of the nodes at left end of the model representing the loaded central section of the specimen. Half of the applied load i.e., the vertical reaction at of the supports was applied at the node corresponding to the support near the right end.

Function/Material	Elastic modulus, MPa	Poisson's ratio	Tensile/compressive strength, MPa
Face/GFRP	26000	0.3	
Main Core/PVC-foam H60	70	0.35	0.9/1.8
Core Patch/PVC-foam H200	310	0.35	4.8/7.1

Table 1: Mechanical properties of the sandwich constituents

4 LOCAL EFFECTS AND CONSIDERATIONS ON DESIGN OPTIMIZATION

The first stage of the experimental study included measurements of the beam centre deflections vs. applied loading. These tests were conducted in order to validate the linearity of the load-response characteristics. A dial gauge (Fig. 3) was placed under the centre of the beam specimens to measure the central displacement of the beam vs. applied load (Fig. 3). The results of measurements and the load-response predicted using FEA are shown in Fig. 4.

From Fig. 4 it is seen that the load-deflection curves are linear in the entire range of applied loads, although the measured displacements were found to be slightly smaller than the predicted results. This might be explained by the uncertainty of determination of the modulus of elasticity of the GFRP faces. The modulus of elasticity of GFRP face given in Table 1 was found experimentally in a tensile test conducted on a GFRP laminate manufactured separately for this particular purpose using vacuum infusion. Given the rather substantial variation of the mechanical properties that may occur due to the manufacturing process, the observed divergence of the numerical and experimental data in the range of 7% in Fig. 4 is considered to be acceptable.

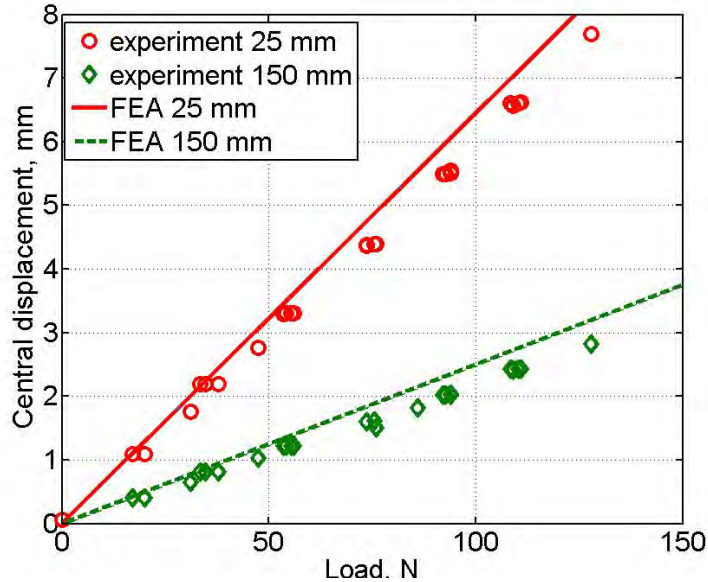


Figure 4: Load response of sandwich specimen shown in Fig. 3 (Loading condition 1, Fig. 1). Measurements were conducted using dial gauges located in the beam centre and at distance of 150 mm from the centre. FEA predictions correspond to the same locations.

Fig. 5 presents the strain distributions along the outer surfaces of the beam faces in the monolithic and sandwich laminate parts. Both experimental and the numerically generated data are included in the figure, and a fairly close match is observed. A significant increase of the strains (and therefore also of the corresponding stress) in the vicinity of the transition zones should be noticed. For example, at the outer surface of the curved face the nominal tensile strain raise from $1650 \mu\epsilon$ to $2500 \mu\epsilon$ at distance of 50 mm from the beam centre. Moreover, the same face experiences compression at the distance of 70 mm from the beam centre, where the classical sandwich laminate starts. An even more drastic strain gradient is observed for the neutral line of the monolithic laminate which continues into the internal surface of the sandwich beam (cf. Fig. 2). Here zero normal strain shoots up to more than $2000 \mu\epsilon$ over a very short distance. Overall, the match between the numerical predictions and the experimental data is very good.

While the numerically predicted strains in Fig. 5 were calculated to provide a direct comparison with the measurements, the strains presented in Fig. 6 are given in the coordinate system XY of the FEA-model related to the sandwich beam (the X-axis is along the beam neutral line, and the Y-axis is the in the thickness direction). The numerical analysis presented in Fig. 6 further reveals the physics of the local effects, namely that severe shear strains (stresses) are present, and that these shear strains trigger the local effects at the transition zones. At a short distance of approximately 5 mm from the beam centre, the shear strain increases from zero up to about $3000 \mu\epsilon$. Sandwich structures are especially well suited for the transfer of shear stresses/strains through the thick core material, and the transition to a

monolithic laminate, which forces the faces to carry the shear loading, therefore disrupts the shear stress distribution and causes high local strain (stress) concentrations (re-distribution of the shear stresses across the geometrical discontinuities).

Obviously stress concentrations arise not only in the faces of the sandwich beam as it was shown in the experiment, but also in the adjacent core. Fig. 7 gives the predicted strain distributions in the faces of the beam similar to these given in Fig.5, but in a more detailed representation. The strains are depicted by dashed lines and specify a significant overshooting of the nominal strains at the transitions. It was not possible at the time to measure the core strains, and therefore Fig. 8(a) gives the numerically predicted principal stresses in the core close to the transition zone for the 2 different configurations shown in Fig. 2. It should be noticed that the maximum stress level is close to the tensile strength of the foam core (DIAB PVC H60).

In order to suppress or reduce the stress concentrations induced by local effects various means can be used. One such measure is to introduce local reinforcements of the faces at the transition from monolithic to sandwich laminate. Another suggestion is illustrated in Fig. 2(b). Here a patch of denser foam, in this case Divinycell H200, is inserted in order to reinforce the core at the transition zone. This configuration is referred to as the “optimized” design. The influence on the strain distribution of the insertion of high density patch or insert as shown in Fig. 2(b) is illustrated in Figs. 7 and 8. It is observed that not only the level of the overall strains in the faces is diminished (Fig. 7), but also the overshooting of the nominal strains is much smaller. It is seen from Fig. 8 that the stresses in the patch/insert for the “optimized” design are of a higher level than for the conventional design. However, the strength of the high density core (H200) is significantly higher than that of the H60 core, which effectively means that the strength margin of the “optimized” design is higher. Thus, the introduction of the patch core has reduced the dangerous stress concentrations in the sandwich beam core in the transition zone between the sandwich and the monolithic laminate.

5 CONCLUSIONS

The results of a preliminary combined study experimental and numerical study of the local strain and stress concentrations in the vicinity of transition zones from sandwich to monolithic laminate configurations have been presented.

The experimental investigations were conducted on test specimens loaded in 3-point bending, with a central monolithic glass epoxy laminate at the beam centre which transforms into PVC foam-cored sandwich laminates (glass epoxy faces) toward the edge supports. The sandwich to monolithic laminate transitions were instrumented with strain-gauge chains, and the beam specimens were instrumented with dial gauges.

The experimental measurements have shown that very high local stress concentrations are induced in the faces and the face-core interfaces in the vicinity of the transition zone. In addition to the experimental measurements, elaborate FEA analyses were conducted using the software package ABAQUS Standard 6.6. The FEA results confirmed the experimental findings, and a good match was found between the experimental findings (strains and displacements) and the FEA results.

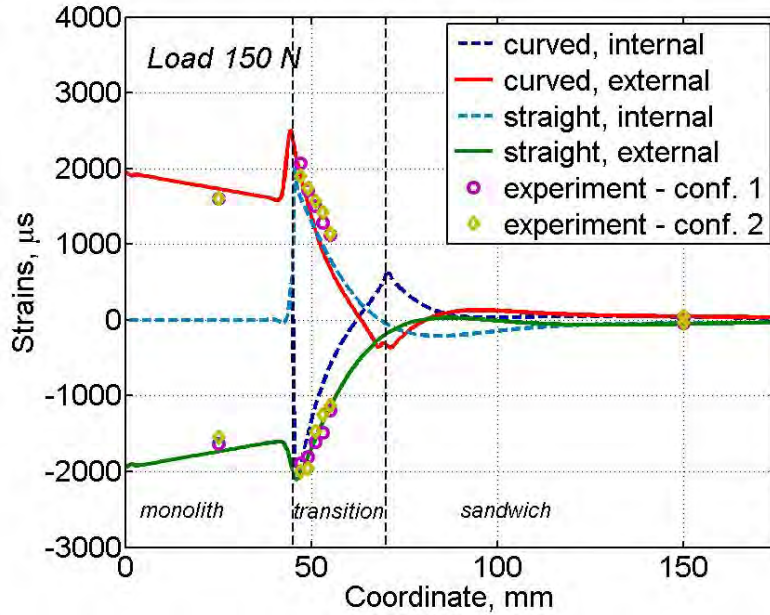


Figure 5: Experimentally measured and numerically calculated strains along the sandwich faces. The coordinate is measured from the centre of the beam (Fig. 1) and the face surfaces are specified in Fig. 2.

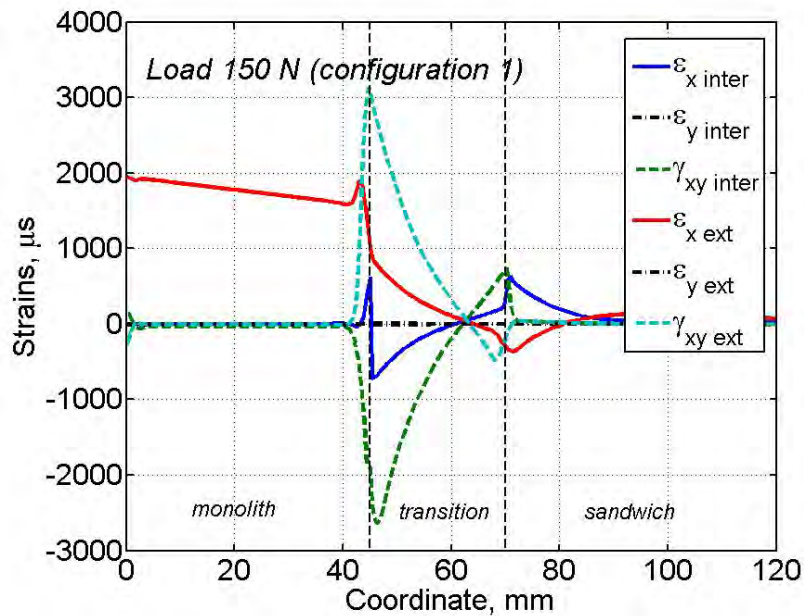


Figure 6: Strains calculated using FEA at the interfaces and external surfaces of the curved face of the sandwich beam (cf. Fig. 2). Loading configuration 2 according to Fig. 1.

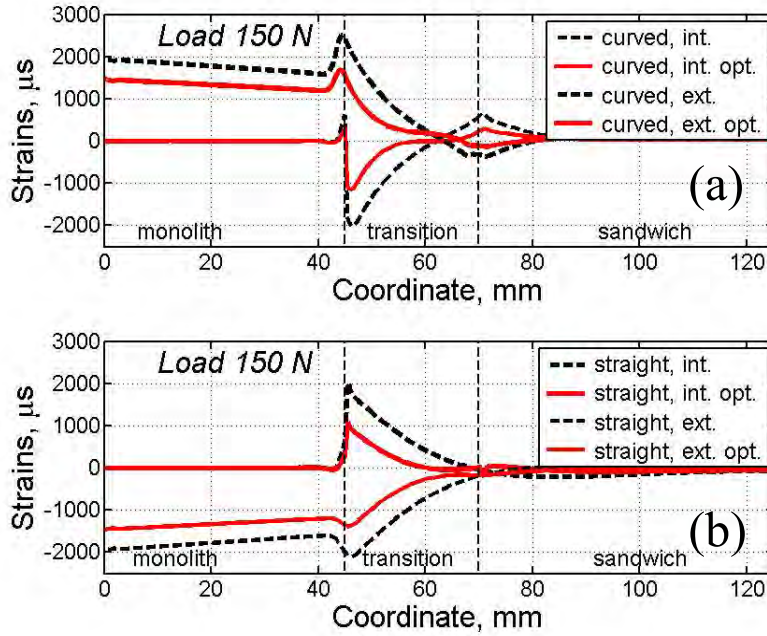


Figure 7: Strains calculated along the interfaces and external surfaces of the beam face for the original (a) and “optimized” (b) design (cf. Fig. 2). Load configuration 1 according to Fig. 1.

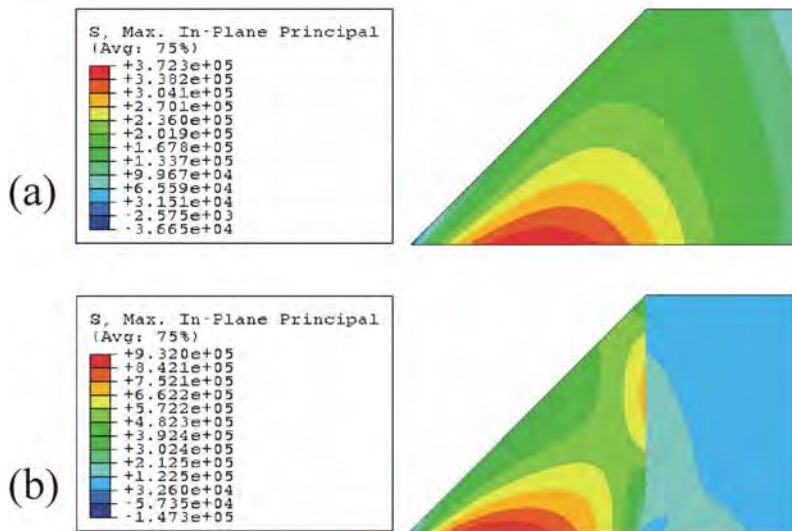


Figure 8: Maximum principal stresses calculated in the sandwich beam core for the original (a) and “optimized” (b) design (cf. Fig. 2). Load is 150 N.

In addition to the investigation of the standard monolithic laminate composite to sandwich panel transition, a modified design or “optimized” design was investigated experimentally as well as numerically. In this “optimized” design a patch or insert of high density PVC foam core material (H200 vs. H60 in the conventional design) was inserted in the transition zone. Both the experimental and the numerical results showed that the stress concentrations in the “optimized” design are relieved considerably in the faces and the core-face interfaces.. Moreover, the strength margin in the higher density core was improved considerably even though the actual core stresses were in fact increased (the higher density core has higher strength). Thus, the introduction of a patch core/insert of higher density has reduced the dangerous stress concentrations in the sandwich beam core in the transition zone between the sandwich and the monolithic laminate.

ACKNOWLEDGEMENTS

The work presented was The Innovation Consortium “Integrated Design and Processing of Lightweight Composite and Sandwich Structures” (abbreviated “KOMPOSAND”) funded by the Danish Ministry of Science, Technology and Innovation and the industrial partners Composhield A/S, DIAB ApS (DIAB Group), Fiberline Composites A/S, LM Glasfiber A/S and Vestas Wind Systems A/S.

REFERENCES

1. Bozhevolnaya, E., Lyckegaard, A. and Thomsen, O. T., “Localized Effects Across Core Junctions in Sandwich Beams Subjected to In-plane and Out-of-plane loading”, *Applied Composite Materials*, 12, 35-147 (2005).
2. Bozhevolnaya, E. and Thomsen, O. T., “Structurally Graded Core Junctions in Sandwich Beams: Static Loading Conditions”. *Composite Structures*, 70(1), 517-527 (2005).
3. Bozhevolnaya, E. and Thomsen, O. T., ”Structurally Graded Core Junctions in Sandwich Beams: Static Loading Conditions”. *Composite Structures*, 70(1), 517-527 (2005).
4. Hentinen, M., Hildebrand, M., “Joints Between FRP-Sandwich and Metal Structures”. In: “Composite and Sandich Structures”, pp. 193-204. Eds. J. Bäcklund *et al*, EMAS Ltd, London, 1997.
5. Brevik, A.F., “Designing and Production of Large Composite Structures for Offshore and Ttransport”. In: “Composite and Sandwich Structures”, pp. 515-523. Eds. J. Bäcklund *et al*, EMAS Ltd, London, 1997.
6. Roth, M.A., “Development of New Reinforced Load Introductions for Sandwich Structures. In: Proceedings of the 7th International Conference on Sandwich Structures (ICSS-7), Aalborg, Denmark, August 29-31, 2005 – “Sandwich Structures 7: Advancing with Sandwich Structures and Materials”, Ed. by Thomsen, O.T. *et al*, Springer, 2005. pp. 1017-1026.
7. Krämer, R., Roth, M.A., “Experimental and Numerical Analysis of Hollow and Foam-Filled A-Stringer/A-Former under Axial Compression Load and Bending Moment”. In: Proceedings of the 7-th International Conference on Sandwich Structures (ICSS-7),

Elena Bozhevolnaya, Abdul H. Sheikh and Ole T. Thomsen.

Aalborg, Denmark, August 29-31, 2005 – “Sandwich Structures 7: Advancing with Sandwich Structures and Materials”, Ed. by Thomsen, O.T. *et al*, Springer, 2005. pp. 987-996.

8. Bozhevolnaya, E., Lyckegaard, A., Thomsen, O.T., Jakobsen. L. “Sandwich Panel and a Method of Producing a Sandwich Panel”. Patent Application P14477USPC, P14477CAPC, December 8, 2006.

MULTILAYER DAMPING TREATMENTS: MODELING AND EXPERIMENTAL ASSESSMENT

R.A.S. Moreira* and J. Dias Rodrigues†

*Departamento de Engenharia Mecânica da Universidade de Aveiro (UA)
Universidade de Aveiro
Campus de Santiago, 4200-465 Aveiro, Portugal
e-mail: rmoreira@ua.pt, web page: <http://www.ua.pt>

†Faculdade de Engenharia da Universidade do Porto (FEUP)
Universidade do Porto
Rua Dr. Roberto Frias, 4200-465 Porto, Portugal
e-mail: jdr@fe.up.pt, santos.silva.joao@fe.up.pt, web page: <http://www.fe.up.pt>

Key words: Viscoelastic Damping Treatments, Multi-Layer Sandwich, Passive Dynamic Control

Summary. *The sandwich panels with viscoelastic cores, which represent the physical application of the viscoelastic integrated damping treatment concept, associate different materials, each one having a specific structural contribution, where the outside faces, usually made from a stiff material, guarantee the stiffness of the composite structure whereas the viscoelastic and soft core provides the damping capability.*

The application of soft cores, specially the thick ones, into sandwich plates produces an important decoupling effect, leading to a significant flexural stiffness reduction of the sandwich plate, as experimental and numerical results evidence. From this observation and pursuing a solution to minimize such effect, the partitioning of the core layer into multiple layers separated by thin constraining layers is hereby considered. Taking advantage of the application of the multiple viscoelastic layers in the sandwich core, it is also analyzed the potential use of different viscoelastic materials in order to spread out the efficient temperature range of the damping treatment.

To verify and evaluate the effects of the multi-layer and multi-material viscoelastic cores in sandwich panels, an experimental and a numerical study was conducted on representative specimens of these design concepts. The results achieved from this study demonstrate the applicability of the two multiple layer configurations, evidencing the effect of the partitioning procedure onto the reduction of the flexural stiffness decay and the efficient temperature range enlargement when adopting viscoelastic materials with different transition temperatures.

1 INTRODUCTION

The application of thin viscoelastic layers in the core of sandwich plates provides an effective passive damping mechanism broadly applied on light structures such as aeronautic fuselage panels and satellite panels. In fact, the viscoelastic core is cyclically shear deformed due to the

relative motion of the external skins of the sandwich, leading to an important thermal dissipative effect and, thus, to a considerable reduction of the vibration energy of the structure.

Usually, very thin viscoelastic layers (0.02-0.10mm) are efficiently applied due to the high shear deformation that is imposed by the adjacent stiff layers. The application of thick viscoelastic layers, which increase the viscoelastic deformation energy, strongly reduces the overall flexural stiffness of the sandwich panel due to the reduced skin stiffness coupling provided by the soft and thick viscoelastic core. Moreover, the relative shear deformation developed within thin viscoelastic layers is significantly higher than the one developed within thick layers.

To solve these restrictions it is proposed to apply several thin viscoelastic layers separated by interlaminar constraining layers. With this configuration, it is possible to increase the amount of viscoelastic material maintaining the flexural stiffness of the sandwich plate. Moreover, by using a multi-layer scheme, it is possible to apply viscoelastic materials with different transition temperatures, which can be useful to enlarge the efficient temperature range of the damping treatment.

The aim of this work is to test and simulate several multi-layer and multi-material specimens in order to verify and validate the feasibility of the proposed treatment configurations.

2 MULTI-LAYER AND MULTI-MATERIAL CORE DAMPING TREATMENTS

The application of multiple viscoelastic layers in free or constrained surface treatments was proposed by Jones [1, 2] as a procedure to increase the treatment efficiency. This multi-layer configuration was also reported as a solution to enlarge the narrow efficient range of the viscoelastic treatments by employing layers of materials with different transition temperatures.

The application of this technique to the integrated layer configuration in sandwich structures, pursuing the same benefits, isn't, however, straightforward. In fact, the number of layers, the relative dimensions of the layers, the material properties and the layering sequence of multi-material configurations are important design parameters and play an important role in the structure behavior. The influence of these variables is considerably of extreme importance when compared to the multi-layer surface treatments, where the damping layer do not greatly modify the flexural stiffness of the structure. On the contrary, the core of the integrated treatment is simultaneously responsible for the dissipative effect and the stiffness coupling between the outside layers, which defines the global flexural stiffness of the structure.

3 EXPERIMENTAL STUDY

The first step of this study was the experimental verification of the feasibility of the multi-layer concept. In this first part of the study, an experimental work on a set of representative specimens was developed to evaluate the variation of the fundamental natural frequency and corresponding modal loss factor when adopting a multi-layer configuration.

The experimental results obtained were also used to validate the model adopted in the numerical analysis of this study.

3.1 Experimental specimens

To develop the experimental study, plate specimens with integrated viscoelastic treatments were produced. Two viscoelastic materials were used to produce the viscoelastic layers applied in the core of the sandwich plates. The first material, 3M ISD112 [3], is designed for room temperature applications presenting an efficiency peak between 20 and 30°C. The other viscoelastic material, 3M ISD110, is designed for higher temperature applications, ranging from 40 to 100°C.

The specimens were produced with aluminum plates with 1mm thickness, 200mm length and 100mm width. A thin aluminum sheet provided the inner constraining layers for the multi-layer and multi-material specimens. Table 1 presents the properties of the materials applied in the study.

Material	Young's modulus [Pa]	Poisson's ratio	Density [Kg/m ³]
AA 1050A H24	70E9	0.32	2708
AA 8050 H24	70E9	0.32	2708
3M ISD112	see [3]	0.49	1140
3M ISD110	see [3]	0.49	1140

Table 1: Material properties

3.1.1 Single-layer specimens

The single-layer specimens, designated by S1 and S2 (Figure 1), were produced by applying a single core layer of 3M ISD112 and 3M ISD110, respectively, with 0.127mm thickness. These specimens provided the reference to evaluate the multi-layer and multi-material benefits/drawbacks.

3.1.2 Multi-layer specimens

Two multi-layer specimens, designated by M1 e M2 (Figure 1), were also produced applying, respectively, 2 and 3 thin layers (0.0508mm) of 3M ISD112 intercalated with thin (0.05mm) aluminum sheets that provided the constraining effect.

3.1.3 Multi-material specimens

The specimens M3 and M4 (Figure 1) represent the multi-material configurations. These specimens are dimensionally identical to the multi-layer ones where some 3M ISD112 layers were replaced by identical 3M ISD110 layers, as depicted in Figure 1.

The Figure 2 illustrates the experimental specimens produced and tested in this study.

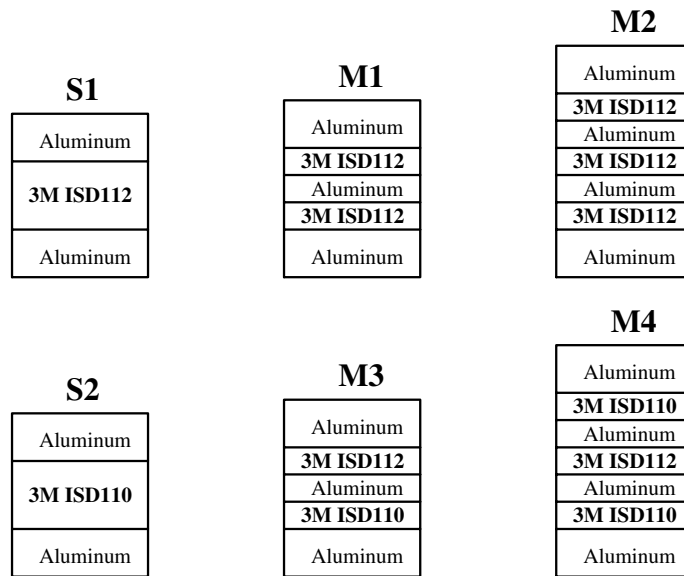


Figure 1: Specimens configuration

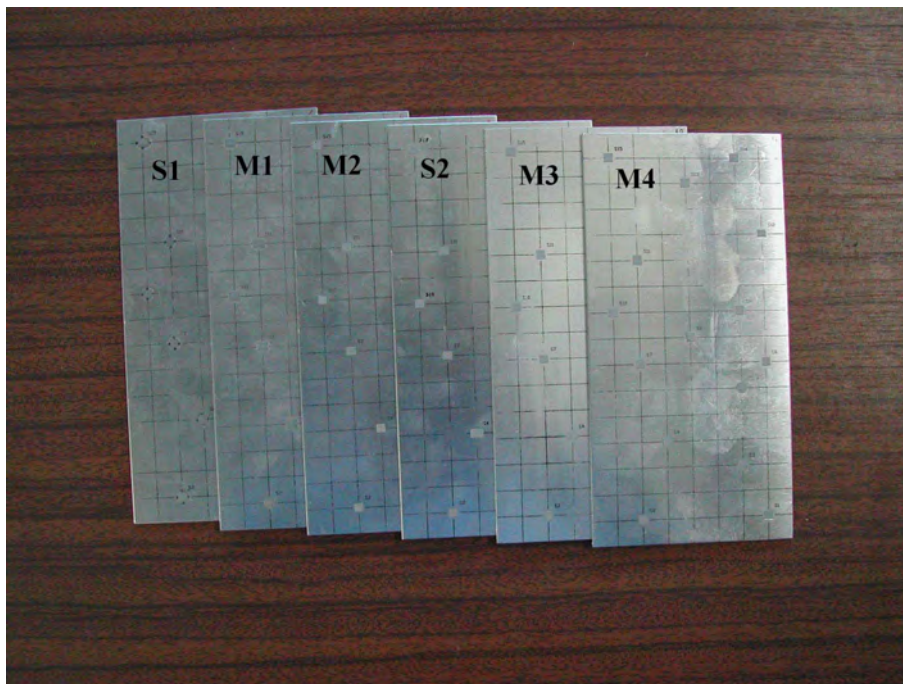


Figure 2: Specimens analyzed

3.2 Experimental setup

As stated above, the experimental study developed in this work had two purposes: to provide a comparison analysis between the damping efficiency and the flexural stiffness achieved for each treatment and to validate the model adopted for the numerical analysis presented in the following section. For both purposes, the aim of the experimental study was the determination of a representative set of frequency response functions providing the input data for a modal parameter identification process and, on the other hand, a reliable basis for the numerical layerwise model [5, 6] validation for a direct frequency analysis using the complex modulus approach [4].

To obtain free boundary conditions, the experimental specimens were suspended by a thin nylon wire from a rigid frame. A mesh with 15 measuring points, as depicted in Figure 3, was defined for all the tested specimens.

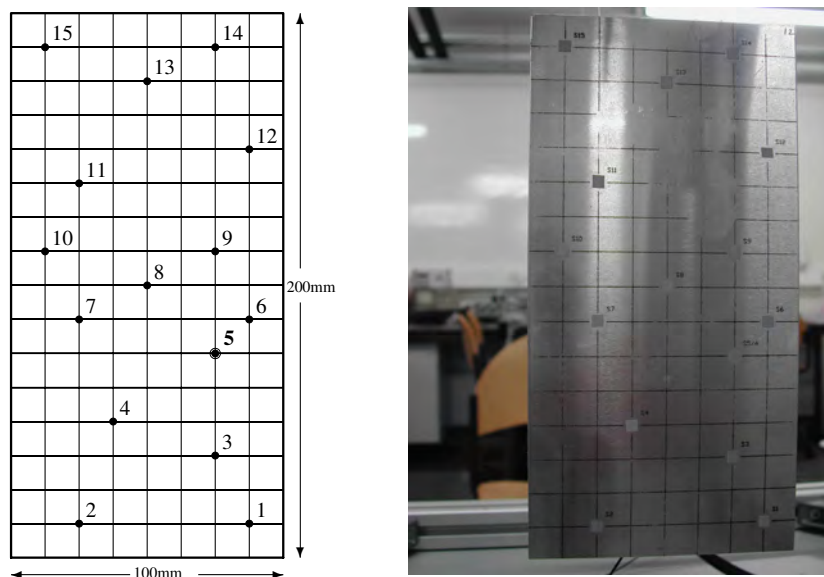


Figure 3: Measuring mesh and specimen boundary conditions

An electrodynamic shaker (Ling Dynamic Systems - model 201), suspended from an independent rigid frame, was utilized to generate a random ([0-800]Hz) excitation in point 5 of each specimen. A thin and flexible stinger was used to link the shaker to the miniature force transducer (Brüel & Kjær - model 8203) attached to the plate surface, which provided the measurement of the applied dynamic force. The specimens responses were evaluated by using a laser vibrometer (Polytec - model OFV303) to measure the velocity of each point of the measuring mesh. The temperature of the measurement was evaluated by a thermocouple located near the specimens.

3.3 Experimental validation of the numerical model

For each specimen, fifteen frequency response functions (mobility functions) were determined. These experimental frequency response functions were compared to the numerical ones generated by using the finite element model adopted in this study [5], which allowed the validation of the finite element model as well as the complex modulus approach to characterize the viscoelastic material. This model assessment was performed by simple visual comparison of the experimental and finite element predicted frequency response functions, as presented in Figures 4-9.

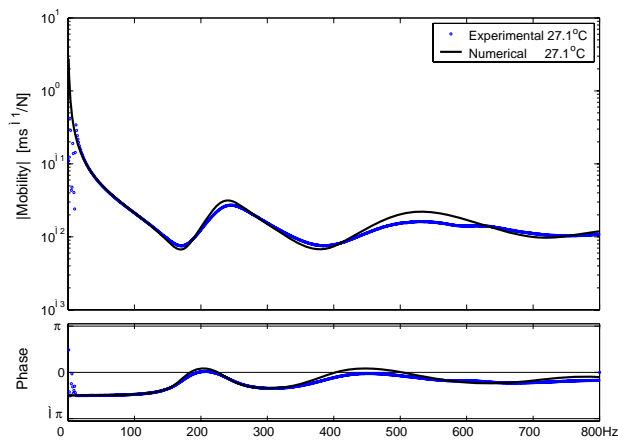


Figure 4: Driving point mobility function for specimen S1 (27.11°C)

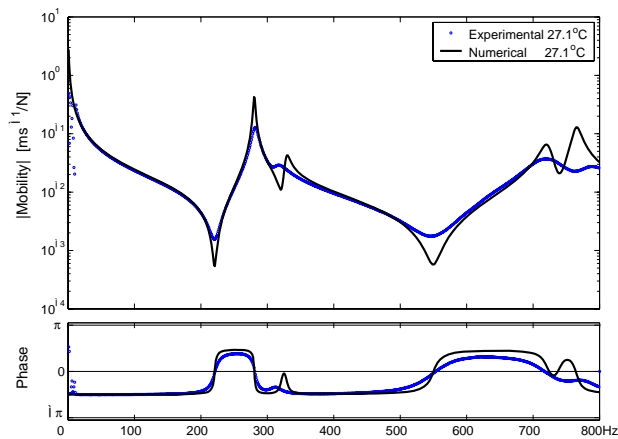


Figure 5: Driving point mobility function for specimen S2 (27.11°C)

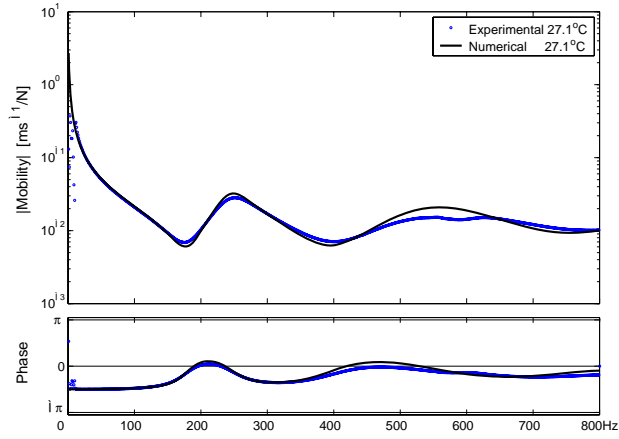


Figure 6: Driving point mobility function for specimen M1 (27.11°C)

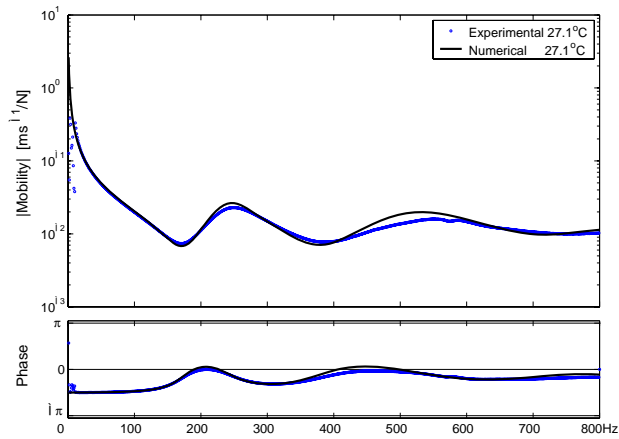


Figure 7: Driving point mobility function for specimen M2 (27.11°C)

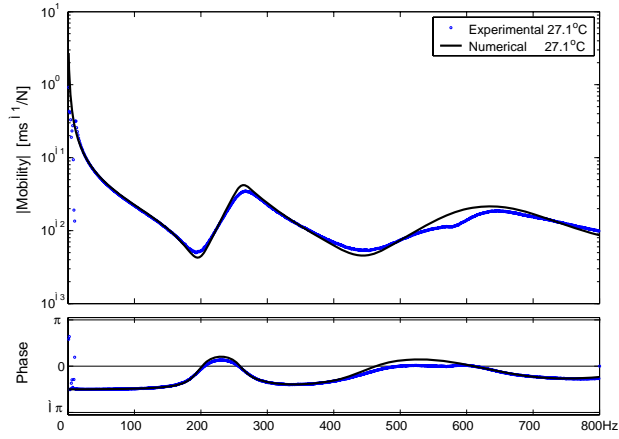


Figure 8: Driving point mobility function for specimen M3 (27.11°C)

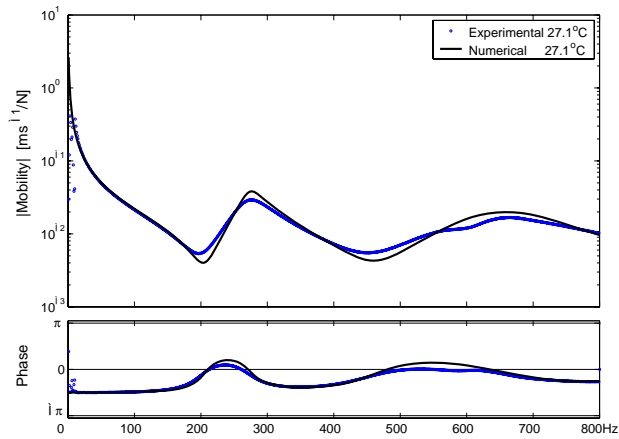


Figure 9: Driving point mobility function for specimen M4 (27.11°C)

3.4 Experimental results - modal identification

Using a circle fit modal parameter identification procedure, the fundamental natural frequency and the corresponding modal loss factor were identified for the six test specimens. The identified values are presented in Table 2.

Specimen	Natural frequency [Hz]	Modal loss factor
S1	238.58	0.270
S2	281.42	0.032
M1	245.32	0.244
M2	250.54	0.299
M3	261.57	0.163
M4	267.21	0.193

Table 2: Fundamental natural frequencies and modal loss factors

While the modal loss factor provides an indicator for the damping efficiency achieved by each configuration, the fundamental natural frequency is useful to evaluate the flexural stiffness variation for each treatment configuration.

Since the inner constraining layer is made of aluminum, the additional mass of the multi-layer treatment is higher than the mass added by the single layer treatment. This observation, along with the higher values for the fundamental natural frequency achieved with the multi-layer and multi-material specimens, supports the assumed benefit of the integrated treatments with multiple layers in the core: the attenuation of the decoupling effect promoted by the soft core.

From the modal loss factor values it was also possible to establish an efficiency relationship between multi-layer and single-layer treatment configurations. Despite the higher damping achieved with the specimen M2, having into consideration the viscoelastic material mass effectively introduced in the dissipative core, specimen M1 presents the highest damping configuration.

The multi-material specimens present higher natural frequencies and lower modal loss factors because the 3M ISD110 material has a higher storage modulus and a low loss factor at the testing temperature conditions (27.1°C).

4 NUMERICAL ANALYSIS

Using a layerwise finite element model proposed by the authors [5], a numerical analysis was performed on the proposed treatment configurations in order to verify their behavior along with the temperature. This study intends to verify the assumed benefits of the multi-material configuration, which is here proposed as a solution to enlarge the efficient range over the temperature.

4.1 Analysis method

Since the aim of this analysis is merely to compare the different multi-layer and multi-material configurations over a large range of temperature, it was used an approximate analysis procedure to determine directly the modal parameters of the specimens.

The Modal Strain Energy (MSE) method [8] was the selected analysis method due to its computational efficiency, providing with relatively low cost the modal model that can be used to compare the treatment configurations through its natural frequencies and corresponding modal loss factors. The MSE method assumes that the modal shapes of the undamped structure are representative of the structure with treatment. Therefore, the approximate loss factor of the damped structure can be easily determined through the ratio between the dissipated energy and the storage energy using the undamped mode shapes.

In this numerical study, a modified version of the original MSE method [9, 10] is applied in order to account for the effects of the viscoelastic core in the modal frequencies of the treated plates.

Modified MSE method algorithm

1. Starting condition:

$$\omega_r^i = \omega_0$$

2. Iterative loop for calculation of undamped natural frequency:
 - eigenvalue problem statement

$$[K_R(\omega_r^i)]\{\phi_r\}^i = (\lambda^2)^i[M]\{\phi_r\}^i$$

- natural frequency determination

$$\omega_r^{i+1} = \lambda_r^i$$

- convergency assessment

$$\Delta_\omega = |\omega_r^{i+1} - \omega_r^i|/\omega_r^{i+1} \leq \Delta_{\max}$$

3. Modal loss factor determination:

$$\eta_r = \frac{\{\phi_r\}^T [K_I(\omega_r^{i+1})] \{\phi_r\}}{\{\phi_r\}^T [K_R(\omega_r^{i+1})] \{\phi_r\}}$$

This iterative procedure allows to get an approximate value to the damped natural frequency and, consequently, a better approximation to the real viscoelastic material properties.

4.2 Numerical results

The proposed modified version of the MSE method was applied to calculate the fundamental natural frequency and corresponding modal loss factor of the analyzed treatment configurations

for a range of temperatures from 0°C to 100°C.

An additional multi-material configuration, M4*, was considered in this analysis. This configuration, based in the M4 treatment configuration, has the middle viscoelastic layer made of 3M ISD 110 and the two outside viscoelastic layers made of 3M ISD112.

The obtained fundamental natural frequency values are represented in Figure 10. The obtained results show that the treatment configurations with the viscoelastic material 3M ISD110, S2, M3, M4 and M4*, present higher natural frequencies than those configurations with the material 3M ISD112. This observed effect is due to the higher transition temperature of the 3M ISD110 viscoelastic material. Additionally, it is also observed that the multi-layer configurations, M1 and M2, present higher natural frequencies than the single-layer configuration S1, sustaining the assumed major benefit of the multi-layer: the attenuation of the decoupling effect.

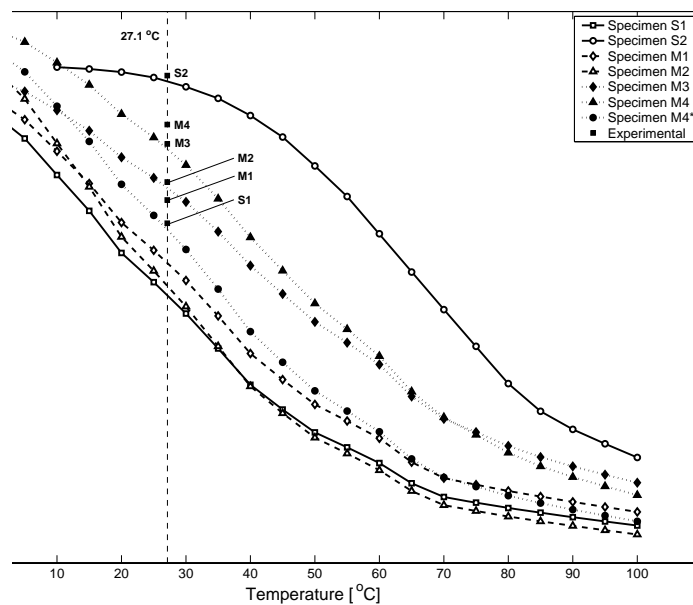


Figure 10: Fundamental natural frequency distribution

On the same graphic it is also represented the identified fundamental natural frequencies listed in Table 2, which present a good agreement with the numerical values.

The modal loss factor distribution, represented in Figure 11, provides the relationship between the temperature and the treatment configuration efficiency.

Globally, it can be observed that the treatment configurations based on the 3M ISD112 material, S1, M1 and M2, present an efficiency peak near the transition temperature of the viscoelastic material. On the other hand, the single-layer treatment made of 3M ISD110 viscoelastic material, is particularly efficient at higher temperatures, showing an efficiency peak at 70÷80°C. As predicted, the multi-material configurations can be regarded as a transition configuration,

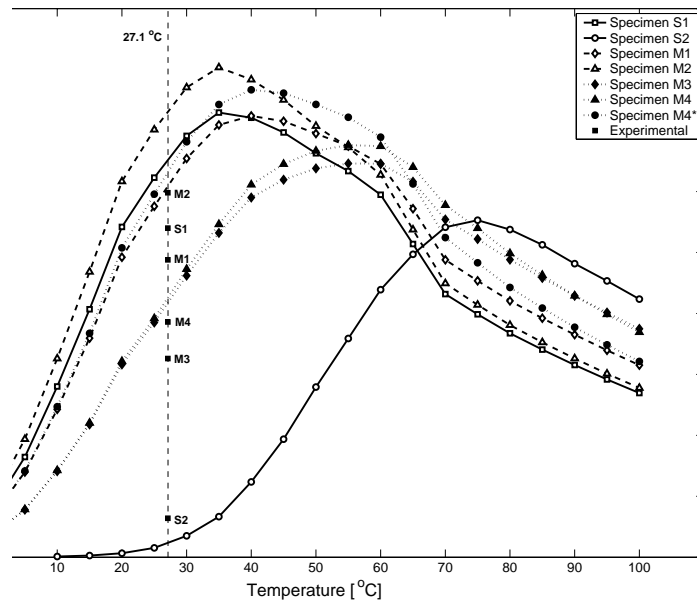


Figure 11: Modal loss factor distribution

showing an efficiency peak in the middle of the transition temperatures of both viscoelastic materials.

When comparing the multi-layer configuration M1 to the multi-material configuration M3, obtained by replacing one of the 3M ISD112 layers by a 3M ISD110 layer, it is possible to observe that the efficiency increase at the high temperature range is accompanied by a reduction of the efficiency at the lower temperatures. Contrary, the M4* configuration, obtained by adding a 3M ISD110 viscoelastic layer into the middle of the M1 core, is able to enlarge the efficient range without an efficiency reduction at the low temperature range. From the results, it is also possible to verify that the sequence of the layering scheme along the dissipative core of the multi-material configuration is of major importance in the flexural stiffness of the treated structure. The treatment efficiency is also highly dependent upon the layering scheme due to its effect onto the shear deformation transmissibility from the outside plates to the dissipative layers.

5 CONCLUSIONS

The present study allowed to evaluate the feasibility of the application of the multi-layer concept into the integrated viscoelastic damping layer configuration.

The application of multiple viscoelastic layers, separated by stiff constraining layers, provide a potential solution to overcome the decoupling effect produced by the soft core of the integrated damping treatments. Moreover, adopting a multi-layer configuration, is possible to increase the shear deformation effect in the individual layers, increasing thus the treatment efficiency.

The multi-material configuration is also a promising solution to enlarge the efficiency range

of the viscoelastic treatments by applying several layers made of viscoelastic materials with different transition temperatures. Nevertheless, the layering sequence of the layers dictates, not only the treatment efficiency but also the stiffness coupling capability developed by the damping core and the deformation pattern inside the sandwich structure.

6 ACKNOWLEDGMENT

The authors gratefully acknowledge 3M Company for providing the viscoelastic materials used in this work.

REFERENCES

- [1] D.I.G. Jones, Design of constrained layer treatments for broad temperature damping, *Shock & Vibration Bulletin*, **5** (44): 1-12, 1974.
- [2] D.I.G. Jones, Damping of stiffened plates by multiple layer treatments, *J. Sound Vib.*, **35**(3): 417-427, 1974.
- [3] 3M, *ScotchDamp TM vibration control systems*, 3M Industrial Specialties division, St. Paul, MN, USA, 1993.
- [4] R. Moreira and J.D. Rodrigues, Constrained damping layer treatments: Finite element modeling, *J. Vib. Control*, **10**(4): 575-595, 2004.
- [5] R.A.S. Moreira, J.D.Rodrigues and A.J.M. Ferreira, A generalized layerwise finite element for multi-layer damping treatments, *Computational Mechanics*, **37** (5): 426-444, 2005.
- [6] R.A.S. Moreira and J.D.Rodrigues, A layerwise model for thin soft core sandwich plates, *Computers and Structures* **84** (19-20): 1256-1263, 2006.
- [7] R.A. Silva Moreira and J.Dias Rodrigues, The modelisation of constrained damping layer treatment using the finite element method: spatial model and viscoelastic behavior, *Proceedings of International Conference on Structural Dynamics Modelling - Test, Analysis, Correlation and Validation*, 287-296 (Paper No 30). Madeira, Portugal, 3-5 June 2002.
- [8] C.D. Johnson and D.A. Kienholz, Finite element prediction of damping in structures with constrained viscoelastic layers, *AIAA J.*, **20** (9): 1284-1290, 1982.
- [9] R.A.S. Moreira, *Modelação e análise de tratamentos viscoelásticos multi-camada para controlo passivo de vibrações*, PhD thesis (in portuguese), Faculdade de Engenharia da Universidade do Porto (2004).
- [10] Vasques, C.M.A., Moreira, R.A.S. and Dias Rodrigues, J., Viscoelastic damping: mathematical modeling and finite element implementation, *In Proceedings of the International Conference on Engineering Dynamics*, Carvoeiro, Portugal, 16-18 April 2007.

PREDICTIVE MODELLING OF THE IMPACT RESPONSE OF THERMOPLASTIC COMPOSITE SANDWICH STRUCTURES

Richard Brooks, Kevin A. Brown, Nicholas A. Warrior and Palanivel P. Kulandaivel

School of Mechanical, Materials and Manufacturing Engineering
University of Nottingham
University Park, Nottingham NG7 2RD, UK
e-mail: richard.brooks@nottingham.ac.uk

Key words: Sandwich Structures; Thermoplastic Composite; Impact Loading; Finite Element Analysis; Damage Mechanisms; Failure

Summary. *This paper reports on work aimed at developing a practical methodology for the predictive modelling of the performance of thermoplastic composite sandwich structures under impact loading. Explicit finite element analysis methods, using LS-DYNA™ software, are described including materials characterisation and material model calibration for the skin and core and validation of deformation response, damage and failure of the sandwich structures. The verified finite element model has been applied to the predictive structural analysis of a full-scale composite sandwich component. Simulations agree well with experimental results.*

1 INTRODUCTION

Today, both motorist and governments are demanding that automotive manufacturers develop cars that offer improved fuel efficiency, greater safety for both occupants and pedestrians, and increased end of life recyclability. Likewise, in the rail industry, train manufacturers are seeking to develop lighter trains in order to minimise wear and tear on railway lines, and decrease maintenance. In response to these concerns, both the automotive and rail industry are showing increased interest in the application of thermoplastic composite (TPC) sandwich structures. TPC sandwich constructions with fibre reinforced thermoplastic face-sheets along with a foam core made from the same thermoplastic material offer several advantages. These include: high stiffness to weight ratio, high energy absorption, potential for high volume manufacture and recyclability. Furthermore, an all thermoplastic composite sandwich allows for greater design freedom as they can be thermoformed into complex shapes. Yet, despite the advantages that TPC sandwiches provide, their application in trains and motor vehicles remains limited due in part to the lack of appropriate design procedures and confidence in their use. Today, finite element techniques are preferred to other analytical methods for the analysis of complex structures [1]. However, finite element modeling of composite sandwich constructions poses several challenges due to their inhomogeneous construction and anisotropic material properties. In addition, complex failure modes exhibited by the sandwich constituent materials under various load conditions offer particularly difficult challenges for modelling.

This paper presents a finite element modeling methodology for predicting the behaviour of

TPC sandwich structures under indentation and bending impact loads. Methods for calibrating the material models and validating the structural response are presented. Finally, some preliminary results on the predictive modelling of a full scale demonstrator TPC sandwich component are outlined.

2 SPECIMEN MATERIAL AND MANUFACTURE

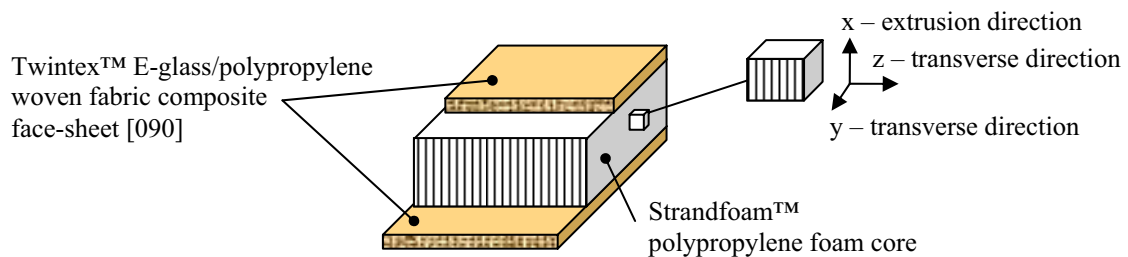


Figure 1: Thermoplastic composite sandwich structure.

The TPC sandwich structure under investigation was manufactured from 60 wt% 0/90 woven fabric commingled glass/polypropylene (Twintex™) face-sheets supplied by OCV Reinforcements. The core was an anisotropic crushable polypropylene foam (Strandfoam™) supplied by Dow Automotive. Strandfoam™ has a high energy absorption efficiency due to its extruded honeycomb like structure [2].

A schematic of the material configuration for the sandwich beam used in this study is shown in Figure 1. The Strandfoam™ extrusion direction is orientated along the thickness of the sandwich beam for maximum crush properties in the loading direction.

Sandwich panels of dimensions 800 mm x 70 mm were manufactured using an optimised one-step vacuum moulding process [3, 4]. A schematic of the process is shown in Figure 2. The vacuum moulding process involved the stacking of preconsolidated layers of Twintex™ (0.5 mm thick) on two aluminium transfer plates. The stacks of Twintex™ were preheated to 200 °C in a hot air oven. The first stack, along with the transfer plate is transferred to the vacuum table. The cold foam core is placed on the stack followed quickly by the second stack which is placed on top of the foam to complete the sandwich assembly. The vacuum membrane is then clamped over the sandwich and a vacuum is applied.

Sandwich beam specimens were cut from the moulded panels using a band saw. Beams were manufactured with two types of core thickness: 50 mm for indentation tests and 25 mm for bending tests. Beams with skin thicknesses of 1, 2 and 3 mm, were manufactured from 2, 4 and 6 layers of preconsolidated Twintex™, respectively.

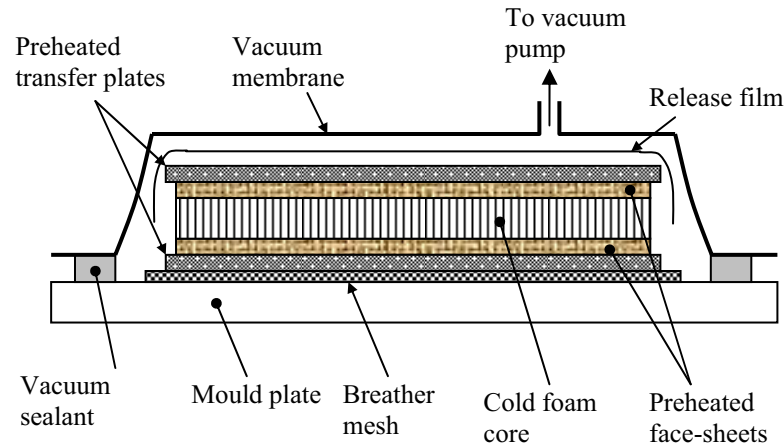


Figure 2: Schematic of the vacuum moulding process.

4 FINITE ELEMENT MODELLING METHODOLOGY

The main objective of this study is to develop a robust modelling methodology for predictive simulations of the behaviour of TPC sandwich structures under impact loading. The proposed methodology consists of: 1) material calibration, 2) material validation and 3) structural validation. A description of each phase is provided below

4.1 Calibration of material models

Composite face-sheet material model

The Twintex™ composite was modelled with the MAT 162 composite material model implemented in the LS-DYNA™ finite element explicit code [5]. MAT 162 is an elastic-damage model which is based on a continuum damage mechanics formulation. It is capable of simulating the various composite failure modes such as fibre fracture, matrix cracking (in-plane and out-of-plane) and delamination. The MAT 162 model has four damage parameters ($m_i \dots i=1, 2 \dots 4$) that are used to model the post-elastic damage response of the material under various loading conditions.

To-date, there are still no clearly defined methods for calibrating the post-elastic damage behaviour of composites [6]. In this study, an inverse modelling technique was developed for calibrating the MAT 162 damage parameters m_i [7]. In this procedure, the damage parameters were systematically obtained by correlating simulations with the static and dynamic coupon stress-strain tests results (tensile, shear and compression). The damage parameters were adjusted, iteratively, over several simulation runs until satisfactory correlation was obtained. An extensive experimental material characterisation program that covered a wide range of static and high strain rate (up to 126 s^{-1}) coupon tests was conducted to support the material model calibration process [7].

Figure 3 shows the calibration results for the static tests. In particular, a novel bi-linear procedure for calibrating the non-linear in-plane shear stress-strain response was developed. The dynamic calibration results are shown in Figure 4. A distinct strain rate effect was identified for the Twintex™ face-sheet laminates during dynamic testing, for both normal and shear loading [7]. Variations in the elastic and strength properties with strain rate are included in MAT 162 through simple logarithmic based functions [5]. Parameters for the strain rate equations were derived from the dynamic test data [7].

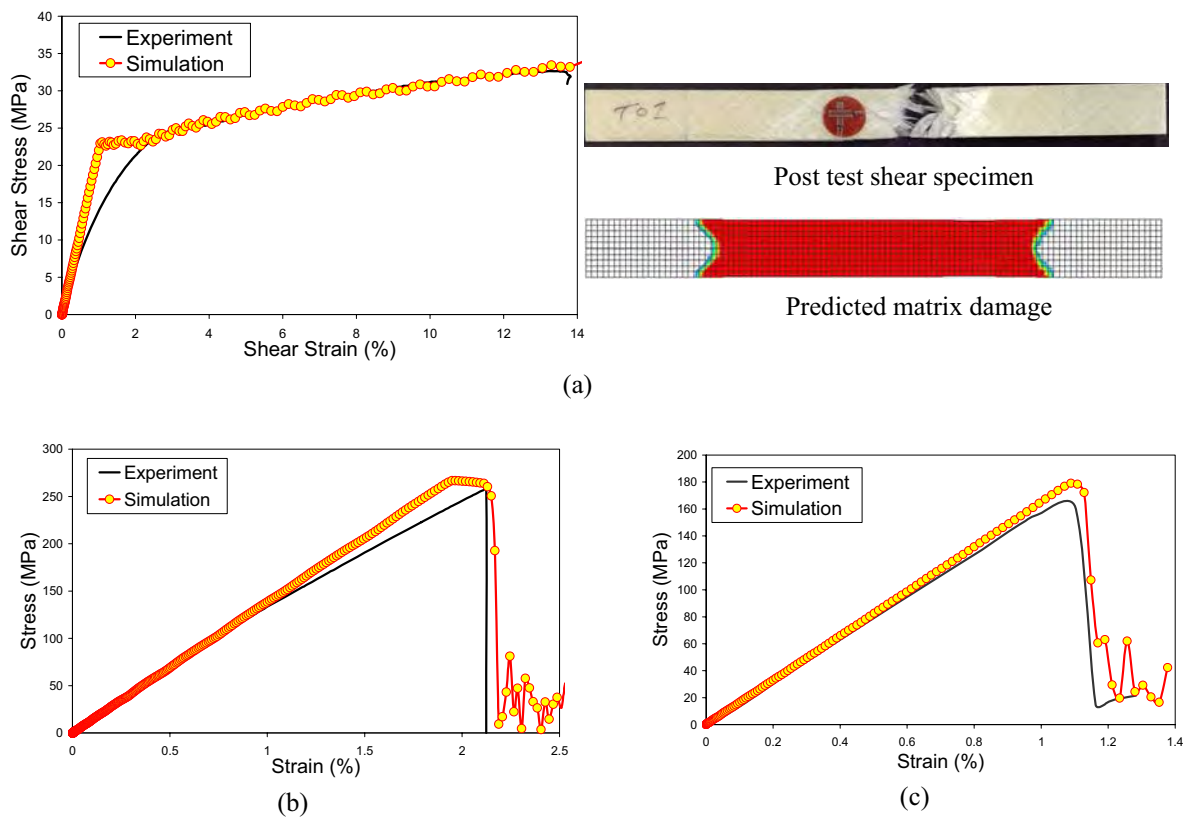


Figure 3: Quasi-static calibration of MAT 162 damage parameters (a) shear (b) tension (c) compression.

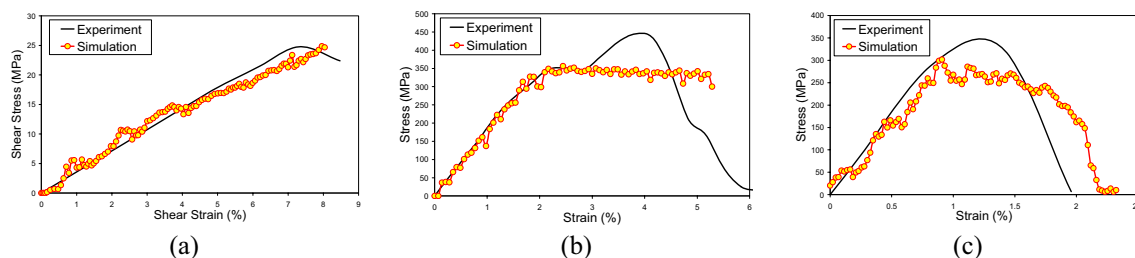


Figure 4: Dynamic calibration of MAT 162 damage parameters (a) shear (strain rate = 91 s^{-1}) (b) tension (strain rate = 70 s^{-1}) (c) compression (strain rate = 126 s^{-1}).

The calibrated material model for the face sheet material was validated by simulating a series of static and dynamic three-point bending and falling dart plate impact tests using the values for the model parameters identified in the calibration procedure. [7].

Figure 5 (a) shows a comparison of the force-displacement curves for the static three-point bending test and simulation results. The curve for the simulation with the calibrated parameters does not correlate well with the test curve. This discrepancy is partly explained by the assumption in the MAT 162 model that the post-elastic damage response under tensile and compressive loading is identical. The model does not allow for the input of different values for the damage parameters for the two modes of loading. This is clearly an over simplification for composites under bending loads where the specimen experiences complex mixed-mode stress fields. The model was subsequently refined with the elastic modulus and damage parameters recalibrated until the correlation improved significantly as depicted by the ‘refined model’ curve in Figure 5 (a). Figure 5 (b) shows that there is also good qualitative agreement between the predicted damage modes for the ‘refined model’ and the experimental observations.

Due to the limitation of MAT 162 as discussed above, the dynamic three-point bending and falling dart plate impact test simulations were conducted with two different sets of values for the damage parameters. The curves in Figure 6 (a) and Figure 7 (a) are labelled as ‘tensile parameters’ and ‘compression parameters’ respectively. For the dynamic three-point bending test the ‘compression parameters’ provided better correlation with the experimental curve which suggests that compression failure is more dominant during dynamic bending as depicted in Figure 6 (a). A comparison of the predicted and experimental damage for the dynamic bending test is shown in Figure 6 (b).

The dart plate impact tests and simulations were conducted at incident energies of 30, 35 and 40 J [7]. Figure 7 (a) shows a comparison of the force-time history curves for the 35 J impact simulation and test. By contrast with the three-point bending simulations, the curve with the ‘tensile parameters’ simulation provided the better correlation with the test curve in this case. This may be a reflection of the clamped boundary conditions for the plate impact which results in membrane tensile stress in the system. The qualitative comparison of predicted delamination damage in the mid-ply to the experimental thermograph image, both of the same scale, shows reasonable agreement as shown in Figure 7 (b).

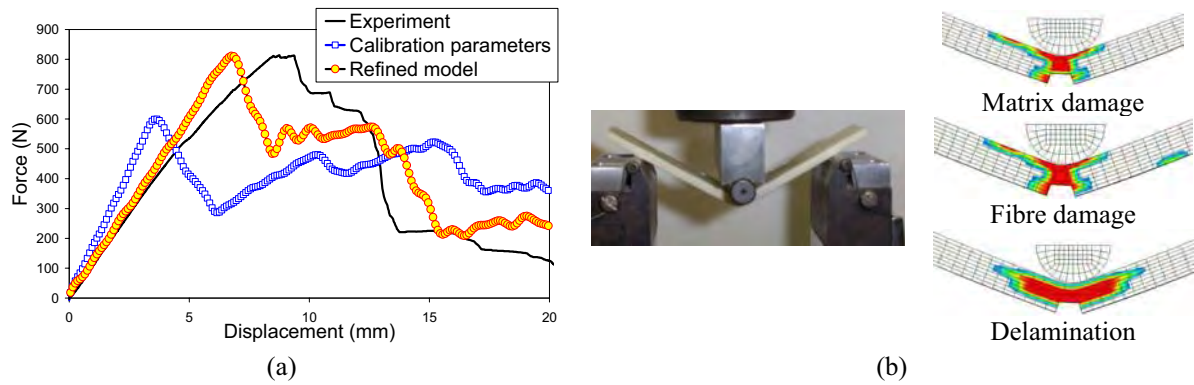


Figure 5: Comparison of quasi-static three-point bending predicted and experimental results.

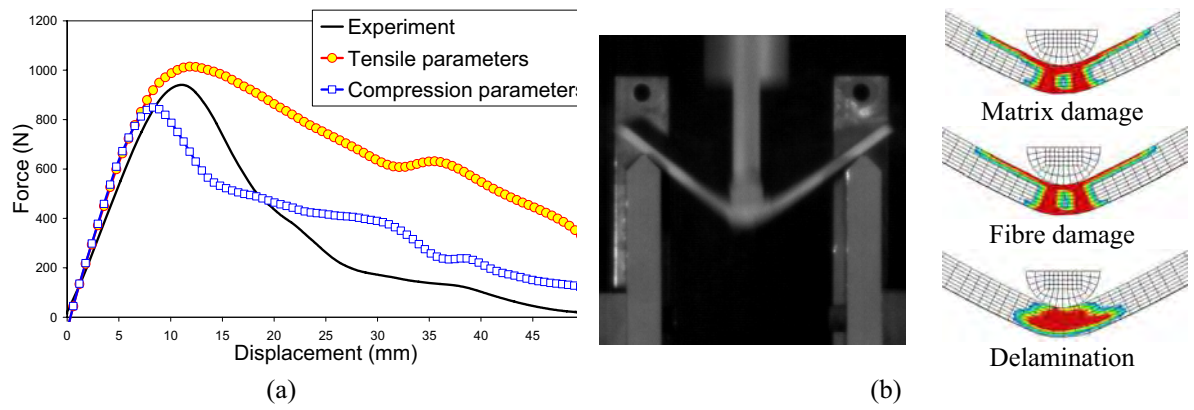


Figure 6: Comparison of dynamic three-point bending predicted and experimental results for a 319 J impact.

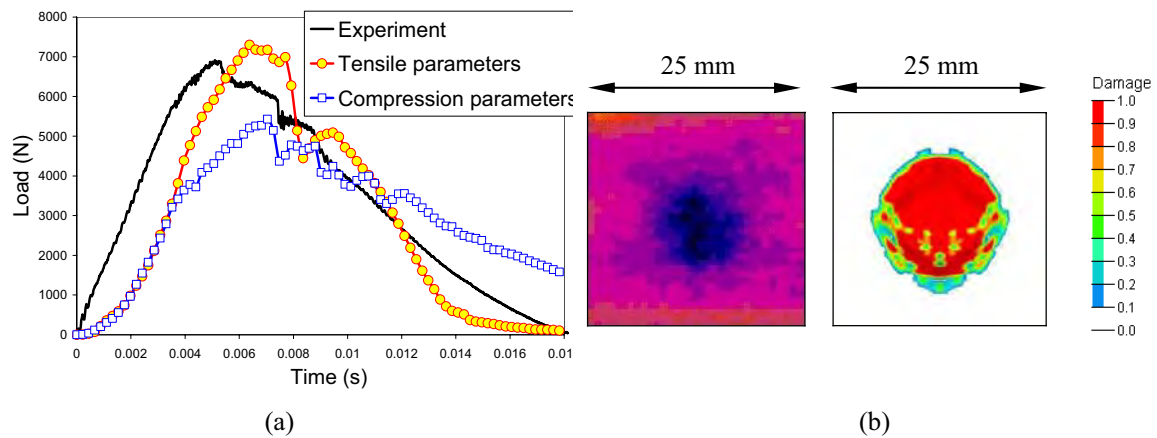


Figure 7: Comparison of dynamic falling dart plate impact predicted and experimental results for a 35 J impact.

Foam core material model

The Strandfoam™ core was modelled with the MAT 142 material model implemented in LS-DYNA™ [5]. MAT 142 is a transversely anisotropic elasto-plastic material model. Failure is based on a modified Tsai-Wu yield surface that hardens or softens as a function of volumetric strain. The growth of the yield surface is directional and follows the growth of the material yield stress along the material axes.

Compression, shear and tensile coupon tests were conducted at quasi-static and dynamic loading rates (Figure 8). The MAT 142 model requires the direct input of the stress-strain curves for normal and shear loads in a tabulated format.

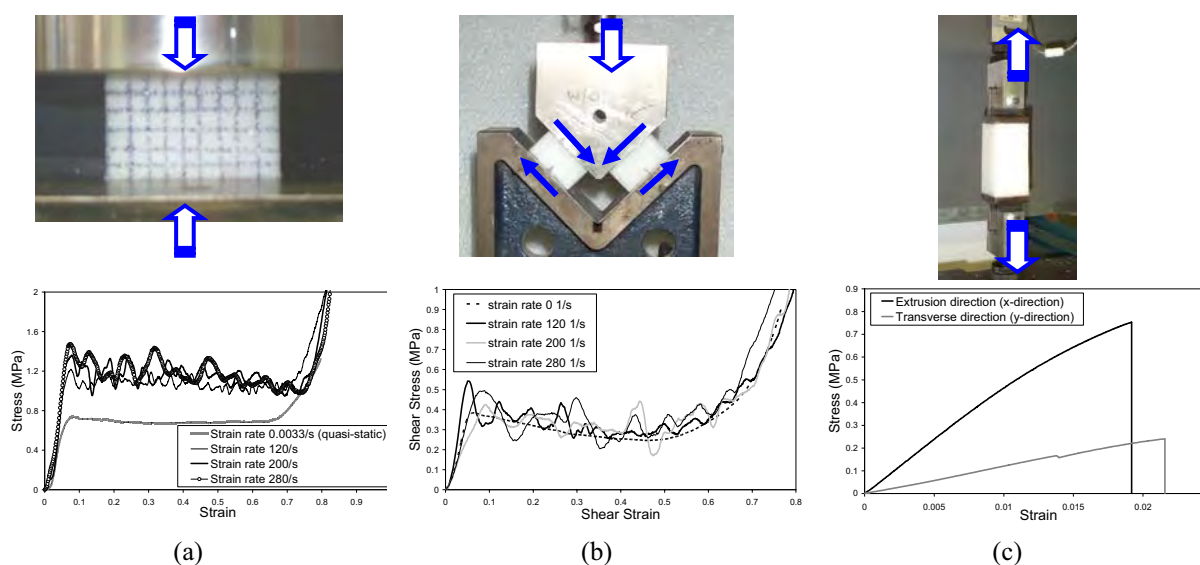


Figure 8: Characterisation of Strandfoam™ (a) compression (b) shear x-y plane (c) tension.

4.3 Validation: coupon sandwich modelling

Following the calibration and validation of the material models for the sandwich face-sheets and core as described in the previous section, simulation of indentation and three-point bending of sandwich structures were performed to further validate the modelling procedure.

Indentation loading of TPC sandwich beams

Quasi-static and dynamic indentation tests were conducted on TPC sandwich beam specimens. The specimens were 250 mm long with a width of 30 mm and nominal core thickness of 50 mm. Sandwich beams with three different skin thicknesses were investigated, (1, 2 and 3 mm). All sandwich beam skins had a [090] fibre orientation aligned along the beam longitudinal axis. The foam was assembled between the skins such that the Strandfoam™ extrusion direction was aligned with the impact direction, i.e. vertical.

Static indentation tests were conducted on a Tinius Olsen electromechanical test machine at a crosshead speed of 5 mm/min. The beams were placed on a flat support plate and indented with a 25 mm diameter cylinder across the whole width of the beam cross-section.

Dynamic indentation tests were conducted in an instrumented falling weight tower with an 8.2 kg impactor at a impact speed of 2 m/s corresponding to an energy level of 15 J.

For simulation, only one-half of the sandwich beam was modelled because of the geometric and material symmetry. Single integration point solid elements are used to model the sandwich face-sheets and core. The calibrated and validated material models described above are also used.

For the quasi-static indentation tests, three distinct regions of deformation were observed. The initial response is linear elastic followed by non-linear yielding. This non-linear behaviour is induced by progressive localised core crush under the cylindrical impactor along with membrane stretching of the top skin. As the impactor moves down into the specimen, the ends of the sandwich are also pulled up. Finally, there is a sharp load increase as foam densification occurs. Minor fibre fracture, matrix cracks and delamination were observed in the top face-sheets. For brevity, only the experimental and simulation results for the 2 mm face-sheet beams are presented here. The simulation force-displacement curves and predicted damage showed good agreement with quasi-static experimental observations as depicted in Figure 9 (a).

The dynamic force-displacement curves are similar to the static case. However, the impactor rebounds before foam densification occurs. The dynamic simulation results shown in Figure 9 (b) are also in good agreement with the experimental results.

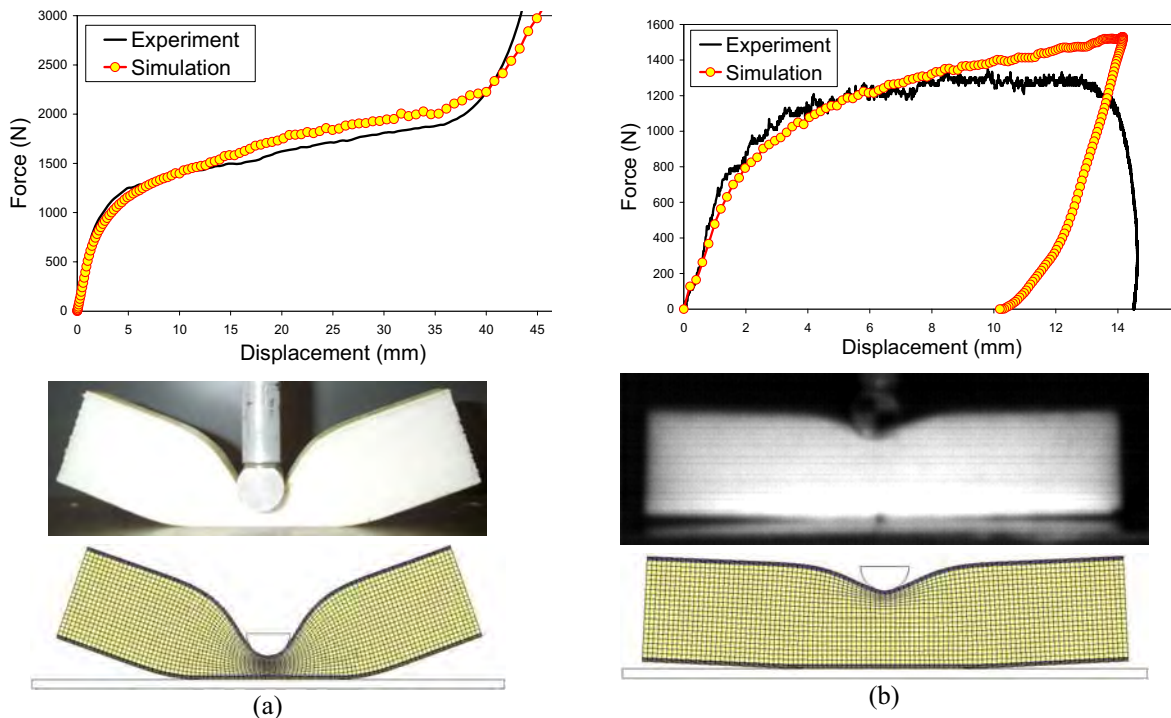


Figure 9: Comparison of the experimental and simulation force-displacement and failure mode results for the (a) quasi-static and (b) dynamic indentation tests for the 2 mm face-sheet TPC sandwich beams.

Three-point bending of TPC sandwich beam

Quasi-static and dynamic three-point bending tests were also used to validate the calibrated material models [8]. The quasi-static tests were conducted in a Tinius Olsen electromechanical test machine at a crosshead speed of 10 mm/min. A 25 mm diameter cylindrical impactor is used to apply a load to the centre of the beam. The bending specimens were 250 mm long with a width of 30 mm and nominal core thickness of 25 mm. They were simply supported over a span of 200 mm on 10 mm diameter cylindrical steel supports. Sandwich beams with three different skin thicknesses were investigated, 1, 2 and 3 mm [7].

For simulation, as with the indentation model, only one-half of the sandwich beam is modelled. Single integration point solid elements are used for all components. The cylindrical impactor and supports were modelled as rigid bodies.

Fracture in the foam was modelled through a maximum principal strain fracture criterion combined with element erosion. Elements are eroded when the maximum principal strain reaches a specified value:

$$\varepsilon_1 \geq \varepsilon_p \rightarrow \text{element erosion} \quad (1)$$

where ε_1 is the maximum principal strain and ε_p is the maximum principal strain at failure.

This fracture criterion was also used to model failure at the sandwich beam skin-core interface. The maximum principal strain, ε_p , was numerically calibrated using an iterative procedure where values for ε_p were determined by correlation of simulations with experimental force-displacement and failure mode results.

Only the experimental and simulation results for the 2 mm face-sheet beams are discussed below. Figure 10 (a), shows a comparison of the simulation and experimental force-displacement results for the 2 mm skin sandwich beam under quasi-static loading. The beam response is linear elastic, followed by non-linear yielding up to a maximum load, after which an abrupt load drop occurs due to core shear fracture. The predicted response up to the point of failure agrees well with the experimental results as depicted in Figure 10 (a). However, the predicted post-failure response deviates from the experimental curve as element erosion results in sharp, large load oscillations up to a displacement of 18 mm after which the load drops to zero. The asymmetric core shear fracture and skin core debonding observed in the actual test has been well predicted by the simulation as shown in Figure 10 (a)

Figure 10 (b) shows a comparison of the simulation and experimental force-displacement results for the 2 mm skin sandwich beam under dynamic loading. The predicted force-time history shows good agreement with the general shape of the experimental response. The predicted initial peak load shows excellent agreement with the experimental results. However, the second peak load is over estimated by 20% and leads the experimental second peak load by 0.42 ms. The primary failure modes were symmetric core shear fracture and skin-core debonding which have been well predicted by the corresponding simulation.

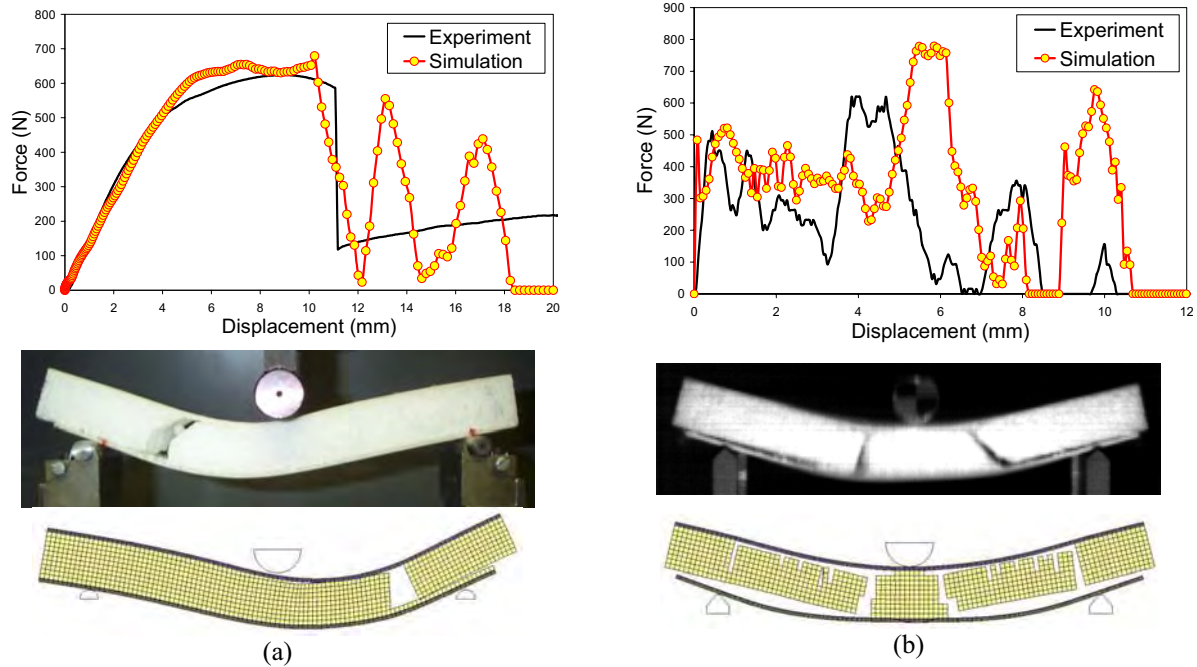


Figure 10: Comparison of the experimental and simulation force-displacement and failure mode results for the (a) quasi-static and (b) dynamic three-point bending tests for the 2 mm face-sheet TPC sandwich beams.

4.4 Structural validation sandwich modelling

Following the successful calibration and validation of the coupon level sandwich models, initial predictive analysis has been carried out on a novel complex shaped structural thermoplastic composite sandwich mounting beam for a metro train bogie designed to replace a conventional metal/wood-based design. A finite element model of the mounting beam, shown in Figure 11, is based on the previously described material models for the sandwich face sheets and core materials. The finite element model was used to analysis the structural performance of the sandwich beam under proof loads imparting both torsion and bending on the beam. For these preliminary simulations, predicted results showed good agreement with test data in terms of both stress levels and structure deflections. Impact analyses are a subject of continuing work. The validated model was used to optimise the design of the demonstrator component without the need for costly prototyping and testing.

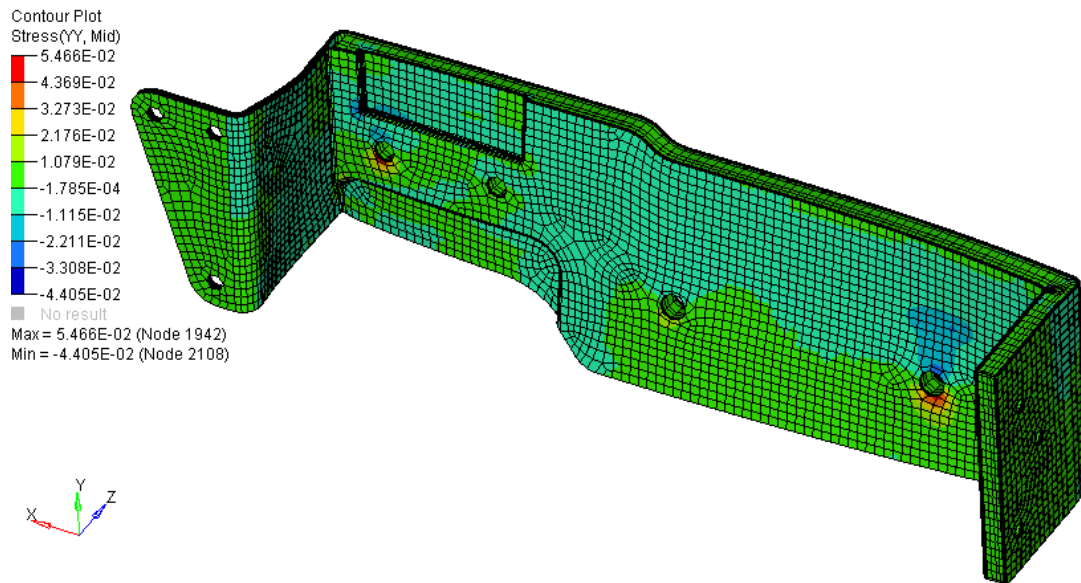


Figure 11: Predicted stress distribution in the TPC sandwich mounting beam under proof loading (stress in GPa).

5 CONCLUSIONS

A practical modelling methodology involving the use of an advanced composite material model and associated material characterisation tests has been developed for impact loading of sandwich structures manufactured using a vacuum moulding process. The thermoplastic composite face-sheets were modelled with the advanced LS-DYNA™ MAT 162 composite material model. The values for the damage parameters required in MAT 162 were obtained through an inverse modelling procedure involving the correlation of simulations with a series of static and dynamic coupon tests including shear, tension and compression. The calibrated material model was validated using coupon three-point bending and dynamic falling weight dart impact tests. It was shown that a limitation of the MAT 162 model was the coupling of the tensile and compressive damage parameters which led to the need for minor recalibration during the validation phase.

The quasi-static and dynamic response for a sandwich beam under indentation loading was well predicted by the finite element model.

For quasi-static bending of the beams, good agreement for both load-displacement and failure was achieved between simulations and experimental results. For dynamic bending, the elastic response, initial peak loads and the occurrence of core shear fracture and skin-core debonding were also simulated well. However, under the dynamic loading rates, the more complex post initial failure response involving beam vibration and multiple load peaks was more difficult to accurately simulate.

The validated sandwich model has been successfully applied to the structural analysis of a full-scale demonstrator component.

The work presented in this study improves the confidence in using predictive finite element techniques for modelling the performance of composite sandwich structures under static and dynamic loading. Predictive analysis contributes to the safe and efficient design of composite sandwich components without the need for costly test programs and by providing more in-depth understanding of the mechanical response of these sandwich constructions. Additionally, this work has shown the potential suitability of TPC sandwich structures for application in advanced transportation related technologies.

ACKNOWLEDGEMENTS

The authors would like to acknowledge the support of OCV Reinforcements and Dow Automotive for supply of materials and of Security Composites Ltd for design support and manufacture of the demonstrator component. This work has been funded by the UK Engineering and Physical Sciences Research Council (EPSRC) through the Nottingham Innovative Manufacturing Research Centre (NIMRC).

REFERENCES

1. Zenkert, D., *The Handbook of Sandwich Construction*. 1997, London: Engineering Material Advisory Services (EMAS).
2. Burr, S.T. and G.D. Vogel, *Material Model Development for Impact Analysis of Oriented Polypropylene Foam Structures*. SAE Paper No. 2001-01-0310, 2001.
3. Kulandaivel, P., *Manufacturing and Performance of Thermoplastic Composite Sandwich Structures*, in *PhD Thesis*. 2006, The University of Nottingham: Nottingham.
4. Brooks, R., P. Kulandaivel, and C.D. Rudd. *Vacuum Moulding of Thermoplastic Composite Sandwich*. in *Proceeding of the 25th Jubilee International SAMPE European Conference*. 2004. Paris, France: SAMPE Europe.
5. Hallquist, J.O., *LS-DYNA Keyword User's Manual Version 971*. 2007, Livermore: Livermore Software Technology Corporation.
6. Xiao, J.R., B.A. Gama, and J.J.W. Gillespie, *Progressive damage and delamination in plain weave S-2 glass/SC-15 composites under quasi-static punch-shear loading*. *Composite Structures*, 2007. 78(2): p. 182.
7. Brown, K., *Finite Element Modelling of the Static and Dynamic Impact Behaviour of Thermoplastic Composite Sandwich Structures*. PhD Thesis. 2007, University of Nottingham.
8. Brown, K., R. Brooks, N.A. Warrior, and P. Kulandaivel. *Modelling the Impact Behaviour of Thermoplastic Composite Sandwich Structures*. in *Proceedings of ICCM-16*. 2007. Kyoto, Japan.

AN ENHANCED LAYERWISE FINITE ELEMENT USING A ROBUST SOLID-SHELL FORMULATION APPROACH

R.A.S. Moreira^{*}, R.A. Fontes Valente^{*} and R.J. Alves de Sousa^{*}

^{*} Departamento de Engenharia Mecânica

Universidade de Aveiro

Campo Universitário de Santiago, 3810-193 Aveiro, Portugal

e-mail: {[@ua.pt](mailto:rmoreira,robertt,rsousa)}

web page: <http://www.mec.ua.pt>

Keywords: sandwich structures, enhanced assumed strain, solid-shell, multilayer model, layerwise

Abstract: The application of layerwise theories to correctly model the displacement field of sandwich structures or laminates with high modulus ratios, usually employs plate or facet-shell finite element formulations to compute the element stiffness and mass matrices for each layer. In this work, a different approach is proposed, using a high performance hexahedral finite element to represent the individual layer mass and stiffness. This 8-node hexahedral finite element is formulated based on the application of the enhanced assumed strain method (EAS) to resolve several locking pathologies coming from the high aspect ratios of the finite element and the usual incompressibility condition of the core materials. The solid-shell finite element formulation is introduced in the layerwise theory through the definition of a projection operator, which is based on the finite element variables transformation matrix.

The new finite element is tested and the implemented numerical remedies are verified. The results for a soft core sandwich plate are hereby presented to demonstrate the proposed finite element applicability and robustness.

1. Introduction

Sandwich structures with soft cores, like those achieved when inserting thin viscoelastic layers or foams between two stiff skin plates for damping purposes [1], are usually

complicated to simulate due to the difficulties related to the spatial model of the layered assembly, which must be able to accurately represent the high shear pattern of the core and, thus, the related damping mechanism.

The usual approach, by means of a layered assembly of plate and solid finite elements with nodal linkage or rigid link elements [2-4], can lead to a hardworking and time consuming spatial modelling task, particularly to model three-dimensional shell-type structures. Moreover, the application of this layered approach to multiple layer sandwich plates, using several viscoelastic layers, is difficult and any reconfiguration of the treatment requires the modification of the entire finite element mesh, which is not a straight-forward methodology during design and optimization simulation tasks [4].

To simplify such cumbersome modelling task, layerwise finite elements [5-7] become popular since they are simple and user-friendly, being easily applied to complex geometry configurations by means of standard shell mesh generators and, additionally, easily tailored to different layering schemes, as this information is externally defined and directly used by the layerwise finite element during elemental matrix computation. The layerwise formulation is able to replicate the out-of-plane displacement field from the tabulated intrinsic element parameters and the bi-dimensional geometry, while maintaining the simplicity of its usage by the end-user.

To compute the element matrices, plate-based or facet-shell formulations are usually applied [6], where plane stress conditions are considered at both layer and composite levels. Though this characteristic isn't usually a limitation to the analysis of thin single or multiple core viscoelastic damped sandwich structures [6,7], it can restrict the application of such finite elements when analysing thick soft core sandwiches [8] like those achieved with cores made of cork compound materials. For this purpose, proper finite elements with complete 3D strain and displacement fields shall be used, capable of handling through-thickness strain gradients during deformation.

Despite the spread use of shell and membrane elements to model thin structures in commercial codes, the interest in eight-node brick-type finite element formulations, based only in translation degrees-of-freedom, has been increasing over the last years [9,10]. Incorporating the kinematics of shell finite elements, although topologically equivalent to solid ones, these elements became known as "solid-shell" finite elements. Besides the simpler formulation, solid-shell elements can account for 3D material laws (contrary to plane stress-based shells), double sided contact conditions and, finally, a direct and exact evaluation of the thickness strain and stress fields.

Regardless the direct 3D kinematics representation, standard solid finite elements possess strong deficiencies in reproducing the behaviour of thin-shell structures, leading to locking phenomena. For 8-node elements entirely based on a displacement formulation, these numerical deficiencies are responsible for the complete deterioration of results, being commonly referred as transverse shear and volumetric locking effects. Amongst the approaches to overcome these problems, the simplest and earliest of all proposed was the use of reduced numerical integration procedures, where the numerical evaluation of strain and stiffness matrices is carried out in an approximated form. This procedure is equivalent to mixed formulations, usually introducing a higher level of flexibility into the formulation, and attenuating the locking otherwise present. However, this procedure can lead to spurious zero energy modes, thus requiring stabilization methods.

Other techniques were proposed to alleviate locking effects, the most successful of them being usually classified as mixed methods. For these formulations independent field assumptions for strains, stress and/or incompatible displacements can be assumed, and afterwards introduced into the corresponding functional. These methods point to procedures such as the Assumed Natural Strain (ANS) approach [11] and the Enhanced Assumed Strain (EAS) formulation [12]. The latter, the EAS method, uses a three field mixed functional in terms of displacements, stresses and an enhanced strain field, relying on the introduction of strain-based enhancing variables into the formulation. In its original form, the total strain field is built up as a direct summation of the (compatible) symmetric gradient of the displacement and the enhanced strain field. The enhancing strain field is not subjected to any inter-element continuity requirement, and can be related to an incompatible mode-based field.

In available solid-shell finite elements, enhanced assumed strain methods, assumed strain approaches and/or selective reduced integration procedures are usually combined to obtain robust formulations [10]. Departing from previous approaches, and to some extent following the works carried out for shell elements, a new class of solid-shell finite elements entirely based on the Enhanced Assumed Strain methodology was introduced in [17], for linear formulations, and extended to non-linear problems in [18]. The distinguish feature of the formulations is the solely use of EAS procedures to simultaneously deal with volumetric and transverse shear locking effects, besides improving the in-plane and mesh distortion sensitivity of the elements.

The main goal of the present work is to establish an innovative approach to layerwise formulations for composites structures, relying on the use of solid-shell finite elements enhanced with strain-based variables. Such EAS finite elements represents the best choice to develop a layerwise based sandwich finite element including through-thickness deformation

capability and 3D displacement field description, without the numerical drawbacks of using conventional 3D continuum finite elements.

2. Layerwise Approach

Assuming that the laminated structure can be divided into n homogeneous material layers, the displacement field for an individual layer can be described as:

$$\{\mathbf{u}\}_k = \begin{Bmatrix} u_k \\ v_k \\ w_k \end{Bmatrix} \quad k = 1, \dots, n \quad (1)$$

which can be derived from the global vector of generalized variables, $\{d\}$, from the relation:

$$\{\mathbf{u}\}_k = [\mathcal{N}]_k \{d\} \quad (2)$$

The matrix $[\mathcal{N}]_k$ is a piecewise interpolation function matrix, being dependent of the layer index.

In a similar way as the one applied in the usual plate-based layerwise models, this interpolation matrix defines the through-the-thickness displacement field. However, in this case this interpolation function is assumed to be directly described in the solid-shell finite element. Therefore, the finite element displacement field of the laminate can be mapped into several solid-shell variable vectors by using a transformation matrix, $[P]_k$, relating the two variable fields:

$$\{d\}_k^{H8} = [P]_k \{d\} \quad (3)$$

where $\{d\}_k^{H8}$ is the usual tri-linear hexahedral finite element variable vector for layer \mathbf{k} .

Using this transformation matrix, the laminate finite element stiffness and mass matrices, as well as the force vectors, can be defined by the projection of the corresponding solid finite element matrices, $[K]_k^{H8}$, $[M]_k^{H8}$, and vector, $\{f\}_k^{H8}$, as:

$$\begin{aligned} [K] &= [P]_k^T [K]_k^{H8} [P]_k \\ [M] &= [P]_k^T [M]_k^{H8} [P]_k \\ \{f\} &= [P]_k^T \{f\}_k^{H8} \end{aligned} \quad (4)$$

where $[K]_k^{H8}, [M]_k^{H8}, \{f\}_k^{H8}$ are computed by using a robust hexahedral finite element formulation, which will be presented in next section.

3. Solid-shell finite element formulation

The grounds of the Enhanced Assumed Strain method come from the classical work of Simo and Rifai [12]. The well known variational formulation inherent to the method, based on the three-field Veubeke-Hu-Washizu functional is here skipped for the sake of succinctness. The crucial point in EAS formulations is the enlargement of the displacement-related strain field, adding a new field of internal variables, the so-called enhancing parameters α .

Similarly to displacement field \mathbf{u} , which is interpolated in the finite element domain by the standard FEM strain-displacement \mathbf{B}_u matrix, the enhancing parameters field is interpolated by a \mathbf{B}_α matrix. At the element level, the enhancing strain field is added to the standard strain field in the form:

$$\tilde{\boldsymbol{\varepsilon}} = \boldsymbol{\varepsilon} + \boldsymbol{\varepsilon}_\alpha = \begin{bmatrix} \hat{\mathbf{B}}_u & \hat{\mathbf{B}}_\alpha \end{bmatrix} \begin{bmatrix} \mathbf{u} \\ \boldsymbol{\alpha} \end{bmatrix} = \tilde{\mathbf{B}} \tilde{\mathbf{u}} \quad (5)$$

being the strain field posed in vector form:

$$\tilde{\boldsymbol{\varepsilon}} = \left\{ \varepsilon_{xx} \quad \varepsilon_{yy} \quad \varepsilon_{zz} \quad \varepsilon_{xy} \quad \varepsilon_{xz} \quad \varepsilon_{yz} \right\}^T \quad (6)$$

The interpolation matrix for the enhancing counterpart is normally first defined in the convective frame (denoted with $\bar{\mathbf{■}}$). The transformation to the local reference frame (denoted with $\hat{\mathbf{■}}$) is performed in the standard form:

$$\hat{\mathbf{B}}_{\alpha\alpha} = \frac{|\mathbf{J}_0|}{|\mathbf{J}|} \mathbf{T}_0 \bar{\mathbf{B}}_\alpha \quad (7)$$

where $\bar{\mathbf{B}}_\alpha$ is defined with natural coordinates. The subscript “0” points to evaluations at the center of a standard element. \mathbf{T} is the second order transformation tensor relating the isoparametric space and the local reference frame at a given point (ξ, η, ζ) ,

$$\mathbf{T} = \begin{bmatrix} J_{11}^{-1}J_{11}^{-1} & J_{12}^{-1}J_{12}^{-1} & J_{13}^{-1}J_{13}^{-1} & J_{11}^{-1}J_{12}^{-1} & J_{11}^{-1}J_{13}^{-1} & J_{12}^{-1}J_{13}^{-1} \\ J_{21}^{-1}J_{21}^{-1} & J_{22}^{-1}J_{22}^{-1} & J_{23}^{-1}J_{23}^{-1} & J_{21}^{-1}J_{22}^{-1} & J_{21}^{-1}J_{23}^{-1} & J_{22}^{-1}J_{23}^{-1} \\ J_{31}^{-1}J_{31}^{-1} & J_{32}^{-1}J_{32}^{-1} & J_{33}^{-1}J_{33}^{-1} & J_{31}^{-1}J_{32}^{-1} & J_{31}^{-1}J_{33}^{-1} & J_{32}^{-1}J_{33}^{-1} \\ 2J_{11}^{-1}J_{21}^{-1} & 2J_{12}^{-1}J_{22}^{-1} & 2J_{13}^{-1}J_{23}^{-1} & (J_{11}^{-1}J_{22}^{-1}) + (J_{12}^{-1}J_{21}^{-1}) & (J_{11}^{-1}J_{23}^{-1}) + (J_{21}^{-1}J_{13}^{-1}) & (J_{12}^{-1}J_{23}^{-1}) + (J_{22}^{-1}J_{13}^{-1}) \\ 2J_{11}^{-1}J_{31}^{-1} & 2J_{12}^{-1}J_{32}^{-1} & 2J_{13}^{-1}J_{33}^{-1} & (J_{11}^{-1}J_{32}^{-1}) + (J_{12}^{-1}J_{31}^{-1}) & (J_{11}^{-1}J_{33}^{-1}) + (J_{31}^{-1}J_{13}^{-1}) & (J_{12}^{-1}J_{33}^{-1}) + (J_{32}^{-1}J_{13}^{-1}) \\ 2J_{21}^{-1}J_{31}^{-1} & 2J_{22}^{-1}J_{32}^{-1} & 2J_{23}^{-1}J_{33}^{-1} & (J_{21}^{-1}J_{32}^{-1}) + (J_{22}^{-1}J_{31}^{-1}) & (J_{21}^{-1}J_{33}^{-1}) + (J_{31}^{-1}J_{23}^{-1}) & (J_{22}^{-1}J_{33}^{-1}) + (J_{32}^{-1}J_{23}^{-1}) \end{bmatrix} \quad (8)$$

where J_{ij}^{-1} relates to the ij components of the inverse Jacobian matrix \mathbf{J}^{-1} ,

$$\mathbf{J}^{-1} = \begin{bmatrix} \frac{\partial \xi}{\partial x} & \frac{\partial \eta}{\partial x} & \frac{\partial \zeta}{\partial x} \\ \frac{\partial \xi}{\partial y} & \frac{\partial \eta}{\partial y} & \frac{\partial \zeta}{\partial y} \\ \frac{\partial \xi}{\partial z} & \frac{\partial \eta}{\partial z} & \frac{\partial \zeta}{\partial z} \end{bmatrix} \quad (9)$$

In the linear range, application of EAS method derives the following system of equations,

$$\begin{bmatrix} \hat{\mathbf{K}}^{uu} & \hat{\mathbf{K}}^{u\alpha} \\ \hat{\mathbf{K}}^{\alpha u} & \hat{\mathbf{K}}^{\alpha\alpha} \end{bmatrix} \begin{Bmatrix} \mathbf{u} \\ \boldsymbol{\alpha} \end{Bmatrix} = \begin{Bmatrix} \mathbf{f}^{ext} \\ \mathbf{0} \end{Bmatrix} \quad (10)$$

where each sub-matrix is defined in domain Ω like follows:

$$\begin{aligned}
 \hat{\mathbf{K}}^{uu} &= \int_{\Omega} \hat{\mathbf{B}}_u^T \mathbf{C} \hat{\mathbf{B}}_u \, d\Omega \\
 \hat{\mathbf{K}}^{u\alpha} &= \int_{\Omega} \hat{\mathbf{B}}_u^T \mathbf{C} \hat{\mathbf{B}}_{\alpha} \, d\Omega \\
 \hat{\mathbf{K}}^{\alpha u} &= \int_{\Omega} \hat{\mathbf{B}}_{\alpha}^T \mathbf{C} \hat{\mathbf{B}}_u \, d\Omega \quad , \\
 \hat{\mathbf{K}}^{\alpha\alpha} &= \int_{\Omega} \hat{\mathbf{B}}_{\alpha}^T \mathbf{C} \hat{\mathbf{B}}_{\alpha} \, d\Omega
 \end{aligned} \tag{11}$$

with \mathbf{C} as the constitutive tensor. From equation (6) and given its discontinuity between elements, it is possible to condense out the enhancing field α at the element level. This static condensation procedure lead to the displacement and enhanced-based equivalent stiffness matrix $\hat{\mathbf{K}}^{u+\alpha}$:

$$\hat{\mathbf{K}}^{u+\alpha} = \hat{\mathbf{K}}^{uu} - \hat{\mathbf{K}}^{u\alpha} (\hat{\mathbf{K}}^{\alpha\alpha})^{-1} \hat{\mathbf{K}}^{\alpha u} \tag{12}$$

Doing so, the unknown's vector $\tilde{\mathbf{u}}$ can be determined in a conventional manner,

$$\tilde{\mathbf{u}} = (\hat{\mathbf{K}}^{u+\alpha})^{-1} \mathbf{f}^{ext} \tag{13}$$

In the work of Alves de Sousa *et al.* [17], using the classical Gauss integration procedure with 8 integration points, several EAS brick elements were proposed. The mathematical ground to derive the formulations was based on a subspace analysis. The subspace analysis made possible the proper choice of the enhanced strain operator $\bar{\mathbf{B}}_{\alpha}$, requiring at the same time the minimum number of enhancing parameters to circumvent both volumetric and transverse shear locking effects.

In this work, the focus is given for the solid-shell HCiS12 solid-shell element. This element is defined by the following interpolation matrix for enhanced strain components, firstly defined in the convective frame:

$$\bar{\mathbf{B}}_{\alpha} = \bar{\mathbf{B}}_{12} = \begin{bmatrix} \frac{\partial N_{\alpha}}{\partial \xi} & 0 & 0 & \frac{\partial^2 N_{\alpha}}{\partial \xi \partial \eta} & \frac{\partial^2 N_{\alpha}}{\partial \xi \partial \zeta} & \frac{\partial^2 N_{\alpha}}{\partial \eta \partial \zeta} & 0 & 0 & 0 & 0 & 0 & 0 \\ 0 & \frac{\partial N_{\alpha}}{\partial \eta} & 0 & \frac{\partial^2 N_{\alpha}}{\partial \xi \partial \eta} & \frac{\partial^2 N_{\alpha}}{\partial \xi \partial \zeta} & \frac{\partial^2 N_{\alpha}}{\partial \eta \partial \zeta} & 0 & 0 & 0 & 0 & 0 & 0 \\ 0 & 0 & \frac{\partial N_{\alpha}}{\partial \zeta} & \frac{\partial^2 N_{\alpha}}{\partial \xi \partial \eta} & \frac{\partial^2 N_{\alpha}}{\partial \xi \partial \zeta} & \frac{\partial^2 N_{\alpha}}{\partial \eta \partial \zeta} & 0 & 0 & 0 & 0 & 0 & 0 \\ 0 & 0 & 0 & 0 & 0 & 0 & 0 & 0 & 0 & 0 & 0 & 0 \\ 0 & 0 & 0 & 0 & 0 & 0 & \frac{\partial N_{\alpha}}{\partial \xi} & \frac{\partial N_{\alpha}}{\partial \eta} & \frac{\partial^2 N_{\alpha}}{\partial \xi \partial \eta} & 0 & 0 & 0 \\ 0 & 0 & 0 & 0 & 0 & 0 & 0 & 0 & 0 & \frac{\partial N_{\alpha}}{\partial \xi} & \frac{\partial N_{\alpha}}{\partial \eta} & \frac{\partial^2 N_{\alpha}}{\partial \xi \partial \eta} \end{bmatrix} \quad (14)$$

using the compatible shape function:

$$N_{\alpha} = \frac{1}{2}(1-\xi^2)(1-\eta^2)(1-\zeta^2) \quad (15)$$

The formulation is characterized by excellent performance in a wide range of applications concerning shell-type structures as stated in references [17] and [18], avoiding both volumetric and transverse shear locking phenomena.

4. Numerical Tests

The example hereby applied to verify the finite element formulation is based on the dynamic analysis of a sandwich plate with thin aluminum skins and a soft core with a high modulus ratio. Both thin and thick sandwich conditions are applied and two different Poisson ratios for the core material are also introduced in this example. The sandwich plate is considered to be clamped in one of its smallest sides and totally free at the remaining ones.

The results obtained with the present finite element model (layw8) are compared with those obtained using a layered model approach with solid brick finite elements (Model 3H). More details on these layered approaches can be found in [4]. Additionally the results obtained by using a facet-plate layerwise finite element [6] are also presented.

The plate was modeled by an 18x12 finite element mesh and, when using model 3H, 3 layers of hexa8 finite elements were applied through the thickness, one for each material layer. Similarly, 3 layers are used for the layerwise models. This through-thickness coarse spatial modeling, which does not introduce an important error in the interesting natural modes,

intends to avoid the large set of deformation mode shapes of the core that is obtained when it is represented by an higher number of solid layers in the model 3H or numerical layers in the layerwise models.

Table1 - Geometry parameters and material properties of Example 1

Geometry		
Length	a	300 mm
Width	b	200 mm
Thickness	h_1	1 mm
	h_2	40 mm / 2 mm
	h_3	1 mm
Material properties		
• Skins - <i>Aluminum</i>		
Young modulus	$E_{1,3}$	$72 \times 10^9 Pa$
Poisson ratio	$\nu_{1,3}$	0.32
Density	$\rho_{1,3}$	$2710 Kg/m^3$
• Core - hypothetical soft foam		
Young modulus	E_2	$2 \times 10^3 Pa$
Poisson ratio	ν_2	0.25/0.49
Density	ρ_2	$1140 Kg/m^3$
Boundary conditions		C-F-F-F

C: clamped / F: free

The computed natural frequencies are listed on tables 2-3, where F_i and T_i stand for flexural mode of order i and torsion mode of order i , respectively.

Table 2 - Natural frequencies of sandwich plate with soft core – Thick core (40mm) [Hz]

Mode	compressible core $\nu_2 = 0.25$			incompressible core $\nu_2 = 0.49$		
	Model 3H	layw4m	layw8	Model 3H	layw4m	layw8
F1	3.25	3.26	3.26	3.23	3.24	3.24
T1	10.62	10.70	10.70	10.58	10.66	10.66
F2	19.50	19.67	19.66	19.47	19.64	19.64
T2	35.13	35.64	35.23	35.10	35.61	35.60

Table 3 - Natural frequencies of sandwich plate with soft core – Thin core (2mm) [Hz]

Mode	compressible core $\nu_2 = 0.25$			incompressible core $\nu_2 = 0.49$		
	Model 3H	layw4m	layw8	Model 3H	layw4m	layw8
F1	8.07	8.08	8.08	8.06	8.07	8.07
T1	26.77	26.96	26.97	26.74	26.95	26.96
F2	49.88	50.07	50.03	49.87	50.06	50.06
T2	90.20	91.12	91.45	90.19	91.12	91.44

The results for the layered model (model 3H) were obtained using a selective integration robust finite element (Nastran hexa8 finite element [19]), which provides a valuable reference to verify the efficiency of the implemented finite element.

5. Conclusion

The proposed finite element provides a valuable tool for the simulation of laminates and sandwich structures. This finite element combines the flexibility of modeling, characterizing the layerwise models, with the robustness, accuracy and full-field description provided by the solid-shell finite element based on the EAS concept. The obtained results indicate that this novel modeling approach is a promising alternative for the layered models that are currently applied when full three-dimensional strain and stress field representation is required.

6. References

- [1] Jones DIG (2001) Handbook of viscoelastic vibration damping, John Wiley & Sons.
- [2] Johnson CD, Kienholz DA (1982) Finite element prediction of damping in structures with constrained viscoelastic layers. AIAA J 20:1284-1290
- [3] Killian JW, Lu YP (1984) A finite element modelling approximation for damping material used in constrained damped structures. J Sound Vib 97:352-354
- [4] Moreira RAS, Rodrigues JD (2004) Constrained damping layer treatments: finite element modelling. J Vib Control 10:575-595
- [5] Suzuki K, Kageyama K, Kimpara I, Hotta S, Ozawa T, Kabashima S, Ozaki T (2003) Vibration and damping prediction of laminates with constrained viscoelastic layers – numerical analysis by a multilayer higher-order-deformable finite element and experimental observations. Mech Adv Mat Struct 10:43–75

- [6] Moreira RAS, Rodrigues JD, Ferreira AJM (2006) A generalized layerwise finite element for multi-layer damping treatments. *Comp Mech*, 37:426-444
- [7] Moreira RAS, Rodrigues JD (2006) A layerwise model for thin soft core sandwich plates. *Computers and Structures*, 84:1256-1263
- [8] Moreira RAS, Rodrigues JD (2006) A plate finite element with through-thickness stiffness for sandwich structures modelling. *COMPTEST2006*, Portugal
- [9] Vu-Quoc L, Tan XG (2003) Optimal solid shells for non-linear analysis of multilayer composites. Part I: Statics, *Comput. Meth. Appl. Mech. Eng.* 192:975-1016
- [10] Harnau M, Schweizerhof K (2006) Artificial kinematics and simple stabilization of solid-shell elements occurring in highly constrained situations and applications in composite sheet forming simulation, *Finite Elem. Anal. Des.* 42:1097-1111
- [11] Dvorkin E, Bathe KJ (1984) A continuum mechanics based four-node shell element for general nonlinear analysis, *Eng. Comput.* 1:77-88
- [12] Simo JC, Rifai MS (1990) A class of mixed assumed strain methods and the method of incompatible modes, *Int. J. Numer. Methods Eng.* 29:1595-1638
- [13] Buchter N, Ramm E, Roehl D (1994) Three-dimensional extension of nonlinear shell formulation based on the enhanced assumed strain concept, *Int. J. Numer. Methods Eng.* 37:2551-2568
- [14] César de Sá JMA, Natal Jorge RM, Fontes Valente RA, Areias PMA (2002) Development of shear locking-free shell elements using an enhanced assumed strain formulation, *Int. J. Numer. Methods Eng.* 53:1721-1750
- [15] Fontes Valente RA, Natal Jorge RM, Cardoso RPR, César de Sá JMA, Grácio JJ (2003) On the use of an enhanced transverse shear strain shell element for problems involving large rotations, *Comput. Mech.* 30: 286-296
- [16] Fontes Valente RA, Parente MPL, Natal Jorge RM, César de Sá JMA, Grácio JJ (2005) Enhanced transverse shear strain shell formulation applied to large elasto-plastic deformation problems, *Int. J. Numer. Methods Eng.* 66:214-249
- [17] Alves de Sousa RJ, Natal Jorge RM, Fontes Valente RA, César de Sá JMA (2003) A new volumetric and shear locking-free 3D enhanced strain element, *Eng. Comput.* 20:896-925
- [18] Fontes Valente RA, Alves de Sousa RJ, Natal Jorge RM (2004) An enhanced strain 3D element for large deformation elasto-plastic thin-shell applications, *Comput. Mech.* 34:38-52
- [19] MacNeal-Schwendler. *MSC Nastran v4.5 Reference Manual*, 2000.

MECHANICAL MODELS OF SANDWICH PANELS ALLOWING FOR LOCAL INSTABILITY

Zbigniew Pozorski

Faculty of Civil Engineering
Poznan University of Technology
ul. Piotrowo 5, 60-965 Poznań, Poland
e-mail: zbigniew.pozorski@ikb.poznan.pl

Key words: Sandwich panels, Wrinkling stress, Computational mechanics, Local effects.

Summary. *The problem of local instability of the compressed facing of a sandwich panel is discussed in this paper. Proper estimation of wrinkling stress has become a challenging issue because of a strong tendency to optimize technical parameters and costs. The aim of the study is numerical and analytical analysis of bending of three-layer panels. Linear constitutive equations and identical elasticity modules in tension and compression are assumed. In practice, wrinkling stress depends on many factors, usually neglected in analytical solutions, though observed in experiments. In this paper we use numerical methods and hence we can allow for the loss of face adhesion or anisotropy of the core. Created models are validated and calibrated by experimental results. The analyses are carried out for various mechanical and geometrical parameters of the sandwich panel. The influence of these parameters on structural response is studied. The range of applicability of classical theoretical models is discussed basing on numerical examples. The study presented in the paper was inspired by sandwich panels producers, with the aim to increase safety and economy.*

1 INTRODUCTION

Sandwich panels are used in industry for many years. They are usually composed of three layers: rigid, external faces and a flexible core. Important role in the analysis of the structures plays the contact between core and faces, evolution of the core parameters induced by creep and influence of thermal excitations.

Classical approach to the problem of sandwich panels was presented in [1, 2]. The simplified theoretical models discussed in these papers have been widely used in an engineering practice. However, increasing industrial requirements enforce more precise and reliable analysis. Therefore, this issue has focused much attention in the last years and many papers went up, where modern FEM models were proposed [4, 8].

Apart from analytical and numerical solutions, real experiments still play important role to find behavior of those structures. They are one of the bases of the determination of the sandwich plate carrying capacity in EC standard [3]. Application of the modern experimental methods to the analysis of sandwich panels was presented in [5, 6, 7].

The aim of the paper is to study the mechanism of local instability of compressed facing of the bending panel [4, 5]. Numerical and analytical models are created, validated and calibrated by the analysis of numerical and experimental results. The models may be particularly useful in evaluation of structure response subjected to, difficult to realize experimentally, thermal actions. Moreover, the models are used to the analysis of influence of structure parameters on the value of wrinkling stress.

2 DESCRIPTION OF THE PROBLEM

The paper is concerned on the problem of localized bending effects in sandwich panels. Our aim is to estimate the influence of the main structural parameters, namely panel depth, face thickness and core stiffness, on the wrinkling stress.

Simply supported, one-span sandwich panel with the length L and the width B is considered. The structure consists of two thin and plain steel faces and flexible core. Both faces have the same thickness t , while depth of the core is D . The geometry of the structure is presented in Fig. 1.

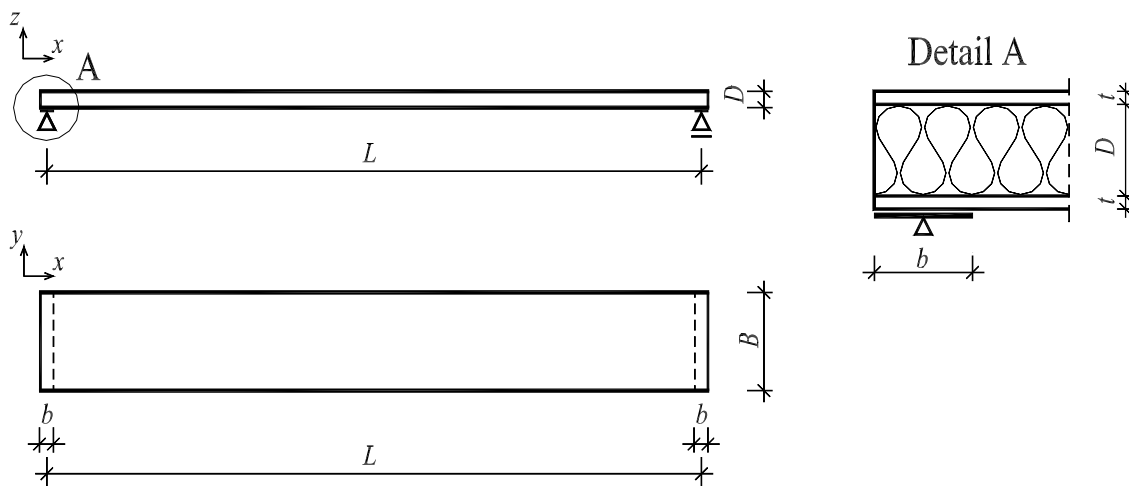


Figure 1: Geometry of sandwich structure

The panel is supported at its two opposite ends. Width of the supports is equal to b . Support conditions refer to real structures. Therefore, it was assumed that a base plate modeled as rigid body is lying at both supports [8]. Reference points describing respective boundary conditions of the whole support are localized in the middle of contact surface between lower face sheet and the supporting plate. For the left supporting base plate (detail A in Fig. 1) all three translations and the rotations with respect to axes x and z are equal to zero. Unconstrained rotation with respect to the axis y is assumed. The right base plate has additionally the possibility of the translation in the direction x . The sandwich panel is subjected to static, uniform distributed suction load on the lower facing.

The main attention in the analysis was focused on the behavior of the structure in bending. The problem of stress concentration and complex interactions between facings and the core were observed. The importance of the problems of debonding and local instabilities of the structure was emphasized in papers [6].

3 ANALYTICAL MODEL

In the classical theory of sandwich panels all materials are assumed as linear elastic, homogenous and isotropic. The external facings are parallel. The Young modulus of the core is very low. Hence, normal stresses are negligible and shear stresses are constant in the core part. Usually, the sandwich panel is analyzed as a beam type structure.

The problem of local instability of compressed facing grounded on the elastic foundation can be described by the differential equation

$$B_{F1} \cdot w^{IV}(x) + P \cdot (w''(x) + w_0''(x)) + k \cdot w(x) = q(x). \quad (1)$$

The symbols B_{F1} , w , k , w_0 and q denote bending stiffness of the facing, transverse displacement, stiffness of foundation, initial displacement and transverse loading, respectively [2]. If we neglect the initial displacement field w_0 , the solution of (1) can be written in a simplified form:

$$w(x) = w_1 \cdot \sin\left(\frac{\pi x}{a}\right), \quad (2)$$

where the coefficient w_1 corresponds to displacement amplitude and a is a half length of deformation wave.

Assuming that the wave length decrease proportionally to the stiffness k with the proportionality factor $f_1 = a \cdot k$, a normal (compressive) force can be expressed as

$$P = \frac{\pi^4 B_{F1} + f_1 a^3}{a^2 \pi^2}. \quad (3)$$

Looking for minimum value of the force P we stipulate $dP/da = 0$ and thus arrive at

$$a = \left(\frac{2\pi^4 B_{F1}}{f_1}\right)^{1/3}. \quad (4)$$

Using (3) and (4), f_1 and P can be expressed as:

$$f_1 = \pi \cdot 2^{1/4} B^{1/4} K^{3/4}, \quad (5)$$

$$P = 3 \cdot 2^{-1/2} B^{1/2} K^{1/2}. \quad (6)$$

Introducing a function (or in the simplest case - a scalar) f_2 , which is scaling a relation between the Young modulus E_c of the core, depth of the core D and stiffness of the foundation k :

$$k = \frac{E_c}{D} \cdot f_2^2, \quad (7)$$

the wrinkling stress is finally obtained as

$$\sigma_{cr} = \frac{P}{t} = \frac{3\sqrt{2}}{2} \cdot \frac{f_2}{t} \cdot \sqrt{\frac{B_{F1} E_c}{D}}, \quad (8)$$

where t is the thickness of the compressed facing. Please note that the term of bending stiffness $B_{F1} = E_F I_{F1}$ contains the Young modulus of the facing material E_F and the moment of inertia of the facing I_{F1} .

The key point is to find the form of f_2 . Generally, f_2 may depend on various geometrical and mechanical parameters. In the simplest case, this term is assumed as a scalar, which is calibrated to comply with experimental results. The laboratory tests are in progress and therefore the results will be presented on the conference.

4 NUMERICAL ANALYSIS

Numerical models were prepared in ABAQUS system environment. The span and width of analyzed sandwich structure are $L = 4.40$ m and $B = 0.50$ m. The following depths of the core were assumed $D = 0.079$ m, 0.099 m and 0.119 m. The width of supporting plates was $b = 0.10$ m. Thickness of facings was equal to $t = 0.4$ mm, 0.5 mm or 0.6 mm.

Steel facings were assumed as elastic - ideal plastic material with the Young modulus $E_F = 210$ GPa, the Poisson ratio $\nu_F = 0.3$ and yield stress $f_y = 280$ MPa. Facings were modeled using four node, doubly curved shell elements SR4 with dimensions 2×2 cm or 3×3 cm.

The core of the panel was modeled using eight node linear brick elements C3D4. The core was divided into two layers of elements. The following parameters of the core material were assumed: $\nu_C = 0.05$ and $E_C = 8$ MPa, 6 MPa or 4 MPa. The isotropic and homogeneous core material was assumed at the first stage of the study.

Between the compressed facing and the core, a layer of interface is introduced. The interface is modeled using COH3D8 8-node, 3D cohesive elements. Interactions between all parts are assumed as TIE type, which makes equal displacements of nodes. The option of leaving the rotations free was chosen.

Elasticity uncoupled law for cohesive material of the interface is defined by the relation

$$\begin{bmatrix} t_n \\ t_s \\ t_t \end{bmatrix} = \begin{bmatrix} K_{mm} & 0 & 0 \\ 0 & K_{ss} & 0 \\ 0 & 0 & K_{tt} \end{bmatrix} \begin{bmatrix} \varepsilon_n \\ \varepsilon_s \\ \varepsilon_t \end{bmatrix}, \quad (9)$$

where t_n is normal traction (stress) and t_s , t_t are shear tractions. Corresponding nominal strains are defined as $\varepsilon_n = \delta_n/T_0$, $\varepsilon_s = \delta_s/T_0$, $\varepsilon_t = \delta_t/T_0$ using separation δ and constitutive thickness of cohesive element T_0 .

Quadratic nominal stress criteria was used in the model for damage initiation:

$$\left\{ \frac{\langle t_n \rangle}{t_n^0} \right\}^2 + \left\{ \frac{t_s}{t_s^0} \right\}^2 + \left\{ \frac{t_t}{t_t^0} \right\}^2 = 1, \quad (10)$$

where $\langle \cdot \rangle$ is Macaulay bracket with the usual interpretation.

Damage evolution is displacement type with linear softening. The stress components of the traction-separation model are affected by the damage according to:

$$\begin{aligned} t_n &= \begin{cases} (1-G)\bar{t}_n & \bar{t}_n \geq 0 \\ \bar{t}_n & \text{otherwise} \end{cases} \\ t_s &= (1-G)\bar{t}_s, \\ t_t &= (1-G)\bar{t}_t. \end{aligned} \quad (11)$$

The scalar damage variable G represents the overall damage in the material. The terms with overbar are the stress components predicted by the elastic traction-separation behavior for the current strains without damage. To describe the evolution of damage, an effective displacement is introduced:

$$\delta_m = \sqrt{\langle \delta_n \rangle^2 + \delta_s^2 + \delta_t^2}. \quad (12)$$

For linear softening, the damage variable G has the following form:

$$G = \frac{\delta_m^f (\delta_m^{\max} - \delta_m^0)}{\delta_m^{\max} (\delta_m^f - \delta_m^0)}, \quad (13)$$

where δ_m^{\max} refers to the maximum value of the effective displacement attained during the loading history, δ_m^0 refers to damage initiation and δ_m^f corresponds to full damage.

5 COMPARISON OF RESULTS

The influence of mesh size on the numerical results was the first problem analyzed in numerical simulations. Three examples of the panel with the parameters $D = 0.119$ m, $t = 0.5$ mm, $E_C = 8$ MPa and the mesh size of compressed facing 0.03 m, 0.02 m, 0.01 m were analyzed. It occurred that for various sizes of FEM elements, wrinkling stresses were different. It was presented in the Table 1.

Mesh size [m]	Wrinkling stress [MPa]
0.03	78.95
0.02	71.91
0.01	71.71

Table 1 : The influence of the mesh size on the wrinkling stress

Above results indicate that the size of the mesh may highly influences numerical solution. The mesh size should be considered in the context of wave length of wrinkled facing. If the mesh is coarse and not appropriate, the wrinkling stresses are overestimated. Evert and al. in [9] recommend the suitable mesh size about 1/8 of the length a , however this requirement is difficult to fulfill because of huge number of FEM elements.

In the following examples the mesh size 0.02 m was used. The results received for various geometrical and mechanical parameters are presented in the Table 2.

1	2	3	4	5	6
Example	D [m]	t [mm]	E_c [kPa]	Wrinkling stress σ_{cr} [MPa] (FEM)	σ_{cr} / f_2 [MPa] (analytical solution)
Ex. 1	0.119	0.50	8000	71.91	51.50
Ex. 2a	0.119	0.50	6000	60.41	44.56
Ex. 2b	0.119	0.50	4000	55.78	36.38
Ex. 3a	0.099	0.50	8000	71.25	56.41
Ex. 3b	0.099	0.40	8000	67.02	50.45
Ex. 3c	0.099	0.60	8000	85.99	61.79
Ex. 4	0.079	0.50	8000	86.09	63.15

Table 2 : Wrinkling stress for various structure parameters

Numerical and analytical results demonstrate considerable similarity. Relations between mechanical parameters and stresses seem reasonable. Higher wrinkling stresses are received for smaller core depth and higher stiffness of core and facing. The results in columns 5 and 6 are in good agreement for the value of f_2 equal to 1.40. The agreement is also in the sense of wave length. The value $a = 0.0424$ m received in the example 1 using updated analytical model is confirmed by the distance between wrinkles visible in Fig. 2.

These results can be compared to the wrinkling stress calculated according to the equation given by Stamm and Witte in [2]

$$\sigma_{cr} = 0.819 \cdot \sqrt[3]{G_c E_c E_F}, \quad (14)$$

or according to corrected equation, where initial imperfections are taken into account:

$$\sigma_{cr} = 0.5 \cdot \sqrt[3]{G_c E_c E_F}, \quad (15)$$

In the examples 1, 3a, 3b, 3c and 4, the stresses (14) and (15) are equal to 152.06 MPa and 92.83 MPa, respectively. Furthermore, using (14) and (15) the same results would be obtained in case of micro-profiled facing. It is because in these equations wrinkling stress doesn't depend on facing stiffness.

Our recently conducted experimental tests indicate that neither analytical nor numerical models describe properly the phenomenon of the local instability of the sandwich panel yet.

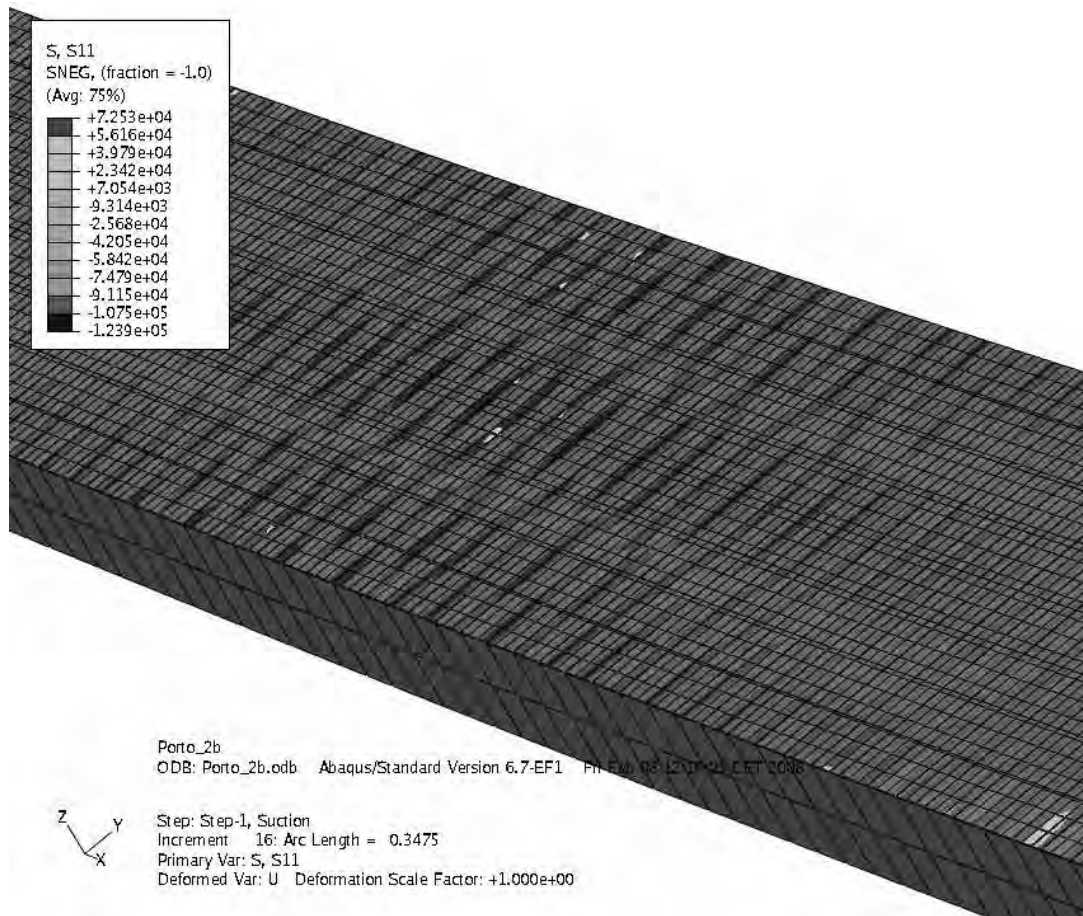


Figure 2: Local effects in bending of sandwich panel: normal stresses and wrinkles in the steel upper facing in direction x

6 CONCLUDING REMARKS

The numerical and analytical analysis as also laboratory tests proved that bending of the sandwich panels and occurring local effects are a complex problem. Various parameters have influence on the results, namely: geometrical values as panel depth and facing thickness and material features of the core and facings. The presented examples verify classical approach to the problem of wrinkling stress of the sandwich panel and demonstrate that hitherto existing in engineering practice simplifications can lead to considerable errors.

Proposed analytical approach express the wrinkling stress as a function of the most important parameters of sandwich structure. In terms of quality, the analytical and numerical solutions are in good agreement. In spite of this, the existing models should be improved with respect to experimental results. Developed models may be particularly useful in evaluation of the structure response subjected to the difficult to realize experimental actions and can significantly minimize number of laboratory tests and costs.

REFERENCES

- [1] H. G. Allen, *Analysis and design of structural sandwich panels*, Pergamon Press, Oxford, 1969.
- [2] K. Stamm, H. Witte, *Sandwichkonstruktionen. Berechnung, Fertigung, Ausführung* (in German). Springer-Verlag, Wien, Austria, 1974.
- [3] prEN 14509 Self-supporting double skin metal faced insulating panels - Factory made products - Specifications, 2004.
- [4] O. T. Thomsen, Y. Frostig, Localized bending effects in sandwich beams: photoelastic investigations versus high-order sandwich theory results. *Composite Structures*, 37, 97-108, 1997.
- [5] Y. Frostig, On stress concentration in the bending of sandwich beams with transversely flexible core, *Composite Structures*, 24, 161-169, 1993.
- [6] W.C. Kim, C. K. H. Dharan, Face sheet debonding criteria for composite sandwich panels under in-plane compression, *Eng. Fract. Mech.*, 42, 4, 643-652 1992.
- [7] Boyle, M. P., Experimental, numerical and analytical result for buckling and postbuckling of orthotropic rectangular sandwich panels, *Compos. Struct.*, 52, 3/4, pp. 375-380, 2001.
- [8] Heder, M., Buckling of sandwich panels with different boundary conditions: a comparison between FE-analysis and analytical solutions, *Compos. Struct.*, 19, 4, pp. 313-332, 1991.
- [9] Evert, E., Banke, F., Schultz, U., Wolters, M., Untersuchung zum Knittern von Sandwichelementen mit ebenen und gesickten Deckschichten, *Stahlbau*, 70, 7, pp. 453-463, 2001.

ACKNOWLEDGMENT

Financial support by Poznan University of Technology grant DS 11-017/2008 is kindly acknowledged.

INFLUENCE OF PROCESS PRESSURE ON LOCAL FACESHEET INSTABILITY FOR ULTRALIGHT SANDWICH STRUCTURES

Julien Rion, Samuel Stutz, Yves Leterrier and Jan-Anders E. Månson

Laboratoire de Technologie des Composites et Polymères (LTC)

Ecole Polytechnique Fédérale de Lausanne (EPFL)

CH-1015 Lausanne, Switzerland

e-mail: yves.leterrier@epfl.ch

Key words: Wrinkling, Honeycomb core, Facesheet waviness

Summary. *The skin wrinkling phenomenon was investigated in case of ultra light sandwich structures with honeycomb core manufactured by one shot vacuum bag processing. A relation between process pressure and compressive strength of the skin was established. It was observed that the size of the adhesive menisci between honeycomb cell walls and skin and the waviness of the skin increased with process pressure. As these two effects have antagonist influence on compressive strength of the skin, an optimal process pressure equal to 0.7 bar was identified experimentally and confirmed by an analytical model.*

1 INTRODUCTION

Composite sandwich structures are very often used for all applications requiring high stiffness and strength with minimal weight. High-tech applications such as satellites, ultra light solar airplanes or solar cars require pushing this type of structures to the limit in terms of lightweight. To this end, sandwich structures with very thin skins and light honeycomb core weighing less than 1 kg/m^2 are used. While traditional sandwich structures used in boat hulls or commercial airplanes have often been studied and optimized, the ultra light sandwich structures require particular attention in designing and manufacturing. Indeed, these structures are extremely sensitive to local buckling of the very thin skins, either through wrinkling or dimpling [1, 2]. Furthermore, this failure mode is very sensitive to local imperfections of the skin which can dramatically reduce the strength of the structure [3-5]. Therefore the processing of ultra-light sandwich panels has to be studied very carefully in order to minimize the local imperfections in the skins.

During one shot manufacturing of sandwich panels with vacuum bag processing, the face sheet on vacuum bag side presents waviness due to the skin penetration into honeycomb cells [4, 6, 7]. This phenomenon decreases significantly the strength of the sandwich panel when the skin is under compressive loads. As the skin waviness is dependent of the level of vacuum applied during curing, the relation between processing pressure, i.e. the difference between atmospheric pressure and pressure in vacuum bag, and wrinkling load was studied in order to determine the optimal process conditions. The process pressure changes not only the waviness of the skin, but it is also expected to influence the formation of the adhesive menisci between honeycomb cell walls and skins. The relation between the amount of adhesive in the menisci and the wrinkling load was therefore considered first.

2 MATERIALS AND METHODS

Three different kinds of ultralight sandwich structures were fabricated in order to evaluate the dependencies between process pressure, waviness of the skin, adhesive weight in menisci and failure load of the skin. All the samples were produced with the same materials and their weight ranged from 700 to 800 g/m². The skins comprised two layers of 70 g/m² UD carbon fibers prepreg with EH84 epoxy matrix (Hexcel) at 0 and 90° respectively. The Nomex[®] honeycomb core was 29 kg/m³ and the hexagonal cell size, i.e. the distance between two parallel cell walls was 3.2 mm. The core was 8 mm thick. The ribbon direction of honeycomb was parallel to the length direction of the sandwich panel. An epoxy adhesive (VTA 260 from Advanced Composite Group) was used to bond the skins to the core.

The first kind of samples was devoted to study the effect of adhesive weight in the resin menisci on the compressive failure load of the skin. The sandwich samples were fabricated in one shot with vacuum bag process. As during one shot curing, the skin on vacuum bag side had a lower quality due to waviness, the study concentrated on the smooth skin on mould side. The effect of the waviness of the skin on vacuum bag side was considered on the other types of samples. Five different adhesive weights between 0 (no supplementary adhesive was used) and 100 g/m² were chosen for the smooth side by using the adhesive deposition method developed by Rion et al [7, 8]. The complete panel was cured under vacuum (-0.9 bar relative pressure) at 120°C during 100 min. An Al frame avoided lateral crushing when vacuum was applied as illustrated in Figure 1. A non-perforated film was placed on the top prepreg to avoid that resin flowed out of the prepreg. Fibre rowings were placed between the Al frame and the non-perforated film to allow air to circulate. As the film prevented air circulation through the thickness of the skin, the vacuum was only applied from the sides of the panels and a good vacuum could not be ensured in the honeycomb cells.

The samples of the second type were produced to study the influence of the processing pressure on the strength of the panel. To allow controlling the vacuum level in the honeycomb cells during curing, the panels were processed in two steps. The wavy skin was fabricated first. The honeycomb was laid onto a plate with a breather cloth in-between channelling the air under the honeycomb. The adhesive film and carbon prepreg were then laid onto the honeycomb and then the consumables were stacked as described in Figure 1. The breather cloth and plastic grid on the top of the panel are not useful during first cure to drain air

because the air was drained below the honeycomb, but it was placed to have the same stacking on the surface as for conventional one shot vacuum processing. Five different relative vacuum pressures (i.e. $P_v - P_{atm}$, where P_v is the absolute pressure in vacuum bag and P_{atm} the atmospheric pressure) were used: -0.1; -0.3; -0.5; -0.7; -0.9 bar. In a second step, the second skin was laid on the Al plate, the honeycomb with the first skin already cured was placed on it with all the consumables and it was cured with -0.9 bar relative vacuum pressure. The vacuum was applied during 5 hours before the second curing cycle began to allow air to circulate to create vacuum in the honeycomb cells. A 50 g/m² adhesive film was used to bond both skins to the core.

The third type of samples was fabricated with the same lay-up and adhesive quantity as the second type, but in one shot. Various relative vacuum pressures (-0.1, -0.5, -0.7, -0.9 bar) were used as for the second type of samples, but as honeycomb cells were closed on both sides by the carbon skins during curing, the absolute pressure in the honeycomb cells could be considerably higher than the one under the vacuum bag. The vacuum was applied during 12 h before curing cycle began to allow air circulation.

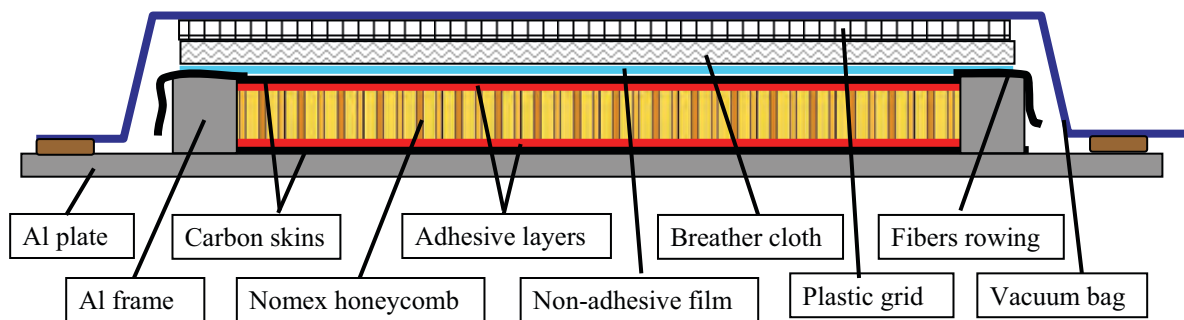


Figure 1: Vacuum processing layout of the sandwich panels cured in one shot.

The panels were cut using a diamond saw in 7 samples of 30 mm width and 450 mm length and tested in 4-points bending. The span between the outer supports in 4-points loading was 400 mm and 100 mm between the loading points. Small carbon plates of 18 mm width and 1.5 mm thickness were placed under the loading points to avoid local indentation.

The waviness W_{meas} of the skin was measured on micrographs of polished cross-sections of the sandwich structures. Figure 2 shows the measured waviness, i.e. the height difference between the top of honeycomb cells and the lower point of the skin in the middle of the honeycomb cell. The size of the adhesive menisci between honeycomb cell walls and carbon skin was also measured on the polished cross-sections and the weight of adhesive in the menisci calculated according to a geometrical model of the menisci [8].

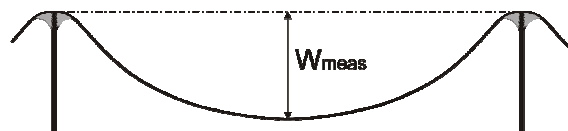


Figure 2: measurement of the amplitude of the waviness on the micrographs of cross-sections

For calculating the wrinkling load of the skin in compression, the bending stiffness of the face sheet has to be known accurately. Therefore, after the test of the sandwich beams in 4-points bending, a part of the skin of 90 mm length was cut from the smooth side of the beams. The honeycomb was removed from the skin by cutting it with a cutter at the top of the adhesive menisci. The stiffness of the skin reinforced by the adhesive menisci was measured in 3-points bending, with a span of 50 mm.

3 MODELLING OF WRINKLING PHENOMENON

As all the samples tested in 4 points bending broke due to wrinkling of the skin in compression between the two loading points as illustrated in Figure 3, this particular failure mode was investigated. The wrinkling problem has been extensively studied by numerous authors. Ley and al. [1] made a review of the most common used models. All the models are based on the same assumption of compressed skin laying on a continuous elastic foundation. The main difference between the various models is the modeling of the elastic foundation according to the core used. When honeycomb core is used, the anti-plane stress assumption is often used, i.e. the core is considered to have an in-plane stiffness being zero and so to have only normal stresses perpendicular to the panel and shear stresses in xz and zy planes, where z is perpendicular to the panel. The model developed by Gutierrez and Webber [9] which was especially developed for bending of sandwich panels uses this assumption and is then well adapted to the case studied in this paper. This model also takes in account the elastic tension-bending coupling in asymmetric composite skins. In fact it was noticed that considering the coupling changed the wrinkling load by less than 1% in the present case, which was then neglected to simplify the study. The equilibrium equations for the skin under compressive load as represented in Figure 3 are then

$$A \frac{d^2 u}{dx^2} = (\tau_{xz})_{z=d} \qquad -D \frac{d^4 w}{dx^4} - N \frac{d^2 w}{dx^2} = (\sigma_z)_{z=d} \qquad (1)$$

where u et w are the displacements in length and out of plane directions, τ_{xz} the shear stress in the core, σ_z the normal stress in the core, A the coefficient A_{11} of the ABD matrix of the skin calculated with classical laminate theory, D the bending stiffness of the skin and N the load per unit width in the skin. The equilibrium equations of the core are given as

$$w = -\frac{z^2}{2E_c} \frac{d\tau_{xz}}{dx} + z \frac{k_1}{E_c} \qquad u = z \frac{\tau}{G_c} + \frac{z^3}{6E_c} \frac{d^2 \tau}{dx^2} - \frac{z^2}{2E_c} \frac{dk_1}{dx} \qquad \sigma_z = -z \frac{d\tau_{xz}}{dx} + k_1 \qquad (2)$$

where k_1 is a coefficient function of x only. The shape of the skin is considered to have a sinusoidal form, and thus the shear stresses in the core, the normal stresses in the core and the coefficient k_1 also have a sinusoidal form:

$$w = W \sin\left(\frac{\pi x}{l}\right) \qquad \tau_{xz} = T_{xz} \cos\left(\frac{\pi x}{l}\right) \qquad \sigma_z = \Sigma_z \sin\left(\frac{\pi x}{l}\right) \qquad k_1 = K_1 \sin\left(\frac{\pi x}{l}\right) \qquad (3)$$

where l is the half-wavelength of the wrinkling form. With the assumption that the displacements of the top of the core are the same as the middle of the skin (valid for thin skins), equations (2) can be substituted in equations (1) and using the sinusoidal forms, we obtain the equation

$$q_1 \left(\frac{\pi}{l} \right)^8 + q_2 \left(\frac{\pi}{l} \right)^6 + q_3 \left(\frac{\pi}{l} \right)^4 + q_4 \left(\frac{\pi}{l} \right)^2 + q_5 = 0 \quad (4)$$

with

$$q_1 = \frac{d^2 D}{6E_c} \quad q_2 = \frac{2dD}{G_c} - \frac{Nd^2}{6E_c} \quad q_3 = \frac{2D}{Ad} + \frac{2d}{3} - \frac{2N}{G_c} \quad q_4 = \frac{2E_c}{G_c d} - \frac{2N}{Ad} \quad q_5 = \frac{2E_c}{Ad^2} \quad (5)$$

By solving numerically equation (4), the wrinkling line load N in the face can be calculated as a function of l . The value of l giving the lowest load corresponds to the critical wavelength and gives the critical wrinkling load of the beam.

In order to take into account the adhesive layer used for core to skin bonding in the model, the bending stiffness of the skin is replaced by the bending stiffness of the skin with adhesive menisci, which was measured with the various adhesive weight.

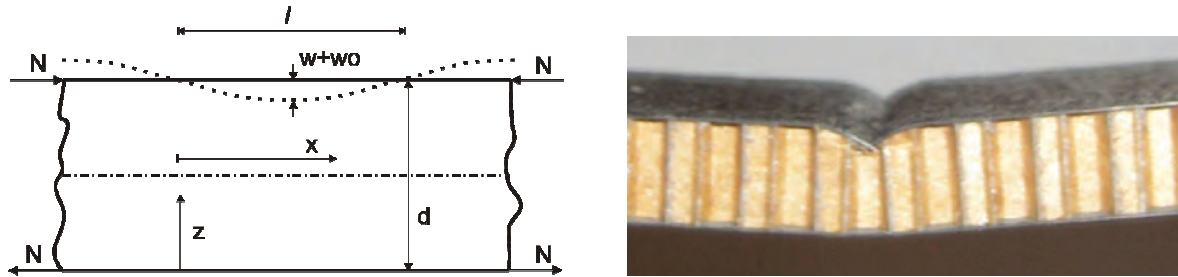


Figure 3: (left) schematic view of the wrinkling phenomenon of the skin under compression during bending of the sandwich beam. The core is considered as a continuum. d is the distance between the center of the two faces. (Right) Failure mode of the skin in compression. The skin became locally unstable and crushed in the core.

This wrinkling formula is only valid for beams with perfectly flat skins. However the skins always contain imperfections. Particularly, the waviness caused by vacuum bag processing changes the wrinkling load and has to be taken in account in the model. Indeed, the initial deflection of the skin will increase during loading and can cause either compressive failure of the core, debonding of the skin, shear failure of the core, or local failure of the skin due to compression and bending deformations. The classical approach to take the initial waviness in account is to consider that the skin as a sinusoidal shape of amplitude W_0 and half-wavelength l_0 before loading, so that the deformed shape has the form

$$w + w_0 = (W_0 + W) \sin \left(\frac{\pi x}{l_0} \right) \quad (6)$$

With the honeycomb core, l_0 is the distance between two cells rows, i.e. 2.77 mm with

3.2 mm cell size. The amplitude of the waviness measured in the panels W_{meas} can not be used directly for W_0 , because the wave measured has a width limited to the cell size, the skin being maintained flat on the cell walls, while the wave extends on the full width of the beam in the model. This discontinuity of the wave in the width direction will significantly reduce the sensitivity to waviness of the structure, and a factor $\theta = W_{meas} / W_0$ has to be identified to use the measured waviness in the model. The equilibrium equations (1) for the skin become

$$A \frac{d^2 u}{dx^2} = (\tau_{xz})_{z=d} \qquad -D \frac{d^4 w}{dx^4} - N \frac{d^2 w}{dx^2} - N \frac{d^2 w_0}{dx^2} = (\sigma_z)_{z=d} \quad (7)$$

By combining it with equations (2), (3) and (7), one obtains the amplitude of shear stresses in the core τ_{xz}

$$\Gamma_{xz} = \frac{NW_0 \left(\frac{\pi}{l_0}\right)^5}{q_1 \left(\frac{\pi}{l_0}\right)^8 + q_2 \left(\frac{\pi}{l_0}\right)^6 + q_3 \left(\frac{\pi}{l_0}\right)^4 + q_4 \left(\frac{\pi}{l_0}\right)^2 + q_5} \quad (8)$$

Then by using equations (2), the amplitudes of the coefficient k_l and of the normal stress in the core σ_z are:

$$K_1 = \frac{2E_c \Gamma_{xz}}{Ad^2} \left(\frac{l_0}{\pi}\right)^3 \left(\frac{Ad}{G_c} \left(\frac{\pi}{l_0}\right)^2 - \frac{Ad^3}{6E_c} \left(\frac{\pi}{l_0}\right)^4 + 1 \right) \qquad \Sigma_z = \Gamma_{xz} d \frac{\pi}{l_0} + K_1 \quad (9)$$

With equations (8) and (9) the critical load N causing shear stresses or normal stresses equal to the strength of the core can be calculated. The maximum local compressive strain in the face due to the compression and the local bending of the face is:

$$\varepsilon_m = \left(-\frac{d^2 w}{dx^2} \right)_m h + \frac{N}{A_{11}} = W \frac{\pi^2}{l_0^2} h + \frac{N}{A_{11}} \quad (10)$$

where h is the distance from the neutral axis of the face to the most loaded fibers, i.e. 40.5 μm for the 0/90° laminate used. By setting this strain equal to the maximum compressive strain of the prepreg, the critical load can be determined for this failure type. The lowest of the loads calculated for the different types of failure is the critical load of the structure.

4 RESULTS

4.1 Flat skins

The failure strength of the sandwich samples increased with adhesive weight. This can be explained by the increased size of the adhesive menisci on the skin which increased significantly the bending stiffness, as shown on Figure 4. Due to the geometry of the adhesive

menisci, for a given adhesive quantity, the reinforcing effect is much more pronounced with menisci than with an even adhesive layer.

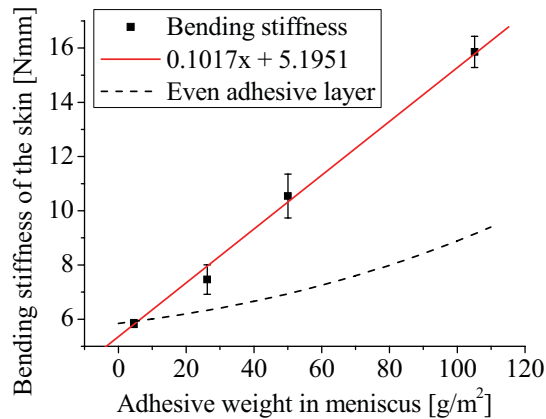


Figure 4: Measured bending stiffness of the skin measured in 3-points bending as a function of adhesive weight in the menisci for skin to core bonding. The theoretical stiffness calculated with CLT for an even adhesive layer is also represented.

By inserting in the wrinkling model the relation between the bending stiffness and the adhesive weight determined in Figure 4, the critical wrinkling load and corresponding critical half-wavelength can be calculated as a function of adhesive weight in the menisci. The result is represented in Figure 5 and the critical load corresponds well to the experimental data, with errors smaller than 5%. The critical half-wavelength, which is calculated in the model by considering a continuous core, ranged from 2.3 to 3.2 mm, which is in fact close to honeycomb cell size. The elastic foundation is thus not continuous in the order of magnitude of the wavelength. However, a line in the width direction of the beam always crosses the same number of honeycomb cell walls independently of the position in length direction of the beam. The support of this line is therefore about constant in the length direction, so that the properties of the foundation can be considered as constant in length direction and the wrinkling model is thus still valid.

Even though the skin was cured against the Al plate, a small initial waviness can not be completely avoided. Furthermore, as the half-wavelength of the preliminary deformation (2.77 mm) is close to the critical half-wavelength calculated for wrinkling of perfectly flat skin, the initial waviness will highly influence the strength of the beam. An arbitrary small waviness $W_0 = 0.5 \mu\text{m}$ was used to calculate the critical loads for core compressive and shear stresses and local strains in the skin. With this small initial deformation, the failure loads for all three models are very close to the wrinkling load calculated and are represented in Figure 5. Predicted loads for shear failure of the core and local compressive failure of the skin are identical and greater than the failure load for core compressive failure which is close to the wrinkling load. The failure mode is thus a coupling between local skin instability and core compressive failure, what is confirmed by the observation of the broken sample illustrated in Figure 3. So when the skin in compression is very smooth, the failure load can be predicted

accurately either by the wrinkling model or by considering a small initial imperfection causing compressive failure of the core, and taking in account the stiffening effect of the adhesive menisci on the skins.

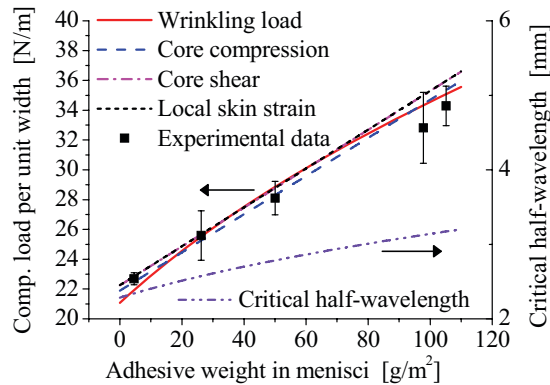


Figure 5: compressive load per unit width in the skin at failure under 4-points bending and critical half-wavelength for wrinkling as a function of adhesive weight in the menisci for core to skin bonding. The critical loads for the different types of failure are represented.

4.2 Influence of the process pressure on microstructure

Figure 6 and Figure 7 show cross-sections of samples cured respectively in two steps and in one shot with relative pressure in vacuum bag ranging from -0.1 to -0.9 bar. Figure 8 shows the measured adhesive weight in the menisci and the waviness amplitude as a function of process pressure. It is important to remind that the pressure represented is the relative pressure in the vacuum bag. The actual absolute pressure in the honeycomb cells may be however significantly higher than the absolute pressure in vacuum bag during one shot curing due to the low permeability of the skins and consumables used. The dependence between process pressure and skin waviness and adhesive weight in menisci is evident. The waviness and adhesive weight increased when the relative pressure in vacuum bag diminished. The increase is less pronounced for the samples cured in one shot because the vacuum was not good in the honeycomb cells due to the low permeability of the lay up as explained previously. As the waviness should be 0 when no pressure is applied, the data were fitted with either a power law of the pressure applied or a linear fit as illustrated in Figure 8.

For the samples cured in two steps, the size of the adhesive menisci forming between core and skin increased between -0.1 and -0.3 bar pressure in the vacuum bag and then stabilized. When pressure was exerted by the honeycomb cell wall, the skin was compacted under the honeycomb cell wall and prepreg resin flowed in the menisci in addition to the 50g/m² adhesive film. As the amount of resin is limited the meniscus size does not change any more above a sufficient pressure level. When low pressure is applied, the menisci form only with the adhesive film near the cell wall. For the samples cured in one shot, the menisci are almost inexistent at -0.1 bar relative pressure in vacuum bag. This is due to bad air circulation in

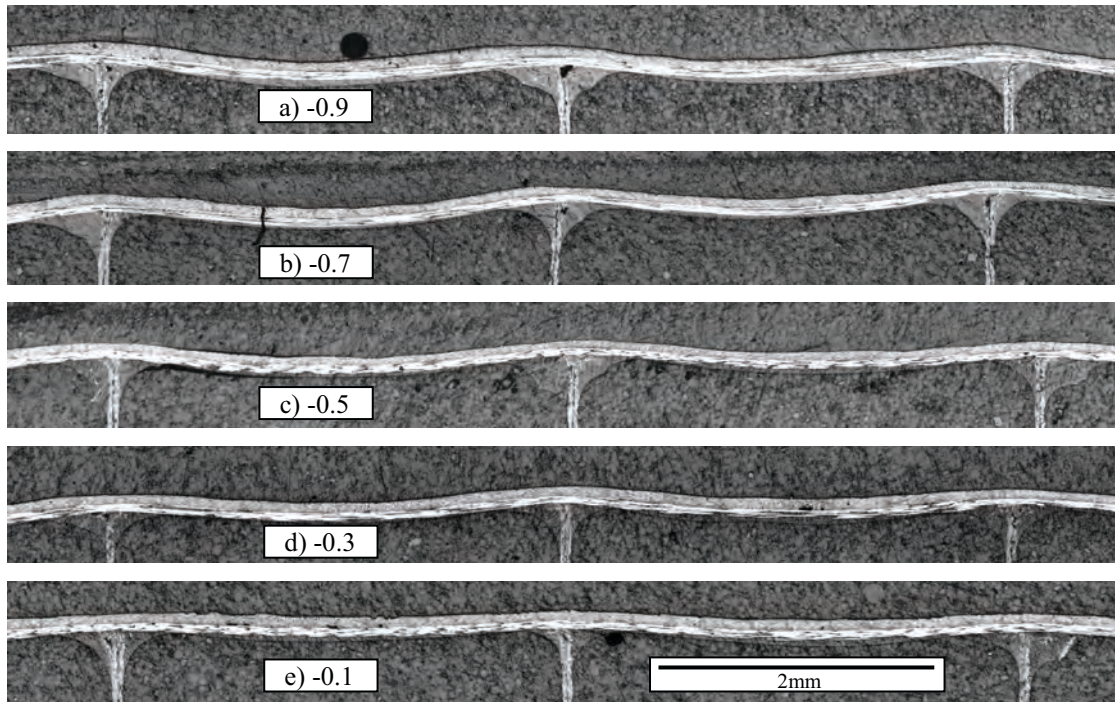


Figure 6: Micrographs of cross sections of the wavy side of sandwich panels cured in two steps. The skin laying on three honeycomb cell walls and bonded with adhesive menisci can be observed. The relative pressure applied during vacuum curing were -0.9, -0.7, -0.5, -0.3 and -0.1 bar.

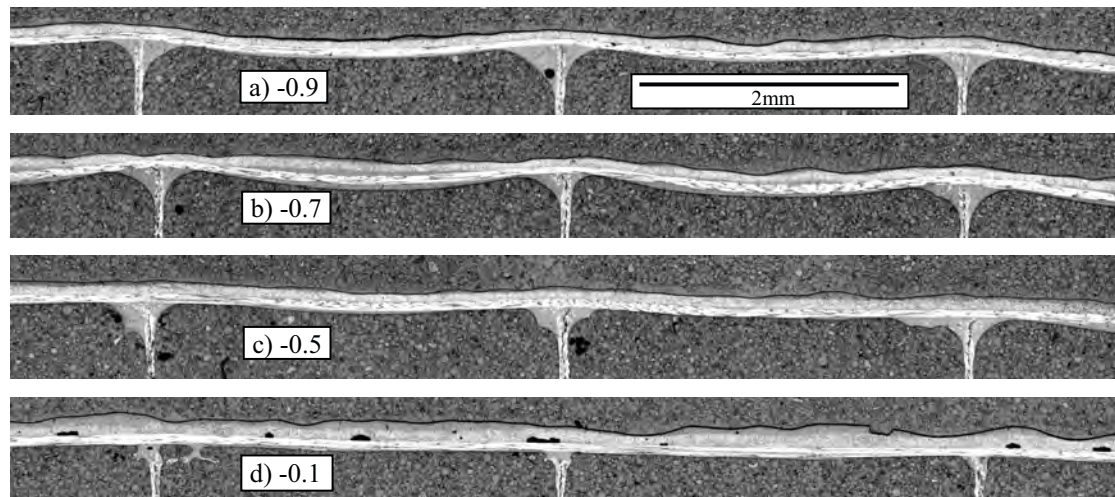


Figure 7: Micrographs of cross sections of the wavy side of sandwich panels cured in one shot. The relative pressure applied during vacuum curing were -0.9, -0.7, -0.5 and -0.1 bar.

honeycomb cells closed by the two skins, causing the pressure to increase when temperature rose. Some air flowed out of the cells through the skin and forced adhesive and prepreg resin to flow out. This can be seen in Figure 7d where a layer of resin is on the top of the prepregs of the panel cured with -0.1 bar relative pressure in vacuum bag. This flowing effect was more pronounced on vacuum bag side than on the Al mould, what explains that the resin fillets were greater on mould side than on vacuum bag side as shown in Figure 8. To fit the data by taking in account the limited amount of adhesive available, functions starting with a finite adhesive weight growing asymptotically to the limit adhesive quantity were chosen and first order exponential decay functions were used as illustrated in Figure 8.

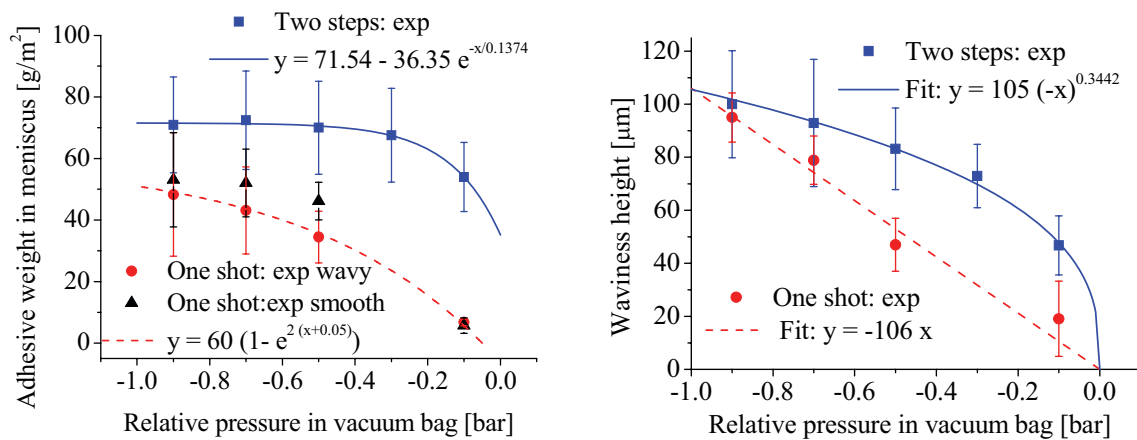


Figure 8: Adhesive weight in the menisci (left) and height of the waviness W_{meas} (right) measured on cross-sections as a function of process pressure for the samples of the samples cured either in two steps or in one shot

4.3 Influence of the process pressure on strength

Figure 9 shows the strength of the panel manufactured with various vacuum pressures and tested in 4 points bending. Interestingly, the strength of the beams increased first when the relative pressure in vacuum bag was decreased, passed by a maximum and then decreased. The same behaviour was observed for the panels cured in two steps and in one shot, only the maximum strength was obtained at different pressures, respectively -0.3 and -0.7 bar relative pressure in vacuum bag. The strength increase is due to the quick increase of adhesive quantity in menisci when relative pressure in vacuum bag decreases. Then the adhesive quantity stabilizes and the increasing waviness of the skin decreases the strength of the face. The maximum strength of the panels cured in two steps is slightly higher than the one of panels cured in one shot. This is due to the bigger size of the adhesive menisci obtained with two steps curing as was observed in Figure 8.

In order to take in account in the model the discontinuity of the waviness in the width direction of the beam which significantly reduced the sensitivity to initial waviness, the factor $\theta = W_{meas} / W_0$ was determined to be 25 by adjusting the model to the experimental data obtained with the panels cured in two steps. Figure 9 shows the evolution of the critical compressive load per unit with in the skin calculated by the models for the different types of

failure as a function of the process pressure. Among the models predicting the different possible failure types of the skin in compression, the one considering compressive failure of the core give the lowest failure load. Thus, this mode is the most sensitive to the initial imperfections of the skin and therefore determines the failure load of the beam. With the parameter θ defined previously the model giving the critical load for core compressive failure is in good agreement with the experimental data with errors less than 5% for both the panels cured in two steps or in one shot. For the panel cured in one shot, the model slightly overestimates the failure load at -0.1 bar relative vacuum pressure due to the bad compaction of the skin at low pressure which was not accounted for. Furthermore, the curve showing critical load fore core compressive failure has exactly the same tendencies as the experimental data, the load increasing first quickly when relative vacuum pressure decreases, then passing through a maximum and decreasing. The model confirms the existence of an optimum process pressure controlled by the interplay between skin waviness and formation of adhesive menisci at the skin / honeycomb interface. The model and the experimental data give the same optimal pressure in the vacuum bag for the sandwich panels cured in two steps at about -0.3 bar for the wavy skin. The optimal pressure for the panels cured in one shot is around -0.7 bar, but the strength does not change significantly between -0.5 and -0.9 bar. Finally, the critical failure mode predicted by the model as the compressive failure of the core is confirmed by observing the broken samples where the skin crushed the core, as illustrated in Figure 3.

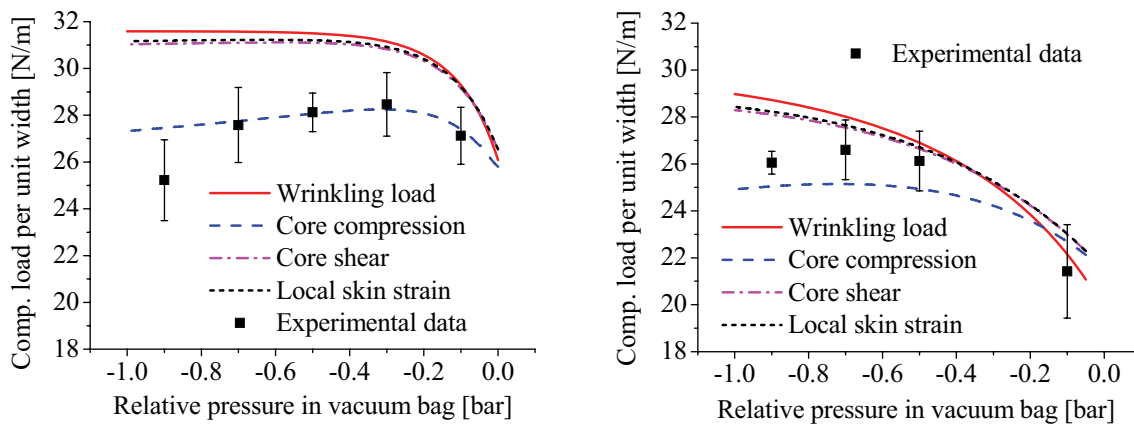


Figure 9: Evolution of the compressive load per unit width in the face at failure during 4-points bending tests as a function of process pressure for the samples cured in two steps (left) and in one shot (right).

5 CONCLUSIONS

The bending strength of ultralight sandwich structures (700 to 800 g/m^2) is very sensitive to the process pressure used during manufacturing. By using vacuum bag processing with various pressures and adhesive weights, it was shown that the waviness of the skin and the size of the adhesive menisci forming between honeycomb cell walls and skins have a direct influence on the wrinkling strength of the skin. During one shot vacuum bag curing, the waviness of the skin and the size of the adhesive menisci both increase with process pressure,

having antagonist effects on the strength. An optimal process pressure has been identified at - 0.7 bar relative pressure in vacuum bag. This pressure is clearly related to the materials used, and also to the curing cycle parameters, a higher temperature creating for example a higher pressure in the honeycomb cells.

A model has been developed to predict the wrinkling load of the skin as a function of process pressure by taking in account the influence of adhesive weight in the menisci and the waviness of the skin. A good agreement was found between experimental data and the model which allows better understanding of the failure mechanisms controlling wrinkling load.

ACKNOWLEDGMENTS

The authors wish to acknowledge the EPFL and Swiss Innovation Promotion Agency (CTI, #8002.1, DCPN-NM) for financial support.

REFERENCES

- [1] R.P. Ley, W. Lin and U. Mbanefo, *Facesheet wrinkling in sandwich construction*, NASA: Langley Research Center, (1999)
- [2] O.T. Thomsen and W.M. Banks, "An improved model for the prediction of intra-cell buckling in cfrp sandwich panels under in-plane compressive loading", *Compos Struct*, 65, (3-4), 259-268, (2004).
- [3] L. Fagerberg and D. Zenkert, "Imperfection-induced wrinkling material failure in sandwich panels", *J Sandw Struct Mater*, 7, (3), 195-219, (2005).
- [4] C. Kassapoglou, S.C. Fantle and J.C. Chou, "Wrinkling of composite sandwich structures under compression", *J Compos Tech Res*, 17, (4), 308-316, (1995).
- [5] S. Yusuff, "Face wrinkling and core strength in sandwich construction", *J R Aeronaut Soc*, 64, 164-167, (1960).
- [6] V. Altstadt, F. Diedrichs, T. Lenz, H. Bardenhagen and D. Jarnot, "Polymer foams as core materials in sandwich laminates (comparison with honeycomb)", *Polym Polym Compos*, 6, (5), 295-304, (1998).
- [7] J. Rion, A. Geiser, Y. Leterrier and J.-A.E. Månson. "Ultralight composite sandwich structure: Optimization of skin to honeycomb core bonding". Proceedings of 27th International Conference of SAMPE Europe, Paris, 2006.
- [8] J. Rion, Y. Leterrier and J.-A.E. Månson, "Prediction of the adhesive fillet size for skin to honeycomb core bonding in ultra-light sandwich structures", *Submitted to Composite Part A*, (2007).
- [9] A.J. Gutierrez and J.P.H. Webber, "Flexural wrinkling of honeycomb sandwich beams with laminated faces", *Int J Solids Struct*, 16, (7), 645-651, (1980).

FEASIBILITY OF THE DEEPAWING PROCESS OF THERMOPLASTIC SANDWICH STRUCTURES

Calogero Macaluso^{*}, Dirk Vandepitte^{*} and Ignaas Verpoest[†]

^{*} Department of mechanical engineering, division PMA
Katholieke universiteit Leuven (KUL)
Kasteelpark Arenberg 41 – bus 2449, 3001 Heverlee, Belgium
E-mail: calogero.macaluso@mech.kuleuven.be

[†] Department of metallurgy and materials engineering (MTM)
Katholieke universiteit Leuven (KUL)
Kasteelpark Arenberg 44 – bus 2550, 3001 Heverlee, Belgium

Key words: Honeycomb, Thermoplastic, Finite elements, Large deformations.

Summary. *In this paper deepdrawing FE analyses are performed on full three-dimensional and geometrically detailed thermoplastic sandwich plates with honeycomb cores. Forming analyses with bending in one and two directions are conducted. The importance of the out-of-plane core shear strength in these deepdrawing processes is pointed out. These full three-dimensional models require a considerable amount of CPU-time. The feasibility of strategies for reduction of calculation time is considered.*

1 INTRODUCTION

Sandwich constructions have proven to be very useful in many application areas due to their high stiffness and strength to weight ratios. However, their production is limited to flat plates. A further expansion of their use is only possible if they can be formed into complex shaped parts.

One can distinguish different families within the group of sandwich materials. These families differ from the way the face sheets are supported by the core. This support can be homogeneous (e.g. foam cores), regional (e.g. perforated cores), structured (e.g. honeycomb cores), unidirectional (e.g. corrugated cores) or punctual (e.g. textile cores made out of pile yarns connecting the face sheets).

Thermoplastic sandwich panels with foam cores have already been successfully thermoformed in short processing cycles, resulting in complex parts that can be used in application areas such as food packaging and automotive (Rozant et al. [1]). Rozant's study revealed the importance of the temperature distribution through the thickness of the sandwich when thermoforming thermoplastic sandwich parts. In [2], Mohr and Straza formed successfully all-metal sandwich sheets with perforated cores. In another paper [3], Mohr pointed out the importance of the out-of-plane core shear strength in a sandwich deepdrawing process with bending in one direction. Based on theoretical considerations he derived a relation between the maximum allowed punch force (directly linked to the core shear

strength) and the minimum allowed deepdrawing tool radius for a certain configuration of the deepdrawing tools, sandwich geometry and sandwich material (core and face sheets).

This relation is adopted in this paper to deduce the minimum forming radius of the forming tools for a certain thermoplastic honeycomb sandwich and the considered deepdrawing configuration with bending in one direction. The shear strength of the sandwich plate is found by performing a non-linear analysis on a geometrically detailed sandwich unit cell. This will form the first part of the paper.

In the second part, deepdrawing FE analyses are performed on full three-dimensional and geometrically detailed sandwich plates with honeycomb cores. First, the previously outlined deepdrawing configuration with bending in one direction is assessed. The minimum tool radius that was found in the previous step is used. Afterwards, this tool radius is used to set up a deepdrawing configuration with bending in two directions. The analyses permit to validate the importance of the out-of-plane core shear strength in forming analyses, but need large CPU-times.

In literature one can find contributions to the homogenisation of sandwich parts with honeycomb cores. With these homogenisation procedures equivalent sandwich models can be build, which should reduce CPU-time when used in FE-analyses.

Most of these models are useful for *linear* analyses of these constructions. Gibson and Ashby [4] started from considerations about the deformation mechanisms of honeycomb cores to find all 9 material constants of the orthotropic honeycomb core. Grediac [5] pointed out the importance of taking the influence of the face sheets into account during the homogenisation of the core material. This is indicated in literature with: “skin effect”, “warping effect”, “thickness effect” or “bending effect”. Using the formalism of the Classical Lamination Theory (CLT) one can homogenise the whole sandwich by determining the sandwich stiffness constants. Hohe and Becker [6] did this using a method of strain energy equivalence between a geometrically correct sandwich unit cell and an equivalent plate element. The equivalent model is based upon a plate theory formalism (CLT) and is therefore confined: it cannot predict e.g. thickness reduction. The first approach (Gibson and Ashby) is more general than the second and can be expanded for a *non-linear* forming problem.

This has been done by Xue and Hutchinson [7]. Non-linear analyses are performed on a geometrically detailed sandwich unit cell (like figure 1) under six elementary loading conditions to extract the equivalent core properties (stress-strain behaviour). They identified with these elementary stress-strain curves the parameters of the Hill yield criterion so that, besides the elastic modulus, also the yield stress is defined separately for each component of the stress tensor.

2 SANDWICH CORE SHEAR STRENGTH AND MINIMUM TOOL RADIUS

2.1 Sandwich specifications

Figure 1 shows the considered honeycomb geometry. The representative unit cell is also indicated. This unit cell is used to evaluate the honeycomb core shear strength. The core cell size S is 6.4mm, the wall thickness t_w is 0.16mm, the core thickness C is 7.3mm and the face

sheet thickness t is 0.8mm. The sandwich material is polypropylene (PP) at room temperature with a Young's modulus E of 1700MPa, yield stress σ_0 of 10MPa and hardening modulus E_T of 410MPa. These data are extracted from tensile tests on 200 μ m PP sheets with talc additives (from the company **alkor**).

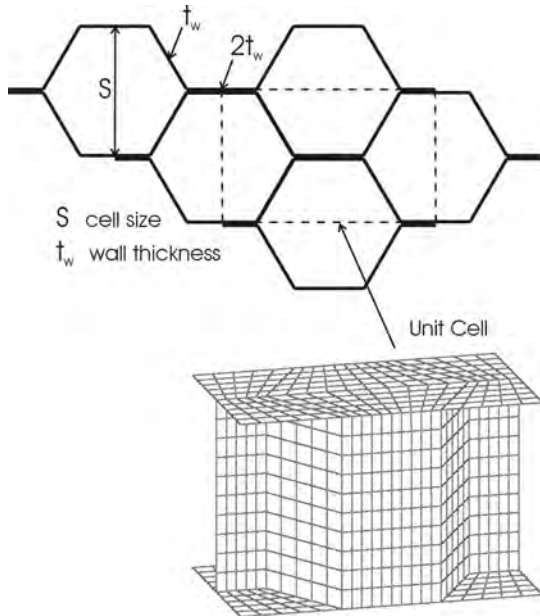


Figure 1: Honeycomb characteristics and sandwich unit cell definition

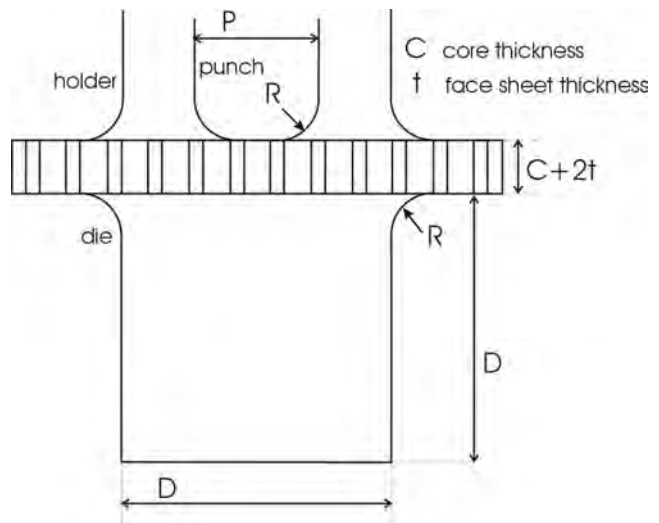


Figure 2: Deepdrawing configuration for bending in one direction

2.2 Analysis of a deepdrawing configuration with bending in one direction

Figure 2 illustrates the forming process configuration for deepdrawing with bending in single curvature. The vertical cell walls of double thickness are perpendicular to the plane of the figure. This set-up is used further in this paper for a deepdrawing analysis on a full 3D sandwich model. In [3], Mohr uses the equivalent mechanical systems of figure 3 to examine this forming process. With help of figure 3(a) Mohr singles out the region of high out-of-plane shear stress where the sandwich is clamped between holder and die. The average shear stress $\langle \tau \rangle$ in the critical cross section is then:

$$\langle \tau \rangle = \frac{P}{2C} \leq \tau_s \quad (1)$$

with τ_s the core shear strength. This shear strength is determined in [3] by finite element calculations on a geometrically detailed model of the core.

An analytical expression for the punch force P is found using the equivalent mechanical system of Figure 3(b) by equating the internal strain energy for successive bending and unbending with the external work delivered by the punch force P . P is expressed relative to the yield stress σ_0 of the considered PP:

$$\frac{P}{\sigma_0 t} = 4 \left\{ (\varepsilon_t^+ - \varepsilon_b^+) + \frac{E_T}{\sigma_0} \left[(\varepsilon_t^+)^2 + (\varepsilon_b^+)^2 \right] \right\} \quad (2)$$

$$\varepsilon_t^+ = \ln \left(1 + \frac{\varepsilon^*}{2 + \varepsilon^*} \right) \quad (3)$$

$$\varepsilon_b^+ = \ln \left(1 - \frac{\varepsilon^*}{2 + \varepsilon^*} \right) \quad (4)$$

$$\varepsilon^* = \frac{\left(\frac{C}{t} \right) + 1}{\left(\frac{R}{C} \right) \left(\frac{C}{t} \right) + \frac{1}{2}} \quad (5)$$

Using equations (1) and (5) a direct relation is found between core shear strength τ_s and minimum allowed tool radius R. Sandwich geometry, material characteristics and deepdrawing configuration (prescribing the mechanism of Figure 3(b)) are kept fixed. In the next section core shear strength is evaluated to determine the minimum allowed tool radius for the considered thermoplastic sandwich and deepdrawing process.

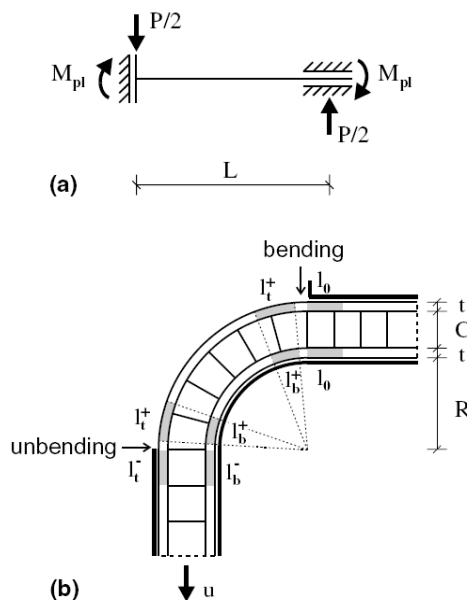


Figure 3: Equivalent mechanical systems (Mohr [3]) for (a) the relation between punch force and highest shear force and (b) the deepdrawing deformation process (bending followed by unbending)

2.3 Shear strength and minimum tool radius for the considered thermoplastic sandwich

A sandwich unit cell finite element model is built using 4-node, reduced integration shell elements; S4R in ABAQUS (figure 1). In this model the influence of the face sheets on the equivalent core properties is accounted for (according to the early work of Grediac [5]).

To simulate the out-of-plane shear behaviour, a deformation u is imposed in the direction parallel to the vertical cell walls of double thickness (figure 4). The bottom surface nodes are prohibited to move in the direction of the imposed deformation. ABAQUS/Standard has been used for the calculation. The sum of the reaction forces in the bottom surface nodes, in the considered direction, is divided by the bottom surface area, giving the needed out-of-plane shear stress. The maximum of the calculated stress-displacement curve (figure 4) gives the shear strength.

Periodic boundary conditions are used to represent the unit cell as a small part of an infinite plate (figure 5). A derivation of the equations expressing periodicity between corresponding degrees of freedom can be found in [8].

With the determined core shear strength of 0.8MPa, the minimal allowed tool radius is 77mm according to equations (5) and (1). In the next sections this tool radius is used to perform deepdrawing FE-analyses.

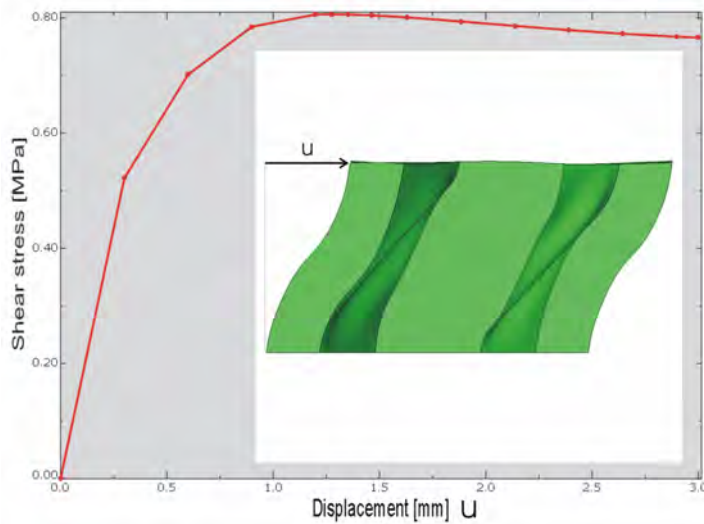


Figure 4: FE-calculation of the out-of-plane honeycomb core shear strength

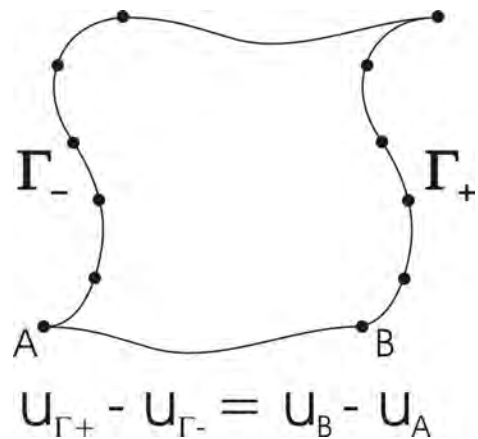


Figure 5: Equation stating periodic boundary conditions between degrees of freedom of corresponding nodes of boundaries Γ_+ en Γ_- .

3 FORMING SIMULATIONS ON FULL 3D SANDWICH MODELS

3.1 Deepdrawing simulation with bending in one direction

The deepdrawing process that is modelled is presented in figure 6 (see figure 2: $D=175\text{mm}$, $P=155\text{mm}$ and $R=77\text{mm}$). The sandwich unit cell defined in figure 1 is used to build up the whole sandwich plate. 26 unit cells (52 hexagonal cells) are used in the bending direction, giving the plate a total length of 293mm. There is only one cell in the width of the model. Periodic boundary conditions are used in this direction, representing the sandwich plate as infinite in this direction. Symmetry conditions are exploited. The model contains 324840 degrees of freedom. ABAQUS/Standard is used for the analysis. The CPU-time needed for this calculation is about 8 hours on a 4 GB RAM processor.

The circles in figure 6 indicate the areas with the highest shear stresses (red and blue indicate equal shear stresses of opposite signs). They appear in the walls of the core. Macroscopically this gives rise to out-of-plane shear stress. Shear stress area A is due to the reaction forces with blank holder and die, consistent with the considerations made in the equivalent mechanical system of figure 3(a). The shear stress in area B is a consequence of the reaction forces due to contact between the blank and the forming tools. Figure 7 shows a zoom of this area at a moment of time when the deepdrawing depth is half the maximum value. The drawn contact forces F explain the presence of high out-of-plane shear stresses in the core.

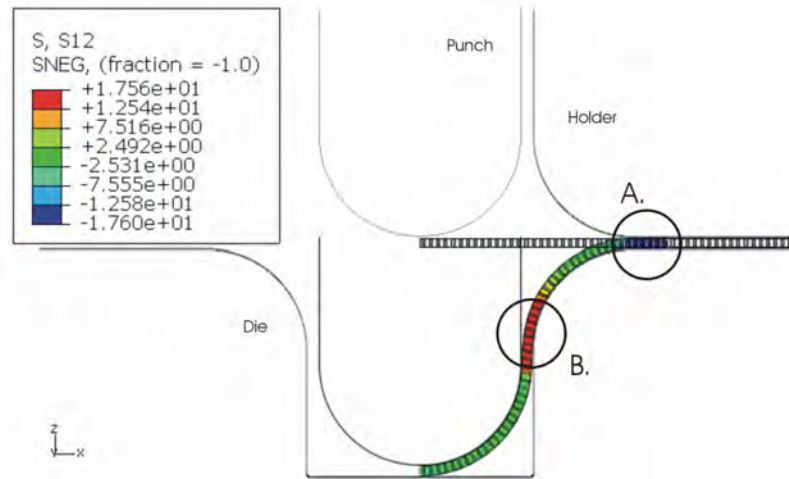


Figure 6: Sandwich forming process with bending in one direction. The contour plot shows the shear stress

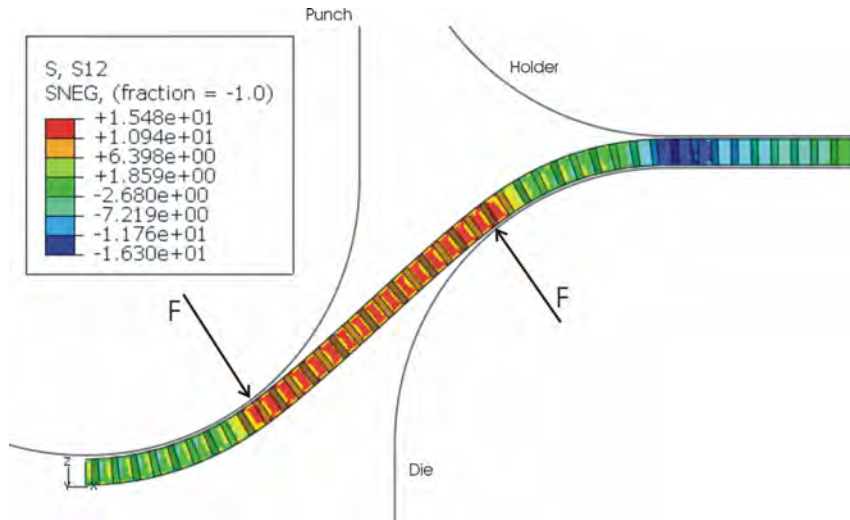


Figure 7: Zoom on area B of figure 6 halfway the sandwich forming process. Contact between the blank and the forming tools introduces shear stresses in the core

3.2 Deepdrawing simulation with bending in two directions

For the simulation of this process the sandwich plate is built using the unit cell of figure 1 in a pattern of 6 by 10 (120 hexagonal cells), giving a plate of 67mm by 67mm. The model contains 705894 degrees of freedom. Symmetry conditions are exploited.

Figure 8 presents the forming configuration for this case together with the shear stresses of the formed sandwich part. In comparison with the forming process with bending in one direction, only a smaller magnitude of deformation is feasible for the simulation, due to a combination of model size limits and a tool radius R of 77m. Figure 9 shows the formed sandwich part in 3D together with the shear stresses. The simulation is conducted with ABAQUS/Standard and takes 12 hours of CPU-time on a 4 GB RAM processor.

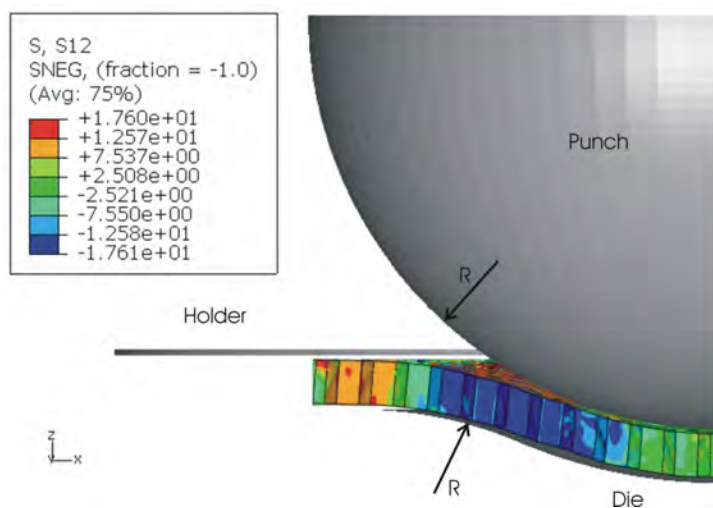


Figure 8: Sandwich forming process with bending in two directions. The contour plot shows the shear stress

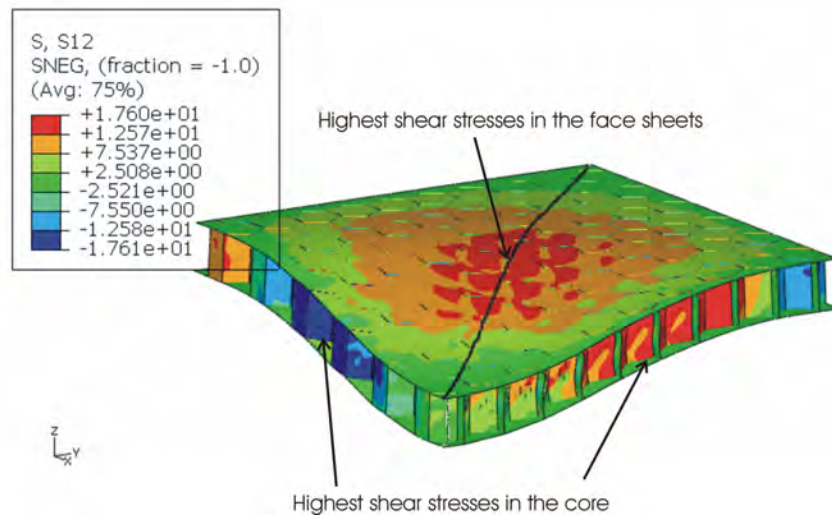


Figure 9: Formed sandwich part with bending in two directions. The contour plot shows the shear stress. The areas with the highest shear stresses are indicated

Shear stresses in the core walls are still dominant. However, in a plane at an angle of 45° with the symmetry planes, high in-plane shear stresses in the face sheets can be distinguished (indicated with the black line in figure 9). In figure 10 a unit cell is singled out from this area. The combination of bending in two directions deforms the unit cell in the indicated direction (45° -direction), leading to shear stress in the principal directions in the face sheets. High bending and shear stresses give rise to a wrinkling phenomenon in the face sheets.

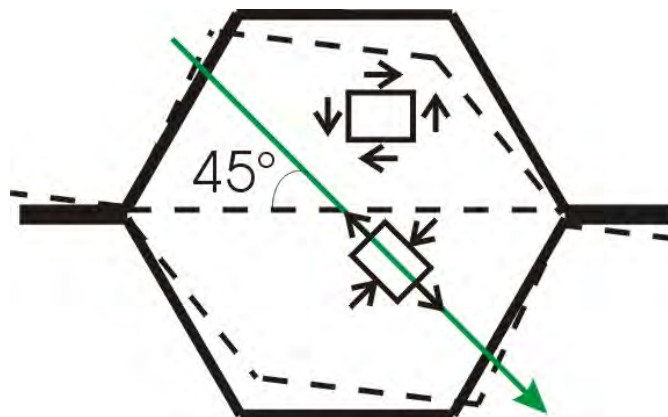


Figure 10: Deformation mechanism of a honeycomb unit cell subjected to bending in two directions. The corresponding stress condition in the face sheets is symbolically presented

4 CONCLUSIONS

It is feasible to predict the deformation of a sandwich panel, yet with a very high computation time.

The out-of-plane shear behaviour is proven to be important in forming sandwich

components. It plays a key factor in an important forming failure: core thickness reduction. The simulations are carried out on small sandwich panels (approximately 100 hexagonal cells), yet the models contain up to 700.000 degrees of freedom, leading to 12 hours of CPU time on a 4Gb RAM processor.

Further research will focus on the development of equivalent models that allow for a shorter analysis time.

ACKNOWLEDGEMENTS

The authors would like to thank the Fund for Scientific Research Flanders (FWO Vlaanderen) for funding this work.

REFERENCES

- [1] O. Rozant, P.E. Bourban and J.A.E. Manson, "Manufacturing of three dimensional sandwich parts by direct thermoforming", *Composites Part A - Applied Science and Manufacturing*, 32 (11), 1593-1601 (2001)
- [2] D. Mohr and G. Straza, "Development of formable all-metal sandwich sheets for automotive applications", *Advanced Engineering Materials*, 7 (4), 243-246 (2005)
- [3] D. Mohr, "On the role of shear strength in sandwich sheet forming", *International Journal of Solids and Structures*, 42 (5-6), 1491-1512 (2005)
- [4] J. Gibson and F. Ashby, *Cellular solids: structure & properties*, Pergamon Press, 1998
- [5] M. Grediac, "A Finite-Element Study of the Transverse-Shear in Honeycomb-Cores", *International Journal of Solids and Structures*, 30 (13), 1777-1788 (1993)
- [6] J. Hohe, "A direct homogenization approach for determination of the stiffness matrix for microheterogeneous plates with application to sandwich panels", *Composites part B*, 34, 615-626 (2003)
- [7] Z. Xue and J.W. Hutchinson, "Constitutive model for quasi-static deformation of metallic sandwich cores", *Int. J. Numer. Meth. Engng.*, 61, 2205-2238 (2004)
- [8] R.J.M. Smit, W.A.M. Brekelmans, H.E.H. Meijer, "Prediction of the mechanical behaviour of nonlinear heterogeneous systems by multi-level finite element modelling", *Comput. Methods Appl. Mech. Engrg.*, 155, 181-192 (1998)

FLOW SIMULATION FOR SANDWICH STRUCTURES: CASE STUDIES AND MODELLING OF HIGH PERMEABLE LAYERS

Florian Klunker*, Gerhard Ziegmann* and Santiago Aranda*

* Institute for Polymer Materials and Plastics Engineering
Clausthal University of Technology
Agricolastrasse 6, 38678 Clausthal-Zellerfeld, Germany
email: florian.klunker@tu-clausthal.de, web page: <http://www.puk.tu-clausthal.de>

Key words: Flow simulation, Darcy, Thin shell, Modelling, RTM, LCM

Summary. *The application of different materials in sandwich structures opens the possibility of combining light weight und functional design. A key task for the successful production of sandwich structures is the design of the manufacturing process. An important field of production techniques is the class of Liquid Composite Moulding - processes (LCM). Flow simulation has become an important tool to predict the complex flow behaviour in LCM, simplifying the design of impregnation processes without remaining dry spots.*

An optimum production of highly integrated sandwich structures with LCM is a challenging task for the designer. Especially in the production of large parts using high permeable layers for resin distribution the use of different, usually impermeable materials increase the complexity of the flow behaviour.

In this paper, case studies are presented where infusion concepts were investigated by LCM-simulation. Due to the large ratios in dimensions of the textile preform, the high permeable layers were modelled with two dimensional surface layers to gain numerical stability and to reduce the number of elements by a factor of 10 and more.

1 INTRODUCTION

The light weight design of the structures by using advanced materials is of increasing importance in many applications. A very interesting class of materials is carbon fibre reinforced plastics (CFRP), as they have excellent specific mechanical properties and fatigue behaviour. In the production of CFRP, the fibres are prefabricated as textile structure and then impregnated with a reactive resin system, which is cured afterwards. Thanks to the variety of textile architectures before curing, complex shapes can be created without the need of machining.

The final mechanical properties of the parts are created during the production process in dependence of several parameters. Some examples are fibre volume content, direction of the fibres and the combination of used chemical components. Due to the flexibility of use the light weight construction can be combined with functional design.

For a reproducible production the control of these parameters is very important. A class of production techniques for advanced composites is the Liquid-Composite-Moulding process (LCM). There are different variants of LCM-processes [1]. For the production of large parts

the Vacuum Assisted Resin Infusion (VARI) is very popular: The dry fibres are placed on a rigid tool and covered with a vacuum bag. A resin is infused by applying vacuum under the bag. For a faster impregnation of the fibres it is convenient to use a distribution medium (High Permeable Layer, HPL) on top of the fibres. A challenging task is to fill the whole part without remaining dry spots.

The prediction of flow pattern in dependence of time is complex due to the anisotropic structure. For simple parts rough estimations are possible. The use of HPL and functional materials for the production of sandwich parts is increasing the complexity of flow prediction, especially in case of impermeable cores or functional materials.

Flow simulation has become a helpful tool for designing and optimizing the process. A lot of different physical effects can already be covered [2] which increases the accuracy of the flow front predictions. Special topics concerning the use and the further development of flow simulation are among others the development and the effects of voids during the impregnation [3–6], their removal [7, 8] and the optimization of gates [9, 10]. Filtration occurs if filler systems are used, decreasing the porosity during impregnation [11]. Due to the high dependence of permeability on the porosity [12], a complex flow behaviour is probably given.

The scope of this paper is to describe the usage of flow simulation for two case studies. The task for the simulation is the fast prediction of the flow behaviour to get decision support for the design of a process. The complexity of the simulations was the result of the use of impermeable core materials, leading to complex flow front patterns and the use of HPL, resulting in a big number of elements. A combination of face and solid elements could decrease the number of elements by a factor of 10 and more, so that several flow front studies could be done in a convenient time as a decision support for material selection and process design.

2 MODELLING THE FLOW PROCESS

The flow in a representative volume has to fulfill the mass balance:

$$\frac{\partial \rho}{\partial t} + \nabla(v\rho) = 0, \quad (1)$$

where ρ describes the mass averaged density and v the mass averaged velocity. As the flow in fibrous materials can be described with the theory of porous media, good results can be achieved by using Darcy's Law (2) as a constitutive equation. It describes a linear relationship of the gradient of pressure $p[Pa]$ and the mass averaged velocity $v[m/s]$. The constant has two parameters: the permeability tensor $K[m^2]$ of the fibre structure and the viscosity $\mu[Pa \cdot s]$ of the fluid.

$$v = -\frac{K}{\mu} \nabla(p). \quad (2)$$

Substituting (2) in (1) and introducing a resin saturation factor S results into a simplified Richard's equation [13, 14]:

$$\phi \frac{\partial S}{\partial t} - \nabla \left(\frac{K}{\mu} \nabla(p) \right) = 0. \quad (3)$$

The result of (3) is the pressure field p . The boundary conditions applied in the simulation are:

- pressure or volume rate conditions in the inlet area,
- slip conditions at the free walls,
- pressure conditions at the outlet, which can also be assumed as the pressure at the flow front area [15] due to the low viscosity of the air.

For solving (3), different techniques are applied. Two examples of them are:

- Models for $S(p)$ resulting in nonlinear parabolic PDE's, examples are van Genuchten, Corey-Brooks [16, 17],
- Volume of Fluid (VOF) - methods or Finite Element/Control Volume - methods to gain a flow front tracking scheme by calculating the stationary part of (3) in elements which are assumed to be completely filled and track the filling of adjacent elements by using (2) [15, 18].

The accurate determination of material parameters is important for the accuracy of the flow simulations. The permeability of the fibre structure is a parameter depending on the fibre volume content. During the VARI-process the fibre volume content varies due to the flexible behaviour of the vacuum bag. This effect has to be taken into account with material models describing the permeability and the compaction of the fibres [12, 19].

3 MODELLING OF HIGH PERMEABLE LAYERS

For the production of large parts, the use of distribution media is often necessary to fill the whole part in a convenient time. These high permeable layers (HPL) are often placed on surfaces of the part so that it can be removed after the process. The permeability of HPL is very high compared to the permeability of the structural material. The ratio in plane direction is about 100, in through-thickness direction even 1000 and higher.

The thickness of HPL is often very small in relation to the size of the part. In order to avoid small angles in the elements of the mesh, the element size has to be reduced, resulting in a big number of elements. Even in case of meshes using increasing element sizes numerical problems appear due to the big differences in permeability between the HPL and the fibre material. So using the geometrical dimensions of the HPL leads to big difficulties in the flow simulation.

In [20] the thickness of the HPL was increased by a transformation. Therefore an equivalent permeability was derived for the in plane permeability of the HPL. This model was corrected [21] calculating an equivalent porosity of the high permeable layer and the through-thickness permeability of the HPL as well. This approach has been validated comparing with traditional FE/CV simulations, giving a difference in filling of 15% with computation time savings about 87%.

As the permeability of the fibres in through thickness direction is much lower than the in plane permeability of the HPL, the flow front pattern change in thickness direction of the HPL can be neglected. This opens the opportunity to model the HPL in three dimensions with two dimensional surface layers [22, 23]. The modelling of 2D layers on 3D-structures only requires a few steps, which will be listed in the following paragraphs.

In fig. 1 a 2D representative elementary volume (REV) of the HPL is shown. It is assumed that the pressure change in thickness direction is neglectible. The thickness of the REV is defined as h . A further assumption is that it is completely filled and so transient terms will be neglected.

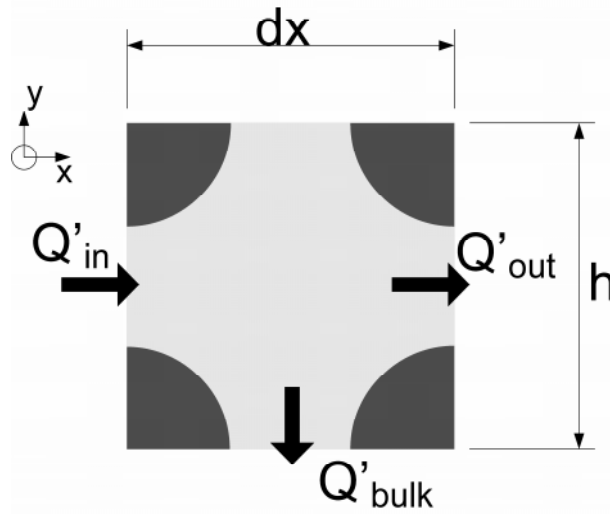


Figure 1: A representative elementary volume in the high permeable layer

The mass balance for this REV is the sum of the inflow (Q'_{in}), the outflow (Q'_{out}) and the flow into the fibre material Q'_{bulk} :

$$Q'_{in} - Q'_{out} - Q'_{bulk} = 0, \quad (4)$$

resulting in following volume averaged velocities:

$$(v_{in} - v_{out}) \cdot h = v_{bulk} dx. \quad (5)$$

If Darcy's Law is applied to (5), having

$$\left(\frac{K_x}{\mu} \left(\frac{\partial}{\partial x} p(x - 0.5 dx, y) - \frac{\partial}{\partial x} p(x + 0.5 dx, y) \right) \right) \cdot h = \frac{K_y}{\mu} \frac{\partial}{\partial y} p(x, y) dx, \quad (6)$$

with $dx \rightarrow 0$:

$$\left(\frac{K_x}{\mu} \frac{\partial^2}{\partial x^2} p(x, y) \right) = \frac{K_y}{\mu} \frac{\partial}{\partial y} p(x, y) \cdot \frac{1}{h}. \quad (7)$$

The right expression of (7) is a finite difference approximation to a neutral boundary, which is also the given boundary condition for wall contact in the flow simulation. For the limit $h \rightarrow 0$:

$$-\frac{\partial}{\partial y}p(x) \cdot \frac{1}{h} = \frac{0 - \frac{\partial}{\partial y}p(x)}{h} \approx \frac{\partial^2}{\partial y^2}p(x), \quad (8)$$

and therefore (7) results into a Laplace equation which shows the consistency of this approach: it is used in the description by (3) without the transient term. This was also assumed in the beginning of these calculations.

The left term in (8) also describes a sink term in the HPL. Using the pressure of the HPL to apply pressure boundary conditions for the flow in the fibre material, a coupled flow is modelled. With such an approach, the number of elements can be decreased dramatically. The final decrease of the number is depending on the geometry itself. Sometimes geometries with 3D representations of the HPL cannot even be meshed with automatic routines. As an example, a $250 \times 250 \times 4$ mm rectangular plate with a 0.8 mm thick HPL was meshed. The number of elements with two different meshing parameters was 8757/207258 elements with the 3D-representation of HPL and 284/5557 elements with the surface layers, so a factor of 40 was achieved.

4 CASE STUDIES

In this section flow simulation is used to get statements for a proper material selection in the design stage of a process. The program used for this investigation was COMSOL. The results of the simulations are approximate filling times in respect to assumptions made for the material and the flow front behaviour could be investigated in dependence of the injection strategy.

4.1 Boat Structure

In this section the application of fill simulation for a boat structure is discussed. The use of flow simulation for material selection will be shown.

As the boat industry builds large structures, the use of high permeable layers (HPL) to distribute the resin is obligatory to assure the viability of the process. For higher stiffness, the boat hull can be created using core materials. In application of infusion techniques, these materials can be impermeable, in order not to increase the weight by a large amount of resin.

It was the task to investigate a process, injecting resin in a structure consisting of ribs with included high permeable layers, impermeable core materials and two large skins as it is sketched in fig.2. The thickness of the fibre material is assumed to be 3 mm and the thickness of HPL is assumed to be 0.8 mm.

Two different filling strategies were investigated in this work: Filling the structure from the outside region (fig.2) and by a point injection in the inner region (fig.4). The coloured areas represent the filled areas while the colours represent the pressure level.

The investigation of the filling of the outside region (fig.3) shows that the flow will be lead into the middle, the flow fronts are running together in the stringers and the skins will be filled last.

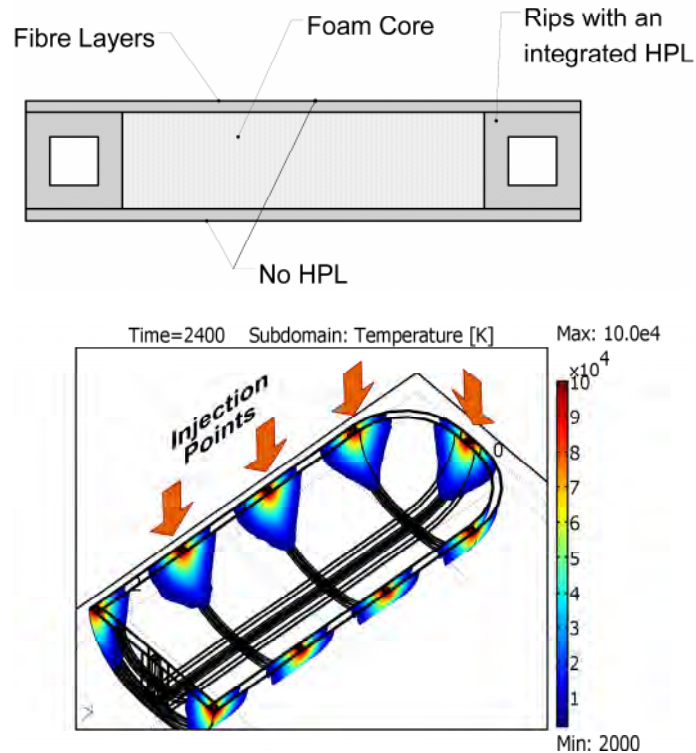


Figure 2: The boat consisting of ribs and sandwich materials

In the figure the flow behaviour with a permeability ratio of $HPL/fibre = 1000$ is shown. It shows that air will be entrapped in the small subareas between the stringers in the centre of the skin.

The higher the permeability of the HPL, the more the spot of enclosed air is moving to the outside. For a low permeability the air is enclosed in the middle of the boat.

Finally the result of the simulation shows that this filling strategy is not recommendable for this special geometry because the permeability of the HPL is getting into practically impossible ranges.

A second approach was investigated, filling the boat with a strategy from the inner area over the branches to the outer area, which is a common technique. In this case the branches are the stringers which are impregnated first, followed by the skins (fig.4). For this geometry this strategy has no regions where entrapped air could be expected, but as it can be seen in the picture, the filling time is already about 3200 s: this strategy causes problems in filling time as it takes over 30000 s, not taking into account the curing of the resin. For an economic filling of this special geometry the use of HPL on the big surfaces is obligatory.

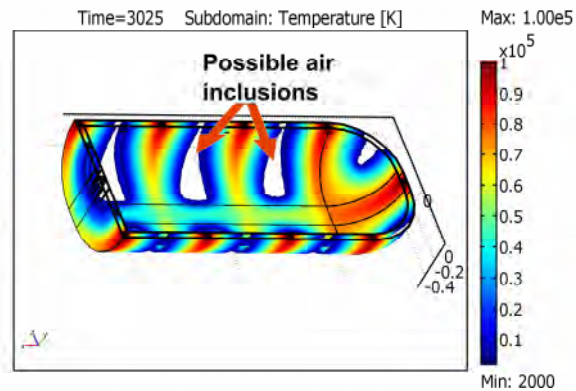


Figure 3: Infusion of a boat structure from the outer area

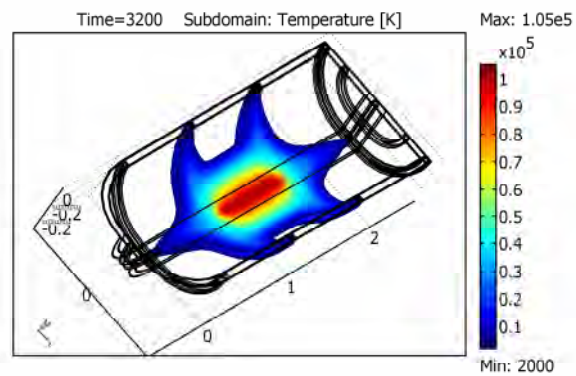


Figure 4: Infusion of a boat structure from the inner area

4.2 Panel Structure

In this section, a simulation of an example of a designed sandwich panel will be discussed. The drawing of the panel is shown in fig.5. Two impermeable sandwich cores are used in the centre. The result of the simulation is that enclosed air can appear due to the cuboid shape of the cores and the low z-permeability of the fibres next to the cores.

In practise usually geometries like frustums of pyramids are used to avoid that problem. If cores with stages are needed, entrapped air can be avoided by cutting the high permeable layer (HPL).

In fig.5, a sketch of the part is shown: Two impermeable cuboid sandwich cores are placed between two skins of 4 mm height. From the cores a chamfer is filled with fibres. A HPL with a thickness of 0.7 mm is placed on top and bottom of the part. The permeability ratio of in plane (IP) and through thickness (TT) permeability is 100 as well as the ratio of HPL and IP.

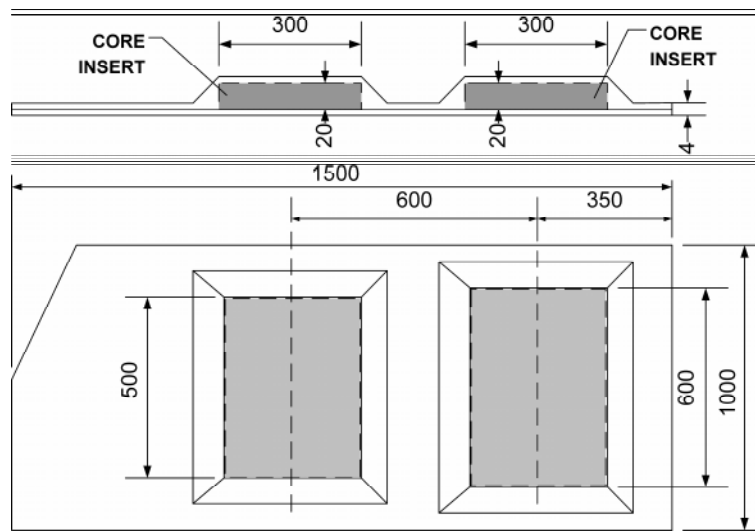


Figure 5: Geometry and dimensions of the sandwich panel

Three injection strategies have been investigated (see fig.6):

- (Ω_1) a line injection on the longest side of the part,
- (Ω_2) a line injection on the long center line,
- (Ω_3) a line injection on the long center line with cut HPL.

As shown in fig.7, the filling strategy (Ω_1) causes dry spots. The HPL on top and bottom are distributing the resin, so that the main flow is in thickness direction. As long as the thickness of the layers do not change, no problem appears. In this case, the flow front is split into two branches, caused by the low permeability in z-direction of the fibres, so that air is enclosed at the core material when the flow front passes it in the top and bottom skin. A similar problem occurs on the other side of the core material. For very high ratios of IP/TT, air can also be enclosed on that side, but the probability is not as high as in the side at the inlet.

The filling strategy (Ω_2) causes the same problem as case (Ω_1) on the side which is close to the vent. In this case the void free impregnation of the part cannot be guaranteed. In order to avoid that problem, the HPL can be cut in the areas where the problem appears (case (Ω_3)). The flow front is slowed down so that its advancement in the HPL decreases with time, all the air can escape before the flow front encloses it.

5 CONCLUSIONS

Flow simulation can be used to answer special questions in different stages of the part design. In this cases simulation showed in an early stage of design if the ideas can lead to success. In this case, the complexity was created by high permeable layers (HPL) combined with impermeable sandwich cores. For a good performance, the HPL's were modelled in 2D, so the necessary

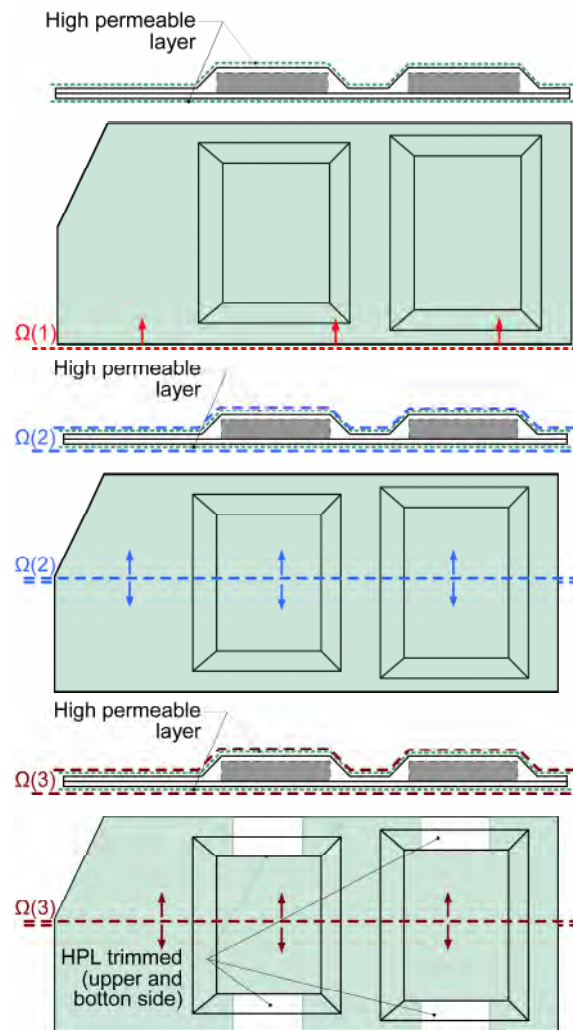


Figure 6: Three investigated strategies

number of elements could be reduced to a smaller amount and the studies could quickly give answers concerning questions of material selection and filling strategy.

References

- [1] M. Flemming, G. Ziegmann and S. Roth. *Faserverbundbauweisen, Fertigungsverfahren mit duroplastischer Matrix*. Springer, Berlin, 1999.
- [2] J.M. Lawrence, P. Simacek and S.G. Advani. Advances in liquid composite moulding flow simulation: fabric and distribution media compaction and tow saturation. *Proceedings of SEICO07*, 28th International Conference, Paris, 683–691, 2007.
- [3] B. Gourichon, C. Binetruy and P. Krawczak. Experimental investigation of high fibre tow

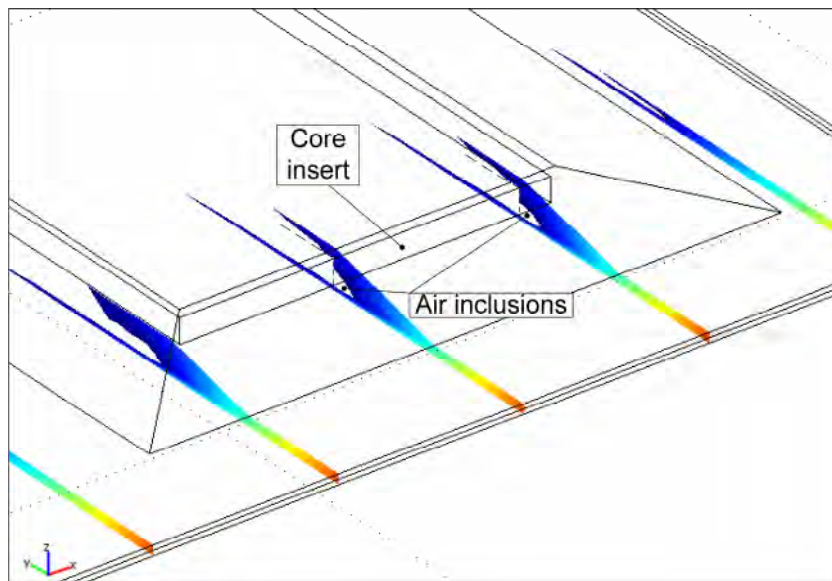


Figure 7: Filling of strategy (Ω_1)

- count fabric unsaturation during RTM. *Composites Science and Technology*, **66**, 976–982, 2006.
- [4] N. Patel, and L. James Lee. Modeling of void formation and removal in liquid composite molding. Part II: model development and implementation. *Polymer Composites*, **17**, 104–114, 1996.
- [5] E. Ruiz, V. Achim, J. Breard, S. Chatel and F. Trochu. A fast numerical approach to reduce void formation in liquid composite moulding. *Proceedings of FPCM8*, July 11-13, Douai, 251–260, 2006.
- [6] T. Roy and K.M. Pillai. Characterization of dual scale fibre mats for unsaturated flow in liquid composite molding. *Polymer Composites*, **26**, 756–769, 2005.
- [7] R. Arbter and P. Ermanni. Simulation of entrapments in LCM processes. *Proceedings of FPCM8*, July 11-13, 2006, Douai, 271–278, 2006.
- [8] T.S. Lundström. Bubble transport through constricted capillary tubes with application to resin transfer molding. *Polymer Composites*, **17**, 770–779, 1996.
- [9] G.A. Barandun and P. Ermanni. Liquid composite molding: influence of flow front confluence angle on laminate porosity. *Proceedings of FPCM8*, July 11-13, Douai, 89–96, 2006.

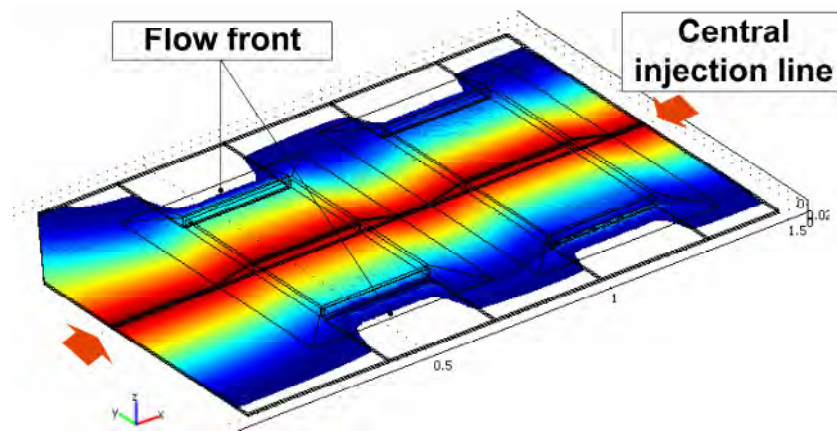


Figure 8: Filling of strategy (Ω_3)

- [10] J. Gou, C. Zhang, Z. Liang, B. Wang and J. Simpson. Resin transfer molding process optimization using numerical simulation and design of experiments approach. *Polymer Composites*, **24**, 1–12, 2003.
- [11] D. Lefevre, S. Comas-Cardona, C. Binetruy and P. Krawzak. Flow of particle-filled resin through a fibrous preform in liquid composite molding. *Proceedings of SEICO07*, 28th International Conference, Paris, 612–617, 2007.
- [12] F. Klunker, Y.M. Liu, G. Ziegmann and S. Aranda. Permeability measurement of flow enhancement layers by an indirect measurement technique using flow simulation; accepted in *Proceedings of SEICO08*, 28th International Conference, Paris, 31st March-2nd April, 2008.
- [13] J.A. Luoma and V.R. Voller. An explicit scheme for tracking the filling front during polymer mold filling. *Applied Mathematical Modelling*, **24**, 575-590, 2000.
- [14] P. Knabner and L. Angermann. *Numerik partieller Differentialgleichungen - eine anwendungsorientierte Einführung*, Springer, Berlin, Heidelberg, New York, 2000.
- [15] F. Trochu, R. Gauvin and D.-M. Gao. Numerical analysis of the resin transfer molding process by the finite element method. *Advances in Polymer Technology*, **12**, 329-342, 1993.
- [16] M.Th. van Genuchten. A Closed-form equation for predicting the hydraulic conductivity of unsaturated soils. *Soil Sci. Soc. Am. J.*, **44**, 892–898, 1980.
- [17] R.H. Brooks and A.T. Corey: Properties of porous media affecting fluid flow. *J. Irrig. Drainage Div. Am. Soc. Civ. Eng.*, **92**, 62–88, 1966.

- [18] M.V. Bruschke and S.G. Advani. A finite element/control volume approach to mold filling in anisotropic porous media. *Polymer Composites*, **11**, 398–405, 1990.
- [19] S. Comas-Cardona, C. Binetruy and P. Krawczak. A global methodology to continuously measure mechanical properties in compression and permeability of fibre reinforcements. *Proceedings of FPCM8*, July 11-13, Douai, 211–217, 2006.
- [20] R. Cheng, C. Dong, Z. Liang, C. Zhang and B. Wang. Flow Modeling and Simulation for Vacuum Assisted Resin Transfer molding Process with the Equivalent Permeability Method. *Polymer Composites*, **25**, 146-164, 2004.
- [21] C. Dong. An Equivalent Medium Method for the Vacuum Assisted Resin Transfer molding Process Simulation. *Journal of Composite Materials*, **4**, 1193-1213, 2006.
- [22] E. Ruiz, S. Chatel and F. Trochu. A simplified numerical approach to simulate resin transfer moulding with a dispersion medium. *Proceedings of FPCM8*, July 11-13, Douai, 331–340, 2006.
- [23] P. Simacek and S.G. Advani. Desirable features in mold filling simulations for liquid composite molding processes. *Polymer Composites*, **25**, 355-367, 2004.

ENERGY ABSORPTION CAPACITY OF 3D “S” SPACE FRAMES PARTIALLY REINFORCED WITH ALUMINUM FOAM

Roselita Fragoudakis^{*} and Anil Saigal[†]

^{*} Graduate Student, Department of Mechanical Engineering
Tufts University, Medford, MA 02155, USA
roselita.fragoudakis@tufts.edu

[†] Professor, Department of Mechanical Engineering
Tufts University, Medford, MA 02155, USA
anil.saigal@tufts.edu

Keywords: Finite element analysis, 3D S-shape space frame, Specific energy absorbed.

Summary. *Passenger safety during a head-on collision depends to a great extent on the capability of the car's front space frame structures to absorb energy generated during the crash, while deforming the least possible.*

Finite element analysis (FEA) models of 3D S-shape extruded aluminum frames were developed using the FEA simulation software ABAQUS/CAE and were simulated for their crashing behavior when loaded axially.

All models investigated possess an aluminum frame, 45° curvature angles, and a square cross-section. The frame can be separated into seven sections: two sections for the front and rear ends, two sections for the bends and three sections for the spaces in between. All models were reinforced with aluminum foam 10.8/40/L with the highest relative density (10.8%) and 40 cpi (cells per inch of foam) tested longitudinally to the direction of solidification and loaded identically. One of the models tested had all its sections filled with foam. The other models were partially reinforced with the same density aluminum foam but (a) at different sections, and (b) either with bulk foam components, or with foam components hollow in the middle.

For each model the Specific energy absorbed (SEA) was calculated. It was found that the frame fully reinforced with foam has the highest capacity to absorb energy during a collision. For partially foam-filled frames, foam reinforcement at the bends increases the energy absorption capacity of the frame the most. Finally, comparison of frames with bulk foam fillings and hollow foam fillings in the middle showed that, although the models with hollow fillings have significantly lower masses, they also have much lower SEA values. However, any increase in total energy absorption due to aluminum foam reinforcement is accompanied by an undesirable increase in the peak force.

1 INTRODUCTION

One of the main concerns in automobile design is passenger safety. In order to reduce the risk to passengers during a head-on collision of a car, it is necessary to examine the crashing behavior of the front members of the car's frame and find a way to increase their energy absorption during the crash. For the past thirty years, researchers have indulged in the study and examination of such space structures. Observations include the increase in the energy absorption capacity of a square tube under dynamic loading, when the tube was filled with foam [1]. Experiments have led to the development of a theoretical analysis of a foam-filled column during a collision [2], while there also exists investigations of prismatic columns reinforced with aluminum foam, undergoing axial crashing [3].

The optimization of the geometry of the frame becomes one of the targets in passenger security improvement. A tube that is not straight but possesses some curvature may prolong the deformation of the frame [4].

These studies have initiated experiments on the crashing behavior of a 3D S-shape space frame [5]. After experimenting with a variety of different curvatures for the frame, it was concluded that among the non-reinforced frames the one possessing curvature angles of 45 degrees, has the most effective energy absorption capacity.

Numerical experiments on frames, of the geometry suggested by these latter studies [5], reinforced with aluminum foam of different densities have shown that the reinforcement with higher density foam, results in a frame with a high energy absorption capacity [6].

The present study deals with the examination of the crashing behavior of 3D S-shape space frames with 45° curvature angles reinforced either fully or partially with high-density aluminum foam (relative density 10.8%).

2 STRUCTURE NOMENCLATURE AND GEOMETRY

The nomenclature used for each of the models is structured in such a way so as to imply all the properties of the frame of the structure, the foam filling, the geometry and to differentiate the models from one another. The names of the models are of the form SS(F)-1-45-45-1.S where each character and number has the following interpretation:

SS S-shape frame without foam filling

SSF S-shape frame with foam filling

1 refers to the square cross-sectional area of the frame

45 refers to each curvature angle of 45°

S refers to the letter identifying the aluminum foam filling

The frame geometry is that of a hollow tube of square cross section, having two curvature angles each of 45° that give it its "S" shape (Figure 1a). The total length L of the frame is 0.780 m, and consists of two straight end parts L_1 , as shown in Figure 1b, each of length 0.200 m.

The "S" configuration of the structure implies that the front and rear ends are not on the same axis but offset. In the x and y directions the offset is $D=D_1=0.150$ m and in the z direction $D_2=0.212$ m (Figure 1b). The size of the radii of curvature, R , are 0.200 m at both points.

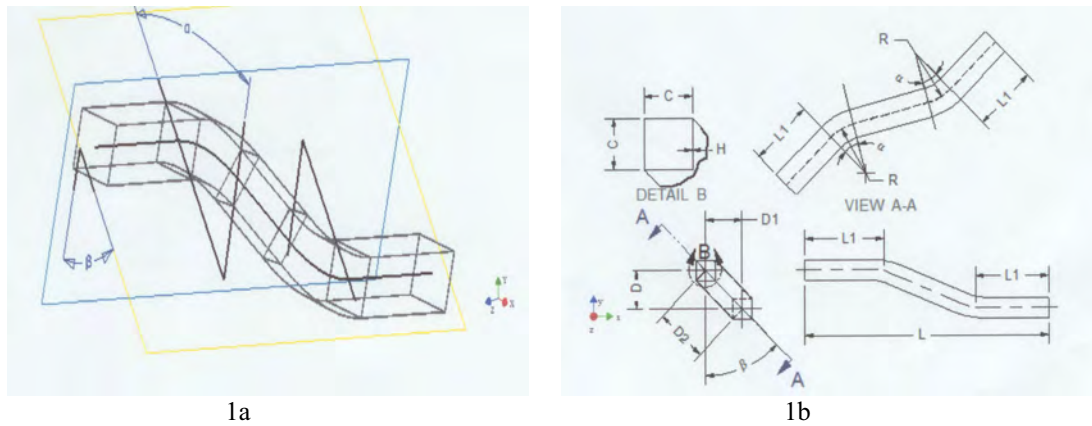


Figure 1: (a) General geometry of “S” frame and (b) Detail on frame geometry ([5])

3 EXTERIOR FRAME SHELL

The properties of the frame were kept identical in all models. The frame is made of aluminum AA 6063 T7 of density 2770 kg/m^3 , modulus of elasticity of 69.0 GPa and yield stress of 86.94 MPa .

The deformation of the frame was simulated with an initial velocity of 11.1 m/s for a time of 0.05 s and a total displacement varying from 0.51 m to 0.55 m , depending on the foam reinforcement pattern of the model. The appropriate force for crashing was provided by axially loading the structures with a 500 kg mass at the rear end.

4 FOAM FILLING

Researchers have studied the properties of Al 6101 foams of different densities and morphologies under compression [7]. This study deals with the foam of the highest density, among those presented in the above experiments [7], namely Al 6101 10.8/40/L. This foam was used as the reinforcing filling of the S-shape frame in the FEA models.

The input data for this study consisted of the compressive stress strain curve of the aluminum foam (Figure 2), together with its modulus of elasticity, density, yield strength ratio and tension yield strength ratio (Table 1).

Foam	Modulus of Elasticity (MPa)	Density [kg/m^3]	Yield Strength Ratio K	Tension Yield Strength Ratio K_t
10.8/40/L	752	299	1.0	0.1

Table 1: Aluminum foam properties

It can be seen in Table 1 that the aluminum foam used has a longitudinal direction of solidification (L), 40 cells per inch – a variable parameter used among the aluminum foams

[7]. The density of the aluminum foam is a relative density expressed as a percentage (10.8%) of the theoretical density of Al 6101, of 2770 kg/m^3 .

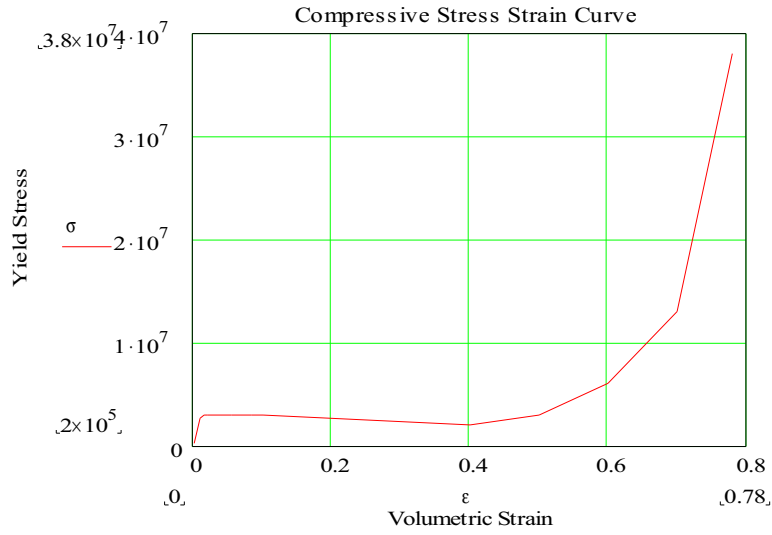


Figure 2: Compressive stress strain curve of Al 6101 foam (10.8/40/L)

The foam in Table 1 was used to partially or completely reinforce the frame. The models were theoretically divided into seven sections: one section for the front end, one for the rear end, one for each bend and three sections for the spaces in between. One of these structures was fully filled with the aluminum foam, one had the foam filling in layers, while the other models were partially reinforced at different sections, either with bulk foam parts or with foam parts hollow in the middle. Tables 2 and 3 show the models investigated in this study, and the sections filled with the aluminum foam in each case. For the means of comparison, and in order to show how foam reinforcement affects the energy absorption capacity of the frame, one model was tested empty inside, with no foam filling.

5 DEFORMED MODELS

For each structure a different deformed contour plot of the S-shape frame was acquired. These plots present the way the deformation of the frame is carried out once the force induced from the collision impact overcomes the yield strength of the frame material, and the frame starts folding.

Tables 2 and 3 show the contour plots of all the deformed structures. A first comparison between the empty structure SS-1-45-45 and the fully reinforced SSF-1-45-45-1 shows that the empty frame does not sustain much pressure at any of its two bends. On the contrary, as one can see from its deformed contour plot, its curvature points are under great compression, which if increased may lead to buckling at these points. For these reasons the empty frame is not an optimum model for improving passenger safety.

A comparison between the models that have their bend sections filled (models SSF-1-45-45-1 through SSF-1-45-45-1.I in Table 2) and those models that do not have their curvature angles reinforced with aluminum foam (models SSF-1-45-45-1.J through SSF-1-45-45-1.P in Table 3) shows that foam reinforcement at the curves allows the model to sustain more pressure at these points, helping in the prevention of the frame buckling.

Model	Undeformed Foam Shape	Sections Filled	Deformed Contour Plot of the Structure
SS-1-45-45		No sections filled	
SSF-1-45-45-1		All sections (1-7) filled	
SSF-1-45-45-1.A		Sections 3, 4 and 5 filled	
SSF-1-45-45-1.B		Sections 3 and 5 filled	
SSF-1-45-45-1.C		Sections 3, 4 and 5 filled and hollow	
SSF-1-45-45-1.D		Sections 1, 2, 3, 5, 6 and 7 filled	
SSF-1-45-45-1.E		All sections (1-7) filled and hollow	
SSF-1-45-45-1.F		Sections 1, 3, 5 and 7 filled	
SSF-1-45-45-1.G		Sections 3 and 5 filled and hollow	
SSF-1-45-45-1.H		Sections 1, 2, 3, 5, 6 and 7 filled and hollow	
SSF-1-45-45-1.I		Sections 1, 3, 5 and 7 filled and hollow	

Table 2: Different models investigated

Model	Undeformed Foam Shape	Sections Filled	Deformed Contour Plot of the Structure
SSF-1-45-45-1.J		Sections 1, 2, 4, 6 and 7 filled	
SSF-1-45-45-1.K		Two layers of foam in the middle along the structure filled	
SSF-1-45-45-1.L		Sections 1 and 7 filled	
SSF-1-45-45-1.M		Sections 2 and 6 filled	
SSF-1-45-45-1.N		Section 4 filled	
SSF-1-45-45-1.O		Section 1 filled	
SSF-1-45-45-1.P		Section 7 filled	

Table 3: Different models investigated (Continued)

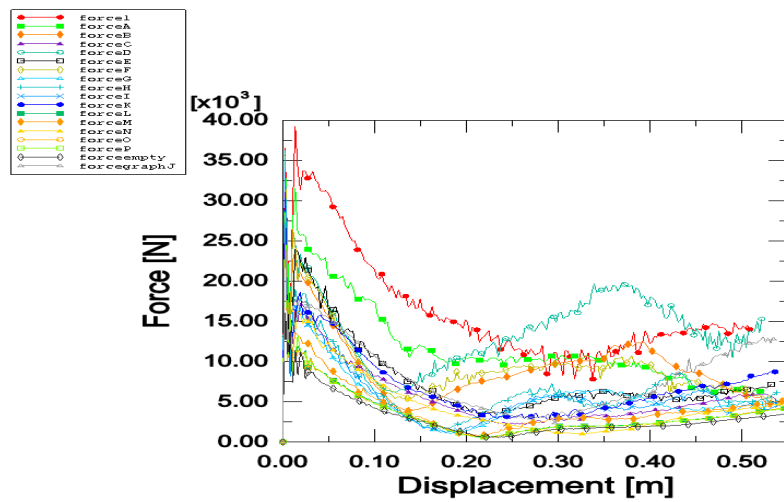


Figure 3: Force vs Displacement

6 IMPACT FORCE

Each frame structure undergoing collision becomes loaded with a force, which results from the collision and induces deformation to the frame. The forces differ in value for each structure. Table 4 gives the peak values of the impact force corresponding to each model. Figure 3 shows the forces for all the frames examined, including the empty frame SS-1-45-45, as a function of displacement. It is clear that structure SSF-1-45-45-1 (the fully reinforced structure) has the highest impact force.

7 ENERGY ABSORBED AND SEA

The area under each force curve gives the energy absorbed by each structure after 0.05 s, which is the time of the simulation. It can, therefore, be assumed that the higher the force curve the greater the amount of energy absorbed by the frame. Figure 4 shows the Energy Absorbed vs. Displacement and that this assumption is true. The graph clearly shows that structure SSF-1-45-45-1, indeed possesses the capacity to absorb the maximum amount of energy, among the models tested, during the front collision.

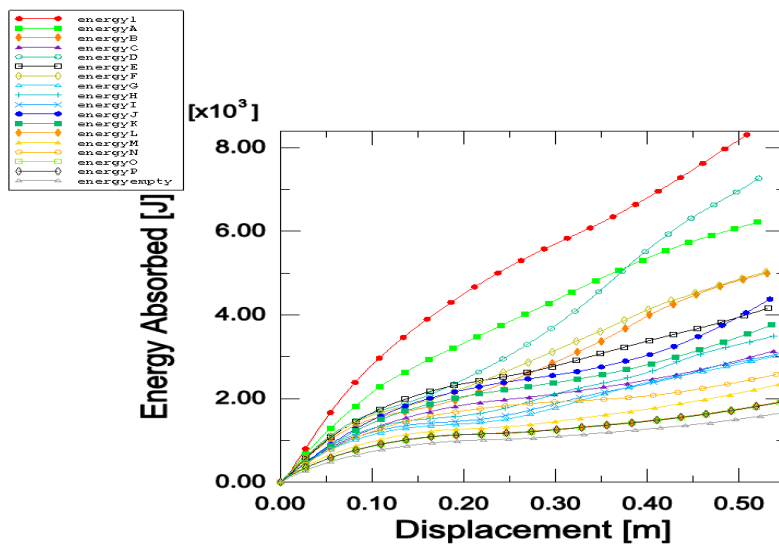


Figure 4: Energy Absorbed vs Displacement

In this study each structure had a different mass. Table 4 shows the numerical values of the maximum energy absorbed as well as the mass of each model. The completely filled model, structure SSF-1-45-45-1, is the heaviest among the models tested, while the empty model SS-1-45-45 is the lightest one. All the partially reinforced structures have a mass in between these two limits.

It has been shown, up to this point, that the completely filled frame, SSF-1-45-45-1, gives the best results as far as energy absorption capacity is concerned, and in addition as shown in Table 4 is displaced the least during the collision, thus keeping the passengers further away

from the collision point, than do the other models. If however, weight and cost are taken into account, a solution of a lighter frame, with partial foam filling must be found. The partially filled and hollow models serve this purpose. In addition, the Specific Energy Absorbed (SEA) was calculated for all the models.

Model	Mass [Kg]	Peak Force [N]	Maximum Energy Absorbed [J]	SEA [J/g]	Displacement [m]
SS-1-45-45	1.50	16,069	1,674	1.12	0.53
SSF-1-45-45-1	3.20	39,224	8,306	2.60	0.51
SSF-1-45-45-1.A	2.45	35,472	6,218	2.54	0.52
SSF-1-45-45-1.B	2.05	34,929	4,991	2.43	0.53
SSF-1-45-45-1.C	2.11	35,159	3,140	1.49	0.54
SSF-1-45-45-1.D	2.85	36,144	7,267	2.28	0.52
SSF-1-45-45-1.E	2.60	35,578	4,164	1.60	0.53
SSF-1-45-45-1.F	2.30	35,475	5,024	2.22	0.53
SSF-1-45-45-1.G	1.85	35,165	3,023	1.63	0.54
SSF-1-45-45-1.H	2.36	35,356	3,495	1.48	0.54
SSF-1-45-45-1.I	1.99	33,872	3,049	1.30	0.54
SSF-1-45-45-1.J	2.63	27,223	4,378	1.66	0.53
SSF-1-45-45-1.K	2.19	30,993	3,766	1.72	0.54
SSF-1-45-45-1.L	1.68	28,375	1,932	1.15	0.55
SSF-1-45-45-1.M	2.05	27,877	2,341	1.14	0.54
SSF-1-45-45-1.N	1.81	27,235	2,577	1.42	0.54
SSF-1-45-45-1.O	1.59	28,105	1,912	1.20	0.55
SSF-1-45-45-1.P	1.59	28,554	1,926	1.21	0.55

Table 4: Mass, Peak Force, Maximum Energy Absorbed, SEA and Displacement Results

The SEA is the ratio of the maximum energy absorbed by the structure to the weight (in grams) of the structure. This way a decision as to which frame is the most appropriate for the passenger's safety is made not only on the premises of energy absorption but also in relation of this energy to the mass of the structure.

Table 4 presents the SEA values for each frame and Figure 5 gives a graphical representation of SEA versus displacement. Structure SSF-1-45-45-1 still presides having the highest SEA value among the models examined.

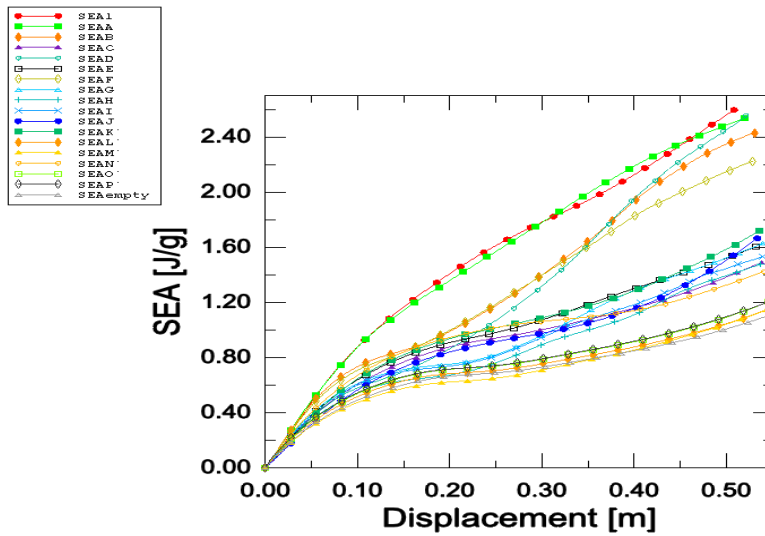


Figure 5: SEA vs Displacement

8 RESULTS AND DISCUSSION

The results of this study have shown that the optimum structure to improve passenger safety is the fully filled structure, SSF-1-45-45-1. This structure has the highest capacity to absorb energy upon the collision, has the highest SEA value among the models tested and the least displacement. However, it also has the maximum impact force as shown in Table 4.

A first look at Table 4 shows that models which have higher absorption capacity and SEA, are the models that have higher impact force. A high value of impact force is an undesirable result that concerns passenger safety in front collisions. A structure must therefore be designed that will have low impact force, high energy absorption capacity, low mass and small displacement, and all this without the risk of buckling.

It can also be concluded from Table 4 that frames that do not have their bends reinforced have lower impact force, but also low SEA values. A comparison between structures SSF-1-45-45-1.B and SSF-1-45-45-1.M is a comparison between two models having the same mass, only the former has its bend sections reinforced while the latter is empty at these points. Table 4 shows that SSF-1-45-45-1.B has more than twice the energy absorption capacity of SSF-1-45-45-1.M, and lower displacement. By the same token, a comparison between structures SSF-1-45-45-1 and SSF-1-45-45-1.A, as well as SSF-1-45-45-1.G and SSF-1-45-45-1.I, can show that models whose ends are reinforced with aluminum foam have higher energy absorption capacity.

Lowering the mass of the structure by reinforcing it with hollow foam parts does not appear to be a good solution. Comparison of models SSF-1-45-45-1 and SSF-1-45-45-1.E as well as SSF-1-45-45-1.F and SSF-1-45-45-1.I - where SSF-1-45-45-1.E and SSF-1-45-45-1.I are the hollow counterparts of SSF-1-45-45-1 and SSF-1-45-45-1.F, respectively – shows a great drop in energy absorption capacity and an increase in displacement. However, a

desirable result of this comparison is that lowering the mass of the frame, reduces the peak impact forces.

The last two models tested, SSF-1-45-45-1.O and SSF-1-45-45-1.P, have exactly the same mass, amount of foam filling, but their filling is at opposite ends. Structure SSF-1-45-45-1.O is reinforced at the front end, while SSF-1-45-45-1.P is reinforced at the rear end of the frame which is the end where the 500 kg mass is applied. It is obvious from the data that the structure reinforced closer to the loaded end has values of peak impact force and maximum energy absorbed higher than the frame reinforced away from the loaded end. However, the difference in the impact force values is higher than the difference in the energy absorption capacity. In the case of the impact force, structure SSF-1-45-45-1.P has 1.6% higher impact force than structure SSF-1-45-45-1.O, while its energy absorption capacity is only 0.6% higher.

It can therefore be concluded that it is not enough to just reinforce a frame with aluminum foam, especially at its curvature and end points, and obtain results of high SEA and small displacement. It is also essential to design a structure that will possess high energy absorption capacity, will have a small displacement during the collision, so as to keep the passengers away from the accident point, but will also result in low peak impact force.

9 CONCLUSIONS

Based on this study, it can be concluded that foam reinforcement is important in maximizing energy absorption capacity of the frame and minimizing displacement. It has been shown that reinforcing the bends and ends of the frame works result in increasing energy absorption, at the expense of a small increase in the peak impact force. In addition, minimizing the mass of the structure is not only a cost effective technique but could result in a decrease of the peak impact force. Finally, it is clear that the position of the reinforcing foam in relation to the position of the load can play a crucial role in maximizing energy absorbed while decreasing the impact force. All these parameters need to be taken into account during the design of optimized aluminum foam reinforced 3D “S” space frame structures.

REFERENCES

- [1] S.R. Reid, T.Y. Reddy, M.D. Gray, “Static and Dynamic Axial Crushing of Foam-Filled Sheet Metal Tubes”, *International Journal of Mechanical Sciences*, 28 (5), 295-322 (1986).
- [2] W. Abramowicz and T. Wierzbicki, “Axial Crushing of Foam-Filled Columns”, *International Journal of Mechanical Sciences*, 30 (3/4), 263-271 (1988).
- [3] S. Santosa and T. Wierzbicki, “Effect of an Ultralight Metal Filler on the Torsional Crushing Behavior of Thin-Walled Prismatic Columns”, *International Journal of Mechanical Science*, 41, 995-1019 (1997).
- [4] J. Han and K. Yamazaki “Crashworthiness Optimization of S-Shape Square Tubes”, *International Journal of Vehicle Design*, 31 (1), 72-85 (2003).
- [5] C. Zhang, *Study of Crash Behavior of a 3-D-Shape Space Frame Using Finite Element Method*, M.S. Thesis, Tufts University, Medford, MA (2005).

- [6] R. Fragoudakis and A. Saigal, "Effect of Aluminum Foam and Foam Density on the Energy Absorption Capacity of 3D S-Space Frames," Paper # 70_Sai, *Proceedings of the International Conference on Experimental Mechanics (ICEM-13)*, Springer, E.E. Gdoutos (Ed.), Alexandroupolis, Greece, July 1-6, 2007.
- [7] T.G. Nieh, K. Higashi, and J. Wadsworth, "Effect of Cell Morphology on the Compressive Properties of Open-Cell Aluminum Foams", *Materials Science and Engineering*, A283, 105-110 (2000).